Investigating DNA−polymer conjugates by low-volume aqueous polymerization-induced self-assembly (PISA)

by

Siriporn Chaimueangchuen

A thesis submitted to the University of Birmingham for the degree of

DOCTOR OF PHILOSOPHY

School of Chemistry

College of Engineering and Physical Sciences

University of Birmingham

September 2023

Abstract

Over the past few decades, deoxyribonucleic acid (DNA)-polymer conjugates have been attracting interest as adaptable functional materials in various biorelated applications. However, determining the optimal synthetic conditions of conjugating hydrophilic DNA with hydrophobic polymers still presents a significant challenge and this limitation currently constrains the progress of research in this field. In recent decades, polymerization-induced self-assembly (PISA) has attracted significant attention for constructing nano-objects with various morphologies such as vesicles, worms, and spheres owing to the one-step nature of the process. To date, the most commonly utilized polymerization technique in PISA is reversible-addition fragmentation chain transfer (RAFT) polymerization due to its versatility and broad applicability.[1, 2] In RAFT-mediated emulsion PISA, a solvophilic macromolecular chain transfer agent (macroCTA) and a solvent-miscible monomer are polymerized to generate solvophobic polymer and create self-assembled nanostructures.[3] Thus, PISA could be a potential method for producing amphiphilic DNA-polymer nanostructures. However, the high cost of DNA necessitates the use of minimal reaction volumes in PISA procedures, which remains an ongoing challenge due to limitations such as oxygen inhibition, low potential reproducibility, and the requirement for special equipment. This Ph.D. project aims to develop reproducible conditions for low-volume PISA reactions in an attempt to utilize a deoxyribonucleic acid macromolecular chain transfer agent (DNA-macroCTA) and 2-hydroxypropyl methacrylate (HPMA) monomer to generate DNA-decorated polymeric nanostructures of various morphologies *via* PISA for future medical applications.

In chapter 2, poly(ethylene glycol) macromolecular chain transfer agent was synthesized, and their corresponding synthetic diblock copolymers with HPMA monomer were prepared *via* RAFT-mediated photoinitiated PISA. The optimalization of a low-volume system was investigated through physical and chemical strategies to eliminate oxygen inhibition in low-volume polymerization. Nitrogen glove bag method was applied for curing in an oxygen-free atmosphere for physical strategy while glucose oxidase (GOx) in the presence of glucose, was applied in chemical strategy. Moreover, phase diagram was investigated in the optimal low volume conditions. This optimal low volume condition was applied with the DNA-macroCTA and the identical HPMA monomer in chapter 3. This chapter was divided into two sections, each focusing on the generation of DNA-PHPMA nanoparticles through different sources of synthesized DNA-macroCTA. The first section utilized DNA-macroCTA received from the Sleiman group, our collaborators while the second section involved DNA-macroCTA synthesized by our group. Additionally, two methods for synthesizing DNA-macroCTA were highlighted, involving both solution-based and solid support approaches. This chapter further explored the impact of salts and hybridization with the DNA-polymer particles. In chapter 4, the combination of PEG-macroCTA and DNA-macroCTA was investigated to facilitate morphological transitions in DNA-decorated particles. Moreover, the utilization of hybridization and hybridization chain reaction (HCR) was explored with the mixture corona of PEG and DNA.

แด่พ่อแม่และครอบครัว

This thesis is dedicated to my family for their invaluable support throughout the years.

Acknowledgements

I firmly believe that no thesis is the result of solitary effort. I owe gratitude to the numerous individuals who supported me throughout my Ph.D. journey, and I am committed to expressing my appreciation to each and every one of them in a meaningful way.

To begin, I would like to sincerely extend my heartfelt appreciation to my supervisor, Professor Rachel O'Reilly, for welcoming me into her research group, on such a productive field of study. I am genuinely grateful for her unwavering support, mentorship, and guidance on scientific, linguistic, and personal fronts.

I would also like to extend my heartfelt gratitude to my first PISA and DNA mentors, Dr. Spyridon Varlas and Dr. Thomas Wilks. I am sincerely appreciative of your mentorship, engaging scientific discussions, idea exchanges, problem-solving skills, and constructive criticism throughout my project. Both of you have played a significant role in deepening my understanding of topics such as RAFT, PISA, block copolymer self-assembly, DNA-polymer conjugates, and more. Your inspiration has touched me in numerous ways, and I've assimilated many of your techniques and practices, contributing to my growth as both a scientist and an individual. A special thank you to Tom – your unwavering positive support has been a cornerstone in every aspect. In the beginning, my English was rudimentary, and you were among the key figures who suggested, encouraged, and guided me through this phase. I must not overlook the presence of the 'lab 715' matriarch, Dr. Jennifer Frommer. Thank you very much, your consistent support and comforting presence have created an inviting atmosphere within our DNA lab. Your encouragement to become an independent and resilient woman resonates deeply with me. Additionally, I express my gratitude to Dr. Calum Ferguson for his support in my work, assistance in refining my writing, and even replenishing my energy with refreshments. The completion

of this thesis wouldn't have been possible without the invaluable contributions from all of you in the fields of DNA and polymers. Your guidance has been crucial in helping me navigate academic challenges and learn how to overcome setbacks in order to survive. Moreover, I would like to thank Dr. Julia Rho for your invaluable academic insights and support. Our discussions have been immensely valuable, given your expertise as a knowledgeable scientist in the area of self-assembly and polymer science.

I would like to thank all our senior members and former colleagues within our research group Dr. Marjolaine Thomas (My nucleobase-PISA project's tutor), Dr. Irem Akar (My north Wales squad), Dr. Simon Dale (Our king of birds), Dr. Cinzia Clamor (Love your beautiful smile), Dr. Eirini Epitropaki (Pretty Mascot), Dr. Maria Pervez (caramel chocolate flappe lover), Dr. Matthieu Miclotte (Daddy of cute baby), Dr. Lucy Arkinstall (DNA professor), Dr. Stefan Lawrenson (DLS teacher), Dr. Maria Chiara Arno (oh my confocal expert), Dr. Bo Li (cake cake cake), Dr. Yujie Xie (Most beautiful figure maker), Dr. Wei You (stress but fun?), Dr. Zehua Li (Rich boss) and Dr. Sètuhn Jimaja (Kind and calm person), Dr. Robert Keogh (Column is fun), Dr. Jon Husband (DNA designer), Dr. Anissa Khalfa (Plant's mom), and Dr Viviane Chiaradia (Queen of happiness) and Dr. Sam Pakinson (Ah I'll really miss your colorful shoes) for all the support you've given me throughout my early years of Ph.D.

I would like to extend my thanks to all my friends from the O'Reilly and Dove groups who have made my daily life in the lab an enjoyable and unforgettable experience. Your support during both the good and more challenging times over the past four years is greatly appreciated. I would like to thank my DNA lab mates: Mr. Ben Allot (HPLC column dad), Ms. Jess Hawkins (So you are HPLC mom), Ms. Bethany Crow (My pretty yoga classmate), Mr. David Londono (Powerful weightlifter), Mr. Jake Barker (my best fume cupboard sharer, you always entertain everyone), Ms. Rachel Stracey (Frank girl),

Ms. Philippa Edge (Sweet girl), Miss Megan Elliott (soulmate will be with you soon) and my Chinese plus badminton team: Mr. Laihui Xiao (I believe we are twins - same birth year and life background!), Mr. Tainlai Xia (Always smile “on” person), Mr. Yu Lu (I know you wanna joy the conversations), Mr. Kaixiang Yang (Cool man), Mr. Jian Zhang (Badminton professional), and Lukmanul Hakim Samada (Indonesian smashed pro), Dr. Stephen Fielden (Daddy of cutie baby girl), Dr. Parvaneh Eskandari (Pretty Iranian butterfly), Dr. Neha Yadav (My Zumba mate), Ms. Ana Cubillo Álvarez (You are the best, Ana), Mr. Daniele Giannantonio (Ciao!), Ms.Bige Bati (I love your tattoo), Ms.Gabriela Garbonova (I hope we can talk about travelling again), Ms. Flore Kilens (my lovely cutie Flower), Ms. Claire Morand (Best weightlifter), Ms. Emma Catterson (Hope to see your horse), Mr. Elliott Smith (So calm), Ms. Susanna Harvey (Lovely smile person), Mr. Adam Redfearn (Flying man), Dr. Natalia Reis (Schrenk line supervisor), Dr Alexis Perrot (French actor), Dr Thiago Ouriques Machado (Brazilian super model).

Next, I would also like to express my gratitude to all the special friends who began their Ph.D. journeys alongside me in the same year. I vividly recall our first year as Ph.D. students. Life was not easy, but we persevered and have all done remarkably well. I would like to thank Mr. Ed Maynard (The kindest person and my English teacher), Ms. Alisha Miller (ROMPISA’s heir from Spyros), Dr. Matt Price (Smart and Colorful man).

I would like to thank all the researchers, technicians and assistants at the University of Birmingham for sharing their expertise and knowledge and spending many hours training me in various characterization techniques. I want to extend special thanks to Ms. Julia Valverde and Dr. Daniel Smith for their collaboration on all lab instruments and supplies. Your efforts have made working in the lab significantly more convenient for all of us. I would like to convey my deep gratitude to our dedicated research administrator, Miss Tessa Kintail. Her unwavering assistance in various matters has been invaluable to me

and all the members of the O'Reilly group. She has made our lives significantly easier by efficiently resolving the numerous administrative issues that have arisen over the years. Furthermore, I want to express my appreciation to the journal editors and reviewers who managed my work. Your dedication of time and the constructive input you provided have been immensely valuable.

Importantly, I would like to thank the DPST for funding my Ph.D. studies, and the funding from my supervisor for contributing to the publication my paper in open-access form and supporting my participation in national and international conferences. I am deeply grateful for their financial support, as without it, I wouldn't have been able to fulfill my dream of pursuing my Ph.D. abroad!

Lastly, but certainly not least, I want to express my heartfelt gratitude to my family and Thai Friends for their unwavering support throughout my Ph.D. journey. To my parents, Mr. Kosan Chaimueangchuen and Ms. Watcharee Chaimueangchuen, I extend my sincerest thanks.

Table of Contents

List of Figures

List of Schemes

List of Symbols and Abbreviations

[M]	Monomer concentration
°C	Degrees Celsius
a	Area
ACVA	Azobis(4-cyanovaleric acid)
ATRP	Atom-transfer radical polymerization
c	Concentration
cDNA	Complementary deoxyribonucleic acid
CD_3OD	Methanol-d_4
$CDCl_3$	Chloroform-*d*
CEPA	4-Cyano-4-[(ethylsulfanylthiocarbonyl)sulfanyl]pentanoic acid
cm^{-1}	Wavenumber(s) per centimeter
cryo-TEM	Cryogenic transmission electron microscopy
CTA	Chain transfer agent
Cu	Copper
Cy5-NHS	Cyanine5 succinimidyl ester
d	Deuterium labelled
D	Diameter
D	Diffusion coefficient
D_{ave}	Average diameter
DCC	*N,N′*-Dicyclohexylcarbodiimide
DCM	Dichloromethane
D_h	Hydrodynamic diameter
DI water	Deionized water

DIAD	Diisopropyl azodicarboxylate
DLS	Dynamic light scattering
$Đ_M$	Dispersity
DMAP	4-(Dimethylamino)pyridine
DMF	*N*,*N*-Dimethyl formamide
DMSO	Dimethyl sulfoxide
dn/dc	Refractive index increment
DNA	Deoxyribonucleic acid
DP	Degree of polymerization
dsDNA	Double stranded deoxyribonucleic acid
EDC.HCl	*N*-(3-Dimethylaminopropyl)-*N*′-ethylcarbodiimide hydrochloride
eq	Equivalent(s)
EtOAc	Ethyl acetate
FAM-NHS	5/6-Carboxyfluorescein succinimidyl ester
FT-IR	Fourier Transform-Infrared
g	Gram(s)
GOx	Glucose oxidase
H	Hairpin
h	Hour(s)
H_2O	Water
H_2O_2	Hydrogen peroxide
HPLC	High-performance liquid chromatography
HPMA	2-Hydroxypropyl methacrylate
I	Initiator
K	Degrees Kelvin

kapp	Kinetic constant
kDa	Kilodaltons
kV	Kilovolts
l	Length
LAMs	Less activated monomers
LED	Light emitting diode
m/z	Mass to charge ratio
mA	Milliamp(s)
macroCTA	Macromolecular chain transfer agent
MAMs	More activated monomers
MeCN	Acetonitrile
MeOH	Methanol
mg	Milligram(s)
$MgSO_4$	Magnesium sulfate
min	Minute(s)
mL	Milliliter(s)
MLVs	Multilamellar vesicles
mM	Millimolar
mm	Millimeter(s)
mmol	Millimole(s)
M_n	Number average molecular weight
mol	Mole(s)
mV	Millivolt(s)
M_w	Weight average molecular weight
mW	Milliwatts

MW	Molecular weight
MWCO	Molecular weight cut-off
MΩ	Megaohm(s)
n	Refractive index
N_2(g)	Nitrogen gas
N_A	Avogadro's number
Na_2SO_4	Sodium sulfate
NaCl	Sodium chloride
N_{agg}	Aggregation number
$NaHCO_3$	Sodium bicarbonate
ncDNA	Noncomplementary deoxyribonucleic acid
NEt^3	Triethylamine
NH_4BF_4	Ammonium tetrafluoroborate
nm	Nanometer(s)
NMP	Nitroxide-mediated polymerization
NMR	Nuclear magnetic resonance
p	Packing parameter
PAA	Polyacrylamide
PD	Polydispersity
PEG	Poly(ethylene glycol)
PEG-*b*-PHPMA	Poly(ethylene glycol)-*b*-poly(2-hydroxypropyl methacrylate)
PET	Photo-induced electron/energy transfer
PGMA-*b*-PHPMA	Poly(glycerol monomethacrylate)-*b*-poly(2-hydroxypropyl methacrylate)
Photo-PISA	Photoinitiated polymerization-induced self-assembly

Photo-RAFT	Photoinitiated reversible addition−fragmentation chain-transfer
PISA	Polymerization-induced self-assembly
PMMA	Poly(methyl methacrylate)
PS	Polystyrene
R	Radius
RAFT	Reversible addition−fragmentation chain-transfer
RDRP	Reversible-deactivation radical polymerization
R_g	Radius of gyration
R_h	Hydrodynamic radius
RI	Refractive index
RP-HPLC	Reverse phase high-pressure liquid chromatography
rpm	Rounds per minute
R_θ	Rayleigh ratio
S	Spherical micelles
s	Second(s)
SAXS	Small-angle X-ray scattering
SEC	Size exclusion chromatography
SLS	Static light scattering
SPTP	Sodium phenyl-2,4,6-trimethylbenzoylphosphinate
ssDNA	Single stranded deoxyribonucleic acid
t	Time
TEM	Transmission electron microscopy
TMS	Tetramethylsilane
Triton X-100	4-(1,1,3,3-Tetramethylbutyl)phenyl-polyethylene glycol
UA	Uranyl acetate

ULVs	Unilamellar vesicles
UV	Ultraviolet
UV-Vis	Ultraviolet–visible
V	Vesicles
V	Volts
vs	Versus
W	Worm-like micelles
δ	Chemical shift
η	Viscosity
λ	Wavelength
$\lambda em.$	Emission wavelength
$\lambda ex.$	Excitation wavelength
µg	Microgram(s)
µL	Microliter(s)
µM	Micromolar
µmol	Micromole(s)
ν	Wavenumbers
T	Temperature
θ	Angle

List of publications

1. Siriporn Chaimueangchuen, Jennifer Frommer, Calum T. J. Ferguson, and Rachel O'Reilly. Surface hybridization chain reaction of binary mixture DNA-PEG corona nanostructures produced by low-volume RAFT-mediated photopolymerization-induced self-assembly. *ACS Bioconjugate Chem*, 2023, **34**, 11, 2007–2013 (**Chapter 4)**

Declaration of Authorship

This thesis is submitted to the University of Birmingham in support of my application for the degree of Doctor of Philosophy. No material contained here has been submitted previously for the award of any degree.

The work presented herein, including project design and performance of experiments, materials characterization, data collection and analysis, figure and manuscript preparation, was carried out by myself except for contributions from other colleagues which are outlined below:

Chapter 2 – The design and construction of the photoreactor used for the photoinitiated polymerizations was carried out by Mr. Rod Wesson at the University of Warwick. Dr. Spyridon Varlas and Dr. Thomas Wilks provided guidance of this project at the University of Birmingham. Prof. Rachel K. O'Reilly supervised the research project at the University of Birmingham.

Chapter 3 – Cryo-TEM imaging of block copolymer nano-objects was performed with assistance from Dr. Marjolaine Thomas at the University of Warwick. Confocal microscopy imaging of dye-containing block copolymers samples was carried out with assistance from Dr. Yujie Xie at the University of Birmingham. Dr. Jennifer Frommer and Dr. Thomas Wilks provided guidance of this project at the University of Birmingham. Prof. Rachel K. O'Reilly supervised the research project at the University of Birmingham.

Chapter 4 – Cryo-TEM imaging of block copolymer nano-objects was performed with assistance from Dr. Stephen Fielden and Miss Alisha Miller at the University of Warwick. Confocal microscopy imaging of dye-containing block copolymers samples was carried out with assistance from Dr. Chiara M Arno at the University of Birmingham. Dr. Jennifer Frommer and Dr. Calum T. J. Ferguson provided guidance and editing of this manuscript

at the University of Birmingham. Prof. Rachel K. O'Reilly supervised the research project, provided guidance and editing of this manuscript at the University of Birmingham.

Parts of this thesis have been submitted for publication by the author in the following scientific journals:

-*ACS Bioconjugate chemistry* (**Chapter 4**) – DOI: 10.1021/acs.bioconjchem.3c00293

The author used ChatGPT during the preparation of this thesis to check the grammar. After utilizing the tool, the author thoroughly reviewed and edited the contents as necessary and assumed full responsibility for the thesis contents.

1 : Introduction

1.1 Functional nanostructures and self-assembly

Functional nanostructures refer to materials or systems made of organised molecules in the range of approximately 1 to 100 nm, which could be in the form of nanoparticles, nanotubes, or nanofilaments.[4] The use of nanostructures has rapidly expanded in popularity over the past few decades because these structures enable new functionalities, either by themselves or by their incorporation in composites.[4] Nanomaterials are now utilized across almost all fields of technology and are generally prepared through two contrasting approaches for the fabrication and assembly *i.e*. "Top-down" strategy and "Bottom-up" strategy.[5] The top-down approach involves commencing with a larger or bulk material and employing various techniques to reduce it to the nanoscale. Common techniques include lithography, grinding, and chemical etching which can offer excellent control and precision over the final product's size, shape, and properties. However, scaling down materials and structures to the nanoscale while preserving the desired properties can be a formidable challenge, and this process may generate waste materials as a byproduct while potentially causing imperfections in the surface structure. Bottom-up methods, on the other hand, initiate with individual atoms, molecules, or nanoparticles, and then proceed to construct larger and more complex structures through self-assembly, which has the potential to create less waste. Self-assembly involves the spontaneous organization of molecules driven by intermolecular interactions such as hydrogen bonding, metal coordination, hydrophobic forces, van der Waals forces, π–π interactions, or electrostatic forces, providing access to a wide range of morphologies.[6] These assemblies can potentially be utilised in numerous fields ranging from drug delivery systems,[7] nanoreactors,[8] and sensors,[9] to electronic components.[10] Nanocomponents prepared by self-assembly may be composed of a range of materials including metals and alloys, semiconductors, biological macromolecules and polymers.[11]

1.2 Polymerization techniques

Polymers play a crucial role in nanotechnology, in particular, are highly appealing as building blocks for self-assembled nanostructures, due to their ability to offer a combination of advantages, including flexibility, processability, cost-effectiveness, nanometer-scale dimensions, diverse functionalities, and the capability for microphase separation.[12] Polymers are macromolecules composed of small repeat units known as monomers, which are mainly divided into two types based on their structure, *i.e.* natural and synthetic polymers. Natural polymers can be ordinarily found in biological systems, such as proteins and DNA, while synthetic polymers are man-made – polyethylene and nylon are two well-known examples.[13] Polymers can be composed of a single type of monomer (homopolymers) or more than one type of monomers (copolymers).[13] The fundamental mechanisms of polymer formation are step-growth and chain-growth polymerization. Step-growth polymerization, also known as condensation polymerization or polycondensation, is a polymerization mechanism in which polymers are formed through the sequential reaction of functional groups on monomers.[14-16] Step-growth polymerization involves the reaction between two different types of monomers, each possessing reactive functional groups, which are able to react with each other, forming covalent bonds and linking the monomers together. In step-growth polymerization, monomers react with each other to initially form dimers, then combine again into longer and longer oligomers and finally into long-chain polymers. The average molecular weight of individual polymer chains remains comparatively low during the polymerization until it approaches near-complete conversion (Figure 1.1A). In principle, polymers with high molecular weights are primarily achieved at the final stages of the reaction, where near-quantitative monomer conversions occur, and oligomers are able to undergo further reactions with each other. This process typically produces numerous potential side-

products and corresponds with a broadening of the molecular weight distribution in the resulting polymers. On the other hand, chain-growth polymerization proceeds between monomers and active sites on the polymer chain involving initiation, propagation, and termination steps. [15] The polymerization process begins with the initiation step, where an initiator molecule or a reactive site on a monomer forms a reactive species called a "free radical" or an "active center". The active center reacts with a monomer molecule in propagation step, forming a covalent bond and creating a new reactive site at the end of the growing polymer chain. This process continues as monomers add one by one to the chain end, leading to chain growth. Termination occurs when two active chain ends react with each other, resulting in the formation of a covalent bond and the end of the polymerization process. Chain termination can also happen if a radical reacts with a terminating agent or if the initiator is depleted. Its main limitation is poor control over polymer chain length due to rapidly proceed of polymerization at the very early reaction stages and low monomer conversions making a challenge to control the reaction rate (Figure 1.1B).

In 1956, Michael Szwarc initially coined the term of living polymerization, where the chain termination reaction was entirely absent from a chain-growth polymerization process.[17] It involves the polymerization process under specific conditions: (a) a linear correlation between polymer molecular weight and monomer conversion exists (Figure 1.1C), (b) the polymer chains being synthesized remain active even after complete conversion, thereby allowing further chain extension with subsequent monomer additions, (c) the resultant polymers exhibit narrow molecular weight distributions, and (d) the final polymer's degree of polymerization (DP) can be controlled by adjusting the stoichiometric ratio of monomer to initiator.[17, 18] Examples of living polymerization are anionic[19] and cationic[20] polymerization, and ring-opening metathesis polymerization

(ROMP).[21] Another key aspect of living polymerization lies in the considerably higher initiation rate compared to the propagation rate, leading to uniform growth for all polymer chains in terms of both timing and rate.[22] Thus, polymers acquired through living polymerization can possess controlled lengths and narrow dispersity.[23] Nonetheless, in the majority of instances, living polymerization methodologies demand rigorously controlled reaction conditions, such as the thorough elimination of oxygen and water from the system, along with the utilization of costly specialized equipment which significantly limits their applicability and potential.[24]

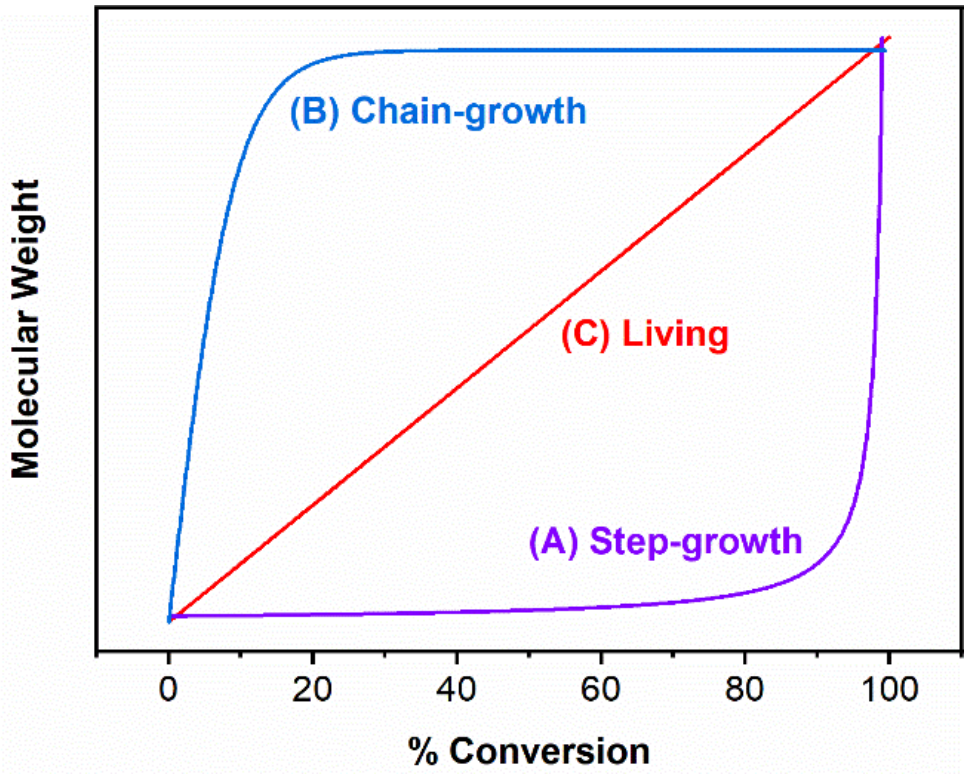

Figure 1.1. Relationship between polymer molecular weight and increasing monomer conversion for (A) step-growth polymerization, (B) conventional chain-growth polymerization, and (C) living polymerization.

1.2.1 Reversible-deactivation radical polymerization (RDRP) techniques

Reversible-deactivation radical polymerization (RDRP), more commonly recognized as controlled radical polymerization (CRP), are a group of controlled polymerization methods that allow for the synthesis of well-defined polymers with controlled molecular weights, narrow molecular weight distributions, and specific architectures.[25] These techniques involve a dynamic equilibrium between propagating active chains and dormant species (inactive chains), by using suitable capping or chain transfer agents (CTAs), leading to a decrease in early termination of the polymerization and an increase in control over chain length.[26] Active chains can either be reversibly trapped in a deactivation/activation process as shown in Scheme 1.1a, or they can be involved in a degenerative exchange process called ‘‘reversible chain transfer’’ according to Scheme 1.1b.[26, 27] There are three main RDRP techniques that employ different types of chain transfer agent (CTA), which are nitroxide-mediated polymerization (NMP),[28] atom transfer radical polymerization (ATRP),[29] and reversible addition-fragmentation chain transfer (RAFT).[30] NMP and ATRP rely on the process of deactivation/activation polymerization, whereas RAFT relies on reversible chain transfer polymerization. Further details about these mechanisms are provided below.

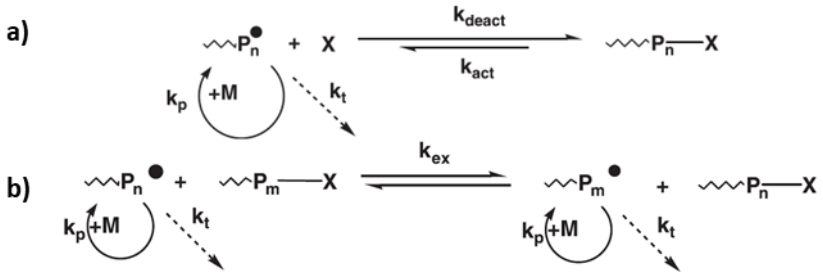

Scheme 1.1. a) Deactivation/activation polymerization b) reversible chain transfer polymerization. Adapted from ref. [26] .

NMP involves the use of a nitroxide-mediated living free radical as a mediator to reversibly deactivate the growing polymer chains, thus allowing control over the polymerization rate. [31-34] The polymerization is initiated using an initiator, alkoxyamines ($R–N–O–R_2'$), which generates radical species ($R^{\cdot}$ and $R_2'–N–O^{\cdot}$), subsequently reacts with the monomer (M), forming a radical ($Pn^{\cdot}$) that initiates the polymerization. As the polymer chain grows, a nitroxide radical ($R_2'–N–O^{\cdot}$) is introduced as a mediator and interacts with the growing polymer chain radical ($Pn^{\cdot}$), leading to a temporary deactivation of the chain ($Pn–N–O–R_2'$) which reduces the polymerization rate. Over time, the nitroxide radical ($R_2'–N–O^{\cdot}$) dissociates from the polymer chain radical ($Pn^{\cdot}$), allowing the polymerization to reactivate and resume the controlled growth of the polymer chain (Scheme 1.2a).[28, 34-36] NMP is a catalyst-free polymerization technique, well-defined molecular weights, narrow molecular weight distributions, and controlled architecture; however, alkoxyamines initiators typically required elevated temperatures (usually > 100 °C).

ATRP is also one of RDRP methods and has gained significant attention in polymer science.[37, 38] ATRP begins with the initiation step, where an initiator molecule (a secondary or tertiary alkyl halide, R–X) undergoes a reversible redox reaction using a transition metal complex (M^xL_n, *e.g.*, Cu^ICl) as the catalyst (or activator), generating an active radical species ($R^{\cdot}$) and an oxidized catalytic species ($X–M^{x+1}L_n$). The active radical ($R^{\cdot}$) reacts with a vinyl-type monomer (M), forming a new radical on the monomer and growing active polymer chain ($Pn^{\cdot}$). In the main equilibrium step, the active polymer chain ($Pn^{\cdot}$) can either continue to propagate by reacting with additional monomer or reversibly react with the oxidized metal complex ($X–M^{x+1}L_n$), leading to the deactivated chain end (Pn–X) and initial catalyst (M^xL_n). The deactivated polymer chain end (Pn–X) can be reactivated by a catalyst (M^xL_n), allowing for the resumption of polymer chain

growth (Pn˙) (Scheme 1.2b).[39] This reversible deactivation is a key feature of ATRP and prevents conventional termination reactions.

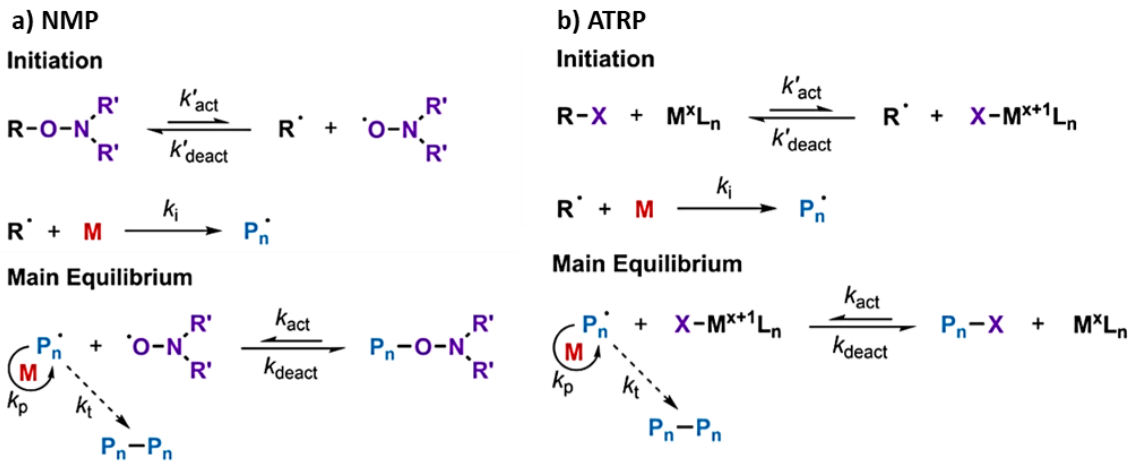

Scheme 1.2. Generic mechanism for (a) nitroxide-mediated radical polymerization (NMP) and (b) atom transfer radical polymerization (ATRP) using a metal-ligand complex and an alkyl halide initiator, along with rate constants in the main equilibrium. Adapted from ref [35] and ref [39] , respectively.

1.2.2 Reversible Addition-Fragmentation Chain Transfer (RAFT) Polymerization

Reversible addition-fragmentation chain transfer (RAFT) polymerization is one of the most popular RDRP techniques due to the excellent control of polymer chain length that can be achieved, its compatibility with a wide range of monomers, and the mild conditions required.[40, 41] RAFT proceeds *via* a reversible chain transfer mechanism while NMP and ATRP are deactivation/activation mechanism. The technique involves the use of a RAFT agent, also known as a RAFT chain transfer agent (CTA), which is a molecule that mediates the polymerization process. The structure of a RAFT-CTA involves a thiocarbonylthio or trithiocarbonate group to control free-radical polymerization *via* a reversible chain-transfer process as shown in Scheme 1.3.[30, 42] In step 1, an initiating radical (**I˙**) reacts with monomers (**M**) providing a propagating radical polymer chain (**Pn˙**). Then, the propagating radical polymer chain (**Pn˙**) attaches to the C=S group of

the CTA (**1**) and an intermediate radical species (**2**) is generated. **2** can fragment either back to the initial state (**Pn**˙ and **CTA**) or to **3** and a new initiating radical, **R**˙. Subsequently, new propagating radical chains (**Pm**˙) are formed after reinitiation by **R**˙ (step 3). In step 4, a rapid equilibrium is established between the dormant species (**3**) and active chains (**Pn**˙ and **Pm**˙) giving equal opportunity for all chains to grow, leading to a low dispersity polymer product. Finally, radical polymerization is inevitably terminated in step 5. It is important to highlight that only one fragmentation can occur at a time, meaning either **Pn**˙ or **Pm**˙ chain can propagate from this equilibrium. The equilibrium constants indicate that *k*add /*k*-add>> *k*p, suggesting that the addition of the growing chain to the CTA occurs more rapidly than fragmentation and propagation. As a result, the concentration of active growing polymer radicals remains low, effectively preventing termination events (Step 5) (*e.g.*, coupling of **Pn**˙ or **Pm**˙). RAFT polymerization can be employed not only for linear block copolymers but also for complex architectures, such as comb-like, star, brush structures, and cross-linked networks.[30]

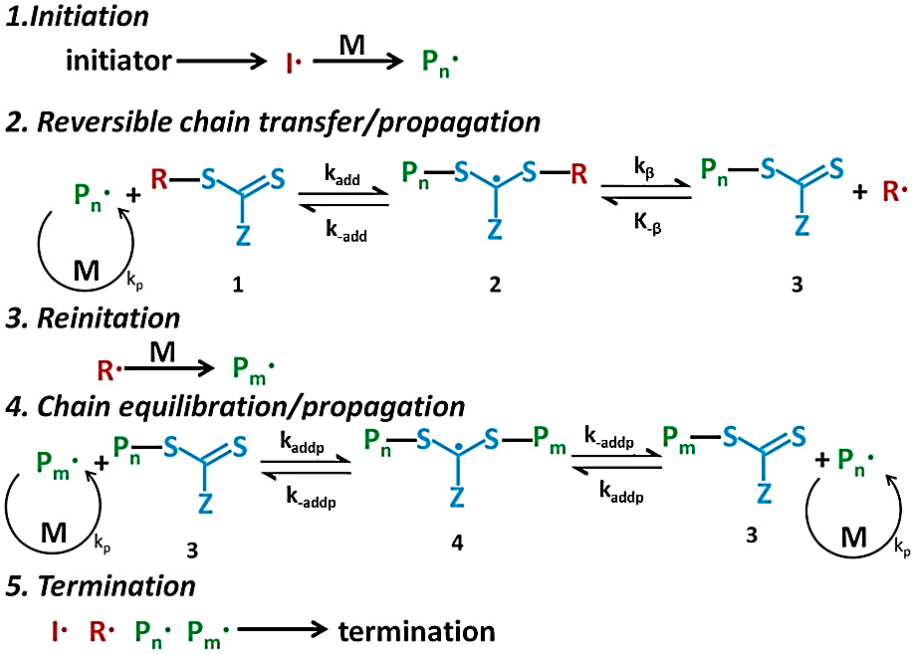

Scheme 1.3. Proposed Mechanism of Reversible Addition−Fragmentation Chain Transfer Polymerization. Adapted from ref. [16].[30]

A RAFT agent typically consists of three main components: a reversible chain transfer group (CTG, **(C=S)-S**), such as a thiocarbonylthio group, a leaving group (**Z**), and a polymerizable unit (**R**), where nature of both **R** and **Z** groups affect their efficiencies to achieve well-controlled RAFT polymerization (Figure 1.2).[42-44] The CTG is responsible for mediating the chain transfer process, allowing for control over the polymerization. The R-group should function as an effective homolytic leaving group from the intermediate CTA-derived radical species relative to the growing polymer chain, ensuring that **R˙** radical must be both proficient and stable in order to reinitiate the polymerization. Additionally, the type of monomer (more activated monomers (MAMs) *vs* less activated monomers (LAMs)) also influences the addition-fragmentation stage, which can impact the control of RAFT polymerization. The leaving ability of the growing **Pn˙** is directly influenced by the composition of the monomer, exhibiting a descending trend in the sequence: methacrylates, methacrylamides >> styrenics, acrylamides, acrylates > N-vinyl amides, vinyl esters.[45, 46] In contrast, the Z-group chemistry in a RAFT agent is responsible for the reactivity of the C=S bond toward radical addition- fragmentation and influences the stability of the CTA-derived radical intermediate. Therefore, the selection of the Z-group must be appropriate to ensure that the intermediate radical species achieve a suitable level of stability, but should also exhibit a controlled level of instability, which facilitate fragmentation events to a certain degree in order to promote propagation. To date, CTAs have been reported in four main categories based on the atom of the **Z** that is connected to the thiocarbonylthio moiety composing of dithioesters (for C), trithiocarbonates (for S), dithiocarbamates (for N), and xanthates (for O) (Figure 1.2). The choice of Z-group can also affect the solubility of the RAFT agent in the reaction medium and the compatibility of the RAFT agent with different monomers and reaction

conditions, while a comprehensive guide for selection of CTA based on each monomer type is shown in Figure 1.3.

Figure 1.2. Typical structures of chain transfer agents (CTAs) based on the functionality of the Z– group. Reproduced from ref.[42]

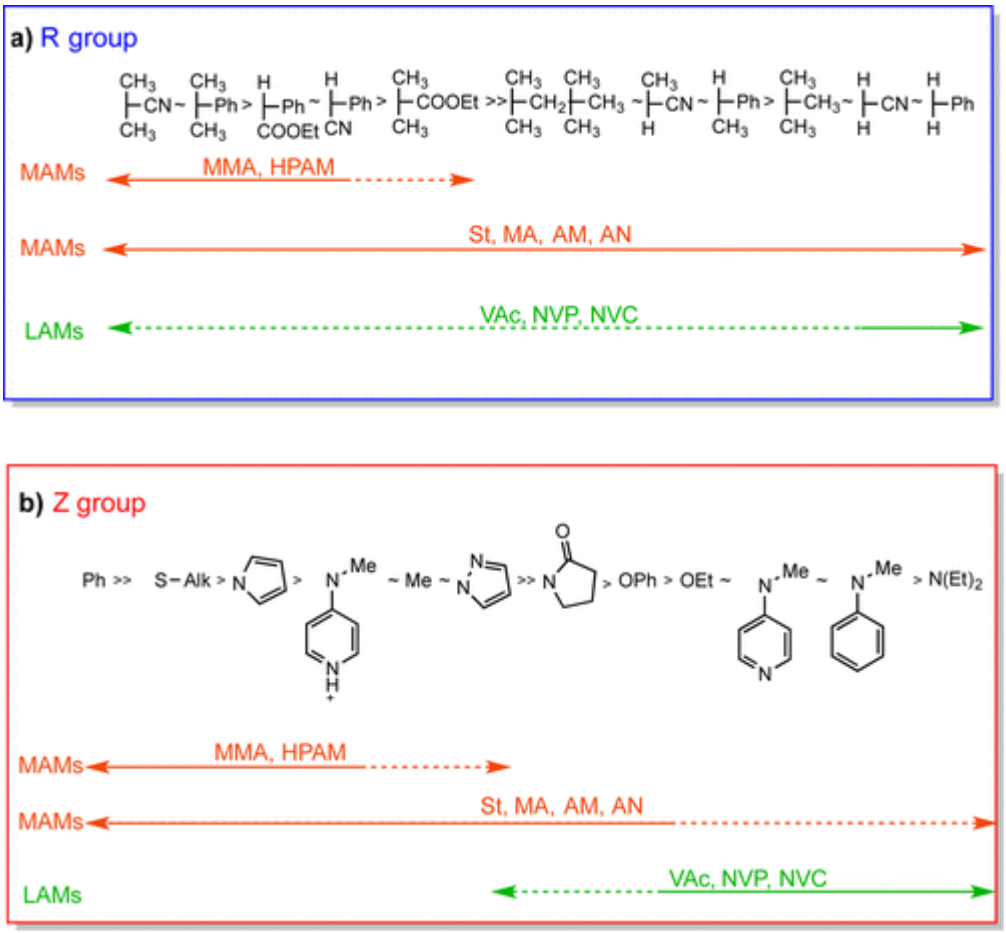

Figure 1.3. Comprehensive guidelines for selection of the R- and Z-group of RAFT agents, presented in relation to the control of RAFT polymerization for diverse monomers. The dashed lines represent limited polymerization control. Abbreviations: MMA = methyl methacrylate, HPMAM = *N*-(2-

hydroxypropyl)methacrylamide, St = styrene, MA = methyl acrylate, AM = acrylamide, AN = acrylonitrile, VAc = vinyl acetate, NVP =*N*-vinylpyrrolidone, and NVC = *N*vinylcarbazole. Reproduced from ref.[42]

By adjusting the concentration of the RAFT agent and the monomers, it is possible to achieve precise control over the molecular weight, polymer architecture, and composition of the resulting polymer. The use of RAFT polymerization and RAFT agents has gained significant attention in recent years due to robustness and versatility, compatibility with a wide range of monomers and solvent, requirement of relatively mild and metal-free conditions, and their ability to produce polymers with controlled structures, including block copolymers, star polymers, and more.[42, 46] Additionally, there is increasing focus on oxygen-tolerant, initiator/catalyst-free, and photoinitiated RAFT methodologies, which can give complete monomer conversions and high degree of livingness with specific relevance to biotechnological applications.[47-49]

1.2.2.1 Photoinitiated RAFT Polymerization (Photo-RAFT)

Recently, significant research has been directed into exploring alternative approaches to generate initiating radicals such as light, enzymes, microwaves, and redox species to enable controlled RAFT polymerization, particularly for biological systems.[30, 50] Specifically, over the last two decades, there has been substantial interest in photoinitiated RAFT polymerization (photo-RAFT).[51] This interest primarily stems from the need for reaction conditions at ambient temperatures and the ability to exert spatiotemporal control through a straightforward “ON/OFF” manipulation of the light source. In other words, radical formation and polymerization proceed when the light source is turned “ON” and energy is provided to the system, but they immediately stop when the source is turned “OFF”. Furthermore, the ability to adjust externally controlled factors, such as the

intensity and wavelength of incident light, has been shown to have a significant impact on both the control and kinetics of polymerization, with photo-RAFT processes demonstrating faster kinetics compared to thermally initiated processes.[2, 51, 52] Photo-RAFT can be mediated using traditional photoinitiators, specialized photocatalysts, or the initiator-free "iniferter" mechanism of CTAs, depending on the specific irradiation wavelength chosen for the reaction.[42, 50] Photoinitiators are compounds capable of generating radicals with labile bonds that are susceptible to photolysis, similar to the way radicals are produced through the thermolysis of temperature-sensitive molecules. They typically operate in the low-wavelength UV-Vis region (λ = 360 - 485 nm). From a mechanistic perspective, the difference between thermally initiated RAFT polymerization and photoinitiator-mediated RAFT is based on the homolytic initiator decomposition step, as shown in Scheme 1.4a.[50, 51] 2,2-dimethoxy-2-phenylacetophenone (DMPA), sodium phenyl-2,4,6-trimethylbenzoylphosphinate (SPTP), and 2-hydroxy-4′-2-(hydroxyethoxy)-2-methylpropiophenone (PP-OH) are common photoinitiators frequently used in photo-RAFT

Over recent years, the Boyer group and others utilized organic dyes (such as Eosin Y and fluorescein) and metal complexes as photoredox catalysts (PC) for the activation of photo-RAFT through a mechanism involving photo-induced electron/energy transfer (PET).[52-54] In this process, visible light can be employed to excite a specific photoredox catalyst, facilitated by the electron-accepting nature of CTAs. This excitation leads to electron transfer to a thiocarbonylthio group, which subsequently undergoes reduction to produce radicals (**R**$^{\bullet}$ or **Pn**$^{\bullet}$), while the CTA itself forms a stable anion. As with conventional RAFT polymerization, the produced radicals can either be used to initiate polymerization, conduct pre- and main-equilibrium reactions, or react with the oxidized catalyst to reactivate the original species and complete the catalytic process (Scheme

1.4b). In addition, molecular oxygen (O_2) can serve as an electron/energy acceptor to produce oxygen radical anion (O_2^-) leading to reduce the overall concentration of oxygen in the system, thus PET-RAFT can also be conducted under the open-air vessels (Scheme 1.4c).[55, 56]

Furthermore, the utilization of CTAs as iniferter molecules has been the subject of comprehensive research as a straightforward and highly efficient method for radical generation in controlled photo-RAFT, without the need of external photoinitiators or photocatalysts.[57] Otsu first introduced the concept of the iniferter ("*ini*tiator - trans*fer* agent - *ter*minator") in 1982, which refers to a molecule capable of functioning as an initiator, transfer agent, and termination agent without requirement of an external radical source.[57] The CTA itself undergoes cleavage by light, leading to a homolytic dissociation of the bond between the thiocarbonylthio and the R-group.[58, 59] The radical derived from the R-group then initiates the polymerization process, while the more stabilized radical from the thiocarbonylthio species is assumed not to directly interact with monomers. The cycle is completed when this persistent thio-centered radical recombines with the active chain end, resulting in a dormant chain. Upon further irradiation, this dormant chain can once again dissociate and incorporate monomers (Scheme 1.4d). Crucially, it has been demonstrated that control over photoiniferter RAFT polymerization is significantly dependent on both the type of CTA employed and the intensity and wavelength of the incident light. Due to the rapid degradation of the CTA end-group during UV irradiation, UV irradiation generally results in limited polymerization control especially at high conversions, whereas visible light generally results in well-controlled polymerization.[2] In addition, low light intensity produces a low amount of active radical species, which ensures good control of polymerization.[60] Due to the simplicity of photoiniferter RAFT

polymerization and its compatibility with sensitive biomacromolecules, such as enzymes, peptides and DNA, this methodology was employed throughout the thesis.

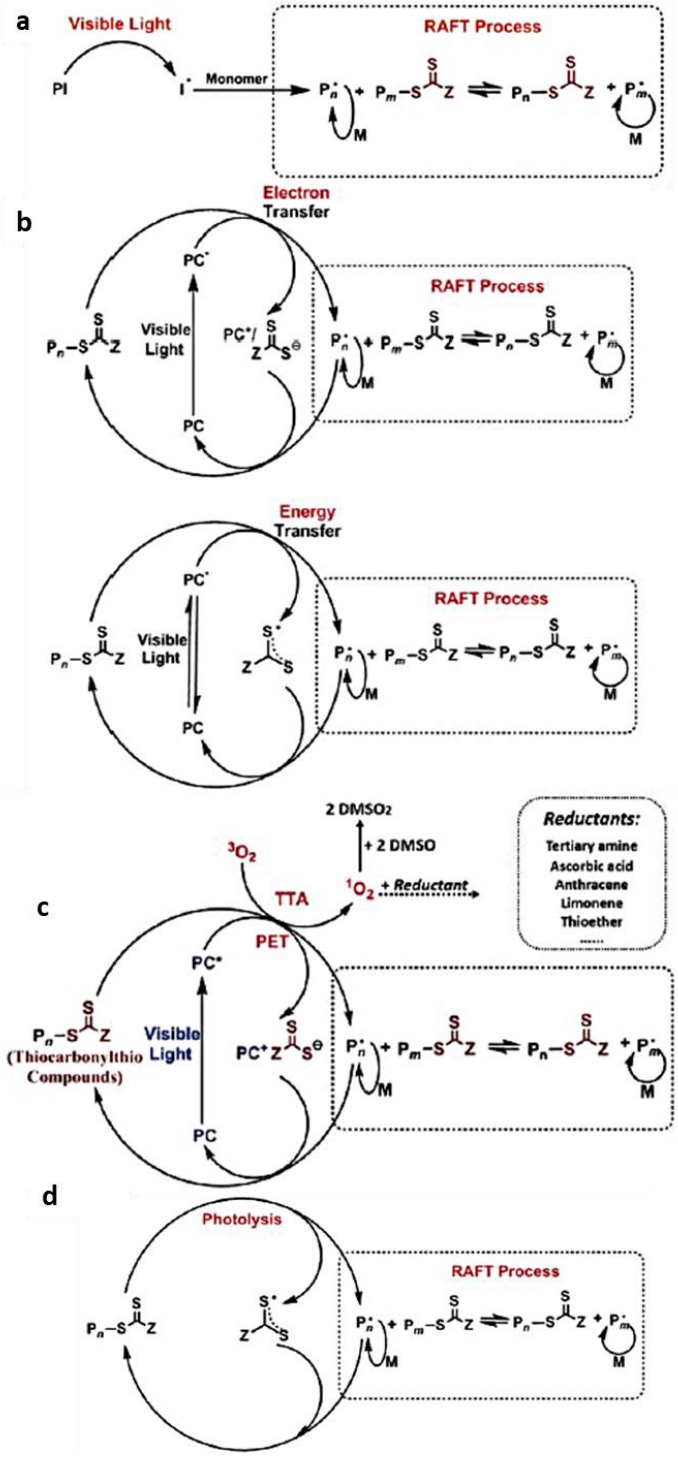

Scheme 1.4. Schematic mechanisms of photo-RAFT including a) photoinitiator-mediated RAFT polymerization, b) PET-RAFT polymerization *via* electron (top) and energy (bottom) transfer, c) oxygen-tolerant PET-RAFT polymerization, and d) photoiniferter-mediated RAFT polymerization. Reproduced from ref.[2, 52]

1.3 Block copolymer self-assembly in solution

As mentioned previously, RAFT polymerization represents excellent methodology to synthesise well-defined block copolymers. Block copolymers are a class of polymers that consist of two or more distinct polymer chains or "blocks" covalently bonded together in a single molecule.[61, 62] Each block can have different chemical or physical properties, such as different monomer units, polarity, or solubility characteristics.[62] These differences in properties between the blocks lead to unique behaviours and self-assembling properties, making block copolymers valuable materials in various scientific and industrial applications.[63] Block copolymer self-assembly in solution is a fascinating phenomenon in materials science where block copolymer molecules spontaneously organize into well-defined nanostructures when they are dissolved in a solvent.[64] In the RAFT process, the block copolymer synthesis process begins with the synthesis of a first block polymer and then a second polymerization is performed by exploiting the active chain end of the first polymer (using it as a macroCTA), generating a diblock copolymer. When the diblock copolymer is suspended in a solvent in which only one of the blocks is soluble, self-assembly is driven by aggregation of the insoluble blocks. The shape of the assembly is determined by the relative volume fractions of the hydrophobic segment and core-forming blocks, known as the packing parameter, $p = v/a_0 l_c$, where v is the volume of the solvophobic segment, a_0 is the contact area of the solvophilic or called head group area as presented in Figure 1.4.[64] As a general guideline, the formation of spherical micelles is favored when $p \leq ⅓$, cylindrical micelles also known as “worm-like”or “rod-like” micelles are favored when $⅓ < p \leq ½$, and finally hollow vesicles or polymersomes are favored when $½ < p \leq 1$.[1, 64] However, it's important to note that calculating precise p-values can be challenging, hence, relative solvophilic/solvophobic volume fractions of the constituent block copolymers are often used to describe a given formulation.[65]

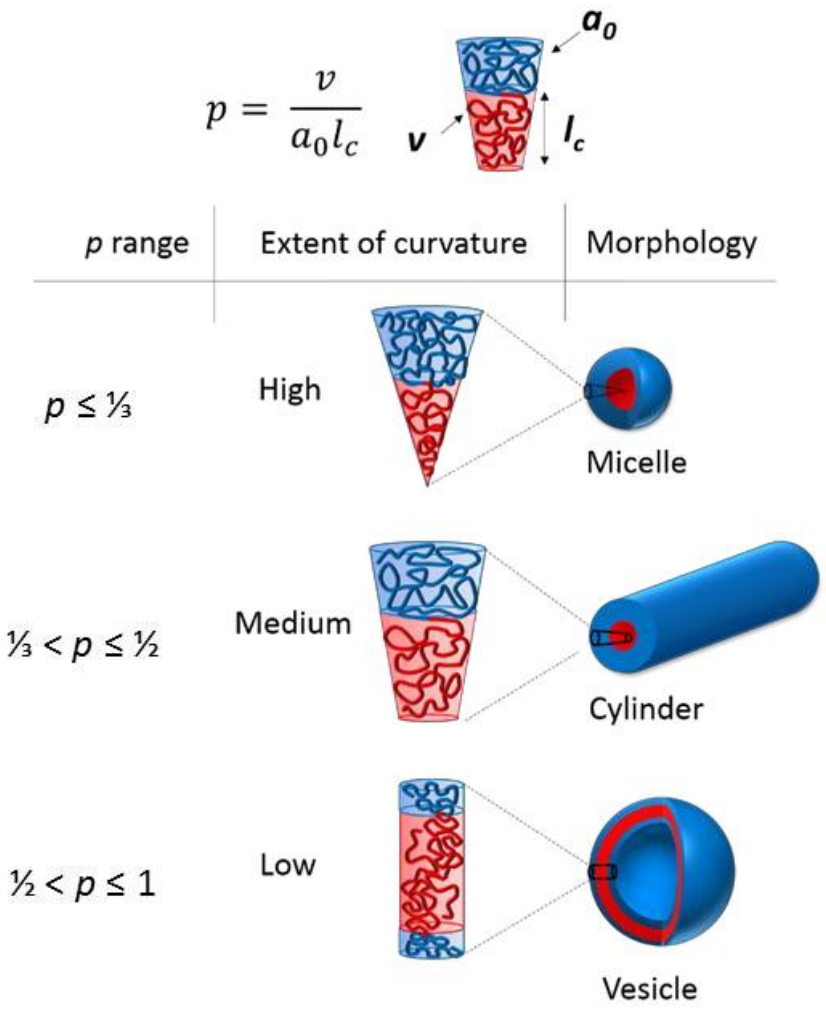

Figure 1.4. Block copolymer self-assembly of various morphologies determined by the packing parameter, *p*. Reproduced from ref.[64]

Generally, the self-assembly process occurs due to the immiscibility of the different polymer blocks and the drive to minimize the system's free energy in a liquid medium. Importantly, a wide-range of factors such as the extent of core-block stretching and its solvophobicity, corona-forming chain repulsion, overall copolymer molecular weight, copolymer architecture, and solvent composition can influence the self-assembly pathway and, consequently, the resulting nanoparticle morphology. [12, 66] Examples of morphologies resulting from block copolymer self-assembly in solution include spherical and worm-like micelles, spherical vesicles, and tubular vesicles (Figure 1.5). [67-70]

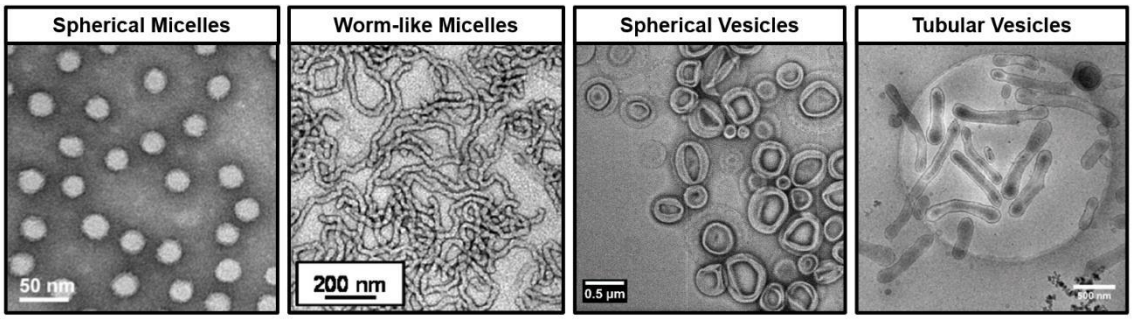

Figure 1.5. Transmission electron microscopy (TEM) images of typical nanostructures arising from amphiphilic block copolymer self-assembly in solution. Images reproduced from the following references : spherical micelles,[67] worm-like micelles,[68] spherical vesicles,[69] and tubular vesicles.[70]

Self-assembly has been employed to create nanostructures that can change shape or colour in response to stimuli to make targeted drug carriers for soft lithography and in many other areas.[71] Nevertheless, synthetic block copolymers remains challenging to replicate the intricate self-assembly behaviour observed in natural polymers, such as proteins and DNA, using synthetic block copolymers.

1.4 DNA-Based Nanostructures and DNA Assembly

Deoxyribonucleic acid, or DNA, is a double-helical molecule responsible for storing and carrying genetic information in biological organisms.[72, 73] It is composed of four different bases: adenine (A), thymine (T), guanine (G), and cytosine (C) (Figure 1.6). The backbone of this polymer consists of sugar-phosphates, which exist as anions at physiological pH levels. DNA assumes a double-helical structure, held together by hydrogen bonds between individual bases on opposite strands, known as Watson-Crick base pairs. Specifically, adenine always pairs with thymine, while guanine pairs with cytosine. As a result, only sequences that are complementary can pair together in an antiparallel manner to create the characteristic double helix.

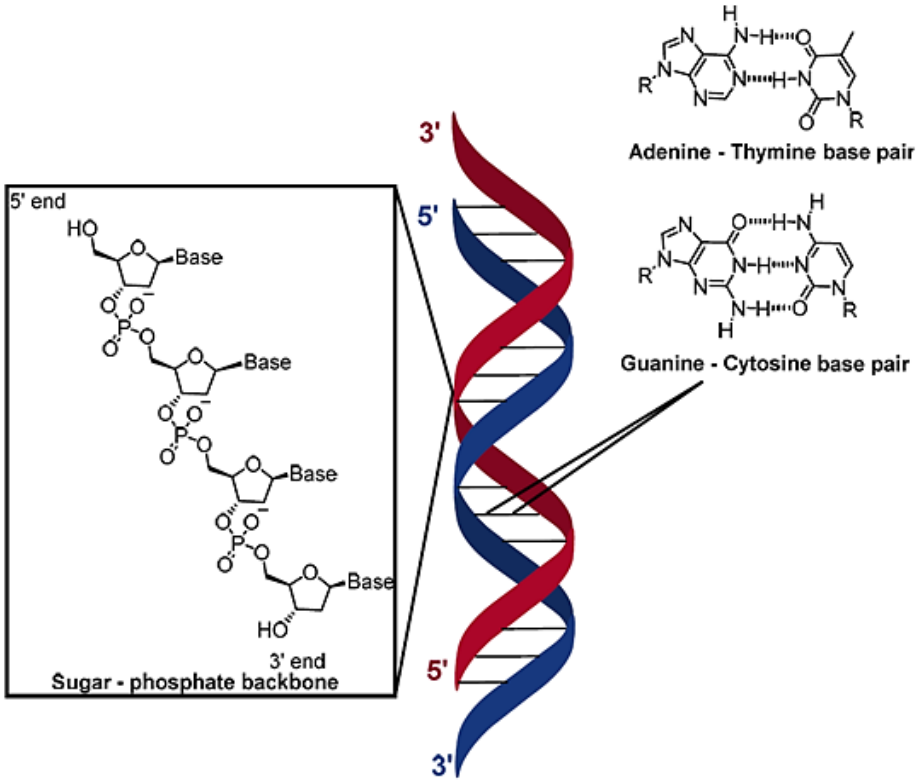

Figure 1.6. A schematic representation of the DNA double helical structure, the chemical composition of the sugar-phosphate backbone, and the specific Watson-Crick base pairs (A-T and G-C) formed within the DNA molecule.

One of the most appealing aspects of DNA in the context of nanotechnology is its ability to predict in sequence-specific binding of oligonucleotides, resulting in the formation of duplex structures.[74, 75] The stability of these resulting duplex structures relies on interactions between strands, including hydrogen bonding and base stacking interactions, which are primarily driven by hydrophobic and electrostatic forces. Base-stacking interactions become higher at increased salt concentrations since the salt effectively screens the repulsive negative charges along the phosphate backbone.[76]

DNA-based nanostructures are a fascinating class of nanoscale materials created by harnessing the unique properties of DNA molecules.[75] These structures are typically designed and constructed through DNA nanotechnology, which is an interdisciplinary

field that combines biology, chemistry, physics, and engineering to manipulate DNA molecules into diverse nanostructures with remarkable precision.[73] In the area of DNA nanotechnology, DNA is taken out of its biological context and used as a non-biological engineering material – its programmability has enabled revolutionary developments in the molecular self-assembly field.[77] The programmability of DNA refers to the ability to design and engineer DNA molecules with precise sequences and structures to perform specific functions or tasks. DNA is often referred to as the "molecular programming language" because it can be manipulated and programmed to assemble into various nanostructures and perform specific operations at the molecular level.[78] Research in DNA nanotechnology involves static structures such as two- and three-dimensional crystal lattices,[79,80] origami structures produced by the controllable nanoscale folding of DNA (Figure 1.7a),[81] nanotubes,[82] dynamic structures (Figure 1.7b),[83] and hierarchical self-assemblies (Figure 1.7c).[84] Precise assembly of nanostructures enables the creation of materials with unique functions such as self-assembly of a nanoscale DNA box with a controllable lid, and take advantage of the self-recognition properties of DNA to control its folding into specific shapes by utilising a bottom-up approach.[85] DNA assembly has received this significant attention for various reasons including the predictable and programmable interactions involved, specificity of binding sites, thermodynamic stability, well-defined structure on the nanoscale, persistence length, capability of synthesis and modification using automated methods, controllable adjustment of structures and a large variety of DNA-acting enzymes for further structure modification.[73] Nevertheless, despite the wide range of innovative nanostructures enabled by DNA nanotechnology, a substantial limitation remains-the high cost of DNA. Thus, combination of DNA with synthetic polymers may enable to retain the advantages of

programmability while reducing the cost and gaining the additional functions of synthetic polymers such as responsiveness and resistance to degradation.

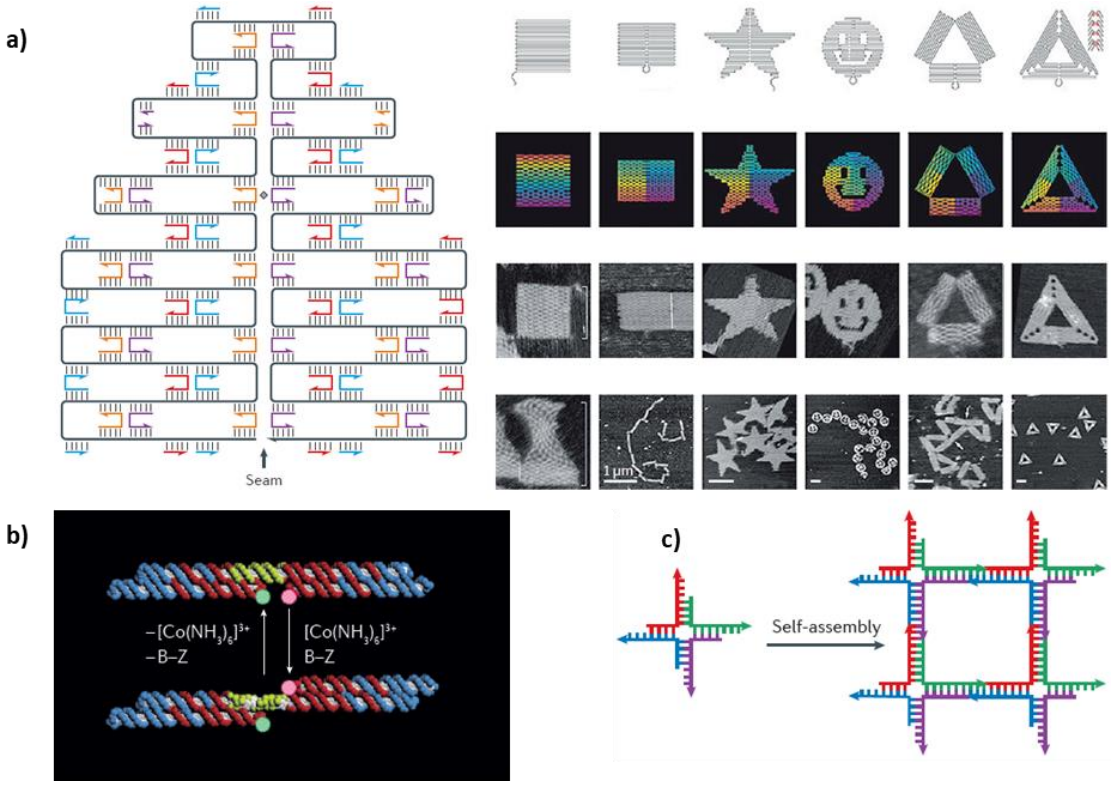

Figure 1.7. a) Scaffolded DNA origami b) dynamic structure of nanomechanical DNA c) Self-assembly of a DNA four-way junction. All figures are adapted from ref.[73]

1.5 DNA-polymer conjugates

DNA-polymer conjugates, also known as DNA-polymer hybrids or DNA-polymer complexes, are bioconjugates formed by attaching synthetic polymer chains to DNA molecules.[86] These conjugates combine the unique properties of both DNA and polymers. The DNA component provides programmability and sequence-specificity, while the polymer component represents robustness and tunability, resulting in materials with diverse applications ranging from nanotechnology to biomedicine.[12]

1.5.1 Synthesis of covalent DNA–Polymer Conjugates

Ordinarily, DNA and synthetic polymers form the covalent attachment of polymer chains to functional groups on DNA. One common approach is to modify the DNA backbone or bases with reactive groups, such as primary amines or thiols, which can then react with polymer precursors or polymerization initiators.[87-90] Alternatively, post-synthetic modifications can be performed by attaching polymer chains to DNA using click chemistry or other conjugation strategies. The first reports of DNA–polymer hybrids started in the late 1980s when antisense oligodeoxynucleotides were conjugated to a poly(L-lysine) (PLL) backbone employed in antiviral agents.[87] Two general approaches to couple between polymer and DNA are *in solution* phase and *on solid* phase method. In the solution phase, the DNA and polymer components are chemically linked together in solution, and generally compose of three common coupling reactions: 1) amide coupling between carboxylic acid terminated polymers and amino-functionalised DNA (Scheme 1.5a).[88] 2) disulfide coupling by both terminal thiol-modified polymers and DNA (Scheme 1.5b).[89] 3) thiol-ene coupling between thiol-modified DNA and terminal maleimide group on polymers (Scheme 1.5c).[90] For the solid phase, where the DNA and polymer components are synthesized separately and then polymers are grafting onto DNA on a solid support (Scheme 1.6).[91] The choice of polymer can vary depending on the desired properties and applications of the conjugate.[92, 93] Synthetic polymers, such as polyethylene glycol (PEG), polyacrylamide (PAA), or polystyrene (PS), are often used due to their versatility, stability, and well-established synthesis methods. These polymers can impart unique characteristics to the DNA, such as increased stability, enhanced solubility, or improved biocompatibility. DNA-polymer conjugates have a wide range of applications such as drug delivery, biosensor, and DNA-nanotechnology.[92] Nonetheless, most synthetic routes result in low yields, arising from the general difficulty of coupling

macromolecules, and the challenge of finding conjugation conditions compatible with contrasting properties between the DNA and polymer components. The straightforward conjugation of a hydrophobic polymer with hydrophilic DNA remains challenging and currently limits development of this research field. [92, 93]

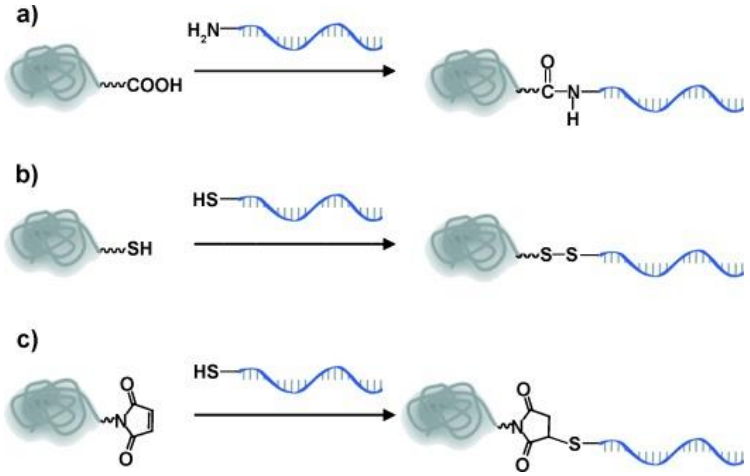

Scheme 1.5. Coupling reactions for the synthesis of DNA-polymer hybrids in solution: a) amide coupling. b) Disulfide coupling c) thiol-ene coupling. Adapted from ref.[92]

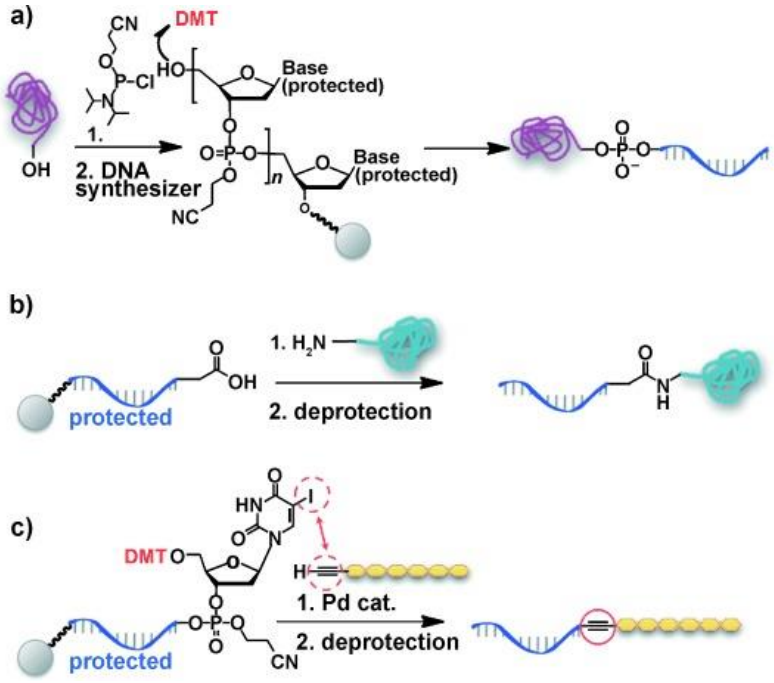

Scheme 1.6. Coupling reactions for the synthesis of DNA-polymer hybrids on a solid support. Adapted from Ref.[92]

1.5.2 Functionalities of DNA-Polymer Conjugates

DNA-polymer conjugates have been explored for targeted drug delivery, leveraging DNA strands to specifically target diseased cells or tissues, while the polymer component provides stability and enables control over the release kinetics of therapeutic payloads.[94, 95] Early research on DNA-polymer conjugates primarily focused on enhancing the stability and cellular uptake of antisense oligonucleotides (AOs). AOs, short sequences of ssDNA or ribonucleic acid (RNA) complementary to specific messenger RNA (mRNA) sequences, have demonstrated efficacy in disrupting gene expression for various diseases.[96] However, AOs often exhibit poor cellular uptake due to enzymatic degradation by nucleases.[97] Park *et al.* illustrated that conjugating AOs with polyethylene glycol (PEG) yields a diblock copolymer, when combined with a cationic complex, self-assembles into a polyelectrolyte complex micelle structure.[98] Inside the core of the micelle contains neutral DNA-complex leading to protect it from from nucleases, while the hydrophilic shell enhances cellular uptake.

There are also used in the construction of nanoscale structures and devices as building blocks for nanomaterials with programmable properties, such as DNA origami,[99] nanoparticle assembly,[100] and nanoscale patterning.[101] In 2026, Tokura *et.al.* presented using ATRP to enable polymerizations from DNA origami allowing reactions to occur under aqueous conditions and at room temperature which are essential parameters for working with DNA origami structures.[101] Under these controlled conditions, polymerization of poly(ethylene glycol) methyl ether methacrylate (PEGMA) successfully produced a polymer brush. Additionally, by incorporating copolymerization with the cross-linker poly(ethylene glycol) dimethacrylate (PEGDMA), a densely cross-linked polymer network was achieved.

Moreover, conjugates incorporating fluorescent DNA and polymers enable the development of advanced imaging probes which be able to target specific biomolecules or cellular structures, providing high-resolution imaging in biological samples as well as detecting biomolecules, pathogens, or genetic variations.[102-104] Besides, DNA-polymer conjugates offer potential in gene delivery and gene editing applications that facilitate cellular uptake and endosomal escape to improve the efficiency and safety of gene therapy approaches.[105]

1.6 Polymerization-Induced Self-Assembly (PISA)

As mentioned in section 1.3, traditional block copolymer self-assembly is a stepwise process that begins with the synthesis of diblock copolymers, followed by purification, and finally self-assembly in dilute concentration. This approach is complicated, demands selective solvents, is time-consuming, and often results in low yields.[106, 107] Over the last two decades, polymerization-induced self-assembly (PISA) has been developed to overcome these limitations. PISA allows the direct construction of polymeric nanoparticles of various morphologies, normally spheres, vesicles or worms.[1, 108, 109, 110] Notable advantages of PISA are the capacity to simultaneously conduct polymerization and self-assembly in one pot and the ability to produce nanoparticles at high concentrations, with typical literature reports ranging between 5-30 w/w% solids in the final concentrations.[111] Armes and co-workers were the first to develop PISA under RAFT polymerization conditions.[112] The principle behind PISA is the capability of solvent-miscible monomers polymerized from a pre-formed solvophilic macroCTA to form solvophobic polymers, leading to self-assembly *in situ* in a selective solvent (Scheme 1.7).[1, 113, 44] The resulting morphology in PISA formulations undergoes changes based on the DP and the %solid concentrations and is frequently visualized through the construction of a phase diagram.[12] The specific morphological outcomes are dictated by

the packing parameter, *p*, akin to the principles governing conventional block copolymer self-assembly techniques (discussed in section 1.3).

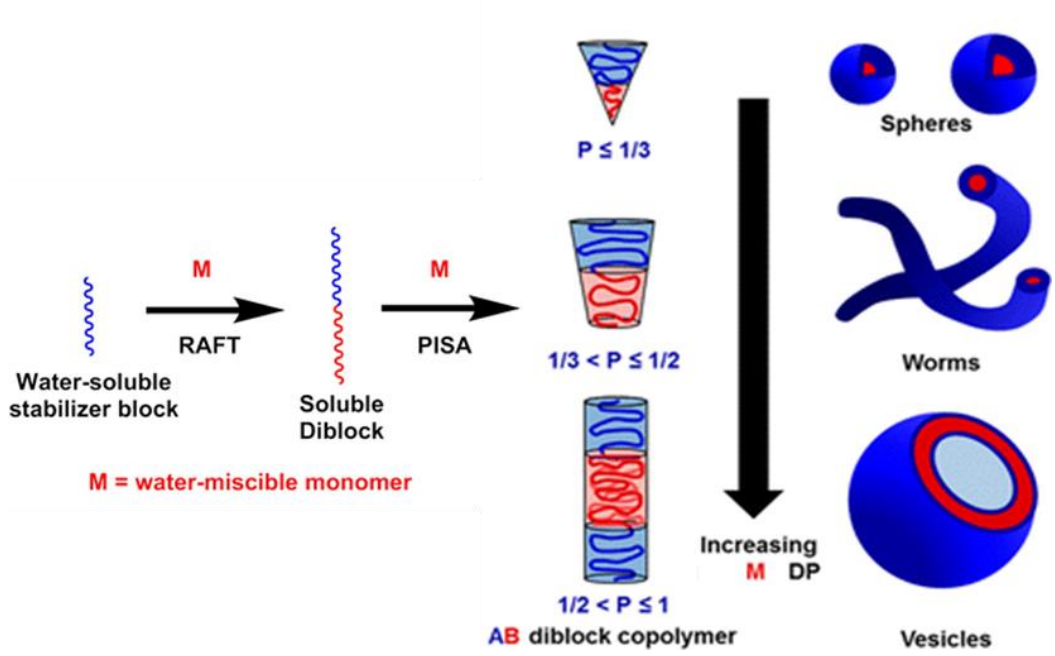

Scheme 1.7. Schematic of RAFT-PISA conducted in aqueous media. Reproduced from ref.[1] A water-miscible monomer is polymerized using a water-soluble polymer macroCTA *via* RAFT polymerization, initially to give a soluble diblock copolymer. Further polymerization leads to an insoluble second block and subsequent self-assembly into various morphologies determined by the packing parameter, *p*.

In general aqueous PISA formulations, an increase in the length of the core-forming block and solid content leads to a higher-order morphology transition, progressing from soluble polymers to spheres, then to worms, followed by vesicles, and finally culminating in multi-lamellae formation as shown in Figure 1.8.[114] In the context of this thesis, PISA could be a very useful tool for the creation of amphiphilic DNA-polymer nanostructures because it removes the need to couple hydrophobic polymers with DNA, which as detailed above has been shown to be challenging.

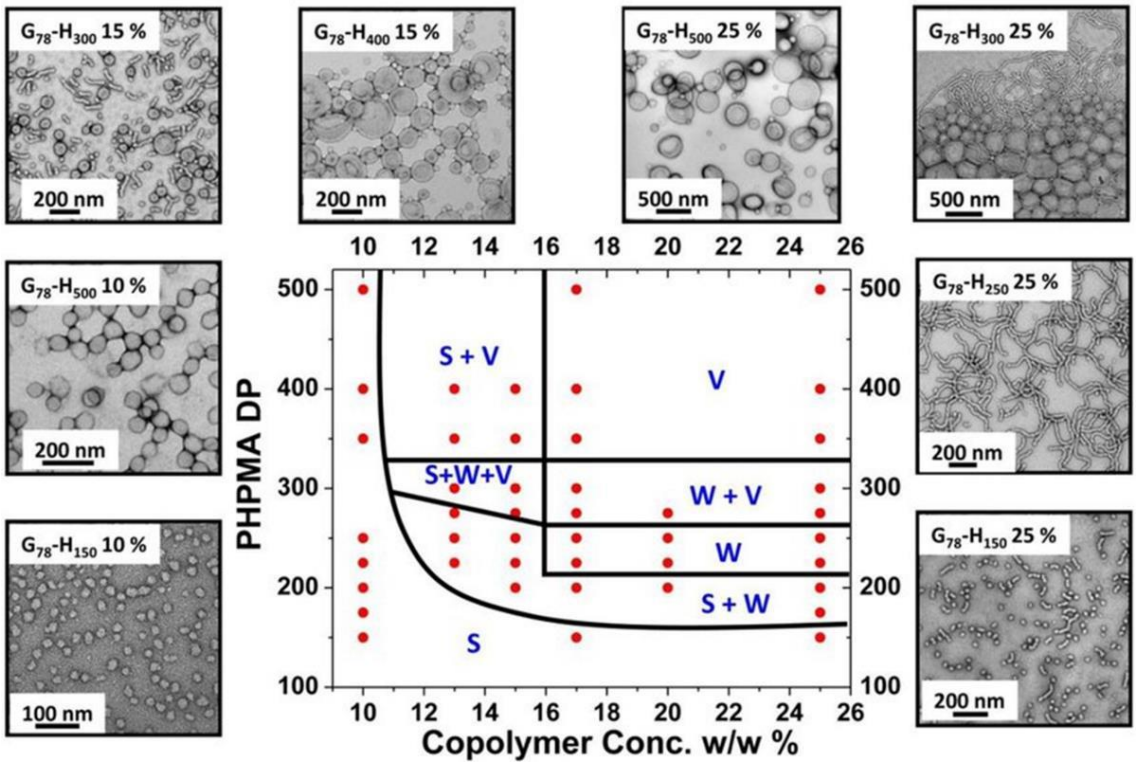

Figure 1.8. Phase diagrams for an aqueous RAFT-PISA system of PGMA-b-PHPMAn with its corresponding TEM images of different morphologies. Key: s = spheres, w = worms, V = vesicles. Reproduced from ref.[114]

1.6.1 Photoinitiated PISA

The use of thermally initiated RAFT polymerization has been extensively used in aqueous PISA reports;[115-118] however, a steadily increasing number of studies have focused on photoinitiated PISA (photo-PISA) approaches. [110-116] Photo-PISA mediated by visible light-active photoinitiators and photoredox catalysts or by the "photoiniferter" mechanism of CTAs, based on the initiation mechanisms described above for conventional photo-RAFT polymerization. Compared to thermally initiated PISA, photoinitiated PISA have increased reaction kinetics.[119] As discussed in section 1.2.2.1, photoinitiated species are activated by specific wavelengths of light, reducing the complexity of the reaction composition and enabling reactions under milder conditions (*e.g.* at room temperature).[2, 3, 119-125] Without the need for high temperatures, the ability

to perform these reactions at room temperature may be crucial when working with temperature-sensitive components. The process is compatible with various types of polymers and macroCTAs.[2, 124, 126]

In 2015, our group pioneered a study that reported on the differences between photo-PISA and thermally initiated PISA on nanoparticle morphology.[3] In this work, the phase diagram of poly(ethylene glycol)$_{113}$-*b*-poly(2-hydroxypropyl methacrylate)$_X$ (PEG$_{113}$-*b*-PHPMA$_X$) from both techniques differed significantly due to differences in the polymerization rate and end group fidelity. The results show that photo-PISA drives the formation of higher order morphologies due to the loss of the end group caused by extended periods of light irradiation. In the photo-PISA approach, detailed morphology diagrams were constructed to determine the optimal total solids content and core-block DP for the consistent production of pure PEG-*b*-PHPMA polymersomes *via* aqueous photo-PISA at 37°C, using a 405 nm light. This temperature and light wavelength were maintained throughout the experiments in this thesis. Moreover, a series of PEG$_{113}$-*b*-PHPMA$_{400}$ polymersome nanoreactors were developed and a number of possibilities were explored for their potential use as artificial cell-mimicking models.[127] Following a subsequent report, the PHPMA polymersome membranes demonstrated their inherent permeability toward small organic molecules, as well as their ability to efficiently retain larger biomacromolecules such as green fluorescent protein (GFP), horseradish peroxidase (HRP) and glucose oxidase (GOx) within the polymersomes, allowing the encapsulated proteins to communicate through enzyme cascades within the internal aqueous compartment of nanostructures.[127]

1.6.2 Low-volume PISA

The typical reaction concentration in PISA is 10-20% solids content by weight, normally in a 1 mL reaction. This scale is very high for expensive materials such as DNA-decorated molecules, leading to the need for low-volume PISA.[124, 126] However, the main limitation of working at low volumes is oxygen inhibition.[128] Removing oxygen is challenging at low volumes using traditional methods (*e.g.* N_2 bubbling, freeze-pump-thaw) without causing concentration changes, and the high surface area-to-volume ratio means oxygen is reabsorbed quickly from the atmosphere into the reaction medium. Interestingly, Boyer and co-workers explored photoinduced electron/energy transfer–reversible addition-fragmentation chain transfer (PET-RAFT) polymerization by exposing reactions to yellow light in photocatalytic ultralow volume polymerization (20 μL) in the presence of air without deoxygenation (Figure 1.9a). [49, 129, 130] In this work, a photocatalyst (5,10,15,20-tetraphenyl-21*H*,23*H*-porphine zinc (ZnTPP)) could capture oxygen molecules and convert them into singlet oxygen, which is captured by a quenching species (DMSO). However, this mechanism requires specific solvents to act as trapping species, such as anthracenes or sulfoxides. An alternative approach is to use an enzyme-assisted approach, such as glucose oxidase, in small volume (40 μL) photo-PISA reaction to allow experiment under oxygen in the open air as shown in Figure 1.9b.[123, 131] However, the use of enzymes is perhaps limited by their stability and poor tolerance to change in experimental conditions. Tanaka *et.al.* also accomplished PISA at a scale of 2 μL by heating system at 100 ˚C in three minutes under the air (Figure 1.9c).[47] This condition requires high temperature and careful cooling steps which can affect the stability of reaction components and is probably not suitable for use with fragile biomolecules.

Our group has been separately developing PISA[69, 124, 126, 127, 132-134] and DNA-polymer hybrids[135] for several years. This thesis investigated the use of DNA as a PISA macroCTA

to provide direct access to amphiphilic DNA-polymer hybrid nanostructures without the requirement for complicated and low-yielding synthesis and isolation of DNA-polymer conjugates. The challenge is not only pioneering an uncomplicated method for making DNA-polymer hybrids but also developing simple and reproducible conditions for performing PISA at low volumes.

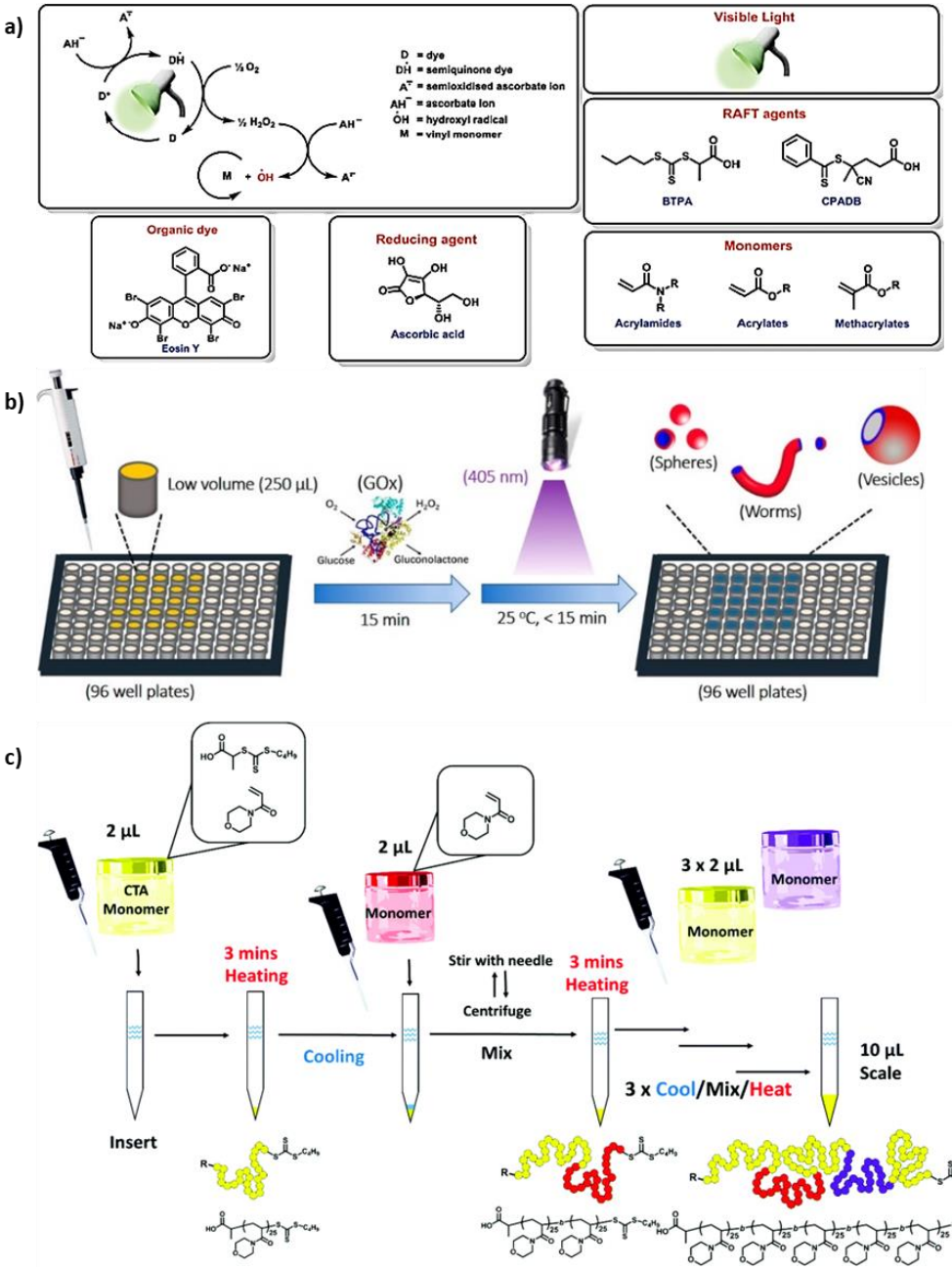

Figure 1.9. Strategies for low volume RAFT polymerization involving a) photocatalysts, b) enzyme-mediated deoxygenation, and c) an ultrafast high temperature approach. Adapted from refs.[47, 130, 131]

1.6.3 DNA-polymer nanoparticles by RAFT-PISA

During this PhD, two publications were introduced to guide the preparation of DNA-polymer nanoparticles using RAFT-PISA while we were working on this topic. In 2020, Weil and coworkers demonstrated that DNA−polymer conjugates can self-assemble into nano-objects by thermal RAFT PISA through the *grafting from* approach using N,N-Dimethylacrylamide (DMA), 4-acryloylmorpholine (NAM), 2-hydroxyethyl acrylate (HEA), and oligo(ethylene glycol) methyl ether acrylate (OEGA) as monomer (Scheme 1.8a).[120] This reaction relied on enzyme degassing with glucose, glucose oxidase, and sodium pyruvate. The monomer to initiator ratio can be controlled precisely and provide medium to high conversion (50-90 % conversions) and thus can allow the manipulation of architectures. However, this method required ambient condition (using mixed t-butanol/DPBS as a solvent at pH=6). The following year, Tan and coworkers modified a photoinitiated chain transfer agent (photo-CTA) to perform the first aqueous RAFT photo-PISA of DNA-polymer nanostructures under enzyme assisted approach (Scheme 1.8b).[136] Sodium phenyl-2,4,6-trimethylbenzoylphosphinate (SPTP) was used as photoinitiator and 2-hydroxypropyl methacrylate (HPMA) was used as monomer to manipulate DNA-polymer nanostructure This work further applied resulting DNA-PHPMA particles to enhanced nuclease resistance and cellular uptake. The details of these two approaches are further discussed in Chapter 3

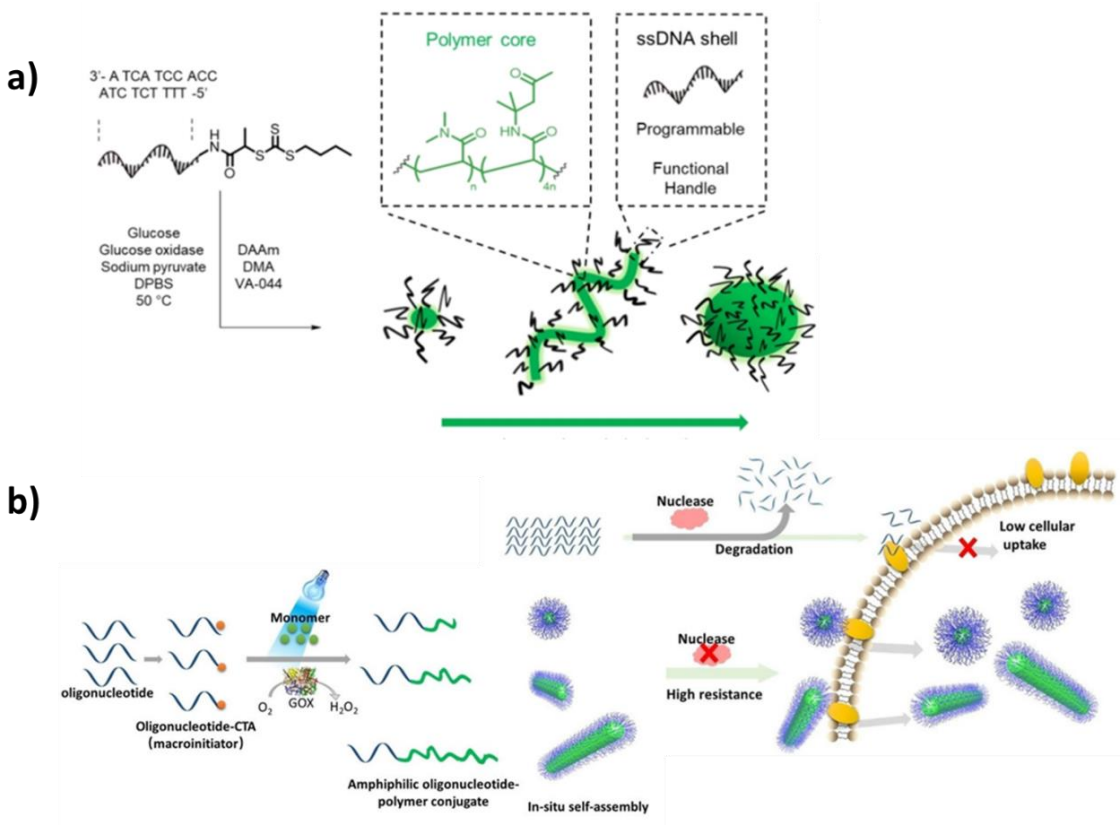

Scheme 1.8. a) Schematic representation of the synthesis of a rhodamine B containing DNA–polymer conjugate (FP1) and its subsequent labelling with a complementary DNA sequence containing Cy5 at its 3'-terminus. b) Design and construction of DNA-polymer nanostructures by photo-PISA and further *in vivo* investigations of stability and cellular uptake efficiency from DNA-polymer nanostructures. Adapted from ref.[136, 137]

1.7 Characterization techniques for polymer self-assemblies

Analysis of particle size and shape is crucial to understanding the mechanisms underlying the self-assembly of polymers as well as the behaviour of these particles in solution. Data discussed in the following chapters will be used to demonstrate how these techniques are used throughout the thesis, however these techniques have been thoroughly reviewed elsewhere.[138-142]

1.7.1 Light scattering techniques

Light scattering techniques are analytical methods that utilize the scattering of light to gain information about the physical and chemical properties of particles or materials.[138] These techniques are widely used in various scientific and industrial applications for characterizing particles, macromolecules, and complex systems. Light scattering is an important technique to determine the size, molar mass, and topology/morphology of a polymer chain, or particle, as well as inter particle interactions, in a non-destructive manner. In addition, scattering techniques can be performed in solution ensuring that the structure being analyzed is not affected during sample preparation or analysis, as opposed to certain microscopy techniques. Furthermore, factors such as the pH, temperature and solvent composition can be easily adjusted to analyze the particles under a variety of conditions, which is useful for analyzing stimuli-responsive systems.

The scattering technique used throughout this thesis is dynamic light scattering (DLS) which is a non-invasive, non-destructive analytical technique used to measure the size and size distribution of particles or molecules in a solution.[138] It is particularly useful for characterizing nanoscale particles or macromolecules, providing insights into the stability and behavior of colloidal systems and nanomaterials. DLS is widely employed in various fields, including chemistry, biology, materials science, and pharmaceuticals.

The principal of DLS is based on the random thermal motion of particles suspended in a fluid, known as Brownian motion. These particles experience continuous collisions with solvent molecules, leading to their random movement. In DLS, a laser beam is directed through the sample containing these particles, and their Brownian motion scatters the laser light. This scattered light interferes with each other, creating fluctuations in intensity over time, which are recorded by a detector. These fluctuations are related to the

movement of the particles. Larger particles move more slowly, resulting in slower fluctuations, while smaller particles move faster, leading to faster fluctuations. The intensity fluctuations are subjected to autocorrelation analysis. This analysis calculates the time-dependent correlation of the intensity fluctuations, providing information about the characteristic timescale of particle motion, and then uses to calculate the particle size distribution. The diffusion coefficient of the particles is related to their size through the Stokes-Einstein equation (equation 1). By analyzing the correlation data, the size of the particles and the distribution of sizes in the sample can be determined.

$$R_{\mathrm{H}} = \frac{k_{\mathrm{B}}T}{6\pi\eta D} \qquad \text{(equation 1)}$$

Where k_{B} is the Boltzmann constant (approximately 1.38×10^{-23} J/K), T is the absolute temperature, η is the dynamic viscosity of the solvent, D is the diffusion coefficient of the particles and R_{H} is the hydrodynamic radius.

The hydrodynamic radius (R_{H}) is the theoretical radius of a perfect hard sphere as they move through the solvent with the same translational diffusion coefficient (D) as the particle being measured. Therefore, R_{H} is a good approximation for the radii of spherical particles, for example spherical micelles and vesicles, but is of less relevance with anisotropic particles such as worm-like micelles. Moreover, it takes into account not only the physical size of the particles but also their interactions with the solvent molecules and the solvent's viscosity. Thus, R_{H} is often reported from a DLS experiment as a relative size of the particles in solution.

1.7.2 Electron microscopy

Unlike the scattering techniques discussed in the previous section, electron microscopy (EM) is a powerful imaging technique that uses a beam of electrons to directly visualize

the ultrastructure of samples with light microscopy. This provides significant advantages, particularly when studying non-spherical particle morphologies, as it eliminates the need to fit the data to a model (*e.g.*, the hard-sphere model in DLS) to extract structural information. The technique is crucial in various scientific and industrial fields, including biology, materials science, and nanotechnology. The primary electron microscopy techniques used throughout this thesis were transmission electron microscopy (TEM) and cryogenic electron microscopy (cryo-TEM).

Transmission electron microscopy in the dry state

TEM involves transmitting a beam of electrons through an ultrathin sample, which allows for high-resolution imaging of the sample's internal structure at nanoscale resolution. In dry state, the process involves preparing samples by drying nanoparticles from a solution onto a thin copper mesh grid coated with a layer of carbon, creating a thin layer of nanoparticles. Polymer nanoparticles primarily consist of organic elements such as carbon, hydrogen, and oxygen which have low atomic masses leading to low contrast between the particles and the carbon coating (the background). It's important to note that the electron scattering ability of an element increases with its nuclear charge, represented as Z leading to more substantial electron scattering enhances the contrast observed in TEM. To enhance contrast and visibility in TEM images, samples are commonly stained with elements of high atomic number, such as molybdenum, tungsten, or uranium salts. These heavy element stains scatter fewer electrons compared to organic elements. This staining technique is referred to as "negative staining" because the stain is primarily localized on the carbon coating, resulting in a darker background and lighter appearance of the sample (Figure 1.10a). Conversely, positive staining is a method where particles are made to appear darker against a lighter background leading to enhance the visibility of the particles in TEM images (Figure 1.10b).

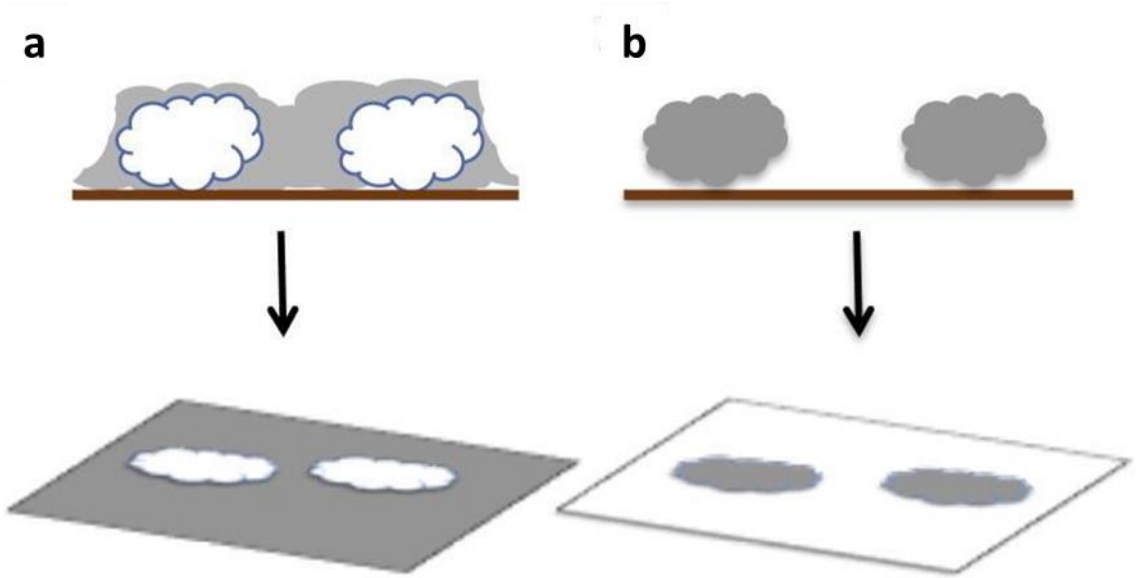

Figure 1.10. Negative and positive staining techniques using heavy metal salts. a) negative staining and b) positive staining. Reproduced from ref.[142]

While staining is valuable for enhancing contrast in electron microscopy, it also has the potential to introduce artifacts stemming from the stain itself. These artifacts can manifest as uneven background staining or the formation of stain crystals. In some cases, staining can obscure the internal details of particles, such as membrane thickness. Recognizing these limitations, research efforts have focused on developing thinner support materials that enable the imaging of weakly scattering particles without the need for staining. An example of such innovation is the use of graphene oxide (GO) grids. These grids were introduced in 2009 and have proven effective in analyzing soft materials, especially when low-contrast supports are employed.[141]

When analyzing a sample using dry-state TEM, drying effects can be observed such as dehydration of the particle corona, particle instability and changes in hollow particles: Dehydration of the particle corona can lead to the appearance of a smaller particle size compared to when the sample is in solution. This effect is commonly referred to as the "drying effect". Particle instability upon drying which the particles may become unstable

during the drying process depending on the properties of the polymer used. This instability can result in particle disassembly or morphological changes. For example, if the core-forming blocks of the particles have a low glass transition temperature (Tg), film formation can occur. Moreover, hollow particles, such as vesicles, may appear to have collapsed or burst when subjected to the drying process under vacuum conditions. These drying effects need to be considered when conducting dry-state TEM analysis, as they can impact the interpretation of results and the accuracy of particle size measurements.

Cryogenic transmission electron microscopy (cryo-TEM)

For preserving the native structure and state of these samples, the preferred technique is cryo-TEM, as it allows for the collection of images that closely resemble particles in aqueous solution. In cryo-TEM, a thin layer of the sample in solution is deposited onto a TEM grid. Afterward, blotting is performed to remove most of the solution, leaving only a thin layer. The grid is then rapidly immersed in liquid ethane, causing the ice layer to vitrify or freeze instantly. The frozen sample can be subsequently analyzed under vacuum conditions at liquid nitrogen temperatures (approximately -173 °C). In contrast to dry-state TEM, cryo-TEM eliminates the need for staining, and it enables the observation of features like membrane thickness, making it a valuable technique for examining complex structures in their native, hydrated state.

While cryo-TEM is an immensely versatile and valuable technique, it is known for being time-consuming, often requiring up to an hour to image a single sample. Additionally, it is not immune to certain artifacts, including ice crystallization, ethane contamination, or the occurrence of empty vitreous ice (Figure 1.11). Furthermore, special attention must be given to the intensity of the electron beam to avoid damaging the sample. High-intensity electron beams can potentially melt the vitrified ice or even result in the

destruction of the sample and the grid. This necessitates a cautious and precise approach when utilizing cryo-TEM for sample analysis.

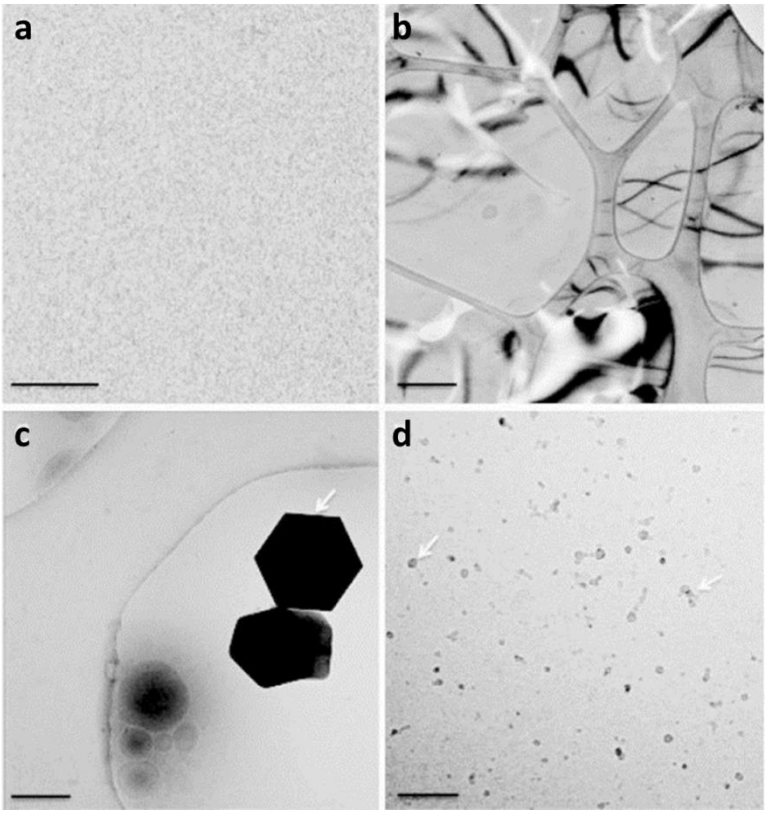

Figure 1.11. Examples of vitreous and non-vitreous ice observed in cryo-TEM imaging. a) Empty, vitreous ice (Scale bar: 50 nm). b) Displays hexagonal ice crystals (Scale bar: 400 nm). c) Large ice crystals (indicated by the white arrow) (Scale bar: 400 nm). d) The presence of ethane contamination (Scale bar: 200 nm). Reproduced from ref.[142]

Finally, the aim of this Ph.D. project is to establish reproducible conditions for low-volume PISA reactions using a deoxyribonucleic acid macromolecular chain transfer agent (DNA-macroCTA), polyethylene glycol macromolecular chain transfer agent (PEG-macroCTA), and HPMA monomer to produce DNA-decorated polymeric nanostructures of diverse morphologies *via* photo-PISA, with the intention of exploring their potential for future medical applications.

1.8 Summary

This chapter provides an overview of the fundamental key concepts that are explored in the experimental chapters of this thesis. A briefly introduction to functional nanostructures and self-assembly of nanostructures has been given. This was followed by the fundamental concepts of polymers and the modern synthetic techniques used to prepare them. The mechanistic insights of RAFT and photo-RAFT polymerization were emphasized on delving into. Subsequently, the concept of amphiphilic block copolymer self-assembly was discussed in detail, including the principles governing the resulting nanoparticle morphology. Furthermore, DNA-based nanostructures, DNA assembly, and DNA-polymer conjugates were introduced and discussed, including the limitations encountered in the synthesis of DNA-polymer conjugates. In this context, the significant topic of polymerization-induced self-assembly (PISA) was highlighted, which is central to the themes of this thesis. PISA is a rapidly growing, one-pot procedure for synthesizing block copolymer nano-objects with predictable morphologies. It was emphasized that PISA can be initiated with light and conducted in low-volume conditions. The chapter also presented examples of DNA-polymer nanoparticles synthesized using RAFT-PISA. Finally, the chapter offered a brief overview of the analytical techniques used to study polymer self-assemblies.

1.9 References

1. Warren, N. J.; Armes, S. P., Polymerization-Induced Self-Assembly of Block Copolymer Nano-objects via RAFT Aqueous Dispersion Polymerization. *Journal of the American Chemical Society* **2014,** *136* (29), 10174-10185.

2. Yeow, J.; Boyer, C., Photoinitiated Polymerization-Induced Self-Assembly (Photo-PISA): New Insights and Opportunities. *Advanced Science* **2017,** *4* (7), 1700137.

3. Blackman, L. D.; Doncom, K. E. B.; Gibson, M. I.; O'Reilly, R. K., Comparison of photo- and thermally initiated polymerization-induced self-assembly: a lack of end group fidelity drives the formation of higher order morphologies. *Polymer Chemistry* **2017,** *8* (18), 2860-2871.

4. Stupp, S., Introduction: Functional Nanostructures. *Chemical Reviews* **2005,** *105* (4), 1023-1024.

5. Iqbal, P.; Preece, J. A.; Mendes, P. M., Nanotechnology: The "Top-Down" and "Bottom-Up" Approaches. In *Supramolecular Chemistry*, 2012.

6. Dalkas, G.; Matheson, A. B.; Vass, H.; Gromov, A.; Lloyd, G. O.; Koutsos, V.; Clegg, P. S.; Euston, S. R., Molecular Interactions behind the Self-Assembly and Microstructure of Mixed Sterol Organogels. *Langmuir* **2018,** *34* (29), 8629-8638.

7. Vrignaud, S.; Benoit, J. P.; Saulnier, P., Strategies for the nanoencapsulation of hydrophilic molecules in polymer-based nanoparticles. *Biomaterials* **2011,** *32* (33), 8593-8604.

8. Vriezema, D. M.; Aragonès, M. C.; Elemans, J. A. A. W.; Cornelissen, J. J. L. M.; Rowan, A. E.; M., N. R. J., Self-Assembled Nanoreactors. *Chem. Rev.* **2005,** *105* (4), 1445-1490.

9. Shi, H.-X.; Li, W.-T.; Li, Q.; Zhang, H.-L.; Zhang, Y.-M.; Wei, T.-B.; Lin, Q.; Yao, H., A novel self-assembled supramolecular sensor based on thiophene-

functionalized imidazophenazine for dual-channel detection of Ag+ in an aqueous solution. *RSC Advances* **2017,** *7* (84), 53439-53444.

10. Niu, R.; Pan, C.; Chen, Z.; Wang, L.; Wang, L., Enhanced thermoelectric performance from self-assembled alkyl chain-linked naphthalenediimide/single walled carbon nanotubes composites. *Chemical Engineering Journal* **2020,** *381*.

11. Zhang, B., Principles, Methods, Formation Mechanisms, and Structures of Nanomaterials Prepared via Self-Assembly. In *Physical Fundamentals of Nanomaterials*, 2018; pp 177-210.

12. Mai, Y.; Eisenberg, A., Self-assembly of block copolymers. *Chemical Society Reviews* **2012,** *41* (18), 5969-5985.

13. Painter, P. C., Fundamentals of polymer science : an introductory text. 2nd ed. ed.; Coleman, M. M., Ed. Technomic Pub. Co.: Lancaster, Pa. :, 1997.

14. Stille, J. K., Step-growth polymerization. *Journal of Chemical Education* **1981,** *58* (11), 862.

15. Penczek, S.; Moad, G., Glossary of terms related to kinetics, thermodynamics, and mechanisms of polymerization (IUPAC Recommendations 2008). *Pure and Applied Chemistry* **2008,** *80* (10), 2163-2193.

16. Billiet, L.; Fournier, D.; Du Prez, F., Step-growth polymerization and 'click' chemistry: The oldest polymers rejuvenated. *Polymer* **2009,** *50* (16), 3877-3886.

17. Szwarc, M., Living'Polymers. *Nature.* **1956,** *178* (4543), 1168-1169.

18. Grubbs, R. B.; Grubbs, R. H., 50th Anniversary Perspective: Living Polymerization—Emphasizing the Molecule in Macromolecules. *Macromolecules* **2017,** *50* (18), 6979-6997.

19. Szwarc, M.; Levy, M.; Milkovich, R., Polymerization Initiated by Electron Transfer to Monomer. A New Method of Formation of Block Polymers. *Journal of the American Chemical Society* **1956,** *78* (11), 2656-2657.

20. Aoshima, S.; Kanaoka, S., A Renaissance in Living Cationic Polymerization. *Chemical Reviews* **2009,** *109* (11), 5245-5287.

21. Bielawski, C. W.; Grubbs, R. H., Living ring-opening metathesis polymerization. *Progress in Polymer Science* **2007,** *32* (1), 1-29.

22. Webster, O. W.; Hertler, W. R.; Sogah, D. Y.; Farnham, W. B.; RajanBabu, T. V., Group-transfer polymerization. 1. A new concept for addition polymerization with organosilicon initiators. *Journal of the American Chemical Society* **1983,** *105* (17), 5706-5708.

23. Webster, O. W., Living polymerization methods. *Science (New York, N.Y.)* **1991,** *251* (4996), 887-893.

24. Hadjichristidis, N.; Iatrou, H.; Pispas, S.; Pitsikalis, M., Anionic polymerization: High vacuum techniques. *Journal of Polymer Science Part A: Polymer Chemistry* **2000,** *38* (18), 3211-3234.

25. Matyjaszewski, K.; Spanswick, J., Controlled/living radical polymerization. *Materials Today* **2005,** *8* (3), 26-33.

26. Braunecker, W. A.; Matyjaszewski, K., Controlled/living radical polymerization: Features, developments, and perspectives. *Progress in Polymer Science* **2007,** *32* (1), 93-146.

27. Shanmugam, S.; Matyjaszewski, K., Reversible Deactivation Radical Polymerization: State-of-the-Art in 2017. In *Reversible Deactivation Radical Polymerization: Mechanisms and Synthetic Methodologies*, American Chemical Society: 2018; Vol. 1284, pp 1-39.

28. Grubbs, R. B., Nitroxide-Mediated Radical Polymerization: Limitations and Versatility. *Polymer Reviews* **2011,** *51* (2), 104-137.

29. Matyjaszewski, K.; Xia, J., Atom Transfer Radical Polymerization. *Chem. Rev.* **2001,** *101* (9), 2921-2990.

30. Tian, X.; Ding, J.; Zhang, B.; Qiu, F.; Zhuang, X.; Chen, Y., Recent Advances in RAFT Polymerization: Novel Initiation Mechanisms and Optoelectronic Applications. *Polymers (Basel)* **2018,** *10* (3).

31. Solomon, D.; Rizzardo, E.; Cacioli, P., Patent 4,581,429, March 27, 1985. *Rizzardo, E. Chem. Aust* **1987,** *54*, 32.

32. Hawker, C. J., Molecular Weight Control by a "Living" Free-Radical Polymerization Process. *Journal of the American Chemical Society* **1994,** *116* (24), 11185-11186.

33. Hawker, C. J.; Barclay, G. G.; Orellana, A.; Dao, J.; Devonport, W., Initiating Systems for Nitroxide-Mediated "Living" Free Radical Polymerizations: Synthesis and Evaluation. *Macromolecules* **1996,** *29* (16), 5245-5254.

34. Hawker, C. J.; Bosman, A. W.; Harth, E., New Polymer Synthesis by Nitroxide Mediated Living Radical Polymerizations. *Chemical Reviews* **2001,** *101* (12), 3661-3688.

35. Nicolas, J.; Guillaneuf, Y.; Lefay, C.; Bertin, D.; Gigmes, D.; Charleux, B., Nitroxide-mediated polymerization. *Progress in Polymer Science* **2013,** *38* (1), 63-235.

36. Nicolas, J.; Guillaneuf, Y., Living Radical Polymerization: Nitroxide-Mediated Polymerization. In *Encyclopedia of Polymeric Nanomaterials*, Kobayashi, S.; Müllen, K., Eds. Springer Berlin Heidelberg: Berlin, Heidelberg, 2021; pp 1-16.

37. Kato, M.; Kamigaito, M.; Sawamoto, M.; Higashimura, T., Polymerization of Methyl Methacrylate with the Carbon Tetrachloride/Dichlorotris-(triphenylphosphine)ruthenium(II)/Methylaluminum Bis(2,6-di-tert-butylphenoxide)

Initiating System: Possibility of Living Radical Polymerization. *Macromolecules* **1995,** *28* (5), 1721-1723.

38. Wang, J.-S.; Matyjaszewski, K., Controlled/"living" radical polymerization. atom transfer radical polymerization in the presence of transition-metal complexes. *Journal of the American Chemical Society* **1995,** *117* (20), 5614-5615.

39. Ribelli, T. G.; Lorandi, F.; Fantin, M.; Matyjaszewski, K., Atom Transfer Radical Polymerization: Billion Times More Active Catalysts and New Initiation Systems. *Macromol Rapid Commun* **2019,** *40* (1), e1800616.

40. Chiefari, J.; Chong, Y. K. B.; Ercole, F.; Krstina, J.; Jeffery, J.; Le, T. P. T.; Mayadunne, R. T. A.; Meijs, G. F.; Moad, C. L.; Moad, G.; Rizzardo, E.; Thang, S. H., Living Free-Radical Polymerization by Reversible Addition-Fragmentation Chain Transfer: The RAFT Process. *Macromolecules* **1998,** *31*, 5559–5562.

41. Hill, M. R.; Carmean, R. N.; Sumerlin, B. S., Expanding the Scope of RAFT Polymerization: Recent Advances and New Horizons. *Macromolecules* **2015,** *48* (16), 5459-5469.

42. Perrier, S., 50th Anniversary Perspective: RAFT Polymerization—A User Guide. *Macromolecules* **2017,** *50* (19), 7433-7447.

43. Perrier, S.; Takolpuckdee, P., Macromolecular design via reversible addition-fragmentation chain transfer (RAFT)/xanthates (MADIX) polymerization. *Journal of Polymer Science Part A: Polymer Chemistry* **2005,** *43* (22), 5347-5393.

44. Moad, G.; Rizzardo, E.; Thang, S. H., Living Radical Polymerization by the RAFT Process – A Third Update. *Australian Journal of Chemistry* **2012,** *65* (8).

45. Inglis, A. J.; Sinnwell, S.; Davis, T. P.; Barner-Kowollik, C.; Stenzel, M. H., Reversible Addition Fragmentation Chain Transfer (RAFT) and Hetero-Diels−Alder

Chemistry as a Convenient Conjugation Tool for Access to Complex Macromolecular Designs. *Macromolecules* **2008,** *41* (12), 4120-4126.

46. Keddie, D. J.; Moad, G.; Rizzardo, E.; Thang, S. H., RAFT Agent Design and Synthesis. *Macromolecules* **2012,** *45* (13), 5321-5342.

47. Tanaka, J.; Gurnani, P.; Cook, A. B.; Häkkinen, S.; Zhang, J.; Yang, J.; Kerr, A.; Haddleton, D. M.; Perrier, S.; Wilson, P., Microscale synthesis of multiblock copolymers using ultrafast RAFT polymerisation. *Polymer Chemistry* **2019,** *10* (10), 1186-1191.

48. Zaquen, N.; Kadir, A. M. N. B. P. H. A.; Iasa, A.; Corrigan, N.; Junkers, T.; Zetterlund, P. B.; Boyer, C., Rapid Oxygen Tolerant Aqueous RAFT Photopolymerization in Continuous Flow Reactors. *Macromolecules* **2019,** *52* (4), 1609-1619.

49. Yeow, J.; Chapman, R.; Gormley, A. J.; Boyer, C., Up in the air: oxygen tolerance in controlled/living radical polymerisation. *Chemical Society Reviews* **2018,** *47* (12), 4357-4387.

50. McKenzie, T. G.; Fu, Q.; Uchiyama, M.; Satoh, K.; Xu, J.; Boyer, C.; Kamigaito, M.; Qiao, G. G., Beyond Traditional RAFT: Alternative Activation of Thiocarbonylthio Compounds for Controlled Polymerization. *Adv Sci (Weinh)* **2016,** *3* (9), 1500394.

51. Chen, M.; Zhong, M.; Johnson, J. A., Light-Controlled Radical Polymerization: Mechanisms, Methods, and Applications. *Chem Rev* **2016,** *116* (17), 10167-211.

52. Phommalysack-Lovan, J.; Chu, Y.; Boyer, C.; Xu, J., PET-RAFT polymerisation: towards green and precision polymer manufacturing. *Chem Commun (Camb)* **2018,** *54* (50), 6591-6606.

53. Xu, J.; Jung, K.; Atme, A.; Shanmugam, S.; Boyer, C., A robust and versatile photoinduced living polymerization of conjugated and unconjugated monomers and its oxygen tolerance. *J Am Chem Soc* **2014,** *136* (14), 5508-19.

54. Xu, J.; Shanmugam, S.; Duong, H. T.; Boyer, C., Organo-photocatalysts for photoinduced electron transfer-reversible addition–fragmentation chain transfer (PET-RAFT) polymerization. *Polymer Chemistry* **2015,** *6* (31), 5615-5624.

55. Shanmugam, S.; Xu, J.; Boyer, C., Photoinduced Electron Transfer–Reversible Addition–Fragmentation Chain Transfer (PET-RAFT) Polymerization of Vinyl Acetate and N-Vinylpyrrolidinone: Kinetic and Oxygen Tolerance Study. *Macromolecules* **2014,** *47* (15), 4930-4942.

56. Ng, G.; Yeow, J.; Xu, J.; Boyer, C., Application of oxygen tolerant PET-RAFT to polymerization-induced self-assembly. *Polymer Chemistry* **2017,** *8* (18), 2841-2851.

57. Otsu, T., Iniferter concept and living radical polymerization. *Journal of Polymer Science Part A: Polymer Chemistry* **2000,** *38* (12), 2121-2136.

58. Easterling, C. P.; Xia, Y.; Zhao, J.; Fanucci, G. E.; Sumerlin, B. S., Block Copolymer Sequence Inversion through Photoiniferter Polymerization. *ACS Macro Lett* **2019,** *8* (11), 1461-1466.

59. Hartlieb, M., Photo-Iniferter RAFT Polymerization. *Macromol Rapid Commun* **2022,** *43* (1), e2100514.

60. Matyjaszewski, K., Atom Transfer Radical Polymerization (ATRP): Current Status and Future Perspectives. *Macromolecules* **2012,** *45* (10), 4015-4039.

61. Hagiopol, C., Copolymers. In *Encyclopedia of Condensed Matter Physics*, Bassani, F.; Liedl, G. L.; Wyder, P., Eds. Elsevier: Oxford, 2005; pp 235-240.

62. Liu, G., 5.08 - Chemical Processing of Assembled Block Copolymers. In *Comprehensive Nanoscience and Technology*, Andrews, D. L.; Scholes, G. D.; Wiederrecht, G. P., Eds. Academic Press: Amsterdam, 2011; pp 225-258.

63. Feng, H.; Lu, X.; Wang, W.; Kang, N. G.; Mays, J. W., Block Copolymers: Synthesis, Self-Assembly, and Applications. *Polymers* **2017,** *9* (10), 1-31.

64. Karayianni, M.; Pispas, S., Block copolymer solution self-assembly: Recent advances, emerging trends, and applications. *Journal of Polymer Science* **2021,** *59* (17), 1874-1898.

65. Discher, D. E.; Ahmed, F., Polymersomes. *Annu Rev Biomed Eng* **2006,** *8*, 323-41.

66. Doncom, K. E. B.; Blackman, L. D.; Wright, D. B.; Gibson, M. I.; O'Reilly, R. K., Dispersity effects in polymer self-assemblies: a matter of hierarchical control. *Chem Soc Rev* **2017,** *46* (14), 4119-4134.

67. Baranello, M. P.; Bauer, L.; Jordan, C. T.; Benoit, D. S. W., Micelle Delivery of Parthenolide to Acute Myeloid Leukemia Cells. *Cell Mol Bioeng* **2015,** *8* (3), 455-470.

68. Lovett, J. R.; Ratcliffe, L. P.; Warren, N. J.; Armes, S. P.; Smallridge, M. J.; Cracknell, R. B.; Saunders, B. R., A Robust Cross-Linking Strategy for Block Copolymer Worms Prepared via Polymerization-Induced Self-Assembly. *Macromolecules* **2016,** *49* (8), 2928-2941.

69. Blackman, L. D.; Varlas, S.; Arno, M. C.; Houston, Z. H.; Fletcher, N. L.; Thurecht, K. J.; Hasan, M.; Gibson, M. I.; O'Reilly, R. K., Confinement of Therapeutic Enzymes in Selectively Permeable Polymer Vesicles by Polymerization-Induced Self-Assembly (PISA) Reduces Antibody Binding and Proteolytic Susceptibility. *ACS Cent Sci* **2018,** *4* (6), 718-723.

70. Toebes, B. J.; Abdelmohsen, L. K. E. A.; Wilson, D. A., Enzyme-driven biodegradable nanomotor based on tubular-shaped polymeric vesicles. *Polymer Chemistry* **2018,** *9* (23), 3190-3194.

71. Grzelczak, M.; Liz-Marzan, L. M.; Klajn, R., Stimuli-responsive self-assembly of nanoparticles. *Chem Soc Rev* **2019,** *48* (5), 1342-1361.

72. Seeman, N. C., DNA in a material world. *Nature* **2003,** *427-431*, 427.

73. Seeman, N. C.; Sleiman, H. F., DNA nanotechnology. *Nature Reviews Materials* **2017,** *3* (1), 1-23.

74. Liu, K.; Zheng, L.; Liu, Q.; de Vries, J. W.; Gerasimov, J. Y.; Herrmann, A., Nucleic acid chemistry in the organic phase: from functionalized oligonucleotides to DNA side chain polymers. *J Am Chem Soc* **2014,** *136* (40), 14255-62.

75. Seeman, N. C., Nanomaterials based on DNA. *Annu Rev Biochem* **2010,** *79*, 65-87.

76. Yakovchuk, P.; Protozanova, E.; Frank-Kamenetskii, M. D., Base-stacking and base-pairing contributions into thermal stability of the DNA double helix. *Nucleic Acids Research* **2006,** *34* (2), 564-574.

77. Bathe, M.; Rothemund, P. W. K., DNA Nanotechnology: A foundation for Programmable Nanoscale Materials. *MRS Bulletin* **2017,** *42* (12), 882-888.

78. Aye, S. L.; Sato, Y., Therapeutic Applications of Programmable DNA Nanostructures. *Micromachines (Basel)* **2022,** *13* (2).

79. Winfree, E.; Liu, F.; Wenzler, L. A.; Seeman, N. C., Design and self-assembly of two-dimensional DNA crystals. *Nature* **1998,** *394* (6693), 539-544.

80. Lin, C.; Liu, Y.; Rinker, S.; Yan, H., DNA tile based self-assembly: building complex nanoarchitectures. *Chemphyschem* **2006,** *7* (8), 1641-1647.

81. Benson, E.; Mohammed, A.; Gardell, J.; Masich, S.; Czeizler, E.; Orponen, P.; Hogberg, B., DNA rendering of polyhedral meshes at the nanoscale. *Nature* **2015,** *523* (7561), 441-444.

82. Xu, F.; Wu, T.; Shi, X.; Pan, L., A study on a special DNA nanotube assembled from two single-stranded tiles. *Nanotechnology* **2019,** *30* (11), 115602.

83. Mao, h.; Sun, W.; Shen, Z.; Seeman, N. C., A nanomechanical devicebased on the B±Z transitionof DNA. *Nature* **1999,** *397* (6715), 144-146.

84. Kuzyk, A.; Schreiber, R.; Fan, Z.; Pardatscher, G.; Roller, E. M.; Hogele, A.; Simmel, F. C.; Govorov, A. O.; Liedl, T., DNA-based self-assembly of chiral plasmonic nanostructures with tailored optical response. *Nature* **2012,** *483* (7389), 311-314.

85. Andersen, E. S.; Dong, M.; Nielsen, M. M.; Jahn, K.; Subramani, R.; Mamdouh, W.; Golas, M. M.; Sander, B.; Stark, H.; Oliveira, C. L.; Pedersen, J. S.; Birkedal, V.; Besenbacher, F.; Gothelf, K. V.; Kjems, J., Self-assembly of a nanoscale DNA box with a controllable lid. *Nature* **2009,** *459* (7243), 73-6.

86. Whitfield, C. J.; Zhang, M.; Winterwerber, P.; Wu, Y.; Ng, D. Y. W.; Weil, T., Functional DNA-Polymer Conjugates. *Chem Rev* **2021,** *121* (18), 11030-11084.

87. Lemaitre, M.; Bayard, B.; Lebleu, B., Specific antiviral activity of a poly(L-lysine)-conjugated oligodeoxyribonucleotide sequence complementary to vesiculars tomatitis virus N protein mRNA initiation site. *Proc. Natl. Acad. Sci. USA* **1987,** *84*, 648-652.

88. Lee, K.; Povlich, L. K.; Kim, J., Label-Free and Self-Signal Amplifying Molecular DNA Sensors Based on Bioconjugated Polyelectrolytes. *Advanced Functional Materials* **2007,** *17* (14), 2580-2587.

89. Oishi, M.; Hayama, T.; Akiyama, Y.; Takae, S.; Harada, A.; Yarnasaki, Y.; Nagatsugi, F.; Sasaki, S.; Nagasaki, Y.; Kataoka, K., Supramolecular Assemblies for the

Cytoplasmic Delivery of Antisense Oligodeoxynucleotide: Polyion Complex (PIC)Micelles Based on Poly(ethyleneglycol)-SS-Oligodeoxynucleotide Conjugate. *Biomacromolecules* **2005,** *6*, 2449-2454.

90. Oishi, M.; Nagatsugi, F.; Sasaki, S.; Nagasaki, Y.; Kataoka, K., Smart polyion complex micelles for targeted intracellular delivery of PEGylated antisense oligonucleotides containing acid-labile linkages. *Chembiochem* **2005,** *6* (4), 718-725.

91. Li, Z.; Zhang, Y.; Fullhart, P.; Mirkin, C. A., Reversible and Chemically Programmable Micelle Assembly with DNA Block-Copolymer Amphiphiles. *Nano Letters* **2004,** *4* (6), 1055-1058.

92. Kwak, M.; Herrmann, A., Nucleic acid/organic polymer hybrid materials: synthesis, superstructures, and applications. *Angew Chem Int Ed Engl* **2010,** *49* (46), 8574-8587.

93. Zimmermann, J.; Kwak, M.; Musser, A. J.; Herrmann, A., Amphiphilic DNA block copolymers: nucleic acid-polymer hybrid materials for diagnostics and biomedicine. *Methods in Molecular Biology* **2011,** *751*, 239-266.

94. Tan, X.; Lu, X.; Jia, F.; Liu, X.; Sun, Y.; Logan, J. K.; Zhang, K., Blurring the Role of Oligonucleotides: Spherical Nucleic Acids as a Drug Delivery Vehicle. *Journal of the American Chemical Society* **2016,** *138* (34), 10834-10837.

95. Zhu, S.; Xing, H.; Gordiichuk, P.; Park, J.; Mirkin, C. A., PLGA Spherical Nucleic Acids. *Adv Mater* **2018,** *30* (22), e1707113.

96. Quemener, A. M.; Bachelot, L.; Forestier, A.; Donnou-Fournet, E.; Gilot, D.; Galibert, M. D., The powerful world of antisense oligonucleotides: From bench to bedside. *Wiley Interdiscip Rev RNA* **2020,** *11* (5), e1594.

97. Wagner, R. W., Gene inhibition using antisense oligodeoxynucleotides. *Nature* **1994,** *372* (6504), 333-335.

98. Jeong, J. H.; Kim, S. W.; Park, T. G., Novel Intracellular Delivery System of Antisense Oligonucleotide by Self-Assembled Hybrid Micelles Composed of DNA/PEG Conjugate and Cationic Fusogenic Peptide. *Bioconjugate Chemistry* **2003,** *14* (2), 473-479.

99. Tokura, Y.; Harvey, S.; Chen, C.; Wu, Y.; Ng, D. Y. W.; Weil, T., Fabrication of Defined Polydopamine Nanostructures by DNA Origami-Templated Polymerization. *Angewandte Chemie International Edition* **2018,** *57* (6), 1587-1591.

100. Luckerath, T.; Koynov, K.; Loescher, S.; Whitfield, C. J.; Nuhn, L.; Walther, A.; Barner-Kowollik, C.; Ng, D. Y. W.; Weil, T., DNA-Polymer Nanostructures by RAFT Polymerization and Polymerization-Induced Self-Assembly. *Angew Chem Int Ed Engl* **2020**.

101. Tokura, Y.; Jiang, Y.; Welle, A.; Stenzel, M. H.; Krzemien, K. M.; Michaelis, J.; Berger, R.; Barner-Kowollik, C.; Wu, Y.; Weil, T., Bottom-Up Fabrication of Nanopatterned Polymers on DNA Origami by In Situ Atom-Transfer Radical Polymerization. *Angew Chem Int Ed Engl* **2016,** *55* (19), 5692-7.

102. Fouz, M. F.; Mukumoto, K.; Averick, S.; Molinar, O.; McCartney, B. M.; Matyjaszewski, K.; Armitage, B. A.; Das, S. R., Bright Fluorescent Nanotags from Bottlebrush Polymers with DNA-Tipped Bristles. *ACS Central Science* **2015,** *1* (8), 431-438.

103. Melnychuk, N.; Klymchenko, A. S., DNA-Functionalized Dye-Loaded Polymeric Nanoparticles: Ultrabright FRET Platform for Amplified Detection of Nucleic Acids. *Journal of the American Chemical Society* **2018,** *140* (34), 10856-10865.

104. Xiao, F.; Lin, L.; Chao, Z.; Shao, C.; Chen, Z.; Wei, Z.; Lu, J.; Huang, Y.; Li, L.; Liu, Q.; Liang, Y.; Tian, L., Organic Spherical Nucleic Acids for the Transport

of a NIR-II-Emitting Dye Across the Blood–Brain Barrier. *Angewandte Chemie International Edition* **2020,** *59* (24), 9702-9710.

105. Banga, R. J.; Krovi, S. A.; Narayan, S. P.; Sprangers, A. J.; Liu, G.; Mirkin, C. A.; Nguyen, S. T., Drug-Loaded Polymeric Spherical Nucleic Acids: Enhancing Colloidal Stability and Cellular Uptake of Polymeric Nanoparticles through DNA Surface-Functionalization. *Biomacromolecules* **2017,** *18* (2), 483-489.

106. Bates, F. S.; Fredrickson, G. H., Block Copolymers—Designer Soft Materials. *Physics Today* **1999,** *52* (2), 32-38.

107. Zhang, L.; Eisenberg, A., Multiple Morphologies of "Crew-Cut" Aggregates of Polystyrene-b-poly(acrylic acid) Block Copolymers. *Science* **1995,** *268* (5218), 1728-1731.

108. Zhang, W. J.; Hong, C. Y.; Pan, C. Y., Polymerization-Induced Self-Assembly of Functionalized Block Copolymer Nanoparticles and Their Application in Drug Delivery. *Macromol Rapid Commun* **2019,** *40* (2), 1800279.

109. Zheng, G.; Caiyuan Pan, C., Reversible Addition-Fragmentation Transfer Polymerization in

Nanosized Micelles Formed in Situ. *Macromolecules* **2006,** *39*, 95-102.

110. Derry, M. J.; Fielding, L. A.; Armes, S. P., Polymerization-induced self-assembly of block copolymer nanoparticles via RAFT non-aqueous dispersion polymerization. *Progress in Polymer Science* **2016,** *52*, 1-18.

111. Blanazs, A.; Armes, S. P.; Ryan, A. J., Self-Assembled Block Copolymer Aggregates: From Micelles to Vesicles and their Biological Applications. *Macromol Rapid Commun* **2009,** *30* (4-5), 267-77.

112. Canning, S. L.; Smith, G. N.; Armes, S. P., A Critical Appraisal of RAFT-Mediated Polymerization-Induced Self-Assembly. *Macromolecules* **2016,** *49* (6), 1985-2001.

113. Lansalot, M.; Rieger, J., Polymerization-Induced Self-Assembly. *Macromol Rapid Commun* **2019,** *40* (2), 1800885.

114. Blanazs, A.; Ryan, A. J.; Armes, S. P., Predictive Phase Diagrams for RAFT Aqueous Dispersion Polymerization: Effect of Block Copolymer Composition, Molecular Weight, and Copolymer Concentration. *Macromolecules* **2012,** *45* (12), 5099-5107.

115. Warren, N. J.; Mykhaylyk, O. O.; Mahmood, D.; Ryan, A. J.; Armes, S. P., RAFT aqueous dispersion polymerization yields poly(ethylene glycol)-based diblock copolymer nano-objects with predictable single phase morphologies. *J Am Chem Soc* **2014,** *136* (3), 1023-33.

116. Warren, N. J.; Mykhaylyk, O. O.; Ryan, A. J.; Williams, M.; Doussineau, T.; Dugourd, P.; Antoine, R.; Portale, G.; Armes, S. P., Testing the vesicular morphology to destruction: birth and death of diblock copolymer vesicles prepared via polymerization-induced self-assembly. *J Am Chem Soc* **2015,** *137* (5), 1929-37.

117. Figg, C. A.; Simula, A.; Gebre, K. A.; Tucker, B. S.; Haddleton, D. M.; Sumerlin, B. S., Polymerization-induced thermal self-assembly (PITSA). *Chem Sci* **2015,** *6* (2), 1230-1236.

118. Figg, C. A.; Carmean, R. N.; Bentz, K. C.; Mukherjee, S.; Savin, D. A.; Sumerlin, B. S., Tuning Hydrophobicity To Program Block Copolymer Assemblies from the Inside Out. *Macromolecules* **2017,** *50* (3), 935-943.

119. Tan, J.; Sun, H.; Yu, M.; Sumerlin, B. S.; Zhang, L., Photo-PISA: Shedding Light on Polymerization-Induced Self-Assembly. *ACS Macro Letters* **2015,** *4* (11), 1249-1253.

120. Couturaud, B.; Georgiou, P. G.; Varlas, S.; Jones, J. R.; Arno, M. C.; Foster, J. C.; O'Reilly, R. K., Poly(Pentafluorophenyl Methacrylate)-Based Nano-Objects Developed by Photo-PISA as Scaffolds for Post-Polymerization Functionalization. *Macromol Rapid Commun* **2019,** *40* (2), e1800460.

121. Liu, D.; Cai, W.; Zhang, L.; Boyer, C.; Tan, J., Efficient Photoinitiated Polymerization-Induced Self-Assembly with Oxygen Tolerance through Dual-Wavelength Type I Photoinitiation and Photoinduced Deoxygenation. *Macromolecules* **2020,** *53* (4), 1212-1223.

122. Tan, J.; Bai, Y.; Zhang, X.; Zhang, L., Room temperature synthesis of poly(poly(ethylene glycol) methyl ether methacrylate)-based diblock copolymer nano-objects via Photoinitiated Polymerization-Induced Self-Assembly (Photo-PISA). *Polymer Chemistry* **2016,** *7* (13), 2372-2380.

123. Tan, J.; Liu, D.; Bai, Y.; Huang, C.; Li, X.; He, J.; Xu, Q.; Zhang, L., Enzyme-Assisted Photoinitiated Polymerization-Induced Self-Assembly: An Oxygen-Tolerant Method for Preparing Block Copolymer Nano-Objects in Open Vessels and Multiwell Plates. *Macromolecules* **2017,** *50* (15), 5798-5806.

124. Varlas, S.; Blackman, L. D.; Findlay, H. E.; Reading, E.; Booth, P. J.; Gibson, M. I.; O'Reilly, R. K., Photoinitiated Polymerization-Induced Self-Assembly in the Presence of Surfactants Enables Membrane Protein Incorporation into Vesicles. *Macromolecules* **2018,** *51* (16), 6190-6201.

125. Zaquen, N.; Zu, H.; Kadir, A. M. N. B. P. H. A.; Junkers, T.; Zetterlund, P. B.; Boyer, C., Scalable Aqueous Reversible Addition–Fragmentation Chain Transfer

Photopolymerization-Induced Self-Assembly of Acrylamides for Direct Synthesis of Polymer Nanoparticles for Potential Drug Delivery Applications. *ACS Applied Polymer Materials* **2019,** *1* (6), 1251-1256.

126. Varlas, S.; Georgiou, P. G.; Bilalis, P.; Jones, J. R.; Hadjichristidis, N.; O'Reilly, R. K., Poly(sarcosine)-Based Nano-Objects with Multi-Protease Resistance by Aqueous Photoinitiated Polymerization-Induced Self-Assembly (Photo-PISA). *Biomacromolecules* **2018,** *19* (11), 4453-4462.

127. Blackman, L. D.; Varlas, S.; Arno, M. C.; Fayter, A.; Gibson, M. I.; O'Reilly, R. K., Permeable Protein-Loaded Polymersome Cascade Nanoreactors by Polymerization-Induced Self-Assembly. *ACS Macro Lett* **2017,** *6* (11), 1263-1267.

128. Ligon, S. C.; Husar, B.; Wutzel, H.; Holman, R.; Liska, R., Strategies to reduce oxygen inhibition in photoinduced polymerization. *Chemical Reviews* **2014,** *114* (1), 557-589.

129. Yeow, J.; Chapman, R.; Xu, J.; Boyer, C., Oxygen tolerant photopolymerization for ultralow volumes. *Polymer Chemistry* **2017,** *8* (34), 5012-5022.

130. Ng, G.; Yeow, J.; Chapman, R.; Isahak, N.; Wolvetang, E.; Cooper-White, J. J.; Boyer, C., Pushing the Limits of High Throughput PET-RAFT Polymerization. *Macromolecules* **2018,** *51* (19), 7600-7607.

131. Chapman, R.; Gormley, A. J.; Stenzel, M. H.; Stevens, M. M., Combinatorial Low-Volume Synthesis of Well-Defined Polymers by Enzyme Degassing. *Angew Chem Int Ed Engl* **2016,** *55* (14), 4500-2503.

132. Varlas, S.; Foster, J. C.; Arkinstall, L. A.; Jones, J. R.; Keogh, R.; Mathers, R. T.; O'Reilly, R. K., Predicting Monomers for Use in Aqueous Ring-Opening Metathesis Polymerization-Induced Self-Assembly. *ACS Macro Lett* **2019,** *8* (4), 466-472.

133. Varlas, S.; Foster, J. C.; Georgiou, P. G.; Keogh, R.; Husband, J. T.; Williams, D. S.; O'Reilly, R. K., Tuning the membrane permeability of polymersome nanoreactors developed by aqueous emulsion polymerization-induced self-assembly. *Nanoscale* **2019,** *11* (26), 12643-12654.

134. Varlas, S.; Foster, J. C.; O'Reilly, R. K., Ring-opening metathesis polymerization-induced self-assembly (ROMPISA). *Chemical Communications* **2019,** *55* (62), 9066-9071.

135. Wilks, T. R.; Bath, J.; Vries, J. W.; Raymond, J. E.; Herrmann, A.; Turberfield, A. J.; O'Reilly, R. K., "Giant Surfactants" Created by the Fast and Efficient Functionalization of a DNA Tetrahedron with a Temperature-Responsive Polymer. *ACS Nano* **2013,** *7* (10), 8561–8572.

136. Yang, L.; Liang, M.; Cui, C.; Li, X.; Li, L.; Pan, X.; Yazd, H. S.; Hong, M.; Lu, J.; Cao, Y. C.; Tan, W., Enhancing the Nucleolytic Resistance and Bioactivity of Functional Nucleic Acids by Diverse Nanostructures through in Situ Polymerization-Induced Self-assembly. *Chembiochem* **2021,** *22* (4), 754-759.

137. Luckerath, T.; Koynov, K.; Loescher, S.; Whitfield, C. J.; Nuhn, L.; Walther, A.; Barner-Kowollik, C.; Ng, D. Y. W.; Weil, T., DNA-Polymer Nanostructures by RAFT Polymerization and Polymerization-Induced Self-Assembly. *Angew Chem Int Ed Engl* **2020,** *59* (36), 15474-15479.

138. Schaertl, W., *Light Scattering from Polymer Solutions and Nanoparticle Dispersions*. 2007.

139. Patterson, J. P.; Robin, M. P.; Chassenieux, C.; Colombani, O.; O'Reilly, R. K., The analysis of solution self-assembled polymeric nanomaterials. *Chem Soc Rev* **2014,** *43* (8), 2412-25.

140. Patterson, J. P.; Xu, Y.; Moradi, M. A.; Sommerdijk, N.; Friedrich, H., CryoTEM as an Advanced Analytical Tool for Materials Chemists. *Acc Chem Res* **2017,** *50* (7), 1495-1501.

141. Wilson, N. R.; Pandey, P. A.; Beanland, R.; Young, R. J.; Kinloch, I. A.; Gong, L.; Liu, Z.; Suenaga, K.; Rourke, J. P.; York, S. J.; Sloan, J., Graphene Oxide: Structural Analysis and Application as a Highly Transparent Support for Electron Microscopy. *ACS Nano* **2009,** *3* (9), 2547-2556.

142. Thompson, R. F.; Walker, M.; Siebert, C. A.; Muench, S. P.; Ranson, N. A., An introduction to sample preparation and imaging by cryo-electron microscopy for structural biology. *Methods* **2016,** *100*, 3-15.

2 : Optimizing conditions for low-volume RAFT-mediated photo-PISA

2.1 Introduction

Synthetic polymers have drastically changed numerous aspects of present-day living. It has played a major role in creating innovative materials, technologies, and products. Over the last two decades, polymerization-induced self-assembly (PISA) has received significant attention in the polymer field due to the method's simplicity,[1, 2] versatility,[3] and diverse range of applications; which include drug delivery,[4] catalysis,[5] and sensing.[6] PISA combines block copolymer synthesis and self-assembly, resulting in well-defined nanoparticles such as spherical micelles, worms, and vesicles with a high degree of control over size, morphology, and functionality.[7-12]

In recent years, photoinitiated polymerization-induced self-assembly (photo-PISA) has been investigated because it enables a high degree of control over the dispersion polymerization process by manipulating the wavelength and intensity of incident light without the need of external heat.[13-21] Photo-PISA introduces light to initiate or control the polymerization process in PISA by incorporating photoactive species, such as photoinitiators, photoiniferters, or photocatalysts. In general, photoactive species generate radical species which can initiate the radical polymerization of vinyl monomers to form a growing polymer chain. If the growing chains becomes increasingly solvophobic, and contains a segregated solvophillic region, the resulting block copolymers can self-assemble with one another, to form nanoparticles.[22] The photo-PISA process can be controlled temporally, which can further enhance the control over the generated nanoparticles.[13, 23] Furthermore, the use of mild room temperature polymerization conditions in photo-PISA allows for the encapsulation of thermally sensitive therapeutics without affecting the polymerization rate or their activities.[18, 24] Finally, the effect of temperature on the self-assembly process and the morphological evolution can be studied using photo-PISA.[25] Reversible addition-fragmentation chain

transfer (RAFT) is commonly used in photo-PISA because it allows for the synthesis of well-defined block copolymers with controlled molecular weights and low dispersities.[20] In 2017, our group investigated the differences between photo- and thermally initiated PISA processes using the well-documented poly(ethylene glycol)-*b*-poly(2-hydroxypropyl methacrylate) (PEG-*b*-PHPMA) PISA system.[13] In this system, chain transfer agent (CTA) derived from 4-cyano-4-(((ethylthio)carbonothioyl)thio)pentanoic acid (CEPA) was applied without the addition of an external photoinitiator or photocatalyst in the photo-PISA system, known as photoiniferter, allowing for the synthesis of well-defined polymers with controlled molecular weight and low polydispersity as discussed in Chapter 1. In this work, photoinitiated PISA offers advantages over thermally initiated PISA, *i.e.* it allows for the formation of predictable morphologies within minutes under very mild reaction conditions, whereas thermal PISA typically requires elevated temperatures for hours. However, the loss of the end group in photoinitiated PISA was shown to drive the formation of higher-order structures, compared to thermally initiated PISA which led to higher end group fidelity. The polymerization method therefore was shown to have a significant impact on the morphology of the resulting polymer self-assemblies.

In this chapter, the established PEG-*b*-PHPMA by PISA system was studied since it is a well-known copolymer and be able to compare with photo-PISA literature.[13] Poly(ethylene glycol) (PEG), which act as our solvophillic stabilizing block, is a hydrophilic polymer known for its excellent biocompatibility and water solubility.[26] It possesses a flexible, hydrophilic chain of repeating ethylene glycol units. PEG has low toxicity, resistance to protein adsorption, and the ability to reduce nonspecific interactions with biological components, making it widely used in biomedical applications. Poly(2-hydroxypropyl methacrylate) (PHPMA) is a synthetic polymer derived from methacrylic

acid.[27-29] It contains hydroxyl groups along its polymer backbone, which contribute to its hydrophilicity. PHPMA has good biocompatibility and can be easily modified to introduce various functional groups or side chains.[30] It shows favorable hydrophobic properties when used as a diblock in self-assembly. By combining PEG and PHPMA in a block copolymer, the resulting PEG-*b*-PHPMA diblock copolymers exhibit unique properties that combine the advantages of both polymers. Though, both photo- and thermal-initiated PISA of PEG-*b*-PHPMA has previously been reported, to date there are no publications of this system in low volume.

As mentioned in Chapter 1, the main objective of this thesis was to a develop a versatile method to synthesis uniform nanoparticles decorated with deoxynucleic acid (DNA). The high-cost and small amounts of precise synthetic DNA produced for biomedical research and commercially, proposes a problem for most PISA reactions. An ongoing challenge in the area of low volume polymerization, is the question of how to remove oxygen which can inhibit the polymerization. Furthermore, low reproducibility and special equipment requirements are also key issues to resolved to conduct low volume PISA.[31] The traditional methods use inert gas bubbling and freeze-pump-thaw cycles to remove oxygen; however, this can be extremely challenging to apply to low volume polymerizations(<300 μL) and cause significant changes in concentration. The aim of this chapter was to develop reproducible conditions of low-volume photo-PISA reactions by using PEG-macroCTA and HPMA monomer to generate polymeric nanostructures of various morphologies. There are two strategies to investigate the optimal low-volume RAFT-mediated photo-PISA condition, composed of physical and chemical strategies for eliminating oxygen inhibition in polymerization. According to the physical strategy, the nitrogen glove bag method was applied for curing in an oxygen-free atmosphere based on the concept of a glove box. It should be noted that this method is a new method for

low-volume photo-PISA. For chemical strategies in low-volume photo-PISA, photoinduced electron/energy transfer-reversible addition-fragmentation chain transfer (PET-RAFT)[32-34] and enzyme-assisted oxygen tolerance[17, 35-38] are most popular. In 2014, Boyer and coworkers first described the use of low-energy visible light for PET-RAFT polymerization by incorporating photoredox catalysts. [32] They also explored low volumes (20 μL)[36] and subsequently applied PISA in the same year.[33] However, this method required certain solvents to act as trapping species which react with singlet oxygen produced during photoredox reaction; these solvents include anthracenes, sulfoxides, or other supplementary reducing agents such as tertiary amines, ascorbic acid, anthracene, limonene, thioethers, and so on.[15, 32, 39, 40] This requirement arises from the photosensitized generation of singlet oxygen, which is rapidly quenched by trapping species. On the other hand, the enzyme-assisted oxygen tolerance method can be performed in aqueous solution, including buffer solution.[17, 35-38] Recently, some enzymes such as glucose oxidase (GOx),[5, 14, 35, 41] pyranoseoxidase (P2Ox), [37] and formate oxidase (FOx)[38] in the presence of glucose have been used to assist oxygen tolerance in polymerization, by using the intrinsic enzymatic activity to reduce oxygen. The exclusive utilization of GOx in photo-PISA has been observed, driven by its established reputation as an efficient enzyme at rapidly and consistently removing dissolved oxygen in the solution.[17, 42] This unique capability facilitates the photo-PISA reaction within ambient air environments. Tan *et al*. investigated GOx in photo-PISA in open batches and multiwell-plates at room temperature.[17] Using this approach, photo-PISA in the smallest volume system (40 μL) could be conducted under open air environments exposed to blue light at 405 nm. Moreover, Touve *et al.* employed UV-initiated PISA in a low-volume system using a 96-well microplate, coupled with automated sampling of each well, along with automated TEM and image analysis, to expedite the generation of phase diagrams.[43]

Samples chosen from these experiments were later scaled up, revealing that both morphologies and sizes remained consistent with those observed in the low-volume experiments.

In this chapter, the design and synthesis of low-volume photo-PISA of PEG-*b*-PHPMA copolymer was investigated to develop an optimal low-volume methodology for the application of DNA-RAFT agents in a robust and controlled manner.

2.2 Results and discussion

2.2.1 Synthesis of poly(ethylene glycol) macro-chain transfer agent (PEG-macroCTA)

To compare the results reported in the literature for similar structures, the reaction studied in this project (Scheme 2.1) uses poly(ethylene glycol) macro-chain transfer agent (PEG-macroCTA) with the same molecular weight (5.0 kg mol^{-1}, degree of polymerization (DP) = 113) as the one used in the studies by the groups of Armes, Zhang[18] and our group[13]. This CTA is a photoiniferter, as mentioned above. In order to synthesise the PEG_{113}-macroCTA, 4-cyano-4-(ethylsulfonylthiocarbonyl) disulfide macro-chain transfer agent (CEPA-CTA) was prepared by a substitution reaction. The synthetic method followed our previous work, as shown in Scheme 2.2 in Experimental section and purified by column chromatography, giving the desired CEPA-CTA in a yield of 36%.[13] The successful synthesis was confirmed by ^{1}H-NMR, ^{13}C-NMR, FTIR and MS, as shown in Figures 2.7, 2.8 and 2.9 in Experimental section, respectively.

The PEG_{113}-macroCTA was synthesised by Steglich esterification of CEPA-CTA with a poly(ethylene glycol) monomethyl ether (PEG_{113}-OH) homopolymer by *N,N′*-dicyclohexylcarbodiimide/4-(dimethylamino)pyridine (DCC/DMAP) coupling reaction. (Scheme 2.3 in Experimental section). The esterification efficiency can be calculated by ^{1}H-NMR spectroscopy from the area ratio of the signal at 4.25 ppm (m, 2H, C(=O)O-C***H₂*** from PEG section) and the signal at 2.64 ppm (m, 2H, C***H₂***-C(=O)O from CEPA-CTA section), indicating that about 96% of PEG_{113}-OH is converted into PEG_{113}-macroCTA (Figure 2.10 in Experimental section).

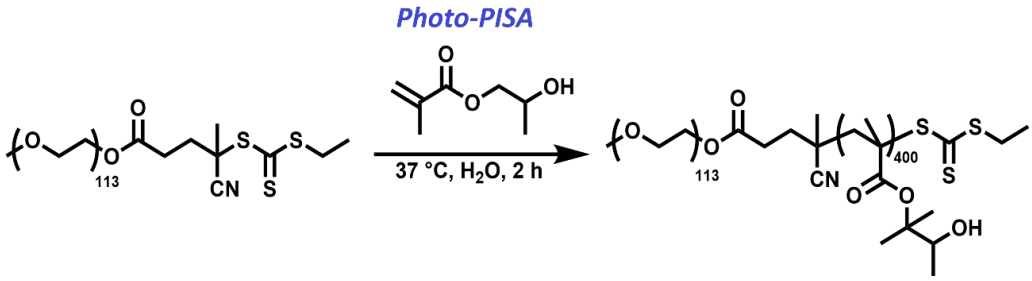

Scheme 2.1. Photo-PISA reaction of PEG_{113}-*b*-$PHPMA_{400}$.

2.2.2 Synthesis of PEG_{113}-*b*-$PHPMA_{400}$ (Benchmark PISA Reaction)

In order to compare with our previous work,[13] PEG_{113}-*b*-$PHPMA_{400}$ was synthesised by a benchmark photo-PISA reaction, as shown in Scheme 2.2. Hydroxypropyl methacrylate (HPMA) was used as a monomer to polymerize with PEG_{113}-macroCTA to form PEG_{113}-*b*-$PHPMA_{400}$ *via* photoinitiated polymerization-induced self-assembly (photo-PISA). HPMA monomer was chosen due to forming a strongly hydrophobic polymer block with PEG_{113}.[44] It should be noted that this monomer is a mixture of 2-hydroxypropyl methacrylate (major), and 2-isopropyl methacrylate (minor), thus the HPMA block is a copolymer of the two isomers.[45] 1 mL aqueous RAFT-mediated photo-PISA of PEG_{113}-*b*-$PHPMA_{400}$ reaction occurred upon 405 nm visible light irradiation of the solution at 37 °C under N_2 atmosphere. Almost complete monomer conversion (>99%) was achieved after 2 hours of reaction, as determined by ^{1}H-NMR spectroscopy. Previously work from our group which establishes a phase diagram for photoinitiated PISA of PEG_{113}-*b*-$PHPMA_X$,[13] reported well-defined unilamellar vesicles (ULVs) when targeting DP_{HPMA}=400 at 10 %w/w HPMA (or 11 %w/w solids content). After the photo-PISA, a change in the turbidity of the solution from transparent to opaque was observed, indicating that the growth of a hydrophobic PHPMA block had led to the formation of higher-order structures. As shown in Figure 2.1a, SEC analysis in DMF (with RI detection) of PEG_{113}-*b*-$PHPMA_{400}$ confirmed the successful chain-extension of HPMA.

The resulting diblock copolymer had relatively narrow molecular weight distribution ($M_{n,SEC\ UV}$ = 78.6 kg mol^{-1}, $Đ_M$ = 1.49) and revealed the controlled character of the photo-PISA process. Transmission electron microscopy (TEM) imaging revealed the successful development of spherical unilamellar vesicles (ULVs) (Figure 2.1b), while DLS analysis also confirmed a unimodal particle size distribution with D_h in the range of 400-500 nm (Figure 2.2).

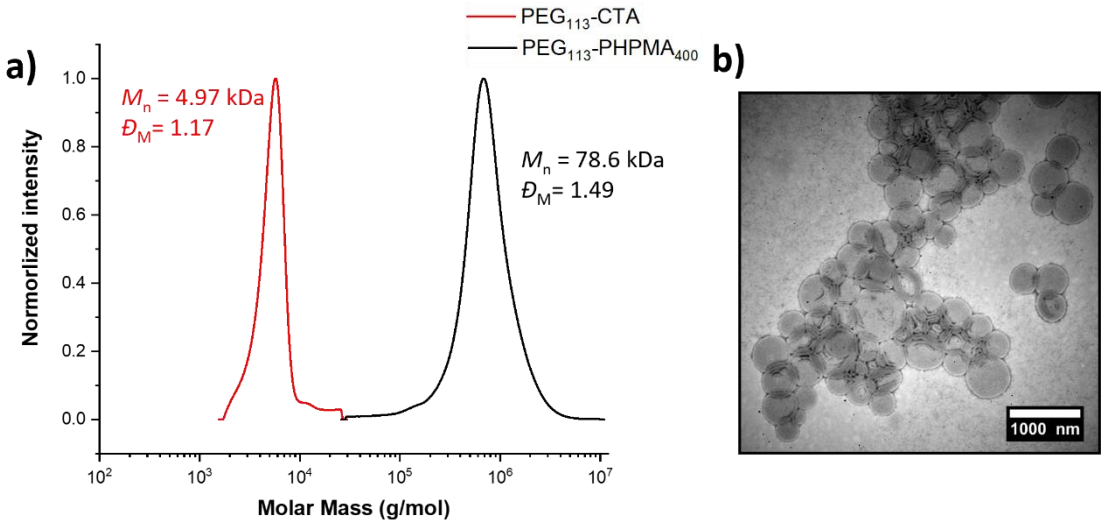

Figure 2.1. a) SEC RI molecular weight distributions for PEG_{113}-macroCTA and benchmark PEG_{113}-*b*-$PHPMA_{400}$ along with the corresponding M_n and $Đ_M$ values. M_n and $Đ_M$ values were calculated from PMMA standards using 5 mM NH_4BF_4 in DMF as the eluent. b) TEM images of PEG_{113}-*b*-$PHPMA_{400}$ of high-volume benchmark photoreaction.

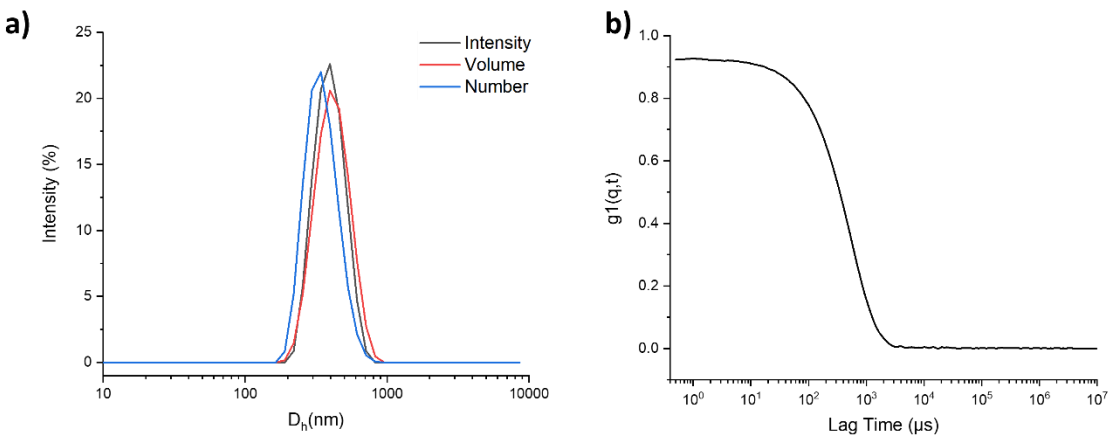

Figure 2.2. DLS a) size distribution and b) correlogram for benchmark PEG_{113}-*b*-$PHPMA_{400}$ vesicles.

2.2.3 Synthesis of low-volume N_2 glove bag PEG_{113}-*b*-$PHPMA_{400}$ in 96 well plate

Moving to a study of low volume, 50, 100, 150, and 200 μL reactions were investigated in a standard 96 well plate in place of the scintillation vial used for larger scale experiments and shaken at 200 rpm on top of a 405 nm LED array in the same UV incubator as that used above. To avoid oxygen inhibition, a N_2 glove bag was used while preparing the polymerization mixture, the plate was then sealed, removed from the glove bag, and transferred to UV incubator (Figure 2.3a). In contrast to the large volume experiments, reactions performed under these conditions were observed to form solid white gels after radiation exposure. The monomer conversion of these gels was observed to be relatively low (63-84%) compared to benchmark scale as shown in Table 2.1. The size of particle from DLS was also larger than observed in the benckmark reaction (431-712 nm) and TEM revealed a mixed phased of unilamellar vesicles and worms (Figure 2.14 and 2.15 in Experimental section, respectively) as shown in Table 2.1. Relating to our previous work that gel formation indicated low efficiency of creating pure morphology,[13] it was hypothesised that low conversion resulted from diffusion of residual oxygen into the solution inhibiting the polymerization. To prevent this, the addition of

mineral oil on top of the polymerization mixture was explored. However, gel formation still occurred (Table 2.1). These results suggested that gel formation was not from residual O_2 from the head space. Another explanation for the gel formation and low conversion was proposed to be the poor mixing of the polymerization solution. So, two methods for mixing were investigated, *i.e.* pipetting and stirring. For the pipetting method, a micropipette was used for mixing the mixtures in a glove bag before covering the plate (Figure 2.3b). This was studied both with and without the addition of mineral oil following mixing. Nevertheless, gelation was consistently observed. Moreover, these experiments suffered from a lack of reproducibility, with some resulting in a white solution while the majority turned to gels relating to varied conversions (60-90%) and fluctuating particle sizes (400-630 nm) as shown in Table 2.1. For the stirring method, a magnetic bar was used to stir the solution at 200 rpm to create a uniform solution (Figure 2.3c). Stirring was observed to result in white solutions, but poor to moderate conversions were observed (27-65%). The stirring is likely accelerating the diffusion of oxygen into the solution. Adding oil on top of the solution did increase conversions (76-85%), but it should be noted that the HPMA monomer is able to dissolve in mineral oil. So, adding mineral oil on top of the mixture in the stirring technique could accelerate the dissolution of HPMA in oil, leading to a lack of conversion accuracy. These results indicated that the N_2 glove bag method was ineffective at removing oxygen, despite the fact that N_2 gas was cycled in and out of the bag three times before the preparation of the reaction solution. Enzyme-mediated oxygen-tolerant PISA was therefore explored as an alternative.

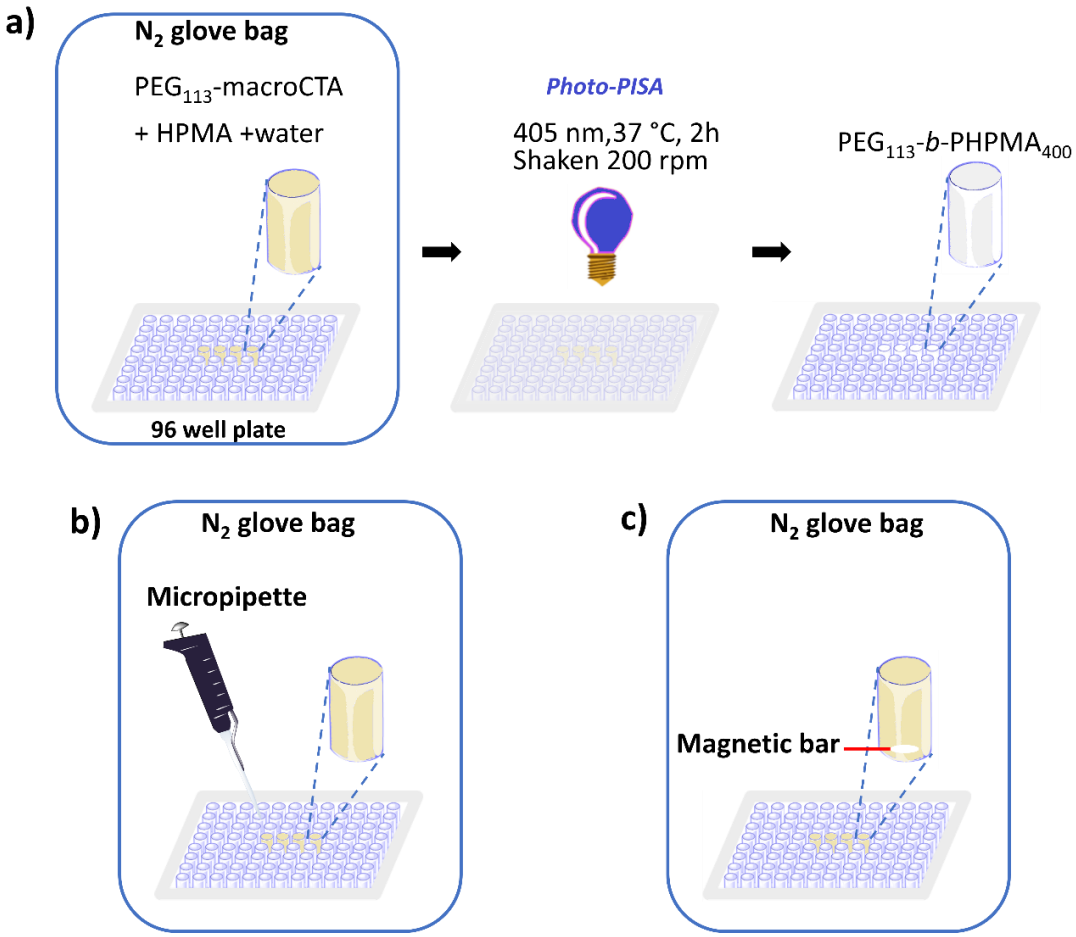

Figure 2.3. Strategies for preparing low-volume PISA reaction in N_2 glove bag of PEG_{113}-*b*-$PHPMA_{400}$ involving a) without mixing, b) mixed by pipette, and c) mixed by stirring.

Table 2.1. Characterization data of PEG_{113}-*b*-$PHPMA_{400}$ by N_2 glove bag method in 96 well plate.

Condition			Volume (µL)	Physical appearance	Conv. (%)[a]	Sizes (nm)[b]	PD[b]	Morpho-logy[c]
1 mL Benchmark PISA*			1000	White solution	>99	403	0.0	v
Shaken	do not mixed	without oil	50	White gel	63	431	0.3	w+v
			100	White gel	82	712	0.3	w+v
			150	White gel	82	506	0.1	w+v
			200	White gel, solution	84	451	0.1	w+v
		with oil	50	White gel	N/A	N/A	N/A	N/A
			100	White gel	90	759	0.3	-
			150	White gel	87	632	0.2	-
			200	White gel, solution	86	451	0.1	v
	mixed by pipette	without oil	50	white solution	56	400	0.4	-
			100	White gel	82	629	0.5	-
			150	White gel	84	592	0.4	-
			200	White gel	82	540	0.3	-
		with oil	50	White gel	78	423	0.4	-
			100	White gel	87	490	0.2	-
			150	White gel	84	437	0.4	-
			200	White gel	93	425	0.7	-
stirred		without oil	50	White solution	27	484	0.5	-
			100	White solution	30	431	0.5	-
			150	White solution	54	135	0.2	w
			200	White solution	65	569	0.4	w+v
		with oil	50	White solution	N/A	N/A	N/A	N/A
			100	White solution	76	439	0.4	-
			150	White solution	85	411	0.1	-
			200	White solution	80	579	0.3	-

[a] Calculated from ^{1}H NMR spectroscopy (400 MHz) in deuterated MeOD.

[b] Determined by DLS.

[c] Determined by TEM. Key: w = worms and v = vesicles.

*1 mL Benchmark PISA refers to a 1 mL volume of aqueous RAFT-mediated photo-PISA reaction that is conducted under a N_2 atmosphere.

2.2.4 Synthesis of low-volume enzyme-mediated oxygen-tolerant PEG$_{113}$-*b*-PHPMA$_{400}$ in 96 well plate.

To increase conversion and prevent gel formation, PEG$_{113}$-*b*-PHPMA$_{400}$ was synthesised by oxygen-tolerant photo-PISA reaction, which followed previous work within the group[46] as shown in Figure 2.4. Initially, the mixed solution was clear and transparent but after polymerization *via* enzyme-mediated oxygen-tolerant photo-PISA using mineral oil on top of the solution for 2 hours to prevent diffusion of residual oxygen into the system which would inhibit the polymerization., the clear solution changed to opaque and milky white, indicating PHPMA polymerization. Nonetheless, conversions were between 83-84% which were not significantly different from those observed with the N_2 glove bag approach and were lower than those achieved in the high-volume benchmark PISA reaction (Table 2). However, this method can be repeated with consistent results, whereas the N_2 glove bag method is not reproducible. From DLS data, the average size of the PEG$_{113}$-*b*-PHPMA$_{400}$ vesicles obtained at low volume was between 510-560 nm, which is larger than those observed for the benchmark reaction (380 nm, Table 2.2, and. Figure 2.16). However, the sizes of particles were within the expected range (400-700 nm) based on our group's previous study.[46] While unilamellar vesicles were observed for the 200 μL reactions, other morphologies such as worms and jellyfish were observed at lower reaction volumes (Table 2.2 and Figure 2.17 in Experimental section). SEC data revealed a lower M_n (62-66 kDa) for these reactions compared to benchmark, which may explain the presence of additional morphologies such as worm-like structures (Table 2.2). However, these data demonstrate that the oxygen-tolerant method achieves relatively

high conversions, consistently produces the desired morphology especially in reactions involving 200 µL, and results in narrower size distributions when compared to the N_2 glove bag method.

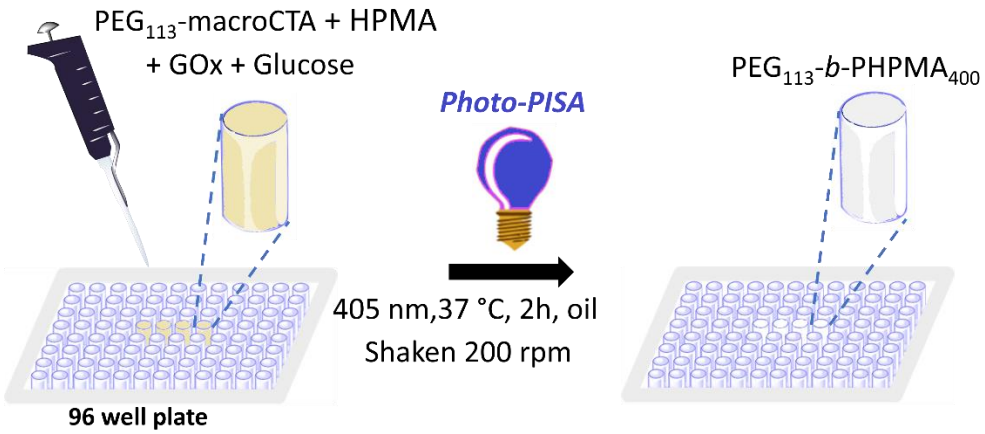

Figure 2.4. Strategy for low-volume enzyme-mediated oxygen-tolerant of PEG_{113}-*b*-$PHPMA_{400}$ in 96 well plate.

Table 2.2. Characterization data of PEG_{113}-*b*-$PHPMA_{400}$ by oxygen-tolerant method in 96 well plate.

Volume of sample (µL)	Physical appearances	Convers.[a] (%)	D_h (nm)[b]	PD[b]	M_n (×10³) (g/mol)[c]	$Đ_M$	Morpho-logy[d]
1000 (Benchmark)	White solution	>99	381	0.0	78.63	1.49	v
100	White solution	83	561	0.1	62.56	1.61	Undefined
150	White solution	84	514	0.1	66.23	1.57	w+v
200	White solution	84	518	0.1	68.07	1.56	v

[a] Calculated from ^{1}H NMR spectroscopy (400 MHz) in deuterated MeOD.

[b] Determined by DLS.

[c] Determined by DMF SEC with poly(methyl methacrylate) (PMMA) standards.

[d] Determined by TEM. Key: w = worms and v = vesicles.

2.2.5 Synthesis of low-volume enzyme-mediated oxygen-tolerant PEG$_{113}$-*b*-PHPMA$_{400}$ in pointed base PCR plate.

To increase conversion, pointed based PCR plate was used in place of a typical 96 well plate due to the lower surface area to volume ratio for the pointed base plates, which may prevent heating/evaporation effects. Interestingly, in the case of changing the container from a typical flat-bottomed 96 well plate to a pointed base PCR plate, conversion was enhanced from 83-84% to 90-95% (Table 2.3). According to DLS data, the particle sizes synthesized in the pointed base PCR plates ranged from 460 to 510 nm (Table 2.3 and Figure 2.18 in Experimental section). TEM showed pure unilamellar vesicles in all volume conditions, suggested this method was efficient (Figure 2.5). These data suggested that using pointed base PCR plates improved the efficiency of low-volume reactions.

Table 2.3. Characterization data of PEG$_{113}$-*b*-PHPMA$_{400}$ by oxygen-tolerant method.

Condition		**Volume (µL)**	**Physical appearance**	**Conv. (%)[a]**	**D_h (nm)[b]**	**PD[b]**	**Morpho-logy[c]**
1 mL Benchmark PISA*		1000	White solution	>99	403	0.0	v
oxygen-tolerant	96 well plates	50	N/A	N/A	N/A	N/A	N/A
		100	White solution	83	561	0.1	Undefined
		150	White solution	84	514	0.1	w+v
		200	White solution	84	518	0.1	v
	pointed base PCR plates	50	White solution	90	462	0.1	v
		100	White solution	93	453	0.1	v
		150	White solution	94	488	0.2	v
		200	White solution	95	509	0.1	v

[a] Calculated from ^{1}H NMR spectroscopy (400 MHz) in deuterated MeOD.

[b] Determined by DLS.

[c] Determined by TEM. Key: w = worms and v = vesicles.

*1 mL Benchmark PISA refers to a 1 mL volume of aqueous RAFT-mediated photo-PISA reaction that is conducted under a N_2 atmosphere.

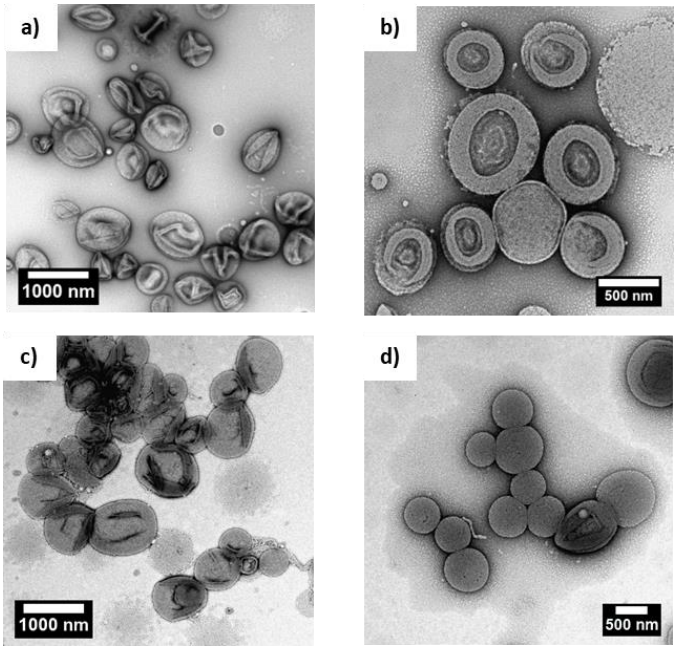

Figure 2.5. TEM images of oxygen-tolerant Photo-PISA of PEG_{113}-*b*-$PHPMA_{400}$ in pointed based plates in the total volume of the solution a) 50, b) 100, c) 150, and d) 200 μL.

The reaction conditions in the pointed base PCR plates were varied to explore if the results could be further optimised. To begin with, the reaction time was extended from 2 to 3 h. This extension in time was made to potentially enhance the conversion while maintaining the concentrations of GOx (2 μM) and glucose (0.1 M) consistent. Nonetheless, the results obtained after 3 h of reaction (87-94 % conversions and 435-699 nm) were not different from those after 2 h (90-95 % conversions and 462-509 nm) in terms of conversions and particle sizes, respectively (Table 2.4). Another condition involved increasing concentration of GOx (5 μM) and glucose (0.2 M) to enhance oxygen-tolerant efficiency resulting increase of conversions (92-97% and 94-98% for 2 and 3 hours of reaction time, respectively) and good control of particle size (460-510 nm, Table 2.4). However, the results obtained did not exhibit significant improvements in terms of conversions and

morphology. Thus, to perform at the lowest volume and concentrations of GOx and glucose in the low-volume system, the reaction with a volume of 50 µL and typical concentrations of GOx (2 µM) and glucose (0.1 M) was selected for further investigation, including the study of the phase diagram of PEG_{113}-*b*-$PHPMA_X$ and its application in DNA-polymer nanoparticles in the subsequent chapter.

Table 2.4. Characterization data of PEG_{113}-*b*-$PHPMA_{400}$ by oxygen-tolerant method in various conditions.

Conditions		**Volume (µL)**	**Physical appearances**	**Conv.[a] (%)**	**Sizes [b] (nm)**	**PD[b]**	**Morpho-logy[c]**
1 mL Benchmark PISA*		1000	White solution	>99	403	0.0	v
[GOx] 2 µM, Glucose 0.1 M (typical concentration)	2 h	50	White solution	90	462	0.1	v
		100	White solution	93	453	0.1	v
		150	White solution	94	488	0.2	v
		200	White solution	95	509	0.1	v
	3 h	50	White solution	87	449	0.0	-
		100	White solution	91	444	0.1	-
		150	White solution	93	699	0.2	-
		200	White solution	94	435	0.1	-
[GOx] 5 µM, Glucose 0.2 M	2 h	50	White solution	92	499	0.1	-
		100	White solution	95	459	0.1	-
		150	White solution	96	456	0.1	-
		200	White solution	97	471	0.1	-
	3 h	50	White solution	94	505	0.1	-
		100	White solution	96	468	0.1	-
		150	White solution	97	506	0.2	-
		200	White solution	98	459	0.0	-

[a] Calculated from ^{1}H NMR spectroscopy (400 MHz) in deuterated MeOD.

[b] Determined by DLS.

[c] Determined by TEM. Key: v = vesicles.

*1 mL Benchmark PISA refers to a 1 mL volume of aqueous RAFT-mediated photo-PISA reaction that is conducted under a N_2 atmosphere.

2.2.6 Synthesis of low-volume enzyme-mediated oxygen-tolerant PEG_{113}-*b*-$PHPMA_X$ at various degree of polymerization (DP) in pointed base PCR plate.

To investigate the robustness of the conditions, a phase diagram constructed for PEG_{113}-*b*-$PHPMA_x$ was created at 50 µL scale (Figure 2.6). According to the literatures, the amphiphile concentration can influence the particle morphology of polymers with identical block ratios and molar mass distributions, potentially resulting in significantly different morphologies.[1, 47, 48] Hence this parameter is represented on the *x*-axis as HPMA monomer concentration (mg mL^{-1}). Based on a fixed PEG stabilizer block DP of 113, systematic variation of the DP of the core-forming PHPMA block resulted in a series of PEG_{113}-*b*-$PHPMA_X$ diblock copolymers, where y represents the targeted DP ranging from 100 to 500. The copolymer morphology was assigned by using TEM to construct the phase diagram.

Phase diagram of enzyme-mediated oxygen-tolerant photo-PISA method was constructed at different monomer contents and DPs under the following condition: glucose oxidase 2 µM, glucose 0.1 M, performing reaction for 2 h at volume 50 µL (Figure 2.6). Each of the polymerizations used to construct the phase diagrams had relatively high conversions (80-95 %conversions), as shown in Table 2.5. SEC analysis of a representative sample of polymers showed that the molar mass distributions detected by the RI detector were almost identical in each case (Figure 2.7 a) and b)). DLS data of the samples are also shown in Table 2.5 and Figure 2.19 in Experimental section.

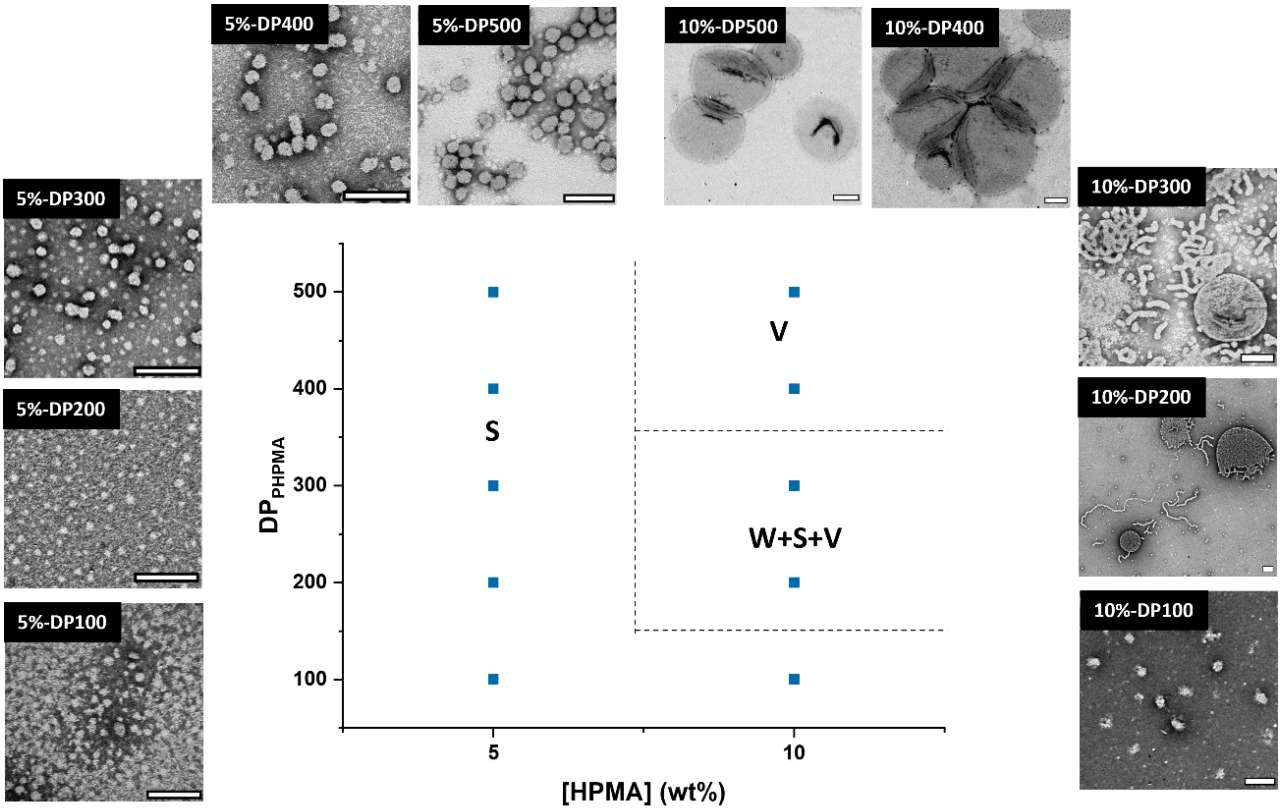

Figure 2.6. Phase Diagram of $mPEG_{113}$-*b*-$PHPMA_X$ formed by photo PISA, conducted at 50 µL with degassing *via* GOx + glucose and a layer of mineral oil. Key: s = spheres, w = worms, and v = vesicles. Scale bars = 200 nm. DP calculated from target DP * reaction conversion. In the case of mixed phases, the predominantly observed phase is listed first. The TEM samples were stained with an aqueous 1 wt% uranyl acetate (UA) solution prior to imaging.

Table 2.5. Characterization data of PEG_{113}-macroCTA and PHPMA diblock copolymers at various concentrations and DPs of HPMA.

[HPMA] (%w/w)	Targeted DP	Conv.[a] (%)	Size[b] (nm)	PD[b]	Morphology[c]
5	100	87	36	0.10	s
5	200	89	39	0.07	s
5	300	87	56	0.05	s
5	400	79	59	0.04	s
5	500	82	79	0.05	s
10	100	93	38	0.03	s
10	200	94	206	0.39	w+s+v
10	300	95	392	0.35	w+s+v
10	400	91	462	0.10	v
10	500	91	460	0.08	v

[a] Calculated from ^{1}H NMR spectroscopy (400 MHz) in deuterated MeOD.

[b] Determined by DLS.

[c] Determined by TEM. Key: s = spheres, w = worms, and v = vesicles. In the case of mixed phases, the predominantly observed phase is listed first.

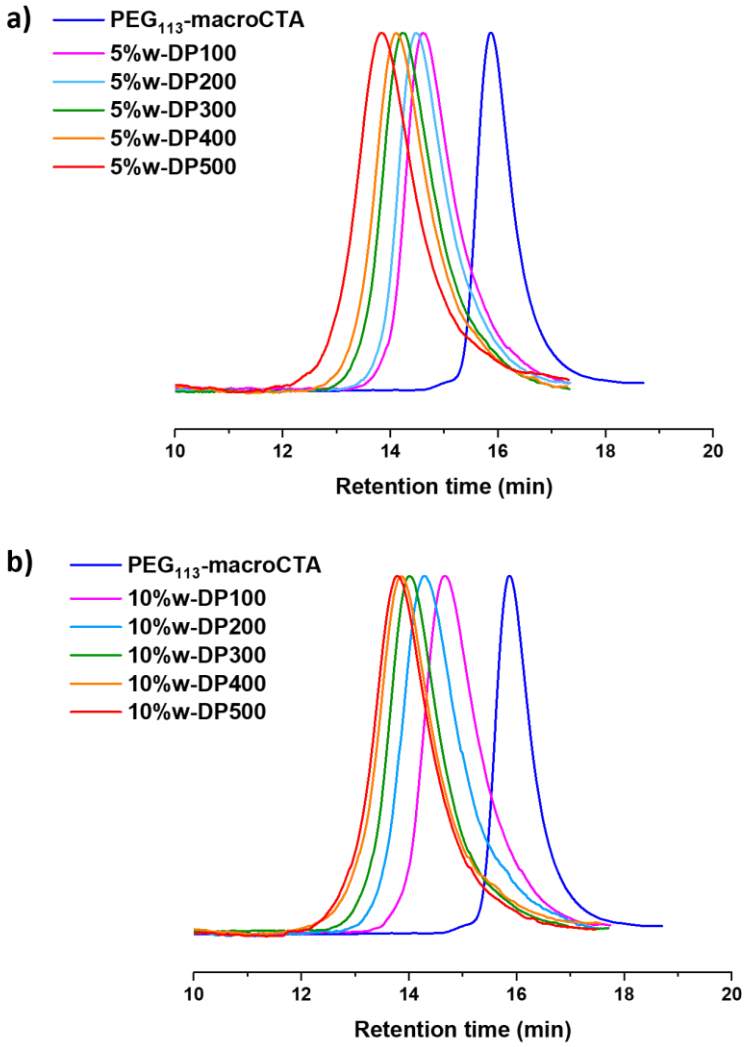

Figure 2.7. SEC RI traces of PEG_{113}-macroCTAs chain extended with different DP of PHPMA, (a) at 5%w/w [HPMA] and (b) at 10%w/w [HPMA] (DMF + 5 mM NH_4BF_4 as eluent, PMMA standard.

When RAFT-mediated photo-PISA are conducted at a HPMA monomer concentration of 5% w/w, only spherical nanoparticles were observed, regardless of the target DP of the core-forming block. The *D*h of these spherical nanoparticles increased from 36 to 79 nm when the DPs of PHPMA block increased from 100 to 500 (Table 2.5). This concept is commonly comprehended through the consideration of interfacial energy between the solvent and the insoluble block, as typically studied in traditional self-assembly.[49] This

interfacial energy is influenced by two main factors which are the core-solvent interaction parameter (χ) and the DP of the core block. As the DP of the core block increases, the aggregation number of the particles also increases in order to decrease the overall number of particles in the solution, thus minimizing the interfacial area between the core components and the solvent. Moreover, when investigating at monomer content of 10% w/w, as higher DPs are targeted, the morphologies evolved from pure spherical micelles (s, spheres) at DP=100 to mixed spherical micelles/ worm-like micelles/ vesicular nanostructures (s+w+v, spheres+worms+vesicles) at DPs = 200 and 300 until finally a pure vesicular nanostructure phase (v, vesicles) at DPs = 400 and 500. This phenomenon occurs when the aggregation number reaches a critical point, where the core chains reach their limit in stretching ability, causing the particles to undergo morphological changes.[49] In the transition of copolymer morphologies throughout the PISA process, two spherical micelles initially fuse to form a spherical dimer, leading to the formation of worm-like micelles and then the creation of vesicles.[1, 3, 50] Additionally, monomer concentration or solid content also plays a crucial role that influencing morphology in the PISA process. Higher monomer concentrations can promote the formation of higher-order morphologies through the polymerization of the core chains and an increased density of particles in the solvent.[51]

2.3 Conclusion

From the two techniques of low volume photo-PISA, N_2 glove bag technique shows low conversion and poor control of reproducibility, dispersity and morphology whereas the enzyme-mediated oxygen-tolerant technique provides higher conversion, and reasonable control of dispersity and morphology. Thus, enzyme-mediated oxygen-tolerant technique was applied to enhance conversion by variation of GOx and glucose concentrations and reaction time. High conversion (98%) of PEG_{113}-*b*-$PHPMA_{400}$ copolymers has successfully been achieved with reasonable dispersity and particle size at 200 µL by using [GOx] 5 µM and glucose 0.2 M under 405 nm light irradiation for 3 h. In order to perform at the lowest reaction volume and concentrations of GOx and glucose in the low-volume system, the reaction with a volume of 50 µL and typical concentrations of GOx (2 µM) and glucose (0.1 M) in pointed based PCR plates was the optimal condition with reasonable dispersity and particle size for further investigation such as the study of the phase diagram of PEG_{113}-*b*-$PHPMA_X$. Overall, this work helps set a precedent for conducting low-volume and high-throughput PISA reactions to utilise a deoxyribonucleic acid macromolecular chain transfer agent (DNA-CTA) and 2-hydroxypropyl methacrylate (HPMA) monomer to generate DNA-decorated polymeric nanostructures of various morphologies *via* PISA.

2.4 Experimental section

2.4.1 Materials

Poly(ethylene glycol) methyl ether (average *M*n=5,000 g mol-1, PEG-OH), carbon disulfide (anhydrous, ≥99%), sodium ethanethiolate, *N,N′*-dicyclohexylcarbodiimide (99%, DCC), 4-(dimethylamino)pyridine (≥98%, DMAP), were purchased from Sigma Aldrich and used without further purification.. Iodine, Diethyl ether, dichloromethane (DCM), and sodium chloride (NaCl) were purchased from Fisher Scientific. Ethyl acetate was purchased from VWR Chemicals. *n*-Dodecylphosphocholine (DPC) was obtained from Anatrace. 2-Hydroxypropyl methacrylate (mixture of isomers, 98%, HPMA) was purchased from Alfa Aesar and was passed through a column of basic alumina to remove inhibitor prior to use. Dry solvents used in the experiments were obtained by passing over a column of activated alumina using an Innovative Technologies solvent purification system. Formvar-coated copper grids were purchased from EM Resolutions.

2.4.2 Instrumentations and analysis

^{1}H-NMR spectra were recorded at 400 MHz on a Bruker DPX-400 spectrometer using chloroform-*d* (CDCl3) and methanol-*d4* (CD_3OD) as the solvent. Chemical shifts of protons are reported as δ in parts per million (ppm) and are relative to tetramethylsilane (TMS) at δ = 0 ppm when using solvent residual peak (CH_3OH, δ = 3.31 ppm).

Fourier transform-infrared (FT-IR) spectroscopy measurements were carried out using a Perkin Elmer Spectrum 100 spectrometer, in the range of 600 to 4000 cm^{-1}.

Size Exclusion Chromatography (SEC) analysis was performed on a system composed of a Varian 390-LC-Multi detector suite equipped with a Varian Polymer Laboratories guard column (PLGel 5 μM, 50 × 7.5 mm), two Mixed-C Varian Polymer Laboratories columns

(PLGel 5 μM, 300 × 7.5 mm) and a PLAST RT auto-sampler. Detection was conducted using a differential refractive index (RI) and an ultraviolet (UV) detector set to λ = 309 nm. The mobile phase used was DMF (HPLC grade) containing 5 mM NH4BF4 at 50 ˚C at a flow rate of 1.0 mL min-1. Poly(methyl methacrylate) (PMMA) standards were used for calibration. Molecular weights and dispersities were determined using Cirrus v3.3 SEC software.

Hydrodynamic diameters (D_h) of particles was determined by dynamic light scattering (DLS) using a Malvern Zetasizer Nano ZS with a 4 mW He-Ne 633 nm laser module operating at 25 ^oC. Measurements were carried out at an angle of 173° (back scattering), and results were analyzed using Malvern DTS 7.03 software. All determinations were repeated 4 times with at least 10 measurements recorded for each run. D_h values were calculated using the Stokes-Einstein equation where particles are assumed to be spherical, while for cylindrical particles DLS was used to detect multiple populations and obtain dispersity information.

Transmission Electron Microscopy (TEM) analysis was performed on a JEOL 2100 electron microscope at an acceleration voltage of 200 kV. All samples were diluted with deionized water and then deposited onto formvar-coated copper grids. After roughly 1 min, excess sample was blotted from the grid and the grid stained with an aqueous 1 wt% uranyl acetate (UA) solution for 1 min prior to blotting, drying and microscopic analysis.

The light source for the benchmark 1 mL photoinitiated PISA reactions (TruOpto OSV5X3CAC1E) was purchased from Rapid Electronics and had an output power of 800 mW at 12V DC operating at a wavelength of 400–410 nm. This was fitted to a custom-built setup fitted with a dimmer switch for controlling the output light intensity.

The LAD-1 LED array driver was purchased from Bio Research Centre Co., Ltd. The array was composed of 405 nm LEDs which each output a light power of 20 mW at 13.5 V when measured with an LMP-100 light power sensor (sensor area: 5.5 mm x 4.8 mm), placed directly above an array LED. For the Thermomixer setup, the LED-array was suspended over the sample holder *via* a clamp stand. For the Incubator setup the LED-array was placed upon a shaker plate, face up with a 96-microwell plate placed directly upon it, into which 150 µL eppendorfs containing sample were placed.

2.4.3 Synthetic Method

Synthesis of 4-cyano-4-[(ethylsulfanylthiocarbonyl)sulfanyl] pentanoic acid (CEPA)

4-Cyano-4-[(ethylsulfanylthiocarbonyl)sulfanyl] pentanoic acid chain transfer agent (CEPA-CTA) was synthesized according to a previously described process.[52] Sodium ethanethiolate (10.0 g, 0.119 mol, 1 eq) was suspended in 500 mL of dry diethyl ether at 0 °C. Carbon disulfide (7.74 mL, 0.131 mol, 1.1 eq) was subsequently added dropwise over 10 min, resulting to the formation of a thick yellow precipitate of sodium S-ethyl trithiocarbonate. After 2 h of stirring at room temperature, solid iodine (15.1 g, 0.059 mol, 0.5 eq) was added to the reaction medium. After 2 h, the solution was washed three times with aqueous sodium thiosulfate (1 M), water and finally saturated NaCl solution. The organic layer was thoroughly dried over $MgSO_4$ and the crude bis-(ethylsulfanylthiocarbonyl) disulfide was then isolated by rotary evaporation (16.0g, 0.058 mol, 98%).

A solution of bis-(ethylsulfanylthiocarbonyl) disulfide (16.0 g, 0.058 mol, 1 eq) and 4,4′-azobis(4-cyanopentanoic acid) (ACVA) (24.5 g, 0.087 mol, 1.5 eq) in 500 mL of ethyl acetate was heated at reflux for 18 h under N_2(g) atmosphere. Following rotary evaporation of the solvent, the crude CEPA was isolated by column chromatography

using silica gel as the stationary phase and 75:25 DCM-petroleum ether as the eluent. The isolated product was precipitated out of solution by using hexane leaving a yellow-light orange solid. The final product was collected and dried under reduced pressure to afford pure CEPA-CTA (10.95 g, 0.042 mol, 36%). ^{1}H-NMR (400 MHz, $CDCl_3$): δ (ppm) 3.35 (q, 2H, S-CH_2-CH_3), 2.38-2.71 (m, 4H, CH_2-CH_2), 1.89 (s, 3H, C(CN)-CH_3), 1.36 (t, 3H, S-CH_2-CH_3). ^{13}C-NMR (100 MHz, $CDCl_3$): δ (ppm) 216.6 (Cc), 176.9 (Ci), 118.9 (Cf), 46.2 (Cd), 33.5 (Cg), 31.4 (Cb), 29.5 (Ch), 24.9 (Ce), 12.8 (Ca). FT-IR (neat): ν (cm^{-1}) 1709 (C=O), 1073 (C=S)), 810 (C-S). HR-MS: m/z $[C_9H_{13}NO_2S_3+Na]^+$ calc. 286.0001 g mol^{-1}, found 286.0001 g mol^{-1}.

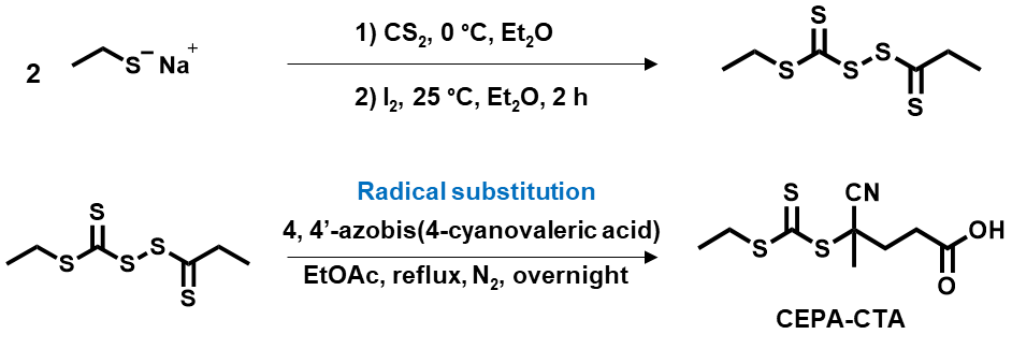

Scheme 2.2. Synthesis of CEPA-CTA.

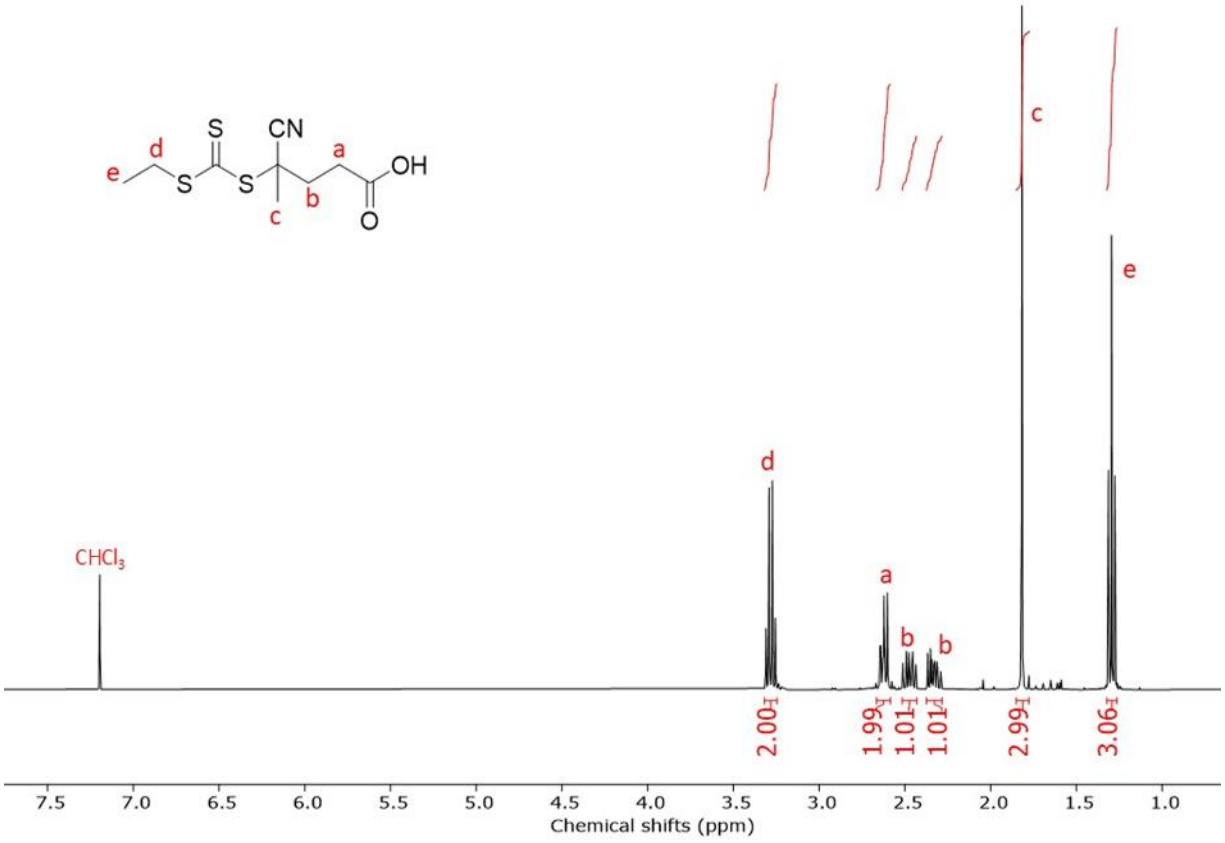

Figure 2.8. ^{1}H-NMR spectrum of CEPA-CTA in $CDCl_3$.

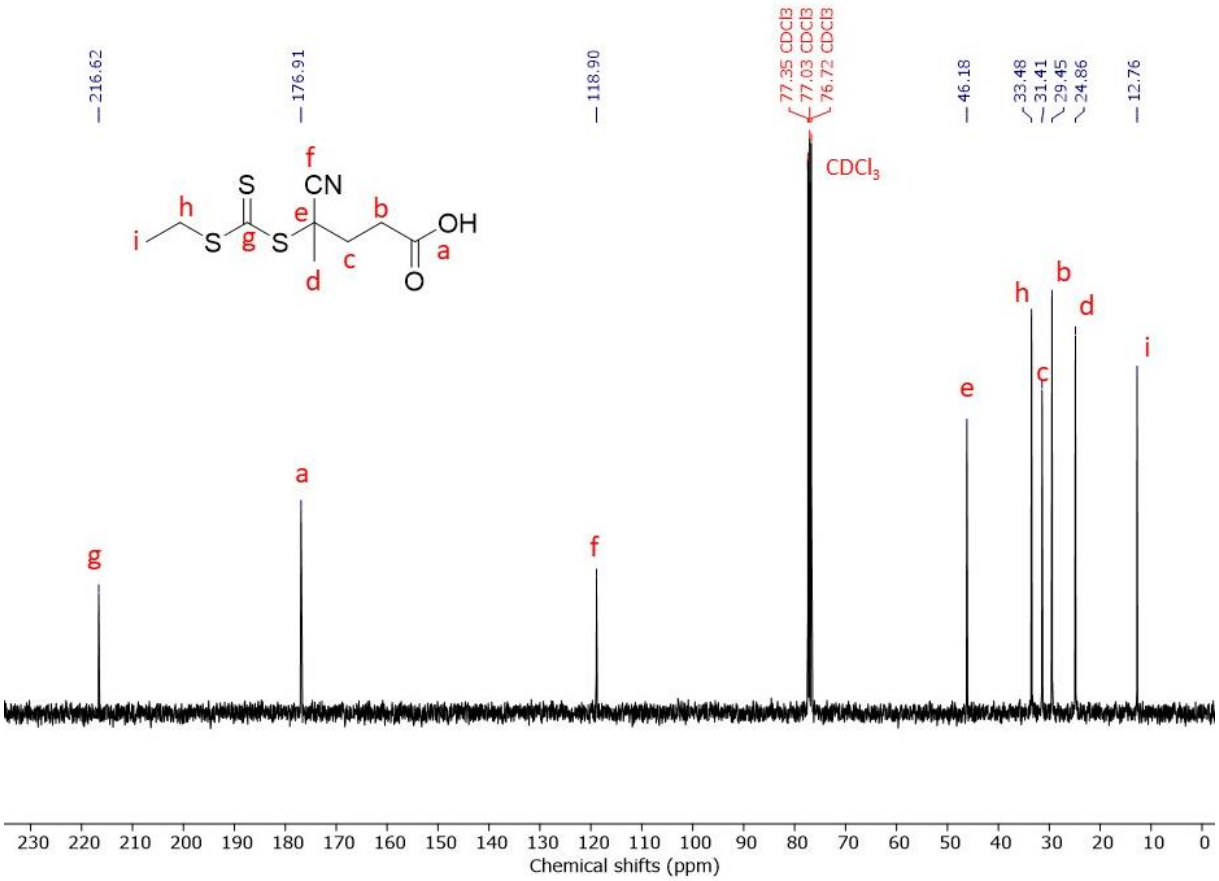

Figure 2.9. ^{13}C-NMR spectrum of CEPA-CTA in $CDCl_3$.

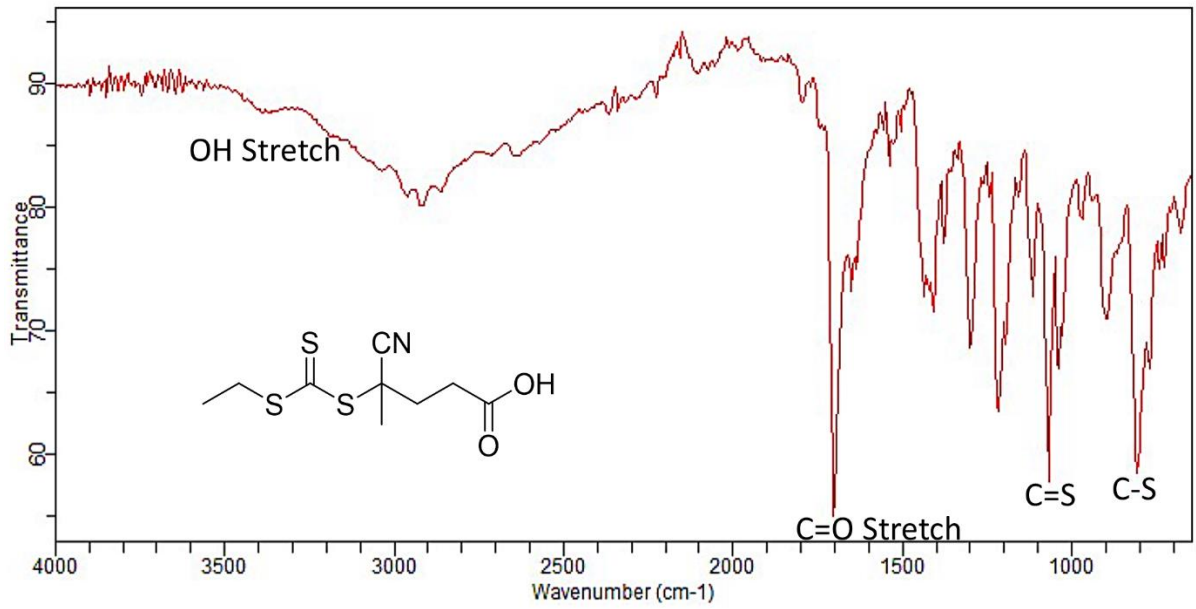

Figure 2.10. FTIR spectrum of CEPA-CTA.

Synthesis of poly(ethylene glycol)$_{113}$-CEPA macroCTA (PEG$_{113}$-macroCTA)

PEG$_{113}$-macroCTA was synthesized according to a previously reported method with slight modification.[18] Poly(ethylene glycol) methyl ether (average M_n=5,000 g mol^{-1}, PEG$_{113}$-OH) (4.75 g, 0.98 mmol, 1 eq) was dissolved in 150 mL of dry DCM. The resulting solution was then purged with N_2(g) for 30 min. After complete dissolution, CEPA CTA (1 g, 3.8 mmol, 4 eq), DCC (392 mg, 1.9 mmol, 2 eq) and DMAP (23 mg, 0.19 mmol, 0.2 eq) were added to the reaction mixture. The esterification reaction proceeded with stirring at room temperature for 18 h under continuous N_2(g) flow. After this period, further DCC (392 mg, 1.9 mmol, 2 eq) and DMAP (23 mg, 0.19 mmol, 0.2 eq) were added to the reaction mixture and then stirred at room temperature for an additional period of 6 h under continuous N_2(g) flow. The solution was then filtered to remove unreacted DCC and DMAP. The product was collected by 5 times of precipitation using cold diethyl ether as non-solvent, redissolved in deionized water and dialyzed against nanopure water using a 1,000 kDa MWCO membrane for 1 day (yield = 58%). The received PEG$_{113}$-macroCTA solution was lyophilized to give a light yellow powder as the final product (2.90 g, 0.55 mmol, 58%).^{1}H-NMR (400 MHz, $CDCl_3$): δ (ppm) 4.25 (m, 2H, CO_2-C***H*****$_2$**), 3.44-3.82 (m, 2H, C***H*****$_2$**O), 3.36 (s, 3H, O-C***H*****$_3$**), 3.34 (q, 2H, CH_3-C***H*****$_2$**), 2.64 (m, 2H, C***H*****$_2$**-CO_2), 2.34-2.56 (m, 2H, C(CN)-C***H*****$_2$**), 1.87 (s, 3H, C***H*****$_3$**-C(CN)), 1.35 (t, 3H, C***H*****$_3$**-CH_2). SEC (5 mM NH_4BF_4 in DMF, λ = 309 nm) M_n = 4.97 kg mol^{-1}, $Đ_M$ = 1.17.

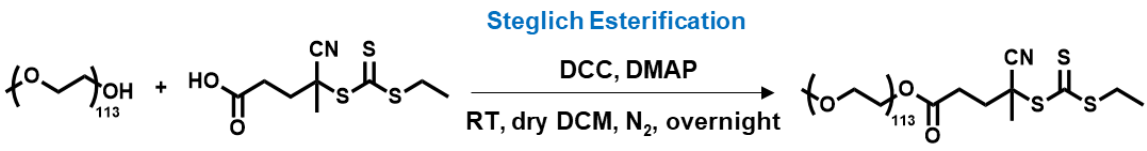

Scheme 2.3. Synthesis of PEG$_{113}$-macroCTA.

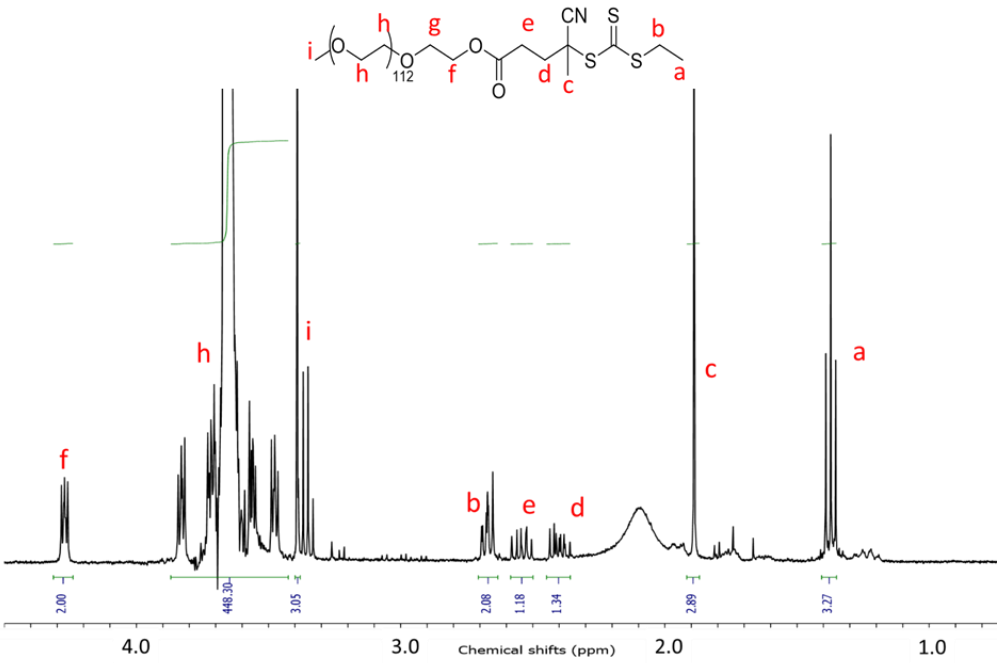

Figure 2.11. ^{1}H-NMR spectrum of PEG_{113}-CTA in $CDCl_3$.

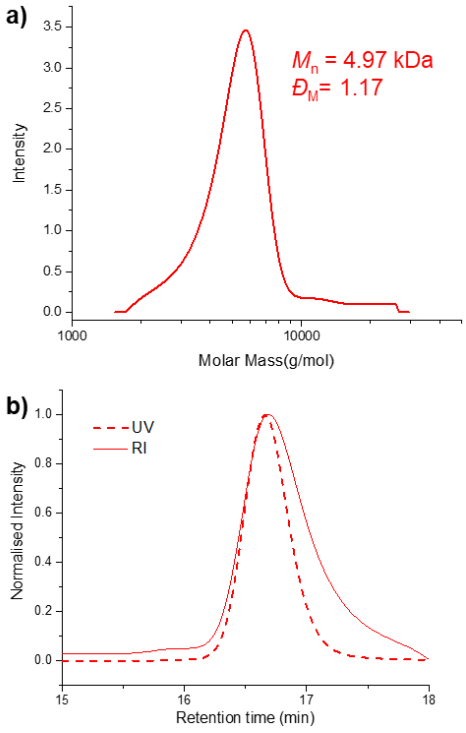

Figure 2.12. a) SEC RI molecular weight distributions for PEG_{113}-CTA along with the corresponding M_n and $Đ_M$ values. b) Normalised SEC RI and UV retention time distributions for PEG_{113}-CTA. M_n and $Đ_M$ values were calculated from PMMA standards using 5 mM NH_4BF_4 in DMF as the eluent.

Synthesis of 1 mL PEG_{113}-*b*-$PHPMA_{400}$ diblock copolymer by photoinitiated PISA in aqueous media (Benchmark reaction)

All photoinitiated PISA reactions were performed in a custom-built photoreactor setup. This ensured the reaction mixture was only exposed to the light from the 400–410 nm LED source placed under the sample.

A typical experiment, to achieve PEG_{113}-*b*-$PHPMA_{400}$ nano-objects at 10 %w/w HPMA (or 11% solids content) by aqueous RAFT-mediated photo-PISA was as follows.[13] PEG_{113}-macroCTA (9.1 mg, 1.7 μmol, 1 eq) and HPMA (100 mg, 0.69 mmol, 400 eq) were dissolved in deionized water (or aqueous detergent solution of desired concentration) (0.9 mL) in a sealed 20 mL scintillation vial with a stirrer bar. The solution was degassed by purging with N_2(g) for 15 min. The sealed vial was incubated at 37 °C with magnetic stirring under 405 nm light irradiation for 2 h. After this time, the content was exposed to air and allowed to cool to room temperature before conversion ^{1}H-NMR and SEC analyses. ^{1}H-NMR in methanol-d_4 and SEC traces of the pure polymer were obtained. TEM and DLS analyses were performed on samples after dilution to an appropriate analysis concentration. ^{1}H-NMR (400 MHz, CD3OD): δ (ppm) 6.17 and 5.67 (s, 2H, vinyl protons of HPMA), 4.52 (s, 1H, OH), 3.92 and 3.76 (s, 3H, C***H*** and C$\boldsymbol{H_2}$ of PHPMA side chain), 3.55 (s, 4H, C$\boldsymbol{H_2}$-C$\boldsymbol{H_2}$O of PEG chain), 3.22 (s, 3H, O-C$\boldsymbol{H_3}$ of PEG end group), 0.84-1.15 (m, 2H, C$\boldsymbol{H_2}$ of PHPMA backbone), 0.84-1.15 (m, 3H, C$\boldsymbol{H_3}$ of PHPMA backbone and C$\boldsymbol{H_3}$ of PHPMA side chain).

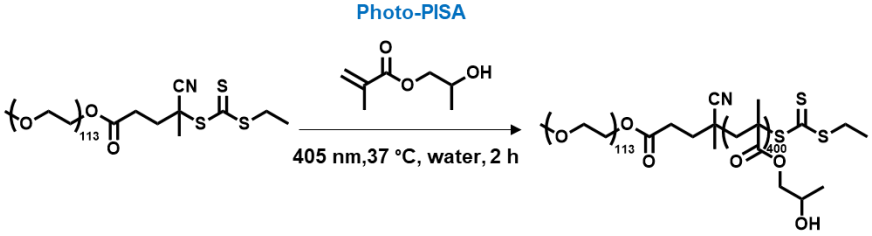

Scheme 2.4. Synthesis of PEG_{113}-*b*-$PHPMA_{400}$.

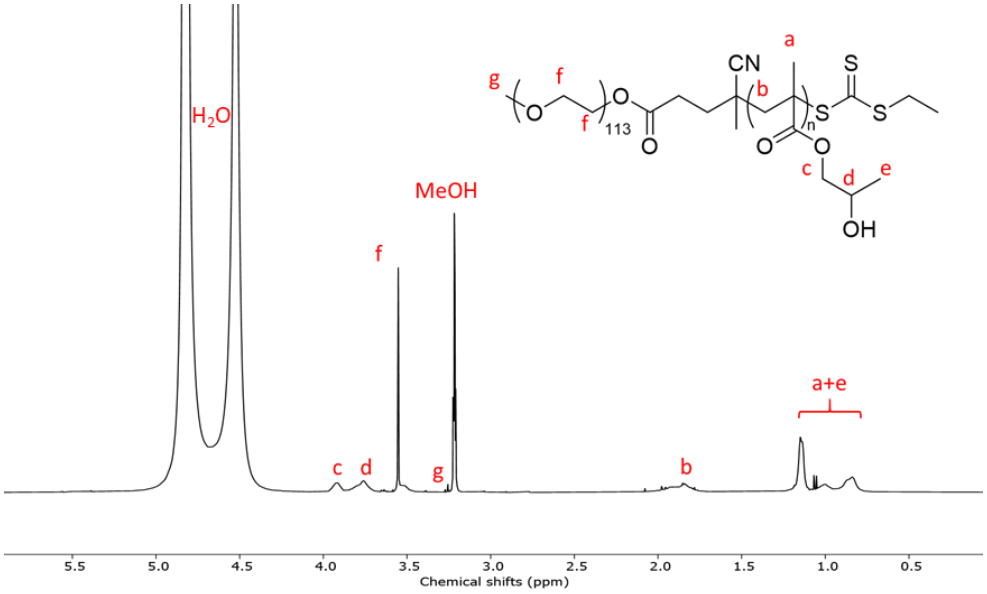

Figure 2.13. ^{1}H-NMR spectrum of PEG$_{113}$-*b*-PHPMA$_{400}$ in MeOD

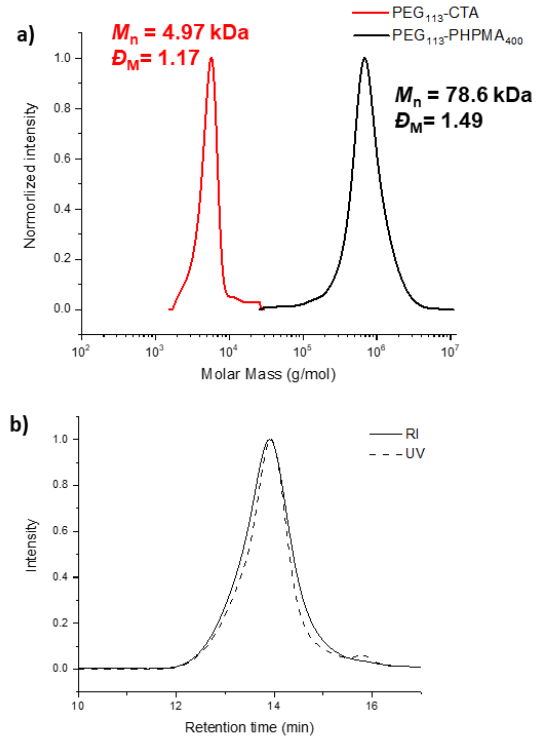

Figure 2.14. a) SEC RI molecular weight distributions for PEG$_{113}$-macroCTA and benchmark PEG$_{113}$-*b*-PHPMA$_{400}$ along with the corresponding M_n and $Đ_M$ values. b) Normalised SEC RI and UV (309 nm) retention time distributions for PEG$_{113}$-*b*-PHPMA$_{400}$. M_n and $Đ_M$ values were calculated from PMMA standards using 5 mM NH_4BF_4 in DMF as the eluent.

Synthesis of low-volume N_2 glove bag PEG_{113}-*b*-$PHPMA_{400}$ in 96 well plate

PEG_{113}-macroCTA stock solution (44.6 mg/mL, 1 eq) and HPMA stock solution (187.5 mg/1.5 mL, 400 eq) were pipetted into 96 well plate followed the volume in the Table 2.6 (and added a stirrer bar in the case of stirring technique) in a glove bag which was blown N_2 in and out to the bag 3 times before final purged of N_2 into the bag. In case of mixing by pipetted, 5 times of pipetting up and down was applied in this stage. Then, mineral oil was added 100 µL on top of the mixture and the plate was covered by plate seal, and transferred to LED array setup, which was contain in an incubator to maintain a temperature of 37 °C, which was contained in an incubator to maintain a temperature of 37 °C. The solution was then exposed to 405 nm light for 2 hrs, resulting in the solution turning opaque and milky white.

Table 2.6. Volume of used stock solutions in low volume reaction

Chemicals	**Volume (µL)**			
	50	**100**	**150**	**200**
macroCTA stock solution (20 mg mL^{-1})	10.2	20.4	30.6	40.8
HPMA stock solution (10 mg mL^{-1})	39.8	79.6	119.4	159.2
Total	50	100	150	200

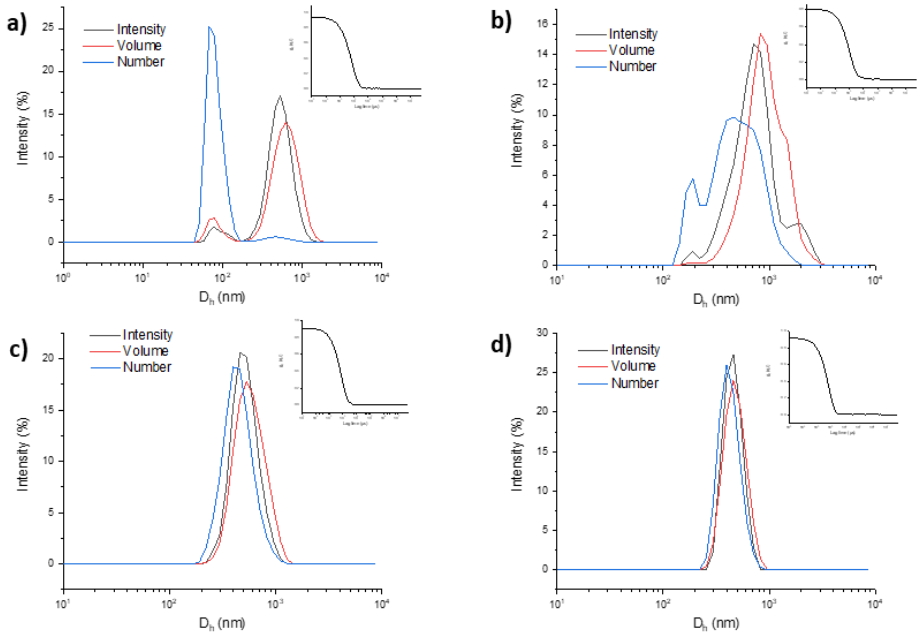

Figure 2.15. DLS data of low volume Photo-PISA of PEG_{113}-*b*-$PHPMA_{400}$ by N_2 glove bag method in the volume of a) 50, b) 100, c) 150, and d) 200 μL.

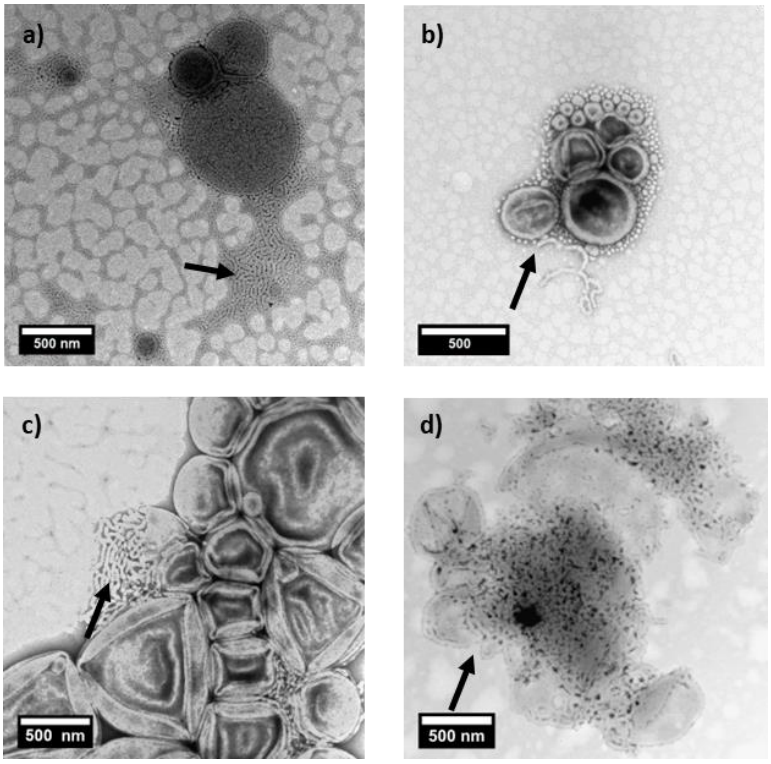

Figure 2.16. TEM images of low volume Photo-PISA of PEG_{113}-*b*-$PHPMA_{400}$ by N_2 glove bag method of PEG_{113}-*b*-$PHPMA_{400}$ in the volume of a) 100, b) 150, and c) 200 μL.

Synthesis of low-volume enzyme-mediated oxygen-tolerant PEG_{113}-*b*-$PHPMA_{400}$

PEG_{113}-macroCTA (250.5 µL, 20 mg mL^{-1}, 1 eq) was added in a vial containing HPMA (54.9 mg, 400 eq). Then, glucose solution (72 µL, 0.84 M), DI water (69.3 µL) and GOx solution (96 µL, 12.5 µM) were added into the mixing vial, respectively. The mixture was shaken *via* vortexer to produce a clear colourless solution which was then transferred 50,100,150, and 200 µL to 96 well plate (or pointed base PCR plate). Mineral oil was added around 200 µL on top of the mixture and the plate was covered by plate seal, and placed in LED array setup, which was contain in an incubator to maintain a temperature of 37 °C, which was contained in an incubator to maintain a temperature of 37 °C. The solution was then exposed to 405 nm light for 2 h (or 3 h), resulting in the solution turning opaque and milky white. In case of increase of concentration, amount of PEG_{113}-macroCTA and HPMA were similar to typical oxygen-tolerant method. However, glucose solution (129.2 µL, 0.84 M) and GOx solution (108.5 µL, 25 µM) were modified.

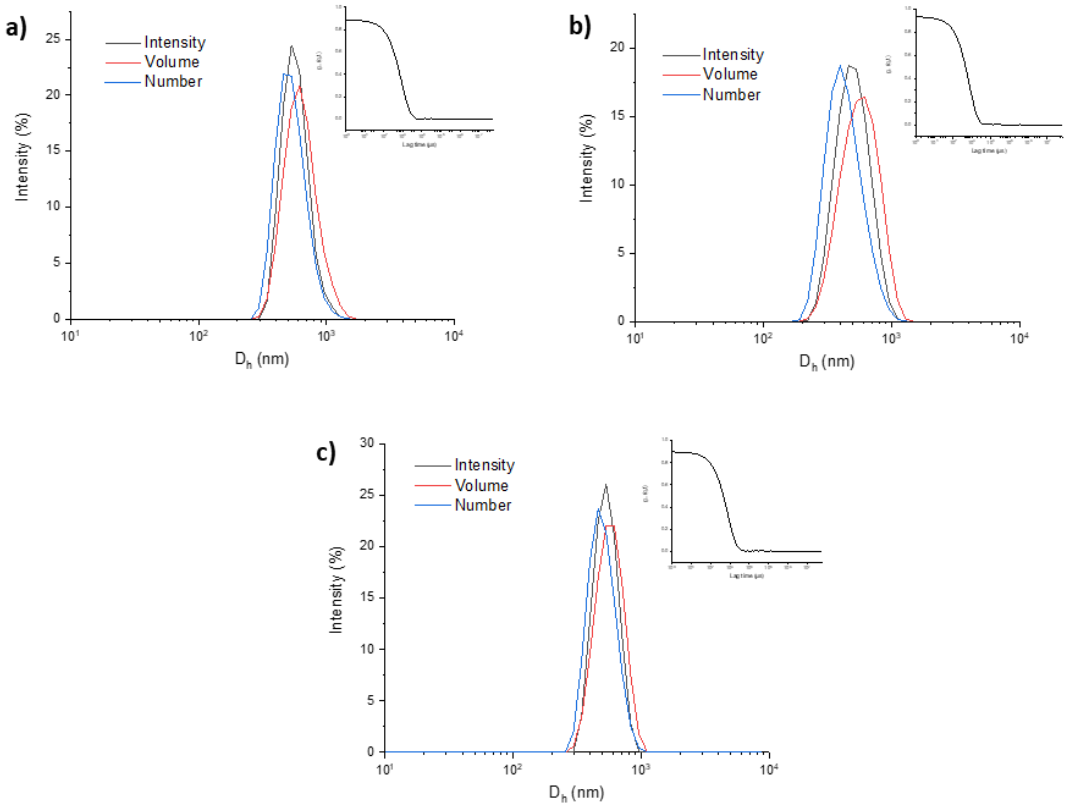

Figure 2.17. DLS data of low volume oxygen-tolerant Photo-PISA of PEG_{113}-*b*-$PHPMA_{400}$ in 96 well plates in the volume of a) 100, b) 150, and c) 200 μL.

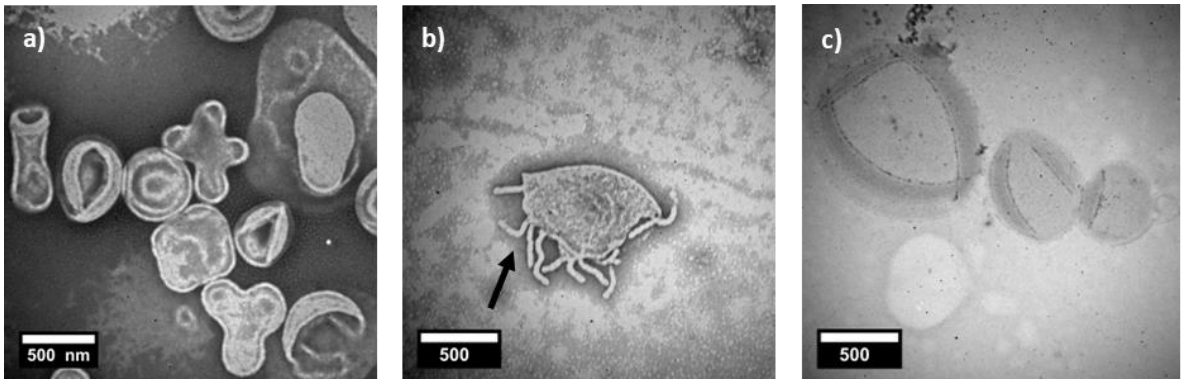

Figure 2.18. TEM images of oxygen-tolerant Photo-PISA of PEG_{113}-*b*-$PHPMA_{400}$ in 96 well plates in the volume of a) 100, b) 150, and c) 200 μL.

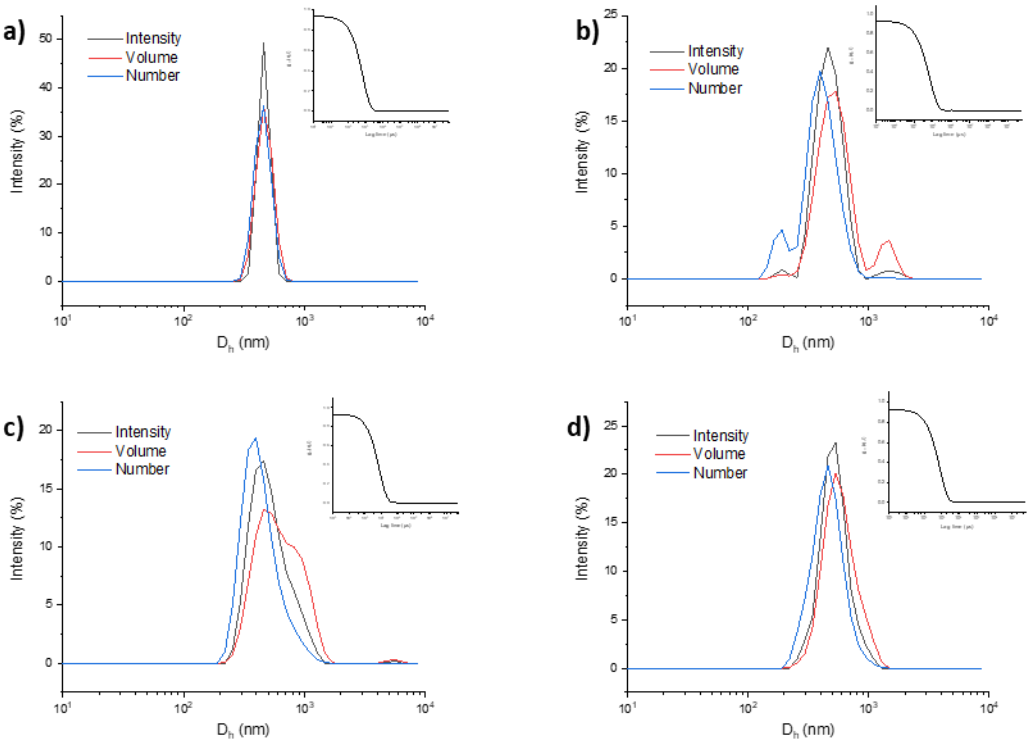

Figure 2.19. DLS data of low volume oxygen-tolerant Photo-PISA of PEG_{113}-*b*-$PHPMA_{400}$ in pointed based plates in the volume of a) 50, b) 100, c) 150, and d) 200 µL.

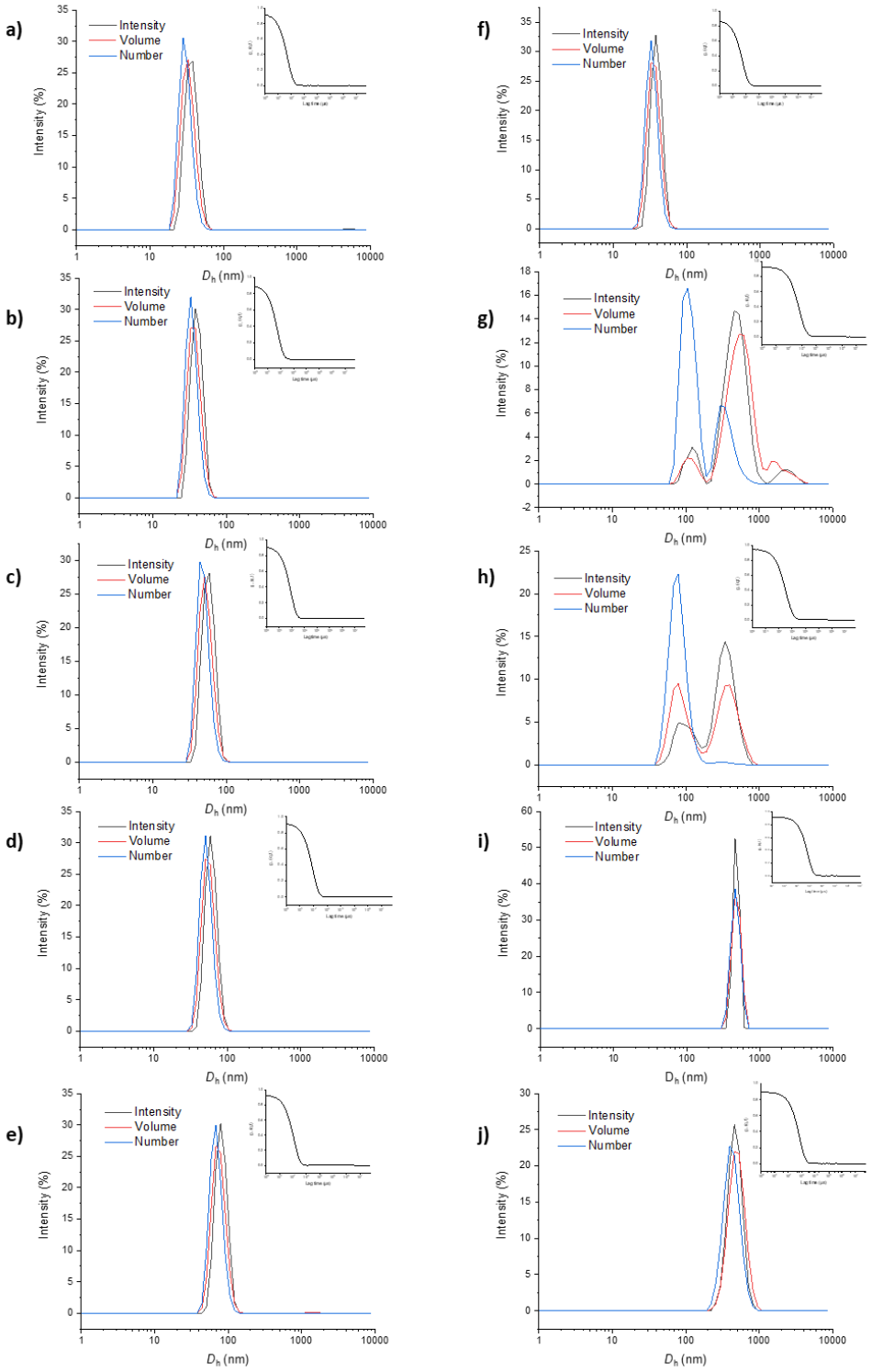

Figure 2.20. DLS data of low volume oxygen-tolerant Photo-PISA of PEG_{113}-*b*-$PHPMA_X$ in pointed based plates in the volume of 50 μL at a-e) [HPMA]=5 %w/w and f-j) [HPMA]=10 %w/w for a and e), b and g), c and h), d and i), and e and j) DP_{PHPMA}=100, 200, 300, 400, and 500, respectively.

2.5. References

1. Warren, N. J.; Armes, S. P., Polymerization-Induced Self-Assembly of Block Copolymer Nano-objects via RAFT Aqueous Dispersion Polymerization. *Journal of the American Chemical Society* **2014,** *136* (29), 10174-10185.

2. Penfold, N. J. W.; Yeow, J.; Boyer, C.; Armes, S. P., Emerging Trends in Polymerization-Induced Self-Assembly. *ACS Macro Letters* **2019,** *8* (8), 1029-1054.

3. Warren, N. J.; Mykhaylyk, O. O.; Mahmood, D.; Ryan, A. J.; Armes, S. P., RAFT aqueous dispersion polymerization yields poly(ethylene glycol)-based diblock copolymer nano-objects with predictable single phase morphologies. *J Am Chem Soc* **2014,** *136* (3), 1023-33.

4. Zhang, W. J.; Hong, C. Y.; Pan, C. Y., Polymerization-Induced Self-Assembly of Functionalized Block Copolymer Nanoparticles and Their Application in Drug Delivery. *Macromol Rapid Commun* **2019,** *40* (2), 1800279.

5. Blackman, L. D.; Varlas, S.; Arno, M. C.; Fayter, A.; Gibson, M. I.; O'Reilly, R. K., Permeable Protein-Loaded Polymersome Cascade Nanoreactors by Polymerization-Induced Self-Assembly. *ACS Macro Lett* **2017,** *6* (11), 1263-1267.

6. Dhiraj, H. S.; Ishizuka, F.; Elshaer, A.; Zetterlund, P. B.; Aldabbagh, F., RAFT dispersion polymerization induced self-assembly (PISA) of boronic acid-substituted acrylamides. *Polymer Chemistry* **2022,** *13* (25), 3750-3755.

7. Canning, S. L.; Smith, G. N.; Armes, S. P., A Critical Appraisal of RAFT-Mediated Polymerization-Induced Self-Assembly. *Macromolecules* **2016,** *49* (6), 1985-2001.

8. Derry, M. J.; Fielding, L. A.; Armes, S. P., Polymerization-induced self-assembly of block copolymer nanoparticles via RAFT non-aqueous dispersion polymerization. *Progress in Polymer Science* **2016,** *52*, 1-18.

9. Rieger, J., Guidelines for the Synthesis of Block Copolymer Particles of Various Morphologies by RAFT Dispersion Polymerization. *Macromol Rapid Commun* **2015,** *36* (16), 1458-71.

10. Pei, Y.; Lowe, A. B.; Roth, P. J., Stimulus-Responsive Nanoparticles and Associated (Reversible) Polymorphism via Polymerization Induced Self-assembly (PISA). *Macromol Rapid Commun* **2017,** *38* (1).

11. Foster, J. C.; Varlas, S.; Couturaud, B.; Coe, Z.; O'Reilly, R. K., Getting into Shape: Reflections on a New Generation of Cylindrical Nanostructures' Self-Assembly Using Polymer Building Blocks. *J Am Chem Soc* **2019,** *141* (7), 2742-2753.

12. Lansalot, M.; Rieger, J., Polymerization-Induced Self-Assembly. *Macromol Rapid Commun* **2019,** *40* (2), 1800885.

13. Blackman, L. D.; Doncom, K. E. B.; Gibson, M. I.; O'Reilly, R. K., Comparison of photo- and thermally initiated polymerization-induced self-assembly: a lack of end group fidelity drives the formation of higher order morphologies. *Polymer Chemistry* **2017,** *8* (18), 2860-2871.

14. Couturaud, B.; Georgiou, P. G.; Varlas, S.; Jones, J. R.; Arno, M. C.; Foster, J. C.; O'Reilly, R. K., Poly(Pentafluorophenyl Methacrylate)-Based Nano-Objects Developed by Photo-PISA as Scaffolds for Post-Polymerization Functionalization. *Macromol Rapid Commun* **2019,** *40* (2), e1800460.

15. Liu, D.; Cai, W.; Zhang, L.; Boyer, C.; Tan, J., Efficient Photoinitiated Polymerization-Induced Self-Assembly with Oxygen Tolerance through Dual-Wavelength Type I Photoinitiation and Photoinduced Deoxygenation. *Macromolecules* **2020,** *53* (4), 1212-1223.

16. Tan, J.; Bai, Y.; Zhang, X.; Zhang, L., Room temperature synthesis of poly(poly(ethylene glycol) methyl ether methacrylate)-based diblock copolymer nano-

objects via Photoinitiated Polymerization-Induced Self-Assembly (Photo-PISA). *Polymer Chemistry* **2016,** *7* (13), 2372-2380.

17. Tan, J.; Liu, D.; Bai, Y.; Huang, C.; Li, X.; He, J.; Xu, Q.; Zhang, L., Enzyme-Assisted Photoinitiated Polymerization-Induced Self-Assembly: An Oxygen-Tolerant Method for Preparing Block Copolymer Nano-Objects in Open Vessels and Multiwell Plates. *Macromolecules* **2017,** *50* (15), 5798-5806.

18. Tan, J.; Sun, H.; Yu, M.; Sumerlin, B. S.; Zhang, L., Photo-PISA: Shedding Light on Polymerization-Induced Self-Assembly. *ACS Macro Letters* **2015,** *4* (11), 1249-1253.

19. Varlas, S.; Blackman, L. D.; Findlay, H. E.; Reading, E.; Booth, P. J.; Gibson, M. I.; O'Reilly, R. K., Photoinitiated Polymerization-Induced Self-Assembly in the Presence of Surfactants Enables Membrane Protein Incorporation into Vesicles. *Macromolecules* **2018,** *51* (16), 6190-6201.

20. Yeow, J.; Boyer, C., Photoinitiated Polymerization-Induced Self-Assembly (Photo-PISA): New Insights and Opportunities. *Advanced Science* **2017,** *4* (7), 1700137.

21. Zaquen, N.; Zu, H.; Kadir, A. M. N. B. P. H. A.; Junkers, T.; Zetterlund, P. B.; Boyer, C., Scalable Aqueous Reversible Addition–Fragmentation Chain Transfer Photopolymerization-Induced Self-Assembly of Acrylamides for Direct Synthesis of Polymer Nanoparticles for Potential Drug Delivery Applications. *ACS Applied Polymer Materials* **2019,** *1* (6), 1251-1256.

22. Chapman, R.; Jung, K.; Boyer, C., Photo RAFT Polymerization. In *RAFT Polymerization*, 2021; pp 611-645.

23. Ng, G.; Yeow, J.; Chapman, R.; Isahak, N.; Wolvetang, E.; Cooper-White, J. J.; Boyer, C., Pushing the Limits of High Throughput PET-RAFT Polymerization. *Macromolecules* **2018,** *51* (19), 7600-7607.

24. Wan, J.; Fan, B.; Thang, S. H., RAFT-mediated polymerization-induced self-assembly (RAFT-PISA): current status and future directions. *Chem Sci* **2022,** *13* (15), 4192-4224.

25. Varlas, S.; Georgiou, P. G.; Bilalis, P.; Jones, J. R.; Hadjichristidis, N.; O'Reilly, R. K., Poly(sarcosine)-Based Nano-Objects with Multi-Protease Resistance by Aqueous Photoinitiated Polymerization-Induced Self-Assembly (Photo-PISA). *Biomacromolecules* **2018,** *19* (11), 4453-4462.

26. Leung, H. W., Polyethylene Glycol. In *Encyclopedia of Toxicology (Third Edition)*, Wexler, P., Ed. Academic Press: Oxford, 2014; pp 1043-1044.

27. Nuhn, L.; Barz, M.; Zentel, R., New perspectives of HPMA-based copolymers derived by post-polymerization modification. *Macromol Biosci* **2014,** *14* (5), 607-18.

28. Sponchioni, M.; Morosi, L.; Lupi, M.; Capasso Palmiero, U., Poly(HPMA)-based copolymers with biodegradable side chains able to self assemble into nanoparticles. *RSC Advances* **2017,** *7* (80), 50981-50992.

29. Chytil, P.; Kostka, L.; Etrych, T., HPMA Copolymer-Based Nanomedicines in Controlled Drug Delivery. *J Pers Med* **2021,** *11* (2).

30. Ali, U.; Karim, K. J. B. A.; Buang, N. A., A Review of the Properties and Applications of Poly (Methyl Methacrylate) (PMMA). *Polymer Reviews* **2015,** *55* (4), 678-705.

31. Ligon, S. C.; Husar, B.; Wutzel, H.; Holman, R.; Liska, R., Strategies to reduce oxygen inhibition in photoinduced polymerization. *Chemical Reviews* **2014,** *114* (1), 557-589.

32. Xu, J.; Jung, K.; Atme, A.; Shanmugam, S.; Boyer, C., A robust and versatile photoinduced living polymerization of conjugated and unconjugated monomers and its oxygen tolerance. *J Am Chem Soc* **2014,** *136* (14), 5508-19.

33. Ng, G.; Yeow, J.; Xu, J.; Boyer, C., Application of oxygen tolerant PET-RAFT to polymerization-induced self-assembly. *Polymer Chemistry* **2017,** *8* (18), 2841-2851.

34. Li, Z.; Kosuri, S.; Foster, H.; Cohen, J.; Jumeaux, C.; Stevens, M. M.; Chapman, R.; Gormley, A. J., A Dual Wavelength Polymerization and Bioconjugation Strategy for High Throughput Synthesis of Multivalent Ligands. *J Am Chem Soc* **2019,** *141* (50), 19823-19830.

35. Lv, Y.; Liu, Z.; Zhu, A.; An, Z., Glucose oxidase deoxygenation−redox initiation for RAFT polymerization in air. *Journal of Polymer Science Part A: Polymer Chemistry* **2017,** *55* (1), 164-174.

36. Yeow, J.; Chapman, R.; Xu, J.; Boyer, C., Oxygen tolerant photopolymerization for ultralow volumes. *Polymer Chemistry* **2017,** *8* (34), 5012-5022.

37. Liu, Z.; Lv, Y.; An, Z., Enzymatic Cascade Catalysis for the Synthesis of Multiblock and Ultrahigh-Molecular-Weight Polymers with Oxygen Tolerance. *Angew Chem Int Ed Engl* **2017,** *56* (44), 13852-13856.

38. Li, R.; Zhang, S.; Li, Q.; Qiao, G. G.; An, Z., An Atom-Economic Enzymatic Cascade Catalysis for High-Throughput RAFT Synthesis of Ultrahigh Molecular Weight Polymers. *Angew Chem Int Ed Engl* **2022,** *61* (46), e202213396.

39. Zaquen, N.; Kadir, A. M. N. B. P. H. A.; Iasa, A.; Corrigan, N.; Junkers, T.; Zetterlund, P. B.; Boyer, C., Rapid Oxygen Tolerant Aqueous RAFT Photopolymerization in Continuous Flow Reactors. *Macromolecules* **2019,** *52* (4), 1609-1619.

40. Li, Z.; Ganda, S.; Melodia, D.; Boyer, C.; Chapman, R., Well-Defined Polymers for Nonchemistry Laboratories using Oxygen Tolerant Controlled Radical Polymerization. *Journal of Chemical Education* **2020,** *97* (2), 549-556.

41. Chapman, R.; Gormley, A. J.; Stenzel, M. H.; Stevens, M. M., Combinatorial Low-Volume Synthesis of Well-Defined Polymers by Enzyme Degassing. *Angew Chem Int Ed Engl* **2016,** *55* (14), 4500-2503.

42. Lee, Y.; Boyer, C.; Kwon, M. S., Photocontrolled RAFT polymerization: past, present, and future. *Chem Soc Rev* **2023,** *52* (9), 3035-3097.

43. Touve, M. A.; Wright, D. B.; Mu, C.; Sun, H.; Park, C.; Gianneschi, N. C., Block Copolymer Amphiphile Phase Diagrams by High-Throughput Transmission Electron Microscopy. *Macromolecules* **2019,** *52* (15), 5529-5537.

44. Boyer, C.; Bulmus, V.; Davis, T. P.; Ladmiral, V.; Liu, J.; Perrier, S., Bioapplications of RAFT Polymerization. *Chemical Reviews* **2009,** *109* (11), 5402-5436.

45. McMinn, R. A. H. B. A. P. H., Determination of Free-Radical Propagation Rate Coefficients for Alkyl Methacrylates by Pulsed-Laser Polymerization. *Macromolecules* **1997,** *30*, 3490-3493.

46. Mcnally, R. G., Optimising Conditions for Low-Volume RAFT-mediated PISA. *University of Birmingham* **2019**.

47. Bohdana M. Discher, Y.-Y. W., David S. Ege,; James C-M. Lee, F. S. B., Dennis E. Discher,; Hammer, D. A., Polymersomes: Tough Vesicles

Made from Diblock Copolymers. *SCIENCE* **1999,** *284*, 1143-1146.

48. Discher, D. E.; Eisenberg, A., Polymer Vesicles. *Science* **2002,** *297* (5583), 967-973.

49. Mai, Y.; Eisenberg, A., Self-assembly of block copolymers. *Chemical Society Reviews* **2012,** *41* (18), 5969-5985.

50. Warren, N. J.; Mykhaylyk, O. O.; Ryan, A. J.; Williams, M.; Doussineau, T.; Dugourd, P.; Antoine, R.; Portale, G.; Armes, S. P., Testing the vesicular morphology

to destruction: birth and death of diblock copolymer vesicles prepared via polymerization-induced self-assembly. *J Am Chem Soc* **2015,** *137* (5), 1929-37.

51. D'Agosto, F.; Rieger, J.; Lansalot, M., RAFT-Mediated Polymerization-Induced Self-Assembly. *Angew Chem Int Ed Engl* **2020,** *59* (22), 8368-8392.

52. Johnson, R. N.; Burke, R. S.; Convertine, A. J.; Hoffman, A. S.; Stayton, P. S.; Pun, S. H., Synthesis of statistical copolymers containing multiple functional peptides for nucleic Acid delivery. *Biomacromolecules* **2010,** *11* (11), 3007-3013.

3 : DNA-polymer conjugates by low-volume RAFT-mediated photo-PISA under enzyme-mediated oxygen-tolerant technique

3.1 Introduction

As mentioned in Chapter 1, the combination of deoxyribonucleic acid (DNA) and synthetic polymers in DNA-polymer conjugates is intriguing due to the programmability and structural diversity of DNA, along with the functional properties of synthetic polymers.[1] This unique combination enables the creation of complex nanostructures with specific properties and functions, with potential applications in a wide range of fields, including drug delivery, biosensing, and nanoelectronics.[2-4] The use of DNA during polymer synthesis provides precise control over the size, shape, and composition of the resulting DNA-polymer nanostructures.[5-8] For instances, Liu and coworkers demonstrated the DNA-templated polymerization of peptide nucleic acid (PNA) aldehyde tetramer or pentamer building blocks with multiple side chains, revealing efficient and sequence-specific polymerization.[5] Additionally, evaluation of 20 different PNA aldehyde pentamer building blocks demonstrated that most combinations of side-chain structures and stereochemistry supported efficient DNA-templated polymerization, paving the way for utilizing functionalized PNA-based building blocks in synthetic polymer evolution efforts with non-nucleic acid backbones. Sleiman's group also reported a straightforward and versatile approach for synthesizing sequence-defined polymers linked to oligonucleotides.[6] By sequentially coupling short, precisely defined oligomers to a DNA strand on a solid support, they achieve high yields and precise control over the length and sequence of the monomer units in the resulting monodisperse DNA-polymer conjugates, incorporating both hydrophilic and hydrophobic components. Furthermore, the complementary base pairing of DNA allows for the development of hybrid materials post synthetically with improved stability and specificity.[9-11] For instance, Ding *et al.* investigated the alteration of DNA-b-poly(propylene oxide) (PPO) block copolymer micelles' structural properties through hybridization, converting the

single-stranded nucleic acid shell into double-stranded DNA using Watson–Crick base pairing.[11] However, there are several challenges known to achieve the successful synthesis of DNA-polymer conjugates in high yields and purity. One of the challenges is the contrasting properties between the hydrophilic DNA and hydrophobic polymer components.[12, 13] DNA is a highly ionic molecule requiring an aqueous environment which is readily compatible with hydrophilic monomers and polymers, while hydrophobic monomers and polymers require a solvent mixture to enable solubility, which can complicate the optimization of the conjugation reaction. In recent years, polymerization-induced self-assembly (PISA) has been utilized to solve this problem by polymerization of a hydrophobic monomer in the presence of DNA stabilizer as a hydrophilic block copolymer.[14-16] The polymerization process is able to generate a high concentration of growing polymer chains, which can interact with the stabilizer to form a variety of nanostructures, including spherical micelles, vesicles, and worm-like micelles *in situ*. The size and shape of the nanostructures depends on the composition and molecular weight of the block copolymer which can be controlled by adjusting the polymerization conditions, such as the monomer concentration, initiator concentration, and reaction temperature. Thus, PISA is a versatile and scalable method for the synthesis of DNA-polymer conjugates, which is easily adaptable and can be used for a several applications.

As mentioned in Chapter 1, Lückerath *et. al.* pioneered applying thermally initiated reversible addition-fragmentation chain transfer (RAFT) - mediated PISA in DNA-polymer conjugates in 2020.[14] They introduced PISA as a new method for synthesizing DNA-polymer nanostructures of various shapes at low-volume reaction (50 µL). The single-stranded DNA (ssDNA) was grafted to form polymer chains and self-assemble to form isotropic and anisotropic nanostructures which was controlled by varying the length

of the polymer block. The resulting DNA-polymer conjugates was further functionalized by hybridization with complementary ssDNA (cDNA). This work involves high temperatures and a large number of components, such as monomer, thermal initiator, glucose oxidase (GOx), glucose, sodium pyruvate, as well as complicated solvent conditions, including N,N-dimethylformamide (DMF), Dulbecco's phosphate-buffered saline (DPBS) buffer, and mixed *tert*-butanol/DPBS.

While we were working on photoinitiated polymerization-induced self-assembly (photo-PISA) in DNA-polymer conjugates, Yang *et al.* published the first photo-PISA in DNA-polymer conjugates in 2021, resulting into nanostructures including micelles, rods, and short worms.[16] They discussed photo-PISA as a new approach to synthesize three-dimensional functional nucleic acids (FNA) nanostructures that offer higher nuclease resistance, greater cellular uptake efficiency, and increased bioactivity. In terms of the applied PISA method, this work required photoinitiator (Sodium phenyl-2,4,6-trimethylbenzoylphosphinate, STPT), long reaction times (6 h) and a constant argon flow through the system. The solid content or monomer concentration of this system can be seen as concerning, as the solid content and total volume of samples were not fixed, which would adversely affect the control in the PISA system.[17]

As discussed in the previous chapter, aqueous low-volume RAFT-mediated photo-PISA under enzyme-mediated oxygen-tolerant technique enhanced the conversion of poly(ethylene glycol) block poly(2-hydroxypropyl methacrylate) (PEG_{113}-*b*-$PHPMA_{400}$) copolymers (>90%conversion) with reproducible results and showed well-controlled polymerizations. The lowest volume ensuring high conversion and reasonable dispersity condition is 50 μL by using [GOx] 2 μM and glucose 0.1 M under 405 nm light irradiation for 2 h. Therefore, this condition was set as a precedent for conducting low-volume photo-PISA reactions by utilising a deoxyribonucleic acid macromolecular chain transfer agent

(DNA-macroCTA) and 2-hydroxypropyl methacrylate (HPMA) monomer for generating DNA-corona polymeric nanostructures.

This chapter aimed to investigate the utilization of DNA-macroCTA in an optimal low-volume photo-PISA system obtained from Chapter 2. It was subdivided into two parts. In the first part, $ssDNA_{14}$-macroCTA from our collaborator the Sleiman group (McGill University, Canada) was used to synthesize $ssDNA_{14}$-*b*-$PHPMA_X$ at various solid contents and degree of polymerizations (DP) of poly(2-hydroxypropyl methacrylate) (PHPMA). Afterwards, the effect of salts and DNA hybridization on the resulting DNA-polymer particles were investigated. The second part contains the synthesis and evaluation of our DNA-macroCTA to create $ssDNA_{14}$-*b*-$PHPMA_X$ at varying solid contents and DP of PHPMA. This section compares $ssDNA_{14}$-macroCTAs synthesized by an *in-solution* method and a *solid support* method, and contains an additional comparison with the DNA-macroCTA synthesized by the Sleiman group. A study of how salts affect the DNA-polymer particles after and during performing PISA reactions was also conducted in this chapter.

3.2. Results and discussion

<u>Part I</u> Synthesis of ssDNA$_{14}$-*b*-PHPMA$_X$ by using DNA-macroCTA from *Sleiman* group.

3.2.1 Synthesis of DNA−Polymer Conjugates by photoinitiated polymerization-induced self-assembly (Photo-PISA)

In order to compare the results from our study in Chapter 2 and a previous MSci thesis, [18] HPMA was chosen as a monomer to polymerize from the ssDNA$_{14}$-macroCTA to form ssDNA$_{14}$-*b*-PHPMA$_X$ *via* optimal low-volume photo-PISA condition as shown in Scheme 3.1. HPMA monomer was originally chosen due to numerous literature precedent and forming a hydrophobic polymer block with hydrophilic polymer chain such as PEG$_{113}$.[19] It should be noted that this monomer is a mixture of 2-hydroxypropyl methacrylate (major) and 2-isopropyl methacrylate (minor), thus the HPMA block is a copolymer of the two isomers.[20]

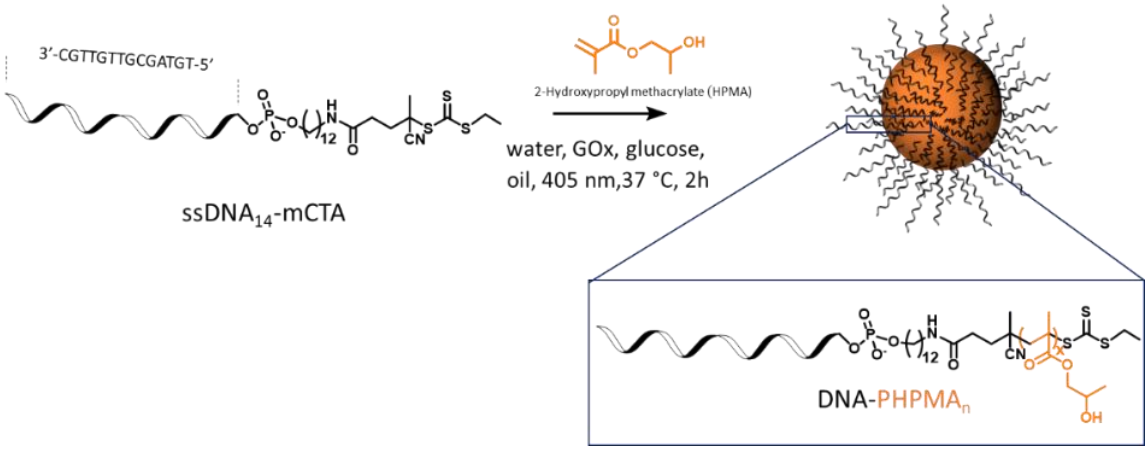

Scheme 3.1. ssDNA$_{14}$-*b*-PHPMA$_X$ diblock copolymer nano-objects produced *via* RAFT aqueous emulsion photo-PISA of HPMA.

A series of ssDNA$_{14}$-b-PHPMA$_X$ conjugates were prepared by using 14-mer ssDNA (5′-5AmMC12-TGTAGCGTTGTTGC-3′) equipped with a 4-cyano-4-

(dodecylsulfanylthiocarbonyl) sulfanyl pentanoic acid group (CEPA) at its 5′ terminus ($ssDNA_{14}$-macroCTA) (Figure 3.1a), which provided approximately 1 µmol by the Sleiman Group, McGill University, Canada. This CTA is a photoiniferter, which cleavages under 405 nm irradiation without the need for additional initiators or heat as discussed in chapter 1. A low-volume system (50 µL), which was discussed in Chapter 2, was introduced in the aqueous RAFT-mediated Photo-PISA to reduce the cost of synthetic oligonucleotides. Thus, this work is the first report of initiating DNA-polymer *via* low-volume PISA without adding external photoinitiator or photocatalyst.

The purity of the $ssDNA_{14}$-macroCTA was investigated by reversed phase-high performance liquid chromatography (RP-HPLC), with UV-vis detection at 260 nm (the maximum absorbance of the DNA bases). Nucleic acids have a strong absorption peak at 260 nm due to the heterocyclic rings within the nucleotide structure. Therefore, monitoring the absorbance at 260 nm over time using a UV chromatogram is a reliable method for evaluating the presence of DNA-containing species. The area under the peak attributed to the macroCTA (Figure 3.1b, red) was compared with the area under all other peaks (Figure 3.1b, yellow). From these data, it was estimated that approximately 70% of the DNA strands in the sample contained the CTA group, which is considered essential for the for successful polymerization. LC-MS: m/z $[C_{159}H_{211}N_{50}O_{91}P_{14}S_3\text{-}H]^-$ calc. 4807.900 g mol^{-1}, found 4807.389 g mol^{-1}.

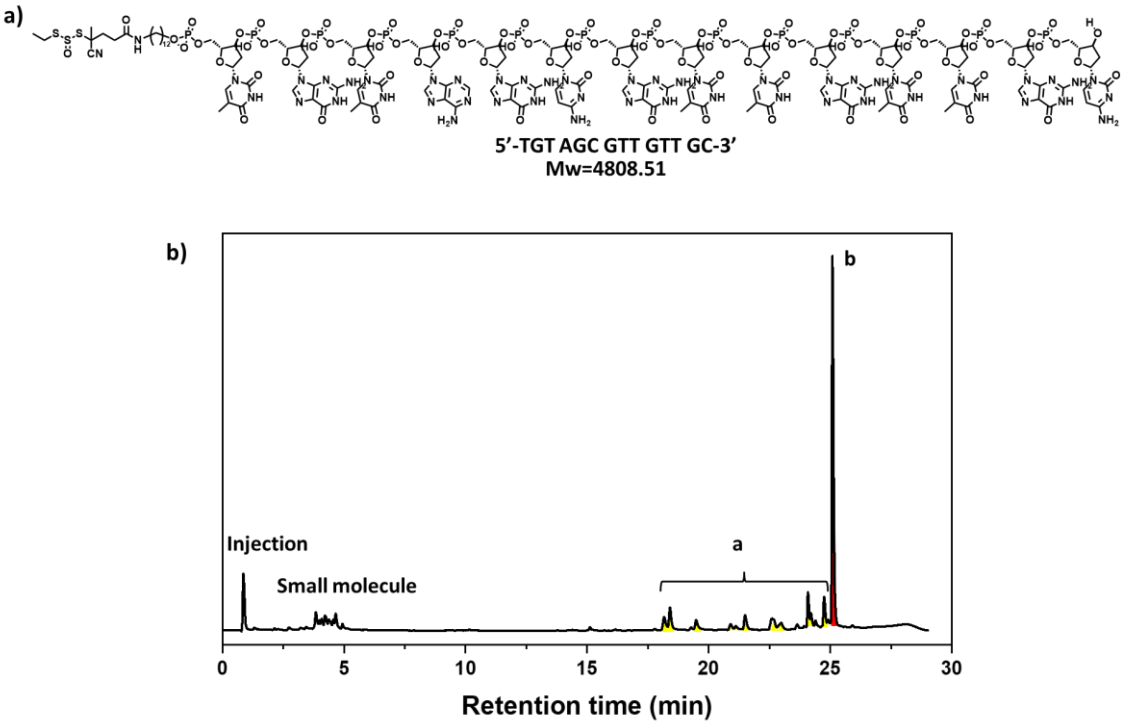

Figure 3.1. a) 5' to 3' structure of the ssDNA$_{14}$-macroCTA and b) RP-HPLC chromatogram at 260 nm of ssDNA$_{14}$-macroCTA. Products eluted with a gradient of buffer A, 0.1 M triethylammonium acetate (TEAA), in a 95:5 mixture of H_2O and acetonitrile and buffer B, 0.1 M TEAA, in a 30:70 mixture of H_2O and acetonitrile. Purity of ssDNA$_{14}$-macroCTA (red) was estimated by taking the area under the peak of interest and dividing it by the area under all DNA-containing peaks (yellow).

Then, low-volume aqueous RAFT-mediated photo-PISA of HPMA was attempted at 405 nm visible light irradiation of the solution at 37 ˚C applying enzyme degassing, *i.e.* glucose oxidase, to facilitate the complete degasification of the very small reaction volume based on other reports[21, 22] while the final concentrations were set to [glucose] = 0.1 M and [GOx] = 2 µM (Scheme 3.4 in Experimental section). Mineral oil was added on top of the 50 µL reaction solution to prevent diffusion of residual oxygen into the system which would inhibit the polymerization.[23]

Almost complete monomer conversion (>99%) was achieved after 2 h of reaction, as determined by ^{1}H-NMR spectroscopy (Table 3.1 and Figure 3.17 in Experimental section). The targeted degree of polymerization (DP) of the PHPMA block and the concentration of monomer were varied to investigate shape and size of the DNA-polymer particles. ssDNA$_{14}$-macroCTA was initially assumed 100% purity which calculated the targeted DP of PHPMA= 200, 300, and 400. However, RP-HPLC chromatogram (Figure 3.1b) showed the actual ssDNA$_{14}$-macroCTA was estimated ~70% purity leading to recalculate the actual DP of PHPMA = 286, 429, and 571, respectively. Size exclusion chromatography (SEC) analysis in DMF (with RI detection) of ssDNA14-b-PHPMAX confirmed the successful chain-extension of PHPMA (Figure 3.2). The polymer lengths (DP=286,429, and 571) could be simply adjusted by altering the monomer to ssDNA$_{14}$-macroCTA ratio. The size exclusion chromatograms revealed shifts towards higher degree of polymerization. In the case of 10% w/w HPMA content, PHPMA were successfully polymerized with significant increase in dispersity (Table 3.1 and Figure 3.2b). The observed relatively high dispersity when targeting DPs more than 429 at 10% w/w HPMA content is well-documented[24-26] and is actually as a consequence of the presence of a small amount (<0.3 mol %) of dimethacrylate in the HPMA monomer, rather than loss of RAFT control. This impurity inevitably leads to light branching as longer PHPMA chains are targeted.[27-29] When HPMA content was 5% w/w, the polymerization could be well-controlled for all targeted DP of PHPMA from 286 to 571 (Figure 3.2a).

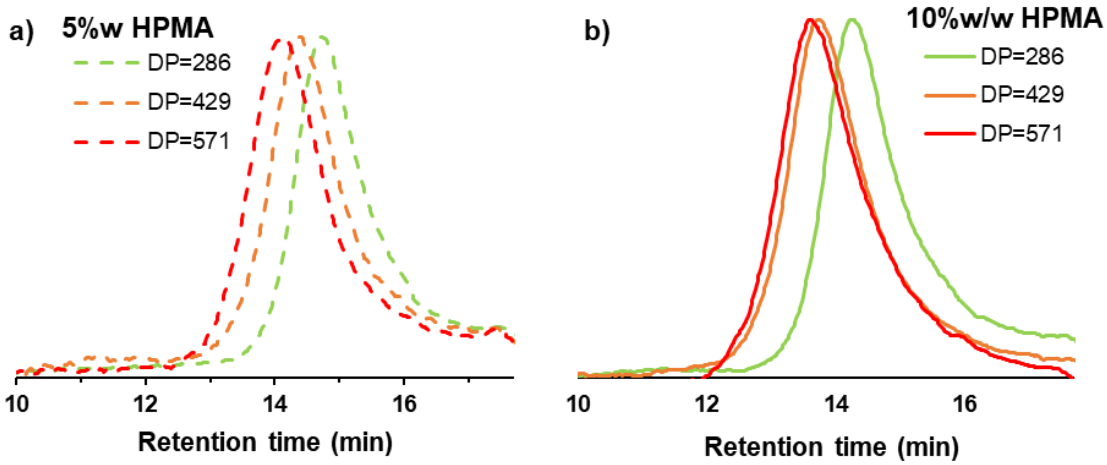

Figure 3.2. SEC RI traces of ssDNA$_{14}$-*b*-PHPMA$_{286}$ (green line), ssDNA$_{14}$-*b*-PHPMA$_{429}$ (orange line), ssDNA$_{14}$-*b*-PHPMA$_{571}$ (red line) a) 5%w/w HPMA (solid line) and b) 10%w/w HPMA (dash line) as measured by DMF SEC using poly(methyl methacrylate) (PMMA) calibration standard with RI detector.

Table 3.1. Polymerization from ssDNA$_{14}$-macroCTA *via* RAFT-mediated photo-PISA under oxygen tolerant conditions.

[HPMA] (%w/w)	Target DP of PHPMA	Actual DP of PHPMA[a]	Conv. (%)[b]	$M_{n,NMR}$ (kDa)[c]	$M_{n,SEC}$ (kDa)[d]	$Đ_M$[d]
5	200	286	>99	46.2	25.2	1.35
5	300	429	>99	66.6	39.1	1.31
5	400	571	>99	87.1	56.9	1.23
10	200	286	>99	46.2	38.1	1.51
10	300	429	>99	66.6	67.0	1.73
10	400	571	>99	87.1	73.5	1.98

[a] Actual DP of PHPMA was alculated from %purity of actual ssDNA$_{14}$-macroCTA *via* RP-HPLC.

[b] Monomer conversion was calculated from ^{1}H NMR spectroscopy (400 MHz) in MeOD.

[c] $M_{n,NMR}$ was calculated from monomer conversions[b].

[d] $M_{n,SEC}$ and $Đ_M$ were determined by DMF SEC with poly(methyl methacrylate) (PMMA) standards.

After the photo-PISA reaction, a change in the turbidity of the solution from transparent to opaque indicated the growth of hydrophobic PHPMA. TEM imaging revealed the successful development of spherical particles (Figure 3.3), while DLS analysis also confirmed a unimodal particle size distribution with D_h in the range of 60-200 nm (Figure 3.9). Cryo-TEM was also applied for imaging the particles; however, the particle was imaged 7 months after polymerization due to the COVID-19 pandemic. Cryo-TEM images of ssDNA$_{14}$-*b*-PHPMA$_X$ which x = 286, 429, and 571 at 10%w/w HPMA (Figure 3.4) revealed various sizes and morphologies – spherical particles, compartment(s) in the particles and large aggregates. These are presumably as a result of reorganisation of the particles over the storage period which has been previously observed to spontaneously occur in a self-assembly system.[30-32] It should be noted that the cryo-TEM images were measured by Marjolaine Thomas, our ex-group member, at the university of Warwick as I mentioned in declaration of authorship. Due to reorganization of particles, it would not worth to investigate the remaining polymers by cryo-TEM. From the particle size in table 3.1 and EM imaging, the morphology of particles was presuming spherical micelles. In order to confirm exact morphology, static light scattering (SLS) or small-angle x-ray scattering (SAXS) study is required. However, the limitation of this project is the amount of samples. Each reaction was performed at 50 µL while SLS involved varying concentrations of the sample solutions and DnDc is required to calculate particle morphology. As a differential refractometer, DnDc 1260, requires samples of at least five concentrations at 5 mL, which is a relatively high volume compared to the total samples we had. Additionally, the particles reorganized their shapes during storage and aggregated. Therefore, SLS and SAXS were not investigated.

Table 3.2. Polymerization from ssDNA$_{14}$-macroCTA *via* photo-RAFT PISA under oxygen tolerant conditions.

[HPMA] (%w/w)	**Actual DP of PHPMA[a]**	**D_h (nm)[b]**	**PD[b]**	**D_{TEM} (nm)[c]**	**D_{Cryo} (nm)[d]**	**Morphology[c,d]**
5	286	66	0.11	61±8	*N/A*	s
5	429	78	0.07	61±7	*N/A*	s
5	571	106	0.05	95±13	*N/A*	s
10	286	76	0.07	67±12	110±64	s
10	429	159	0.10	137±26	115±69	s
10	571	170	0.10	128±28	141±59	s

[a] Calculated from %purity of actual ssDNA$_{14}$-macroCTA *via* RP-HPLC.

[b] Hydrodynamic diameter and polydispersity (PD) were determined by DLS at concentration 0.50 mg·mL^{-1}.

[c] D_{TEM} and Morphologies were determined by dry state TEM.

[d] Morphologies were determined by cryo-TEM. s = spherical micelles.

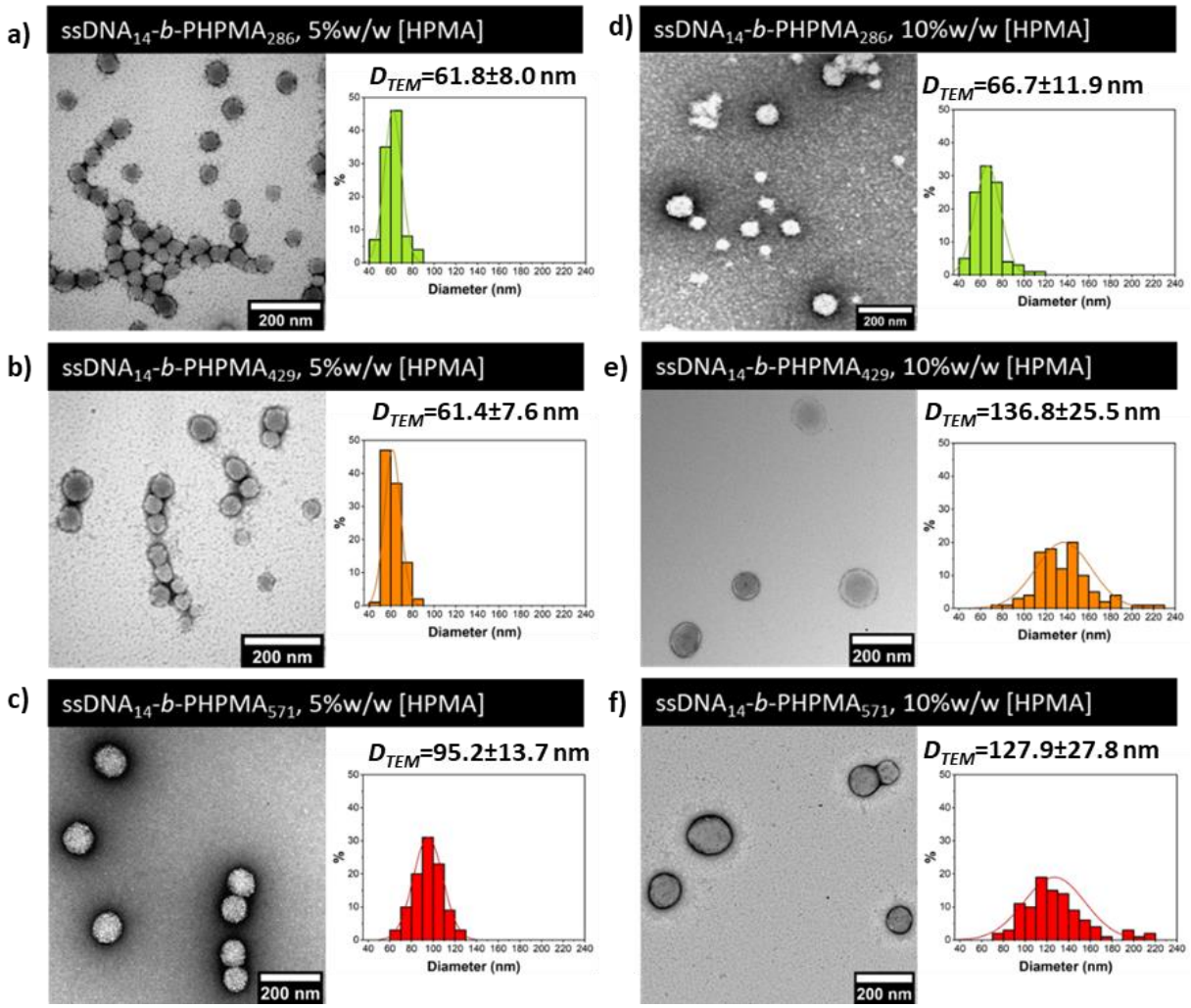

Figure 3.3. Representative TEM images of particles of different DP and [solids] along with their corresponding diameters measured over at least 100 particles using image J.

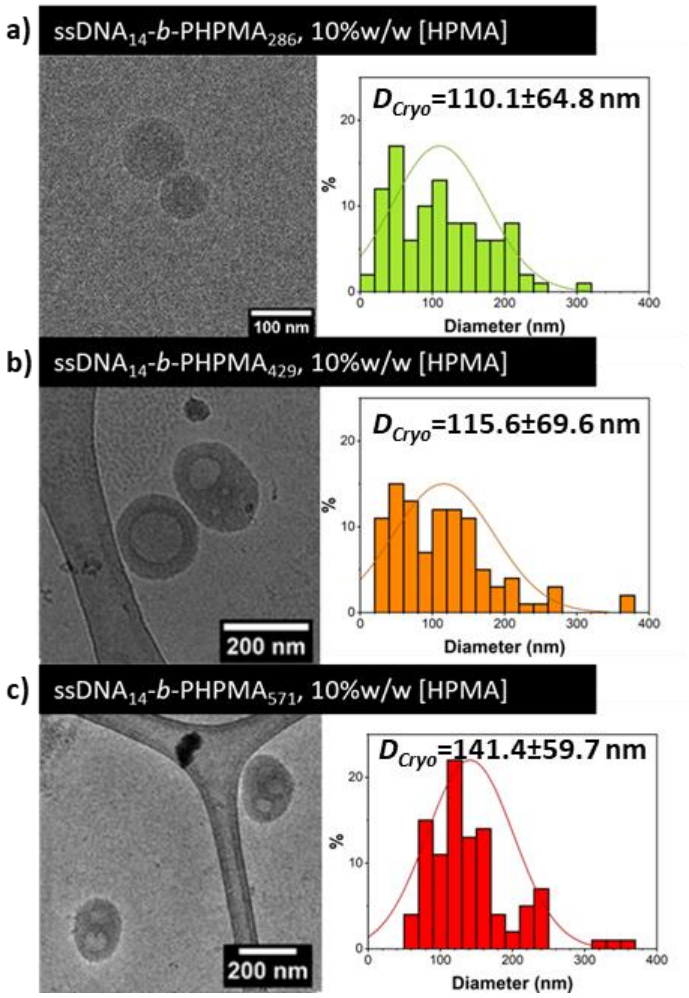

Figure 3.4. Representative cryo-TEM images of vesicles of different DP and [solids] along with their corresponding diameters measured over at least 100 particles using image J.

The accomplishment of self-assembly polymerizations of DNA-polymer conjugate was also characterized by 15% native polyacrylamide gel electrophoresis (PAGE) gel. Native PAGE gel is primarily used for separating and analyzing proteins or nucleic acids based on their size and charge.[33] The principle of PAGE gel electrophoresis is based on the migration of charged molecules through a gel matrix when an electric field is applied. The gel matrix is composed of polyacrylamide, a porous material that forms a network when polymerized, creating a sieving effect that separates molecules based on their size. Smaller molecules can move more easily and faster through the pores, while larger

molecules encounter more resistance, move more slowly and remain closer to the top of the gel. The PAGE gel revealed after SYBR Gold staining that ssDNA$_{14}$-*b*-PHPMA$_X$ conjugates staying on the top of the gel (Figure 3.5). SYBR Gold is a widely used fluorescent nucleic acid stain in electrophoresis gels, primarily employed for visualizing and detecting DNA or RNA molecules in the context of molecular biology research.[34, 35] This stain is highly sensitive and offers several advantages, including low background fluorescence and the ability to detect small amounts of nucleic acids.[35] From Figure 3.5, the top bands with extremely low mobility of ssDNA$_{14}$-*b*-PHPMA$_X$ in each lane indicated successful polymerization-induced self-assembly.[16] Minor leftover bands corresponding to unreacted-ssDNA functionality, such as ssDNA-NH_2 and DNA dimer, suggesting that some left over unreacted-ssDNA mixed in the system and these correspond with the obtained RP-HPLC trace of ssDNA$_{14}$-macroCTA (Figure 3.1b).

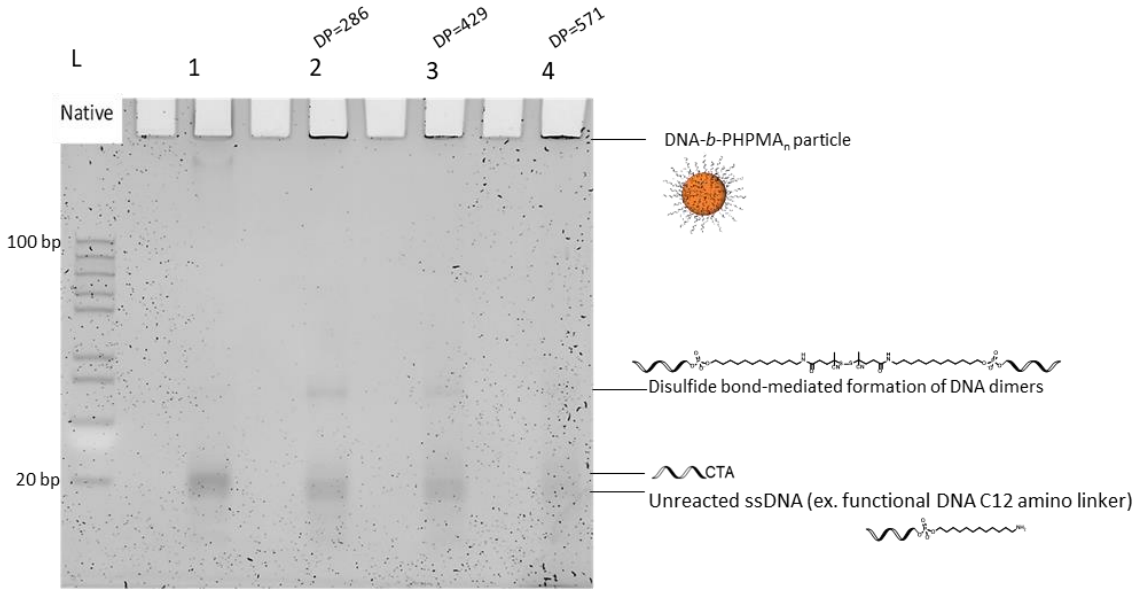

Figure 3.5. ssDNA$_{14}$-macroCTA and the ssDNA$_{14}$–polymer conjugates analysed by 15% native PAGE after SYBR Gold stain visualized using the SYBR Gold channel on the gel imager (BioRad). L: DNA ladder; lane 1: ssDNA$_{14}$-macroCTA; lane 2: ssDNA$_{14}$-PHPMA$_{286}$; lane 3: ssDNA$_{14}$-PHPMA$_{429}$; lane 4: ssDNA$_{14}$-PHPMA$_{571}$.

3.2.2 Screening effect of salts (NaCl and $MgCl_2$)

In order to study DNA hybridization on the DNA-polymer particle surface, the system was required to perform under buffer solution containing salt to improve the stability of the double strand nucleic acid. Thus, screening effects of salt on particles have been investigated before performing DNA hybridization on the particle corona to ensure particles were stable in the presence of salts. The screening effect refers to the influence of added salt on the strength of the electrostatic attraction between anionic DNA and cationic species. [36] This effect arises from the presence of positive counterions, introduced by ionic salt in the solution, which shield the negatively charged phosphate groups on DNA strands and reduce the electrostatic repulsion between each DNA strand. In this study, sodium chloride (NaCl) and magnesium chloride ($MgCl_2$) were used to study screening effects of mono- and divalent salts, respectively, *via* DLS. NaCl and $MgCl_2$ were chosen to investigate the stability of the self-assembled particles since there are well-known to stabilize double stranded DNA (dsDNA).[37, 38] DLS was employed to investigate particle stability in a solution following the addition of salts. In this study, a DNA-*b*-$PHPMA_{429}$ solution (10 mM) was monitored *via* DLS at different concentration of salts (10 mM and 100 mM). Table 3.3 shows that the NaCl and $MgCl_2$ salts do not affect the size of particles at salt concentrations of 10 mM. On the other hand, at 100 mM $MgCl_2$ caused aggregates in solution while NaCl did not affect the size of particles at the same concentration. These results indicate that the concentrations of Mg^{2+} had an influence on the self-assembly process and that high Mg^{2+} concentrations were detrimental to the stability of DNA self-assemblies.[39]

Table 3.3. DLS data of screening effect of salts (NaCl and $MgCl_2$)

Condition	NaCl		$MgCl_2$	
	D_h (nm)	PD	D_h (nm)	PD
Before adding salts	192	0.12	192	0.12
At 10 mM	205	0.09	204	0.11
At 100 mM	201	0.13	ERROR	ERROR

Key: ERROR = poor quality result from DLS.

3.2.3 A study of Hybridization

Hybridization of DNA is a fundamental process in many biological and biotechnological applications, such as DNA sequencing,[40, 41] polymerase chain reaction (PCR),[42, 43] and DNA microarray analysis.[44] DNA is intrinsically functional and can be post-modified by DNA hybridization. Hybridization of DNA was used to functionalize the DNA-polymer nanostructures by attaching dye-labeled cDNA to the surface of the nanostructures. This allowed for the characterization and detection to assist confirmation of DNA-attachment on the surface of particle and functionalised particle by hybridization. Hybridization of DNA refers to the process of forming a double-stranded DNA molecule by pairing two complementary single-stranded DNA molecules.[45] During this process, the two strands of DNA form an anti-parallel double helix structure through the formation of hydrogen bonds between the complementary base pairs (adenine-thymine and guanine-cytosine).[46-49] DLS, gel electrophoresis, and confocal fluorescence microscopy were applied using 14-mer ssDNA sequence 5**'**-GC AAC AAC GCT ACA-3'as a complementary DNA strand (cDNA) and 5**'**-TGT AGC GTT GTT GC-3' as a noncomplementary DNA strand (ncDNA) to investigate the interaction of DNA-polymer particles with non-matching DNA, serving as a negative control.

Effect of cDNA to ssDNA-*b*-polymer particle was investigated by adding cDNA to $ssDNA_{14}$-*b*-$PHPMA_{429}$ solution at different ratios of cDNA to the DNA-polymer chain in the solution. Table 3.4 illustrates DLS data of a mixture of DNA-Polymer nanoparticles and ssDNA at different ratios. After conducting experiments with ratios of [$ssDNA_{14}$-*b*-$PHPMA_{429}$] to [cDNA], it was observed that a ratio of 0.25 cDNA did not result in any significant changes in the size of the particles. Above this ratio, the quality of the DLS data deteriorated indicating particle disassembly and/or aggregation. This suggested that the cDNA hybridized with the DNA-polymer particles, causing a decrease in curvature and an increase in particle size until it reached a critical point where the particles became unstable and could no longer be detected by DLS. In contrast, ncDNA did not affect to the size and the stability of $ssDNA_{14}$-*b*-$PHPMA_{429}$ particles, implying that hybridization did not occur (Table 3.4). This provided first evidence of successful hybridization between DNA-$PHPMA_{429}$ and cDNA. However, DNA-polymer system has approximately 30% of left over unreacted-ssDNA which could hybridize with the added cDNA, so further analysis and investigation is necessary to fully understand the hybridization process on the DNA-particle corona.

Table 3.4. DLS data of mixture between DNA-Polymer particles and ssDNA (cDNA and ncDNA) at different ratios.*

Ratio of ssDNA: DNA-Polymer	ssDNA$_{14}$-*b*-PHPMA$_{429}$+cDNA		ssDNA$_{14}$-*b*-PHPMA$_{429}$+ncDNA	
	D_h (nm)	PD	D_h (nm)	PD
0.00	195	0.12	194	0.14
0.10	206	0.13	194	0.10
0.11	210	0.13	192	0.09
0.13	219	0.13	190	0.10
0.14	211	0.11	190	0.10
0.17	206	0.12	194	0.10
0.20	207	0.12	194	0.10
0.25	246	0.12	193	0.08
0.33	812	0.14	190	0.11
0.50	ERROR	ERROR	192	0.09
1.00	-	-	193	0.11

Key: ERROR = poor quality result from DLS.

*It should be noted that in DNA-polymer system has approximately 30% of left over unreacted-ssDNA

Additionally, 15% Native PAGE gel was used to study the hybridization process of ssDNA$_{14}$, ssDNA$_{14}$-macroCTA, ssDNA$_{14}$-*b*-PHPMA$_{429}$ by mixing each sample with fluorescent complementary DNA strand (TAMRA-5’GC AAC AAC GCT ACA3’ or TAMRA-cDNA) at ratio 1:1 except ssDNA$_{14}$-*b*-PHPMA$_{429}$ prepared at ratio [ssDNA$_{14}$-*b*-PHPMA$_{429}$]:[TAMRA-cDNA)] 1:0.08 and 0.17 (Figure 3.6). The selection of ratios 0.08 and 0.17 was based on their determined by their representation of one-quarter and one-half, respectively, of the ratio (0.33) at which the sample began to exhibit instability, as mentioned above in the DLS analysis (Table 3.4). The faint fluorescent bands in the wells in lane 8 and 9 of the gel indicate hybridization occurred with the particles. It should

be noted that leftover ssDNA band was also able to hybridize with cDNA as shown in lane 4, 8 and 9. However, the faint fluorescent bands in the wells did not strong evident to proof the successful hybridization of cDNA with ssDNA$_{14}$-*b*-PHPMA$_{429}$ on the surface of the particles. Thus, the particles at a cDNA ratio of 0.17 were further imaged using confocal fluorescence microscopy (Figure 3.7).

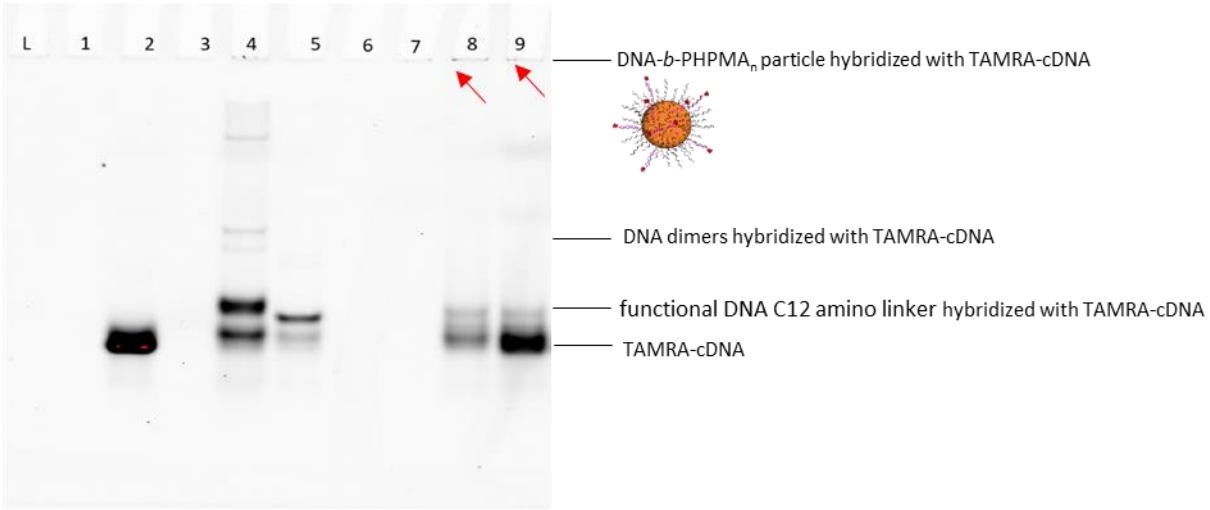

Figure 3.6. The hybridization between ssDNA/DNA-macroCTA/DNA–polymer and fluorescent complementary DNA analysed by 15% native PAGE. L: DNA ladder; lane 1: ssDNA$_{14}$; lane 2: TAMRA-cDNA; lane 3: ssDNA$_{14}$-macroCTA; lane 4: Mixture of [ssDNA$_{14}$-macroCTA]:[TAMRA-cDNA]=1:1; lane 5: Mixture of [ssDNA$_{14}$]:[TAMRA-cDNA]=1:1; lane 6: ssDNA$_{14}$-*b*-PHPMA$_{429}$; lane 7: Mixture of [ssDNA$_{14}$-*b*-PHPMA$_{429}$] :[ssDNA$_{14}$]=1:0.17; lane 8: Mixture of [ssDNA$_{14}$-*b*-PHPMA$_{429}$]:[TAMRA-cDNA]=1:0.09; lane 9: Mixture of [ssDNA$_{14}$-*b*-PHPMA$_{429}$]:[TAMRA-cDNA]=1:0.17

3.2.4. Evaluation of successful DNA hybridization *via* confocal fluorescence microscopy

To provide clear evidence of hybridization between cDNA and ssDNA$_{14}$-*b*-PHPMA$_{429}$ on the surfaces of DNA-decorated nanoparticles, confocal laser scanning microscopy (CLSM) was utilized to image the fluorescent cDNA hybridized with DNA particles.

CLSM, also known as confocal spectroscopy, is an advanced imaging technique that offers high-resolution (around 180 nm), three-dimensional views of both biological and non-biological specimens.[50] Confocal microscopy typically involves the use of fluorescence to visualize and study samples, with specific molecules or structures within a sample being labeled using fluorescent dyes or fluorophores.[51] The confocal spectroscope employed in this thesis is also able to capture bright field images, where the specimen is illuminated with white light, and the entire field of view is observed simultaneously. It should be noted that the confocal microscope has a detection limit of around 200 nm,[52] which means that it can only visualize aggregates rather than single particles. The sample preparation was carried out at the specific ratio of 0.17 cDNA to ensure the DNA particles remained stable in solution. Using mixture of cDNA and ssDNA as a control, the confocal fluorescence microscope cannot capture particles in the bright field due to the small size of DNA molecules, but fluorescent specks in the fluorescence was observed which can occur when dye molecules dry and aggregate known as a background (Figure 3.7a). For ssDNA$_{14}$-*b*-PHMPA$_{429}$ alone, particles were observable in the bright field images but not in fluorescence. (Figure 3.7b). On the other hand, mixture of TAMRA-cDNA and ssDNA$_{14}$-*b*-PHMPA$_{429,}$ particles were clearly observed in both the bright field and fluorescence images (Figure 3.7c). This suggests that cDNA has interacted and hybridized with the DNA on the surface of particles successfully. To confirm that cDNA was not entangle but has hybridized on the surface of DNA-polymer particles, PEG$_{113}$-*b*-PHPMA$_{429,}$ synthesized from the low volume photo PISA in Chapter 2, was used to compare with ssDNA$_{14}$-*b*-PHPMA$_{429.}$ PEG$_{113}$-*b*-PHPMA$_{429}$ particle was clearly captured in bright field but does not show particle on fluorescent field due to non-interact between PEG and cDNA(Figure 3.7d). Thus,

Confocal imaging confirmed the presence of DNA at the particle surface and its ability to hybridize with a complimentary strand.

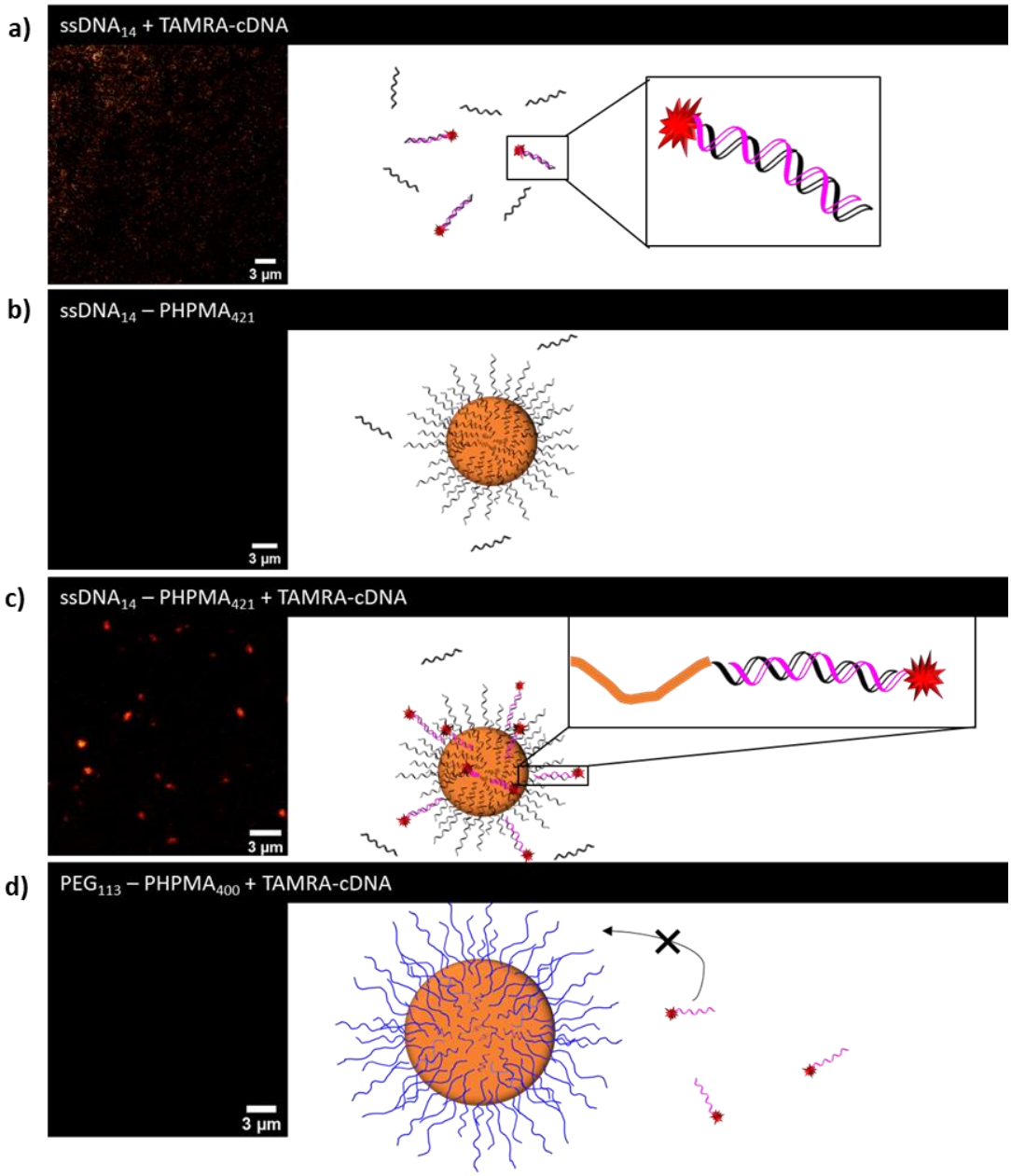

Figure 3.7. Confocal images of hybridization of DNA-polymer micelles as using a ratio of 0.17 TAMRA-cDNA a) $ssDNA_{14}$+TAMRA-cDNA , b) $ssDNA_{14}$-*b*-$PHPMA_{429}$, c) ssDNA-*b*-$PHPMA_{429}$+TAMRA-cDNA, and c) PEG_{113}-*b*-$PHPMA_{400}$+TAMRA-cDNA

<u>Part II</u> Synthesis of ssDNA$_{14}$-*b*-PHPMA$_X$ by using DNA-macroCTA from *our* group.

Due to the limiting amount and purity of DNA-macroCTA from Sleiman group, the synthesis of DNA-macroCTA was investigated by our group with two methods composing of an *in solution* method and a *solid support* methods. The total amount of DNA-macroCTA from the Sleiman group was approximately 1000 nmol, and about 100-200 nmol was used in each PISA reaction leading to limitation of the ability to repeat the reaction or perform any additional experiments, even in small-volume reactions (50 µL). Moreover, the purity of the ssDNA$_{14}$-macroCTA was investigated using RP-HPLC equipped with a UV-vis detector to monitor the eluted DNA solution at 260 and 309 nm, corresponding to the maximum absorbance of DNA and the trithiocarbonate group, respectively (Figure 3.8). The DNA-macroCTA exhibited second and third signals at 309 nm, indicating the presence of impurities from the trithiocarbonate group. These impurities could lead to uncontrolled polymerization and potentially affect the actual DP of PHPMA. In this part, both an *in solution* method and a *solid support* method involved a substitution reaction of the carboxylic acid group from CEPA with the amine group from ssDNA-NH_2 to investigate the most effective approach for synthesizing DNA-macroCTA.

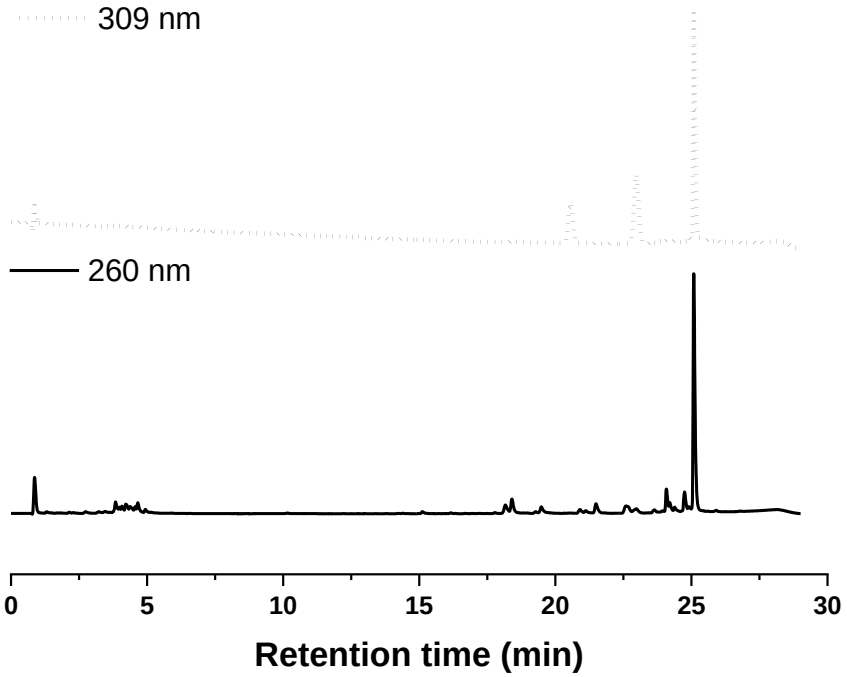

Figure 3.8. RP-HPLC chromatograms of DNA-macroCTA synthesized by the Sleiman group. The chromatograms were investigated at detector wavelength 309 nm (dash line) and detector wavelength 260 nm (solid line). Products eluted with a gradient of buffer A, 0.1 M triethylammonium acetate (TEAA), in a 95:5 mixture of H_2O and acetonitrile and buffer B, 0.1 M TEAA, in a 30:70 mixture of H_2O and acetonitrile.

DNA modification carried out applying the *in solution* method refers to the chemical modification of DNA molecules using various reagents and reaction conditions in a solution. This approach allows the introduction of specific modifications to DNA sequences, such as adding functional groups, labeling with fluorescent dyes, or attaching other molecules of interest. There are several commonly used *in solution* methods for DNA modification,[53] including: 1. Chemical modification utilizes reactive compounds to covalently modify the DNA molecule.[54] For example, DNA can be modified by reaction with specific chemical reagents like alkylating agents, acylation agents, or nucleophilic reagents.[55] These reactions can introduce various functional groups onto the DNA, such as methyl, amino, carboxyl, or biotin groups.[53, 55] 2. Enzymatic modification utilizes

specific enzymes to introduce modifications to DNA. For instance, DNA methyltransferases can be used to add methyl groups to specific nucleotide bases, such as cytosine, resulting in DNA methylation.[56] 3. Click chemistry refers to a set of highly selective and efficient reactions that can be used for DNA modification.[57] One popular example is the copper(I)-catalyzed azide-alkyne cycloaddition (CuAAC), which involves the reaction between an azide-modified DNA molecule and an alkyne-modified molecule, resulting in a stable triazole linkage.[58] Click chemistry offers versatility and bioorthogonality, allowing for precise and specific DNA modifications.[57] 4. Photocrosslinking method utilizes photoactive compounds or photoreactive DNA probes that can form covalent linkages upon exposure to specific wavelengths of light.[59] Photocrosslinking can be used to covalently attach functional groups or molecules to specific DNA sequences or to crosslink neighboring DNA strands. These methods enable researchers to tailor DNA molecules for various applications, such as DNA sequencing,[60] gene expression analysis,[61, 62] DNA-protein interaction studies,[63] and the development of DNA-based nanotechnology.[64] It's worth noting that the choice of specific method depends on the desired modification, experimental conditions, and the specific goals of the research.

DNA solid-phase functionalization by solid support involves attaching specific chemical groups or ligands to DNA molecules while they are immobilized on a solid support.[65, 66] This method is used to introduce functional groups onto DNA strands for various applications, such as conjugation to other molecules, surface attachment, or the creation of modified DNA probes.[67] Here is a general outline of the process:[65] 1) Prepare the solid support: The DNA molecules are initially immobilized on the solid support, typically through bonding between the DNA and the solid support. The solid support is then washed to remove any unbound DNA and other contaminants. 2) Functionalization

reaction: 2a) Prepare functionalization reaction mixture: Prepare a solution containing the functionalization reagents and any necessary reaction buffers or co-factors. The choice of functionalization reagents relies on the specific chemical modification being targeted. 2b) Incubate with solid support: Apply the functionalization reaction mixture to the solid support containing the immobilized DNA. Ensure that the entire surface is covered with the functionalization solution. 2c) Incubation: Allow the functionalization reaction to proceed for a specific period at an appropriate temperature. The reaction time and temperature will vary depending on the functionalization reagents used and the desired degree of modification. 3) Washing: Wash the solid support thoroughly with appropriate buffers or solvents to remove unreacted functionalization reagents, and reaction by-products. It should be noted that effective washing is essential to minimize background signal or contamination. 4) Elution: Detaching the modified DNA from the solid support while preserving the introduced chemical groups with appropriate elution buffers. 5) Analysis or application: The functionally modified DNA can be used for various applications, depending on the introduced chemical groups. For example, it can be conjugated to other molecules (*e.g.*, proteins or nanoparticles), immobilized on surfaces, or used as probes in assays.

The specific choice of functionalization reagents and solid support depends on the desired modification and the intended application. DNA solid-phase functionalization is a versatile technique used in molecular biology, bioconjugation, and the development of functionalized DNA-based materials for a wide range of biotechnological and biomedical applications.[68-70]

3.2.5 Synthesis of deoxyribonucleic acid macromolecular chain transfer agent (ssDNA$_{14}$-macroCTA) by *in solution* method and *solid support* method

In this approach, 14-mer ssDNA (5′-5AmMC12-TGTAGCGTTGTTGC-3′) equipped with a CEPA at its 5′ terminus (ssDNA$_{14}$-macroCTA) (Figure 3.1a) by a substitution reaction of the carboxylic acid group from CEPA with the amine group from ssDNA-NH_2 using N-ethyl-N'-(3-(dimethylamino)propyl)carbodiimide (EDC) and N-hydroxysuccinimide as coupling reagents.

For the *in solution* method, the conjugation of the RAFT agent to DNA was accomplished by amide conjugation with the activated NHS ester of the RAFT agent in a mixture of water and DMF (1:1), which was necessary to ensure sufficient solubility of all reagents (Scheme 3.2 in Experimental section). Due to the presence of competitive hydrolysis reactions in a partially aqueous medium, the activated ester was added in a significant excess (500 eq.) along with N,N-diisopropylethylamine (DIPEA) as an auxiliary base to increase the reactivity of the amine moiety.

With the utilization of a *solid support* method, DNA is selectively immobilized on an inert solid support, *i.e.* diethylaminoethanol (DEAE) Sepharose. Subsequently, a chemical reaction takes place in pure DMF, and the DNA is eventually eluted from the solid support without the necessity for additional purification steps ((Scheme 3.3 in Experimental section)). This method follows the solid support steps discussed in the previous section.

The purity of the ssDNA$_{14}$-macroCTA was investigated using RP-HPLC with a UV-vis detector that monitored the eluted DNA solution at 260 and 309 nm, corresponding to the maximum absorbance of DNA and the trithiocarbonate group, respectively. High conversion and purity (>95%) of the targeted ssDNA$_{14}$-macroCTA strand were achieved

using the *solid support* method, as evidenced by the presence of a single DNA-species signal at both detector wavelengths of 260 nm and 309 nm (Figure 3.9). LC/MS further confirmed the successful formation of the desired product. LC-MS: m/z $[C_{159}H_{211}N_{50}O_{91}P_{14}S_3\text{-}H]^-$ calc. 4807.900 g mol^{-1}, found 4807.314 g mol^{-1}. In contrast, the *in solution* method exhibited a second signal at 309 nm, indicating the presence of impurities from the trithiocarbonate-group containing starting material which may result in uncontrolled polymerization, potentially impacting the actual DP of PHPMA. To achieve comparable purity, additional purification steps, including HPLC purification, spin filtration, and ethanol precipitation, were necessary. These time-consuming purification procedures may not be feasible, particularly when high quantities of $ssDNA_{14}$-macroCTA are needed.

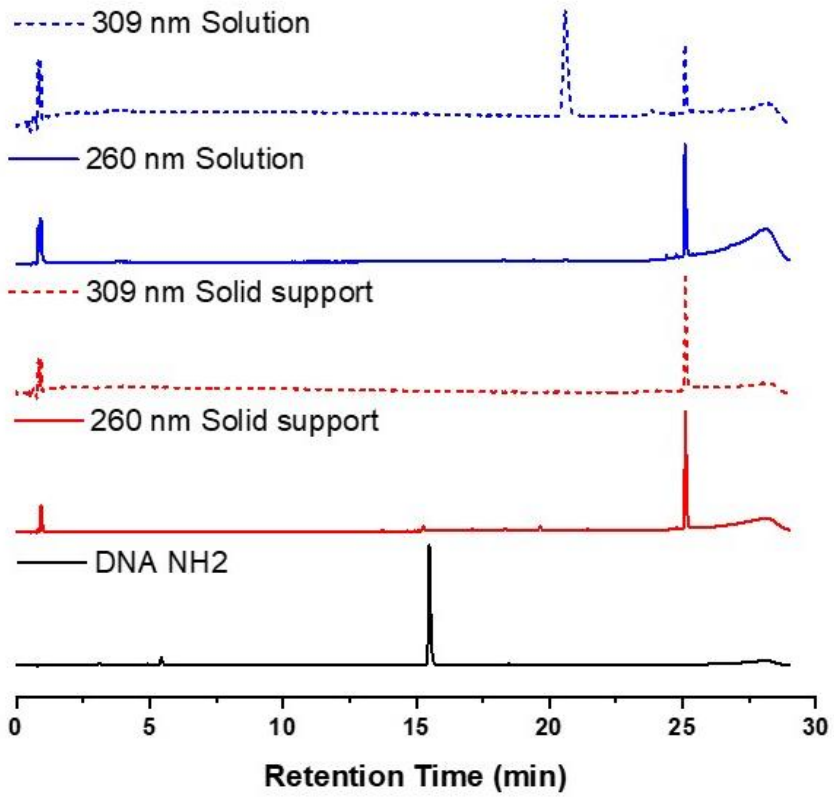

Figure 3.9. RP-HPLC chromatograms of DNA-macroCTA synthesized by *in solution* method (blue line), *solid support* method (red line) using NH_2-ssDNA as a starting material (black solid line). The chromatograms were investigated at detector wavelength

309 nm (dash line) and detector wavelength 260 nm (solid line). Products eluted with a gradient of buffer A, 0.1 M triethylammonium acetate (TEAA), in a 95:5 mixture of H_2O and acetonitrile and buffer B, 0.1 M TEAA, in a 30:70 mixture of H_2O and acetonitrile.

3.2.6 Synthesis of DNA−Polymer Conjugates by Photoinitiated polymerization-Induced Self Assembly

As well as the DNA-polymers conjugation performed in Part I, a series of DNA-copolymers bearing the same targeted DPs of PHPMA (300, 400, and 500) and monomer concentrations (5%w/w and 10%w/w) but with different batch of $ssDNA_{14}$-macroCTA which synthesized by *solid support* method. The low-volume aqueous RAFT-mediated photo-PISA was also repeated the condition in part I. Low-volume aqueous RAFT-mediated photo-PISA of HPMA was undertaken under 405 nm visible light irradiation at 37 ˚C using an enzyme degassing approach, *i.e.* glucose oxidase.[21, 22] (Scheme 3.2 in Experimental section)

Interestingly, moderate monomer conversions (62-87%) were achieved after 2 hours of reaction, as determined by ^{1}H-NMR spectroscopy (Table 3.5). The targeted DPs of the PHPMA block and the concentrations of monomer were varied within the ranges of 300 to 500 DPs and 5 to 10% w/w [HPMA], respectively, to explore the shape and size of the DNA-polymer particles. SEC analysis in DMF (with RI detection) of $ssDNA_{14}$-*b*-$PHPMA_X$ confirmed the successful chain-extension of PHPMA (Figure 3.10). The polymer lengths (DP=300, 400, and 500) could be simply adjusted by altering the monomer to $ssDNA_{14}$-macroCTA ratio. It should be noted that the monomer HPMA at targeted DP=300 showed very poor solubility in high monomer concentration (10 w/w %), so this condition was not performed. The size exclusion chromatograms revealed shifts towards higher degree of polymerization and the polymerization was well-

controlled for all targeted DP of PHPMA from 300 to 500 (Figure 3.10). However, due to the moderate conversions from polymerization, the further condition was required to investigate for achieving higher conversion.

Table 3.5. Characterization data of ssDNA$_{14}$-*b*-PHPMA$_X$ nanoparticles obtained from RAFT-mediated photo-PISA at different monomer concentrations and DPs.

Sample	Targeted DP	Actual DP[a]	Conv. (%)[a]	Size (nm)[b]	PD[b]	Morphology[c]
5%w-DP300	300	234	78	63	0.28	s
5%w-DP400	400	288	72	63	0.21	s
5%w-DP500	500	310	62	63	0.21	s
10%w-DP400	400	320	80	90	0.12	s
10%w-DP500	500	435	87	154	0.12	s

[a] Calculated from ^{1}H NMR spectroscopy (400 MHz) in deuterated MeOD.

[b] Determined by DLS.

[c] Determined by TEM. Key: s = spherical micelles

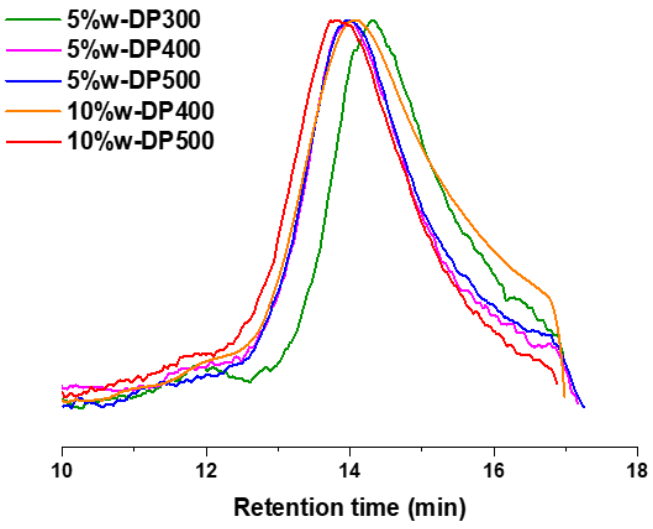

Figure 3.10. SEC RI traces of the ssDNA$_{14}$-*b*-PHPMA$_X$ polymer conjugates as measured by DMF GPC using polymethylmethacrylate (PMMA) calibration standards with RI detector.

After the photo-PISA reaction, a change in the turbidity of the solution from transparent to opaque indicated the growth of hydrophobic PHPMA. Similar to part I, TEM imaging revealed the successful development of only spherical particles (Figure 3.11), while DLS analysis also confirmed a unimodal particle size distribution with D_h in the range of 60-154 nm (Figure 3.20 in Experimental section). The shape and size of particles were nearly identical to the DNA-polymer nanoobjects achieved using DNA-macroCTA from the Sleiman group. The assumption that spherical micelles were achieved is likely due to electrostatic repulsion from the negative charge on DNA strands, preventing the merging of micelles to form worms or vesicles, thus avoiding morphology transition. This phenomenon is also commonly observed in electrostatically stabilized nanoparticles produced through the PISA technique.[71] In polyelectrolyte-stabilized particles, the transition of higher-order morphologies is restricted due to electrostatic repulsion among ionic units.[71-74]

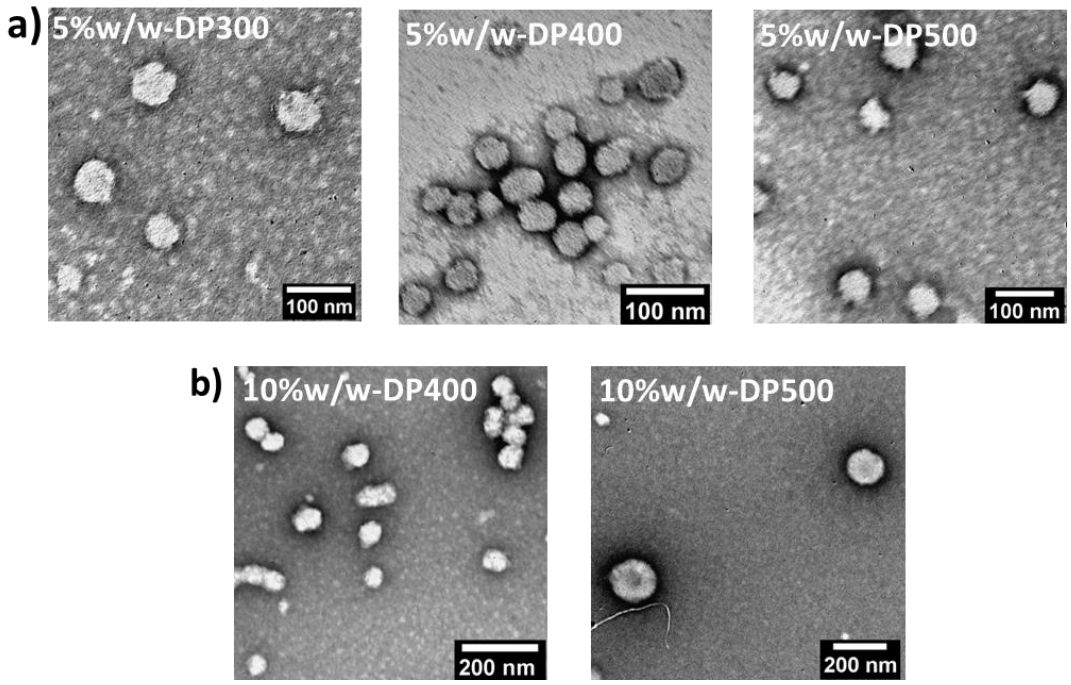

Figure 3.11. TEM images of ssDNA$_{14}$-*b*-PHPMA$_X$ diblock copolymers.

It should be noted that the cryo-TEM images were measured by Marjolaine Thomas, our ex-group member, at the university of Warwick as I mentioned in declaration of authorship. Due to the time-consuming nature of the technique, cryo-TEM imaging was investigated in only one sample, specifically a sample obtained from the 10%w/w and DP_{PHPMA}=400, which served as a representative for all the obtained spherical particles. (Figure 3.12). From the particle sizes listed in Table 3.5, EM imaging, and the existing literature on polyelectrolyte-stabilized particles,[72-74] the achieved particle morphology is potentially spherical micelle.

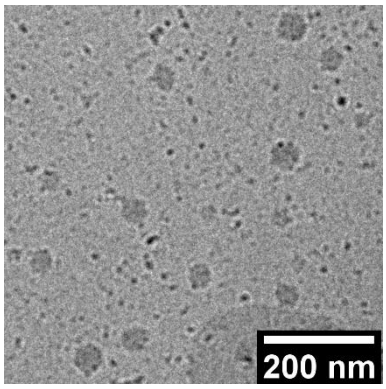

Figure 3.12. Cryogenic transmission electron microscopy (Cryo-TEM) images of $ssDNA_{14}$-*b*-$PHPMA_{400}$ at 10%w/w monomer concentration.

To improve the conversion of DNA-polymer conjugates, 5% w/w [HPMA] with a targeted DP_{HPMA} of 500 was chosen for investigation under various conditions through RAFT-PISA method due to having the lowest conversion among all monomer concentrations and DPs of HPMA. Firstly, the reaction time was increased from 2 h to 6 h while maintaining typical concentration of GOx (2 µM) and glucose (0.1 M). A reaction time of 6 h corresponds with the timeframe described in Yang's report,[16] thereby extending the polymerization duration in the synthesis of DNA nanoparticles through photo-PISA reaction. The results obtained after 6 h of reaction showed a significantly increased conversion from 60 to 80% as well as the size of particles increased from 60

nm to 70 nm (Table 3.6). Another condition to improve polymerization conversion involved increasing the concentration of GOx (5 μM) and glucose (0.2 M) while maintain reaction time at 2 h to enhance oxygen-tolerant efficiency resulting almost completed conversion (>99%) and good control of particle size (60 nm, Table 3.6). Interestingly, SEC analysis in DMF (with RI detection) of $ssDNA_{14}$-b-$PHPMA_{500}$ from each sample did not reveal chain-extension of PHPMA as conversion increased (Figure 3.13 in Experimental section). Instead, a small shoulder peak with a lower retention time occurred, indicating a higher molecular weight. The observed small shoulder peak at high MW when targeting high DPs (DP_{HPMA}>400) is well-documented[24-26] and is actually as a consequence of the presence of a small amount (<0.3 mol %) of dimethacrylate in the HPMA monomer, rather than loss of RAFT control. This impurity inevitably leads to light branching as longer PHPMA chains are targeted.[27-29]

Table 3.6. Characterization data of 5%w/w $ssDNA_{14}$-*b*-$PHPMA_{500}$ nanoparticles obtained from RAFT-mediated photo-PISA at different conditions.

[HPMA] (%w/w)	Targeted DP	Reaction time (h)	[GOx] (μM)	[Glucose] (M)	Actual DP[a]	Conv. (%)[a]	Size (nm)[b]	PD[b]
5	500	2	2	0.1	310	62	63	0.21
5	500	6	2	0.1	405	81	71	0.32
5	500	2	5	0.2	500	>99	63	0.26

[a] Calculated from ^{1}H NMR spectroscopy (400 MHz) in deuterated MeOD.

[b] Determined by DLS.

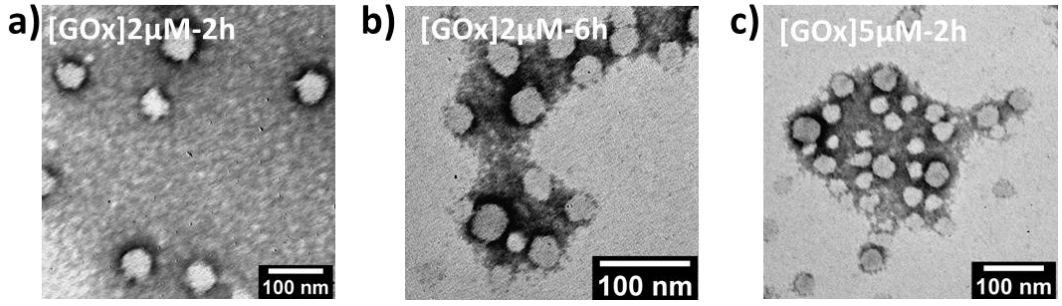

Figure 3.13. TEM images of 5%w/w ssDNA$_{14}$-*b*-PHPMA$_{500}$ nanoparticles using a) 2 µM [GOx] at 2 h reaction time b) 2 µM [GOx] at 6 h reaction time, and c) 5 µM [GOx] at 2 h reaction time.

To compare the DNA-polymer particles synthesized using ssDNA$_{14}$-macroCTA from our group with those from the Sleiman group, it was evident that the Sleiman group achieved significantly higher conversions (>99%) compared to the conversions obtained with DNA-macroCTA from our group (62-87%). This could be due to the presence of trithiocarbonate impurities in the DNA-macroCTA from the Sleiman group (Figure 3.8), which may have also contributed to RAFT polymerization. Interestingly, the morphology and shape of the particles were identical, and the size of the particles did not differ significantly. This could potentially be a result of electrostatic repulsion from the DNA strands on the corona, as mentioned above. To achieve nearly complete conversion (>99%) in the synthesis of DNA-polymer by DNA-macroCTA from our group, GOx (5 µM) and glucose (0.2 M) for 2 h was applied. This condition not only achieved high conversion but also provided good control over polymerization and particle size.

3.2.7 Screening effect of salts (NaCl and $MgCl_2$)

The screening effect of salts on particle stability was also investigated in this part, following a similar approach in part I. NaCl and $MgCl_2$ were also utilized to investigate the screening effects of monovalent and divalent salts, respectively, *via* DLS and TEM. A 10 mM solution of ssDNA$_{14}$-*b*-PHPMA$_{500}$ was monitored by DLS and TEM after the

addition of salts to achieve a final concentration of 10 mM. DLS and TEM images indicated that NaCl did not affect the size of particles and particle morphology of DNA-polymer (Figure 3.14a) while $MgCl_2$ caused aggregates and morphology deformation in solution (Figure 3.14b). These results indicate that Mg^{2+} impacts the self-assembly process and the stability of DNA-polymer nanoparticles leading to detrimental to the stability of DNA self-assemblies.[39] Due to the instability of DNA-corona nanoparticles in 10 mM $MgCl_2$, which is typically used in hybridization studies, the hybridization study was unable to be investigated in this part. Interestingly, this unstable particle behaviour led to the idea of adding salt before conducting the RAFT-PISA to investigate the effect of salts on the PISA process. Some literature suggests that salt could affect electrostatic polymers in PISA reactions by reducing the charge on the electrostatic macroCTA.[71-74] Moreover, the DNA-polymer particles tend to aggregate and disassemble in 1×TAE buffer leading to difficulty in studying DNA hybridization on the particle surface. (Figure 3.24 in Experimental section)

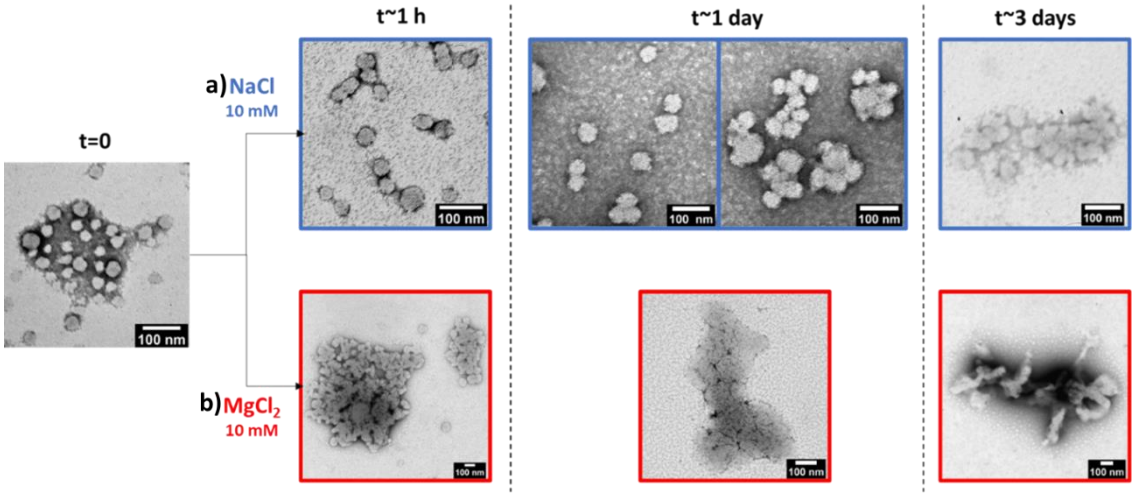

Figure 3.14. TEM images of ssDNA$_{14}$-*b*-PHPMA$_{500}$ particles in 10 mM salt solution a) NaCl and b) $MgCl_2$.

3.2.8 Study effect of salts (NaCl and $MgCl_2$) during ssDNA$_{14}$-PHPMA$_{500}$ PISA reaction

As mentioned earlier, salt has the potential to influence the particle morphology of electrostatic polymers in PISA reactions by reducing the charge on the electrostatic macroCTA.[71, 74] Thus, NaCl and $MgCl_2$, representing monovalent and divalent salts, respectively, were used to study the particle morphology from the PISA polymerization in salt solution. The final concentrations of both NaCl and $MgCl_2$ were set to [Salts] = 10 mM and 20 mM. Low-volume aqueous RAFT-mediated photo-PISA of HPMA was attempted at 405 nm visible light irradiation of the solution at 37 ˚C applying [glucose] = 0.1 M and [GOx] = 2 µM with mineral oil was added on top of the 50 µL reaction solution, which was the same condition in the previous topic, 3.2.10. 5% w/w [HPMA] with a targeted DP_{PHPMA} of 500 was chosen for investigating polymerization in salt solution conditions because it required the lowest amount of DNA-macroCTA and featured the longest hydrophobic chain length from PHPMA, which is more likely to transition to higher-order morphologies.

Almost complete monomer conversion (>99%) was achieved after 2 hours of reaction, as determined by ^{1}H-NMR spectroscopy (Table 3.7). After the photo-PISA reaction, a change in the turbidity of the solution from transparent to opaque indicated the growth of hydrophobic PHPMA. The final concentrations of salts *i.e.*, NaCl and $MgCl_2$ solutions, were adjusted to 10 mM and 20 mM to investigate shape and size of the DNA-polymer particles under different salt concentration. SEC analysis in DMF (with RI detection) of ssDNA$_{14}$-*b*-PHPMA$_{500}$ confirmed the successful chain-extension of PHPMA (Figure 3.21 in Experimental section).

TEM images of ssDNA$_{14}$-*b*-PHPMA$_{500}$ at 5%w/w HPMA from NaCl solution revealed only spherical micelles in both 10 mM and 20 mM NaCl solutions (Figure 3.15a), while DLS analysis also confirmed a unimodal particle size distribution with D_h in the range of 60-80 nm (Table 3.7 and Figure 3.27a and b in Experimental section), which is similar to TEM image and D_h (63 nm) from the PISA reaction without added salt using the same procedure. In contrast, TEM images of ssDNA$_{14}$-*b*-PHPMA$_{500}$ at 5%w/w HPMA from $MgCl_2$ solution revealed the successful development of short worms (Figure 3.15b), corresponding with the increased D_h in the range of 100-126 nm (Table 3.7 and Figure 3.27c and d in Experimental section). These results are presumably due to the fact that Mg^{2+}, as a divalent ion, has a stronger charge compared to the monovalent ion Na+ and, therefore, has a greater ability to reduce the electrostatic repulsion between DNA chains resulting in the fusion of spherical micelles into short worm-like micelles. Another assumption of morphology transition from sphere to short worm is that divalent ions were potentially capable of bringing two DNA strands closer together and promoting the transition to higher-order morphology. The aggregate and deformation of DNA-particles also occurred when $MgCl_2$ was added as previously explained in topic 3.2.9.

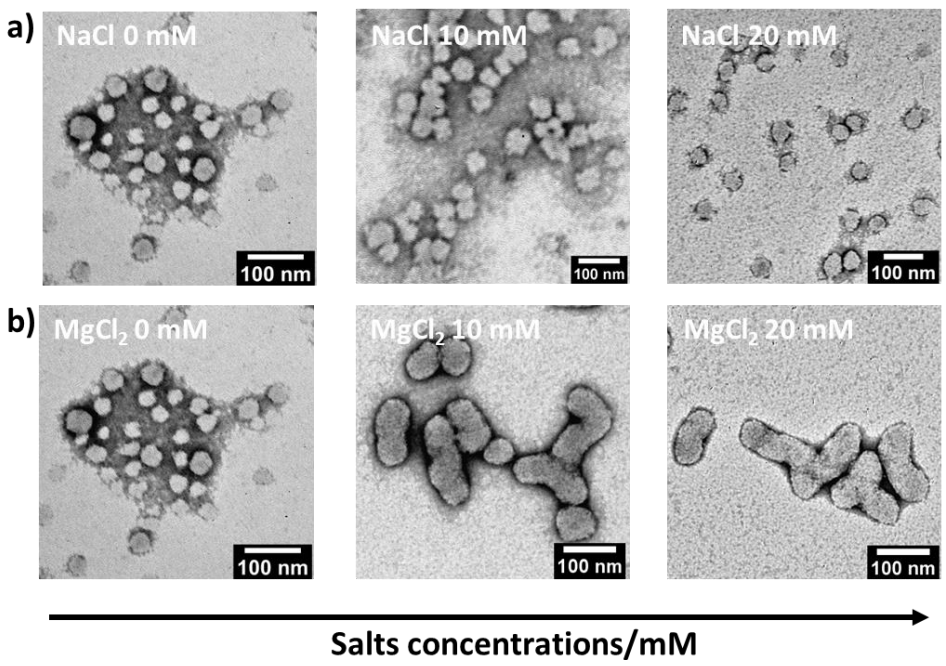

Figure 3.15. Schematic TEM images of ssDNA$_{14}$-*b*-PHPMA$_{500}$ nanoparticles in salt solutions a) NaCl and b) $MgCl_2$ with different salts concentration.

Considering the formation of short worms with the addition of $MgCl_2$, it is possible that higher concentrations of $MgCl_2$ could induce a transition to higher-order morphologies. Therefore, the effects of $MgCl_2$ at final concentrations of 50 mM and 100 mM were also investigated using the same low-volume PISA reaction at 50 µL. In these systems, DLS showed poor data quality in these two samples, as indicated by the "ERROR" in Table 3.7. Interestingly, long wormlike aggregates were investigated in a 50 mM $MgCl_2$ solution and rodlike aggregates with a potential hollow cavity were also observed under the same condition (Figure 3.16). Thus, DNA$_{14}$-*b*-PHPMA$_X$ particles was driven to higher order morphology transition with increasing salt concentrations.

Table 3.7. Characterization data of 5%w/w ssDNA$_{14}$-*b*-PHPMA$_{500}$ nanoparticles obtained from RAFT-mediated photo-PISA at different concentrations of salt solutions.

Sample	[Salt] (mM)	Targeted DP	Actual DP[a]	Conv. (%)[a]	Size (nm)[b]	PD[b]	Morphology[c]
No Salt	0	500	500	>99	63	0.28	s
NaCl-10	10	500	500	>99	74	0.31	s
NaCl-20	20	500	500	>99	62	0.17	s
$MgCl_2$-10	10	500	500	>99	126	0.16	sw
$MgCl_2$-20	20	500	500	>99	100	0.11	sw
$MgCl_2$-50	50	500	500	>99	ERROR	ERROR	lw
$MgCl_2$-100	100	500	480	96	ERROR	ERROR	r

[a] Calculated from ^{1}H NMR spectroscopy (400 MHz) in deuterated MeOD.

[b] Determined by DLS.

[c] Determined by TEM. Key: s = spherical micelles, sw = short wormlike micelles, lw = long wormlike aggregates, and r= rodlike aggregates.

Key: ERROR = poor quality result from DLS.

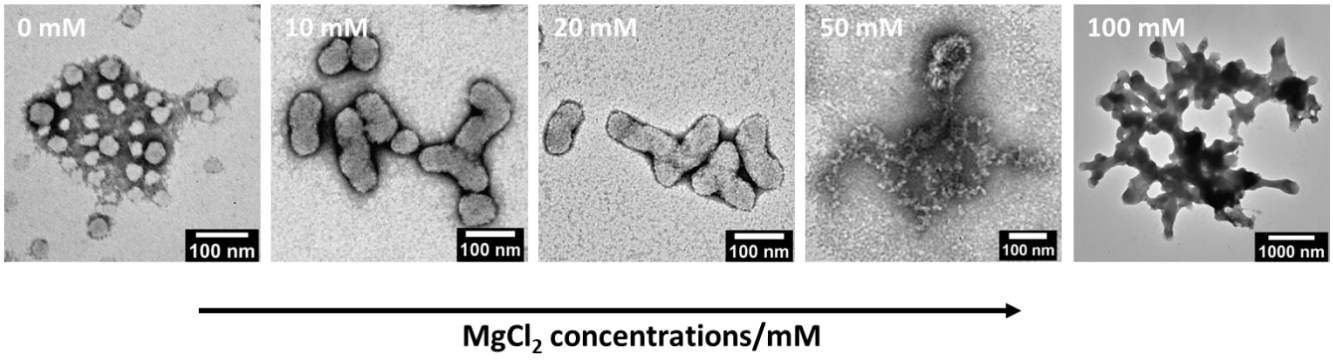

Figure 3.16. Schematic TEM images of ssDNA$_{14}$-*b*-PHPMA$_{500}$ nanoparticles at different $MgCl_2$ concentration.

3.3 Conclusion

In conclusion, the first ssDNA-macroCTA has been introduced for the fabrication of DNA-polymer nano-objects without the addition of an external photoinitiator or photocatalyst *via* low-volume RAFT-mediated photo-PISA under enzyme-assisted degassing conditions. The synthesis of DNA-macroCTA was studied using both *in solution* and *solid support* methods to determine the most suitable approach for obtaining high purity, high yield, and scalable amounts of DNA-macroCTA without requiring HPLC purification. DNA-macroCTA synthesized by both the Sleiman group and our group successfully enabled the synthesis of a series of DNA–polymer conjugates with high conversion, narrow molecular weight distributions, and narrow particle size distributions. Furthermore, DNA-corona particles synthesized using the DNA-macroCTA from the Sleiman group were functionalized with TAMRA-cDNA and then imaged using confocal fluorescence microscopy to confirm both hybridization and the presence of DNA on the particles. However, the DNA-corona particles synthesized by DNA-macroCTA from our group did not exhibit stability in the same salt solution conditions as those used for the DNA-particles from the Sleiman group. This led to the idea of studying polymerization in salt solutions using NaCl and $MgCl_2$. Finally, the DNA-decorated nanoparticles in the presence of $MgCl_2$ can transition from small spherical micelles (60 nm) to higher-order morphologies, including short wormlike micelles (100 nm), long wormlike aggregates, and large rodlike aggregates with a hollow cavity. Considering the successful conjugation of DNA with block copolymers in low-volume RAFT-mediated photo-PISA reactions and the subsequent characterization, we anticipate that this strategy will broaden the application scope of DNA-polymer nanoobject in PISA.

3.4 Experimental section

3.4.1. Materials

2-Hydroxypropyl methacrylate (mixture of isomers, 98%, HPMA) was purchased from Alfa Aesar and was passed through a column of basic alumina to remove inhibitor prior to use. sodium chloride (NaCl) and magnesium chloride ($MgCl_2$) were purchased from Fisher Scientific. Formvar-coated copper grids were purchased from EM Resolutions. SYBR™ Gold Nucleic acid gel stain (10,000X concentrate in DMSO) was purchased from ThermoFisher. Tris-acetate-EDTA (TAE) buffer was purchased from Sigma-Aldrich and contains 0.4 M Trisacetate and 0.01 M EDTA. Oligonucleotides were purchased from Integrated DNA technologies, Inc. and resuspended in 18MΩ H_2O to a concentration of 100 μM before use. Concentrations were calculated from the absorbance values at 260 nm using the reported extinction coefficients.

Name	**Sequence (5'- 3')**	**Extinction coefficient (L (mole·cm)$^{-1}$)**
$ssDNA_{14}$	TGTAGCGTTGTTGC	128,400
cDNA	GCAACAACGCTACA	139,600
TAMRA-cDNA	/56-TAMN/GCAACAACGCTACA	168,700
ncDNA	TGTAGCGTTGTTGC	128,400

3.4.2. Instrumentations and analysis

^{1}H-NMR spectra were recorded at 400 MHz on a Bruker DPX-400 spectrometer using chloroform-*d* (CDCl3) and methanol-*d4* (CD_3OD) as the solvent. Chemical shifts of protons are reported as δ in parts per million (ppm) and are relative to tetramethylsilane (TMS) at δ = 0 ppm when using solvent residual peak (CH_3OH, δ = 3.31 ppm).

Reversed Phase High Performance Liquid Chromatography (RP-HPLC) analysis of oligonucleotides was performed on a modular Shimadzu instrument with the following modules: CBM-20A system controller, LC-20AD solvent deliver module, SIL-20AC HT autosampler, CTO-20AC column oven, SPD-M20A photodiode array UV-Vis detector, RF-20A spectrofluorometric detector and a FRC-10 fraction collector. Chromatography was performed on a Waters XBridge™ OST C18 2.5 µM column heated to 60 °C. Flow rate was set at 0.8 mL min^{-1} using buffers A and B: buffer A, 0.1 M triethylammonium acetate (TEAA, pH 7.0), in a 95:5 mixture of H_2O and acetonitrile; buffer B, 0.1 M TEAA (pH 7), 30:70 mixture of H_2O and acetonitrile. The buffer gradient for analysis and purification was 1% buffer B for 5 minutes, 1% to 30% B over 15 minutes, 30% to 95% B over 5 min, 95% to 1% B over 1 min and finally 1% B for 3 min.

Liquid Chromatography-Mass Spectrometry (LC-MS) analysis of oligonucleotides was performed on an Agilent 1200 HPLC system coupled to a Bruker AmazonX high resolution ion trap, in negative ion mode. The desalted oligonucleotide samples were eluted through a XBridge oligonucleotide BEH C18 column (130 Å, 2.5 µm, 4.6 x 50 mm) using a 5 vol% MeOH, 10 mM ammonium acetate (buffer A) and a 70 vol% MeOH, 10 mM ammonium acetate (buffer B) solvent system at 0.8 mL/min flow. The data was processed using Compass Data Analysis (Bruker) v.4.1 software, and the MaxEnt integrated deconvolution algorithm. Alternatively, LCMS analysis was performed on a Waters ACQUITY UPLC system coupled to a Xevo G2-XS QToF mass spectrometer in negative ion mode. The oligonucleotides were eluted through an AQUITY UPLC oligonucleotide BEH C18 column (130 Å, 1.7 µm, 2.1 x 50 mm) using a 75 mM triethylammonium acetate (TEAA, pH 7.0) solution in H_2O (buffer A) and a 75 mM TEAA solution in MeCN (buffer B) at 60 °C and a 0.2 mL/min flow. Leucine enkephalin was used as the reference for the LockSpray correction. The raw continuum data was

deconvoluted to produce zero charge mass spectra using ProMass HR for MassLynx (Novatia) software.

Gel Electrophoresis - Native polyacrylamide gel (15%) was prepared by mixing 2.5 mL 30% 29:1 acrylamide:bisacrylamide, 4.25 mL H_2O, 0.75 mL 10×TAE, 75 µL 10% (w/v) ammonium persulfate (APS), and 7.5 µL tetramethylethylenediamine (TEMED). Different percentage gels were prepared by varying the proportions of acrylamide and water. After removing well combs, wells were rinsed with running buffer (1×TAE) using a pipette before loading 2 µL samples typically diluted to 200 nM in loading buffer (1×TAE, 50% glycerol). Native polyacrylamide gels were run at room temperature in 1×TAE buffer at 180 V using a vertical nucleic acid electrophoresis cell connected to a PowerPack basic power supply (BioRad). Samples were combined with 20% loading buffer (0.05% bromophenol blue, 25% glycerol, 1×TAE) prior to running. Non-fluorescent DNA was stained using a 1:1000 aqueous SYBR® Gold nucleic acid gel stain (ThermoFisher) and visualized using a BioRad ChemiDoc™ MP Imaging system. The images were processed using ImageLab software v 6.0.1.

Agarose gel (10%) was run at room temperature in 1×TAE buffer at 75 A using Bio-Rad Mini-Sub® Cell GT System apparatus connected to a PowerPack basic power supply (BioRad). Samples were combined with 20% loading buffer (0.05% bromophenol blue, 25% glycerol, 1xTAE) prior to running. Non-fluorescent DNA was stained using a 1:1000 aqueous SYBR® Gold nucleic acid gel stain (ThermoFisher) and visualized using a BioRad ChemiDoc™ MP Imaging system. The images were processed using ImageLab software v 6.0.1.

1×TAE buffer consisted of 40 mM Tris-acetate and 1 mM EDTA. 1×TBE buffer consisted of 89 mM Tris-borate and 2 mM EDTA. 1×TAE buffer consisted of 10 mM

Tris-HCl and 1 mM EDTA. The native loading buffer consisted of 25 % glycerol and 0.05 % bromophenol blue in 1×TAE buffer, and was diluted five-fold before use.

Size exclusion chromatography (SEC) analysis was performed on a system composed of a Varian 390-LC-Multi detector suite equipped with a Varian Polymer Laboratories guard column (PLGel 5 μM, 50 × 7.5 mm), two Mixed-C Varian Polymer Laboratories columns (PLGel 5 μM, 300 × 7.5 mm) and a PLAST RT auto-sampler. Detection was conducted using a differential refractive index (RI) and an ultraviolet (UV) detector set to λ = 309 nm. The mobile phase used was DMF (HPLC grade) containing 5 mM NH4BF4 at 50 ˚C at a flow rate of 1.0 mL min-1. Poly(methyl methacrylate) (PMMA) standards were used for calibration. Molecular weights and dispersities were determined using Cirrus v3.3 SEC software.

Hydrodynamic diameters (D_h) of particles were determined by dynamic light scattering (DLS) using a Malvern Zetasizer Nano ZS with a 4 mW He-Ne 633 nm laser module operating at 25 ^oC. Measurements were carried out at an angle of 173° (back scattering), and results were analyzed using Malvern DTS 7.03 software. All determinations were repeated 4 times with at least 10 measurements recorded for each run. D_h values were calculated using the Stokes-Einstein equation where particles are assumed to be spherical, while for cylindrical particles DLS was used to detect multiple populations and obtain dispersity information.

Transmission Electron Microscopy (TEM) analysis was performed on a JEOL 2100 electron microscope at an acceleration voltage of 200 kV. All samples were diluted with deionized water and then deposited onto formvar-coated copper grids. After roughly 1 min, excess sample was blotted from the grid and the grid stained with an aqueous 1 wt% uranyl acetate (UA) solution for 1 min prior to blotting, drying and microscopic analysis.

Cryogenic Transmission Electron Microscopy (Cryo-TEM) imaging was performed on a JEOL JEM-2100 plus microscope operating at an acceleration voltage of 200 kV. Samples for cryo-TEM were prepared on lacey carbon grids (EM Resolutions). After 200-fold dilution with deionized water, 8 µL of sample were deposited onto the grid followed by blotting for approximately 5 s and plunging into a pool of liquid ethane, cooled using liquid nitrogen in order to vitrify the samples. Then, transfer into a pre-cooled cryo-TEM holder using liquid nitrogen, was performed prior to the microscopic analysis.

Confocal Laser Scanning Microscopy (CLSM) was performed on FV3000 (Olympus) confocal microscope and the 60x oil lens was used for imaging. Images were acquired using the 488 nm (green channel) and the 561 nm (red channel) excitation wavelengths. Freshly prepared and purified solutions of FAM-**H2** (green-emitting dye), TAMRA-**cDNA** (red-emitting dye) and mixed 50% DNA_{14}-$PHPMA_{400}$ copolymer nano-objects at 100-fold dilution were deposited on a glass slide before imaged by CLSM. Images were processed using cellSens (Olympus) and ImageJ image processing software. The LAD-1 LED array driver was purchased from Bio Research Centre Co., Ltd. The array was composed of 96 405 nm LEDs which each output a light power of 20 mW at 13.5 V when measured with an LMP-100 light power sensor (sensor area: 5.5 mm x 4.8 mm), placed directly above an array LED. For the Thermomixer setup, the LED-array was suspended over the sample holder *via* a clamp stand. For the Incubator setup the LED-array was placed upon a shaker plate, face up with a 96-microwell plate placed directly upon it, into which 150 µL eppendorfs containing sample were placed.

The LAD-1 LED array driver was purchased from Bio Research Centre Co., Ltd. The array was composed of 405 nm LEDs which each output a light power of 20 mW at 13.5 V when measured with an LMP-100 light power sensor (sensor area: 5.5 mm x 4.8 mm), placed directly above an array LED. For the Thermomixer setup, the LED-array was

suspended over the sample holder *via* a clamp stand. For the Incubator setup the LED-array was placed upon a shaker plate, face up with a 96-microwell plate placed directly upon it, into which 150 µL eppendorfs containing sample were placed.

3.4.3. Synthetic Method

Synthesis of ssDNA$_{14}$-macroCTA by *in solution* approach

Amine-modified oligonucleotide (ssDNA$_{14}$-NH$_2$) (1 mM, 1 µl, 1 eq.) was mixed with borate buffer pH 7.5 (45 µl), then mixed with CEPA (0.5 M, 20 µL, 500 eq.), EDC·HCl (1 M, 10 µl, 500 eq), NHS (1 M, 10 µl, 500 eq), and DIPEA (1 M, 10 µl, 500 eq) in DMF at 21 °C 400 rpm overnight. Residual chemicals were removed *via* ethanol precipitation by adding 300 vol% ethanol to the reaction mixture and incubating the samples at -20 °C for 6 hours. After centrifugation at 15000 rpm for 30 min at 4 °C the supernatant was removed, and the DNA pellet washed with ice-cold 70% ethanol followed by a repeated centrifugations using the same settings as described above. The supernatant of the washing solution was removed and the DNA pellet was dried on air.

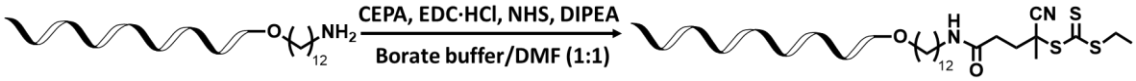

Scheme 3.2. Synthesis of ssDNA$_{14}$-macroCTA by *in solution* approach.

Synthesis of ssDNA$_{14}$-macroCTA by *solid support* approach

250 µL of DEAE Sepharose suspension was used as solid support and pipetted into an empty Glen Research column housing and washed with 20 ml of H_2O followed by 12 ml of DEAE binding buffer (10 mM acetic acid and 0.005% Triton X-100) using a syringe. The DNA-NH$_2$ (10 µM, 1 ml, 1 eq) was loaded onto the column after dissolving in 1 ml of DEAE binding buffer. The column was then washed with 3 ml of DEAE binding buffer, followed by 1 mL of H_2O and 4 ml of DMF to switch the solvent system from

water to DMF. At least 50 nmol of oligonucleotide can be loaded onto one 250-µL DEAE Sepharose column. The activated ester solution was composed of CEPA (0.5 M, 100 µL, 500 eq), EDC·HCl (1M, 50 µL. 500 eq), NHS (1 M, 50 µL. 500 eq), and DIPEA (1 M, 50 µL. 500 eq) in solvent (DMF) and was incubated at 21 °C for 30 min before use. The CEPA active ester solution was loaded onto the solid support column in 1 ml of DEAE bind buffer and incubated for 10 min. After the reaction was completed, the column was washed with 4 ml of the reaction solvent (DMF) followed by 3-5 ml of DEAE binding buffer. Finally, the DNA was eluted with 4 ml of DEAE elution buffer (1.5 M NaCl, 50 mM Tris-HCl [pH 8.0], and 0.005% Triton X-100) using a syringe. Product formation was verified *via* LC-MS: m/z [C159H211N50O91P14S3-H]¯ calc. 4807.900 g mol-1, found 4807.314 g mol^{-1}.

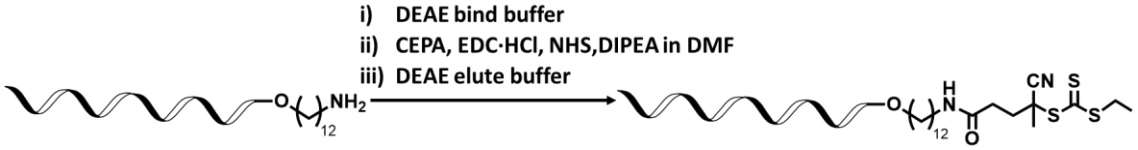

Scheme 3.3. Synthesis of ssDNA$_{14}$-macroCTA by *solid support* approach.

Synthesis of of ssDNA$_{14}$-*b*-PHPMA$_X$ conjugates by photoinitiated polymerization-induced self-assembly

ssDNA$_{14}$-macroCTA (250.5 µL, 20 mg/mL, 1 eq) was added in a centrifuge tube containing HPMA (2.5 mg for 5%w/w, 5 mg for 10%w/w, 200,300,400 eq). Then, glucose solution (6 µL, 0.84 M), nanopure water (8.4 µL) and GOx solution (8 µL, 12.5 µM) were added into the mixing vial, respectively, resulting in a total volume of 50 μL. The mixture was shaken *via* vortexer to produce a clear colourless solution which was then transferred to pointed base PCR plate. Mineral oil was added around 200 µL on top of the mixture and the plate was covered by plate seal, and placed in LED array setup, which was contain in an incubator to maintain a temperature of 37 °C. The solution was

then exposed to 405 nm light for 2 h, resulting in the solution turning opaque and milky white.

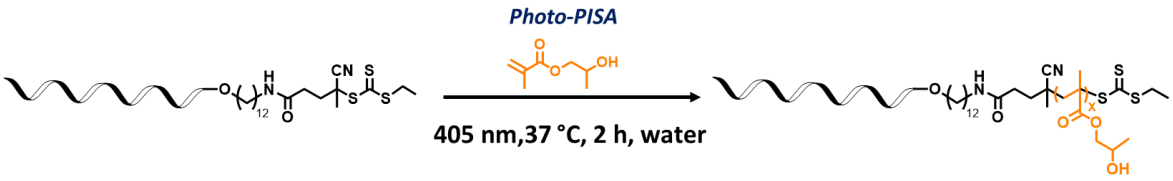

Scheme 3.4. Synthesis of ssDNA$_{14}$-*b*-PHPMA$_X$.

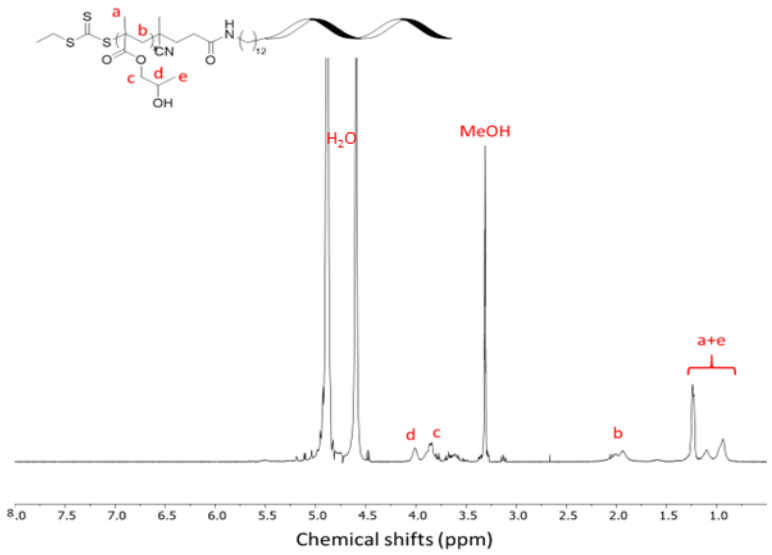

Figure 3.17. ^{1}H-NMR spectrum of ssDNA$_{14}$-*b*-PHPMA$_{429}$ in MeOD

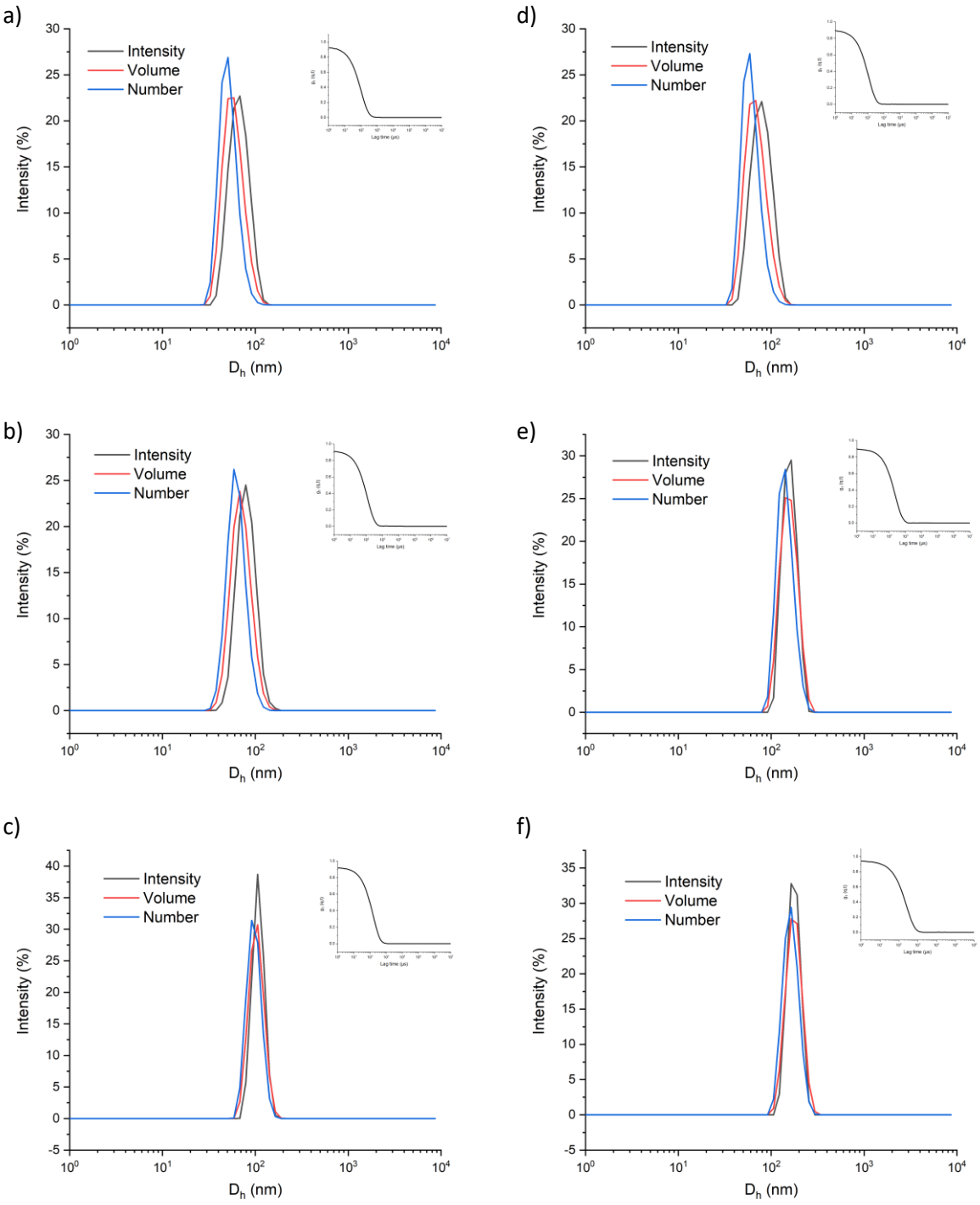

Figure 3.18. DLS data of ssDNA$_{14}$-*b*-PHPMA$_X$ a) ssDNA$_{14}$-*b*-PHPMA$_{286}$, b) ssDNA$_{14}$-*b*-PHPMA$_{429}$, and c) ssDNA$_{14}$-*b*-PHPMA$_{571}$ at condition 5%w/w [HPMA], d) ssDNA$_{14}$-*b*-PHPMA$_{286}$, e) ssDNA$_{14}$-*b*-PHPMA$_{429}$, and f) ssDNA$_{14}$-*b*-PHPMA$_{571}$ at condition 10%w/w [HPMA]

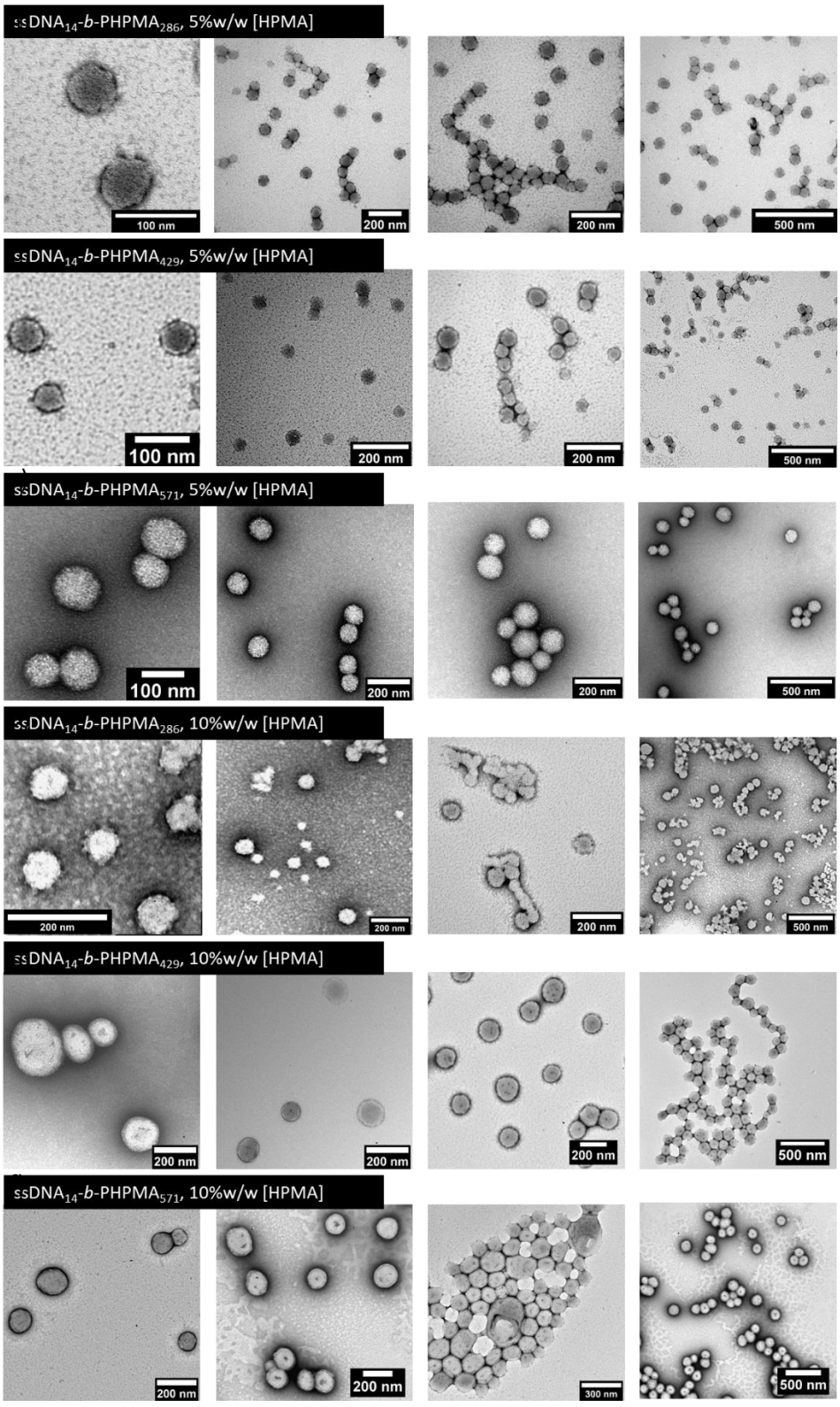

Figure 3.19. a-c TEM images of ssDNA$_{14}$-*b*-PHPMA$_X$ at condition 5%w/w [HPMA]. d-f TEM images of ssDNA$_{14}$-*b*-PHPMA$_X$ at condition 10%w/w [HPMA]. Different degrees of polymerization were targeted: DP$_n$=286 (a, d), 429 (b, e), 571 (c, f).

Screening effect of salts study (NaCl and $MgCl_2$)

Nanopure water (177 or 159 µL) was added into NaCl or $MgCl_2$ (2 or 20 µL, 1M), $ssDNA_{14}$-$PHPMA_{429}$ (1 µL, 100 mg/ml), TAE (20 µL, 10×) to prepare $ssDNA_{14}$-$PHPMA_{429}$ solution under buffer/salts condition (10 or 100 mM, respectively) in a centrifuge tube. The eppendoff was shaken at room temperature at least 30 min and then transferred to DLS microcuvette. DLS was used to investigate particle size and size dispersity.

Hybridization study

cDNA (varied amount, 100µM, varied eq.) was added to mixture of $ssDNA_{14}$-$PHPMA_{429}$ (1 µL, 100 mg mL^{-1}, 1 eq.), TAE (20 µL, 10×), $MgCl_2$ (2µL, 1M) and nanopure water (177 µL) in a centrifuge tube. The centrifuge tube was shaken at room temperature at least 30 min before investigation by DLS.

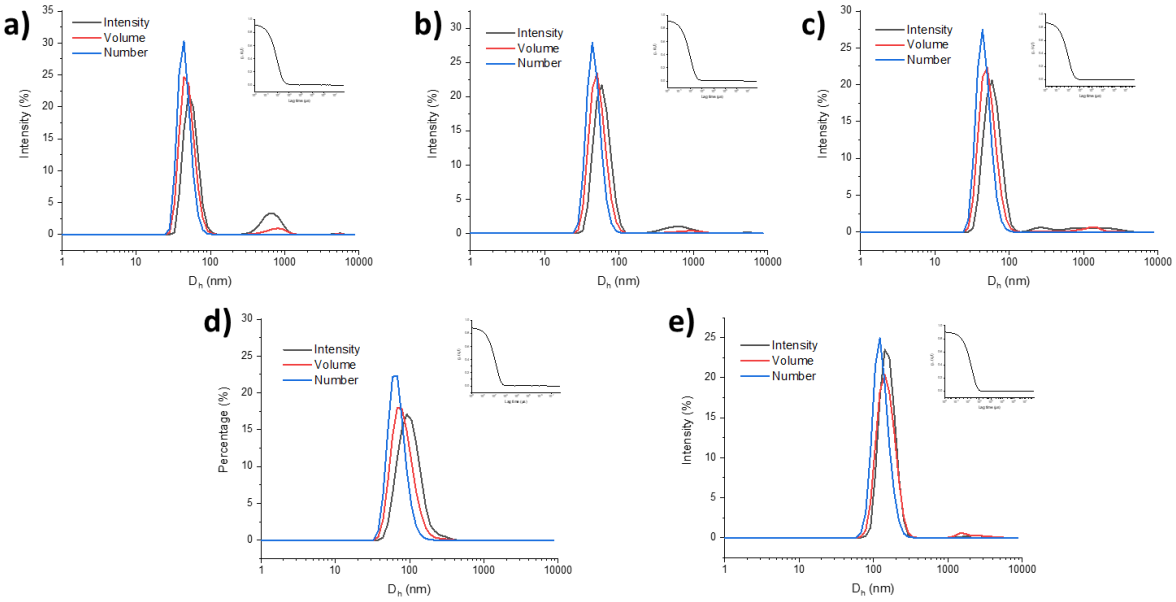

Figure 3.20. DLS data of ssDNA$_{14}$-*b*-PHPMA$_X$ where a) x=300, b and d) x=400, and c and d) x= 500, which performed at monomer concentration a-c) 5%w/w and d-e) 10 %w/w.

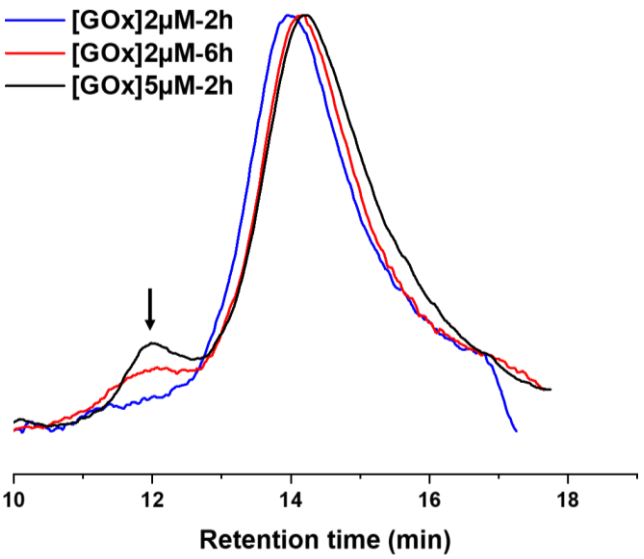

Figure 3.21. SEC RI traces of ssDNA$_{14}$-*b*-PHPMA$_{500}$ perform under different [GOx]s and reaction times at 5%w/w [HPMA] as measured by DMF SEC using PMMA calibration standard with RI detector.

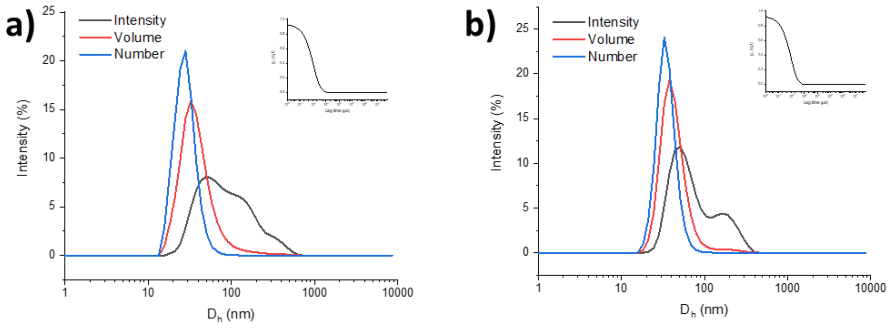

Figure 3.22. DLS data of ssDNA$_{14}$-*b*-PHPMA$_{500}$ synthesized from a) [GOx]=2 µM at 6 h reaction time and b) [GOx]=2 µM at 6 h reaction time at 5%w/w [HPMA]

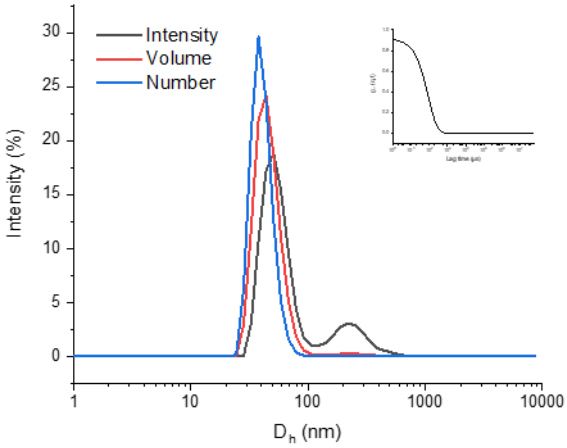

Figure 3.23. DLS data of ssDNA$_{14}$-*b*-PHPMA$_{500}$ in 10 mM NaCl solution.

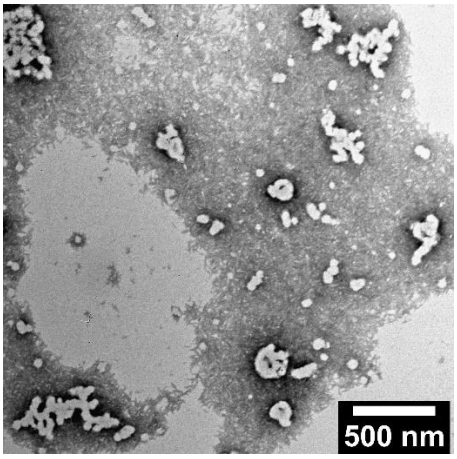

Figure 3.24. TEM images of ssDNA$_{14}$-*b*-PHPMA$_{500}$ particles in 1×TAE buffer solution.

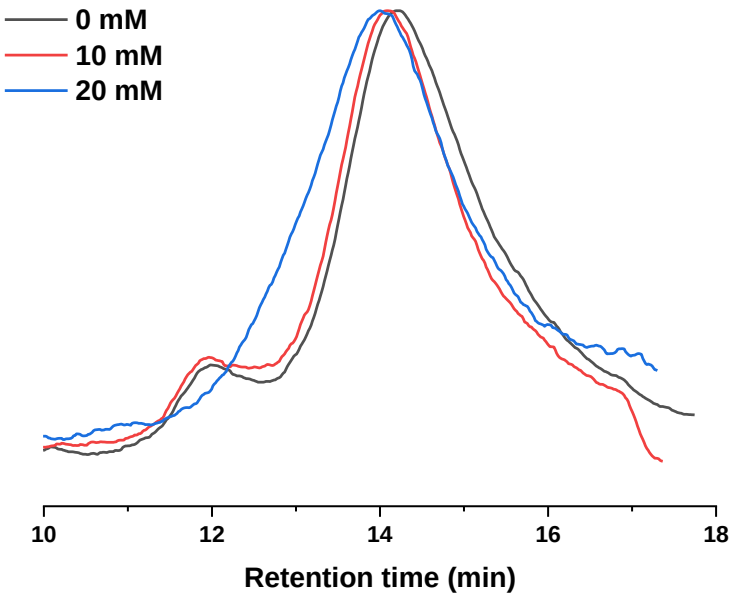

Figure 3.25. SEC RI traces of ssDNA$_{14}$-*b*-PHPMA$_{500}$ under different NaCl concentrations at 5%w/w [HPMA] as measured by DMF SEC using PMMA calibration standard with RI detector.

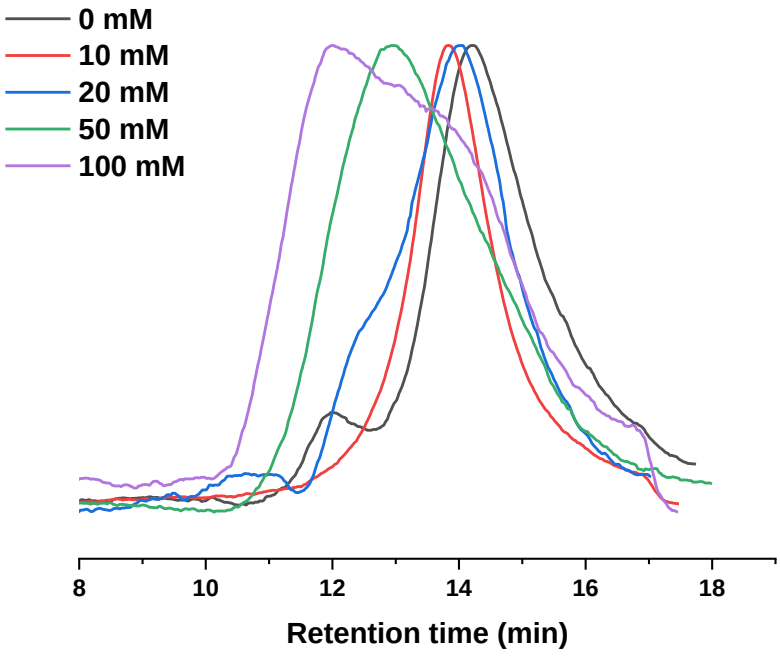

Figure 3.26. SEC RI traces of ssDNA$_{14}$-*b*-PHPMA$_{500}$ under different $MgCl_2$ concentrations at 5%w/w [HPMA] as measured by DMF SEC using PMMA calibration standard with RI detector.

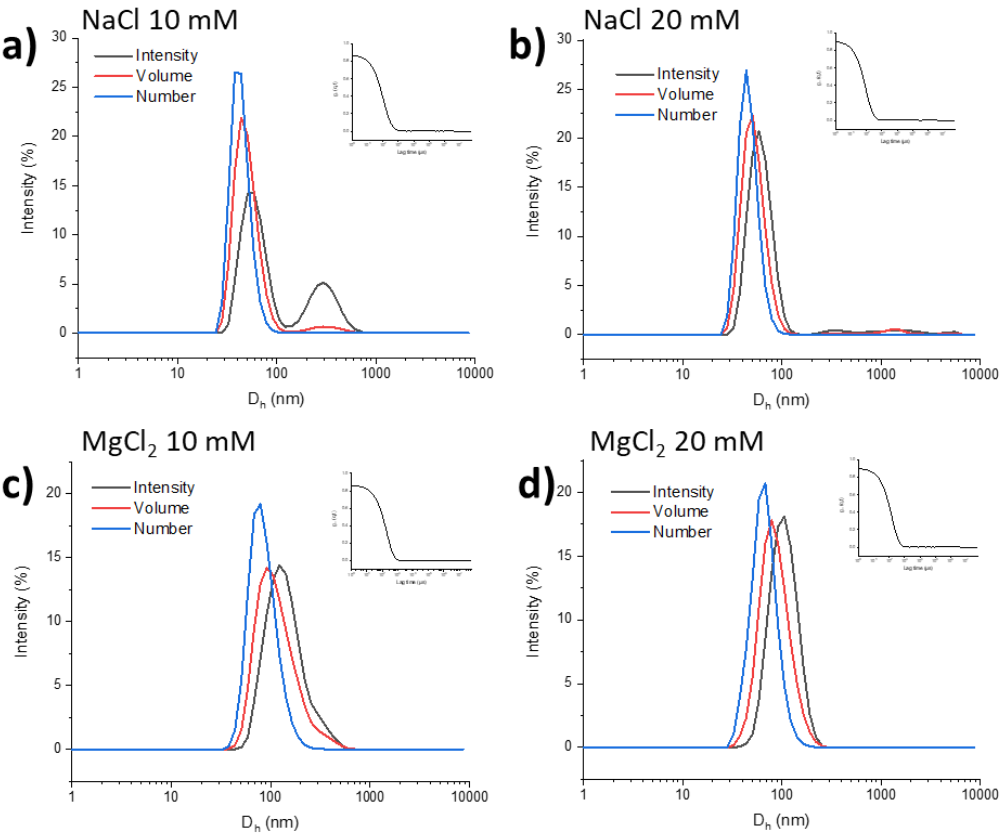

Figure 3.27. DLS data of ssDNA$_{14}$-*b*-PHPMA$_{500}$ synthesized in salt solution a and b) NaCl, and c and d) $MgCl_2$ performed at monomer concentration 5%w/w.

3.5. References

1. Whitfield, C. J.; Zhang, M.; Winterwerber, P.; Wu, Y.; Ng, D. Y. W.; Weil, T., Functional DNA-Polymer Conjugates. *Chem Rev* **2021,** *121* (18), 11030-11084.

2. Iqbal, P.; Preece, J. A.; Mendes, P. M., Nanotechnology: The "Top-Down" and "Bottom-Up" Approaches. In *Supramolecular Chemistry*, 2012.

3. Mai, Y.; Eisenberg, A., Self-assembly of block copolymers. *Chemical Society Reviews* **2012,** *41* (18), 5969-5985.

4. Tian, X.; Ding, J.; Zhang, B.; Qiu, F.; Zhuang, X.; Chen, Y., Recent Advances in RAFT Polymerization: Novel Initiation Mechanisms and Optoelectronic Applications. *Polymers (Basel)* **2018,** *10* (3).

5. Kleiner, R. E.; Brudno, Y.; Birnbaum, M. E.; Liu, D. R., DNA-templated polymerization of side-chain-functionalized peptide nucleic acid aldehydes. *J Am Chem Soc* **2008,** *130* (14), 4646-59.

6. Edwardson, T. G. W.; Carneiro, K. M. M.; Serpell, C. J.; Sleiman, H. F., An Efficient and Modular Route to Sequence-Defined Polymers Appended to DNA. *Angewandte Chemie International Edition* **2014,** *53* (18), 4567-4571.

7. Chidchob, P.; Edwardson, T. G. W.; Serpell, C. J.; Sleiman, H. F., Synergy of Two Assembly Languages in DNA Nanostructures: Self-Assembly of Sequence-Defined Polymers on DNA Cages. *Journal of the American Chemical Society* **2016,** *138* (13), 4416-4425.

8. Milnes, P. J.; McKee, M. L.; Bath, J.; Song, L.; Stulz, E.; Turberfield, A. J.; O'Reilly, R. K., Sequence-specific synthesis of macromolecules using DNA-templated chemistry. *Chem Commun (Camb)* **2012,** *48* (45), 5614-6.

9. Jeong, J. H.; Park, T. G., Novel Polymer−DNA Hybrid Polymeric Micelles Composed of Hydrophobic Poly(d,l-lactic-co-glycolic Acid) and Hydrophilic Oligonucleotides. *Bioconjugate Chemistry* **2001,** *12* (6), 917-923.

10. Jeong, J. H.; Kim, S. W.; Park, T. G., Novel Intracellular Delivery System of Antisense Oligonucleotide by Self-Assembled Hybrid Micelles Composed of DNA/PEG Conjugate and Cationic Fusogenic Peptide. *Bioconjugate Chemistry* **2003,** *14* (2), 473-479.

11. Ding, K.; Alemdaroglu, F. E.; Börsch, M.; Berger, R.; Herrmann, A., Engineering the Structural Properties of DNA Block Copolymer Micelles by Molecular Recognition. *Angewandte Chemie International Edition* **2007,** *46* (7), 1172-1175.

12. Kwak, M.; Herrmann, A., Nucleic acid/organic polymer hybrid materials: synthesis, superstructures, and applications. *Angew Chem Int Ed Engl* **2010,** *49* (46), 8574-8587.

13. Zimmermann, J.; Kwak, M.; Musser, A. J.; Herrmann, A., Amphiphilic DNA block copolymers: nucleic acid-polymer hybrid materials for diagnostics and biomedicine. *Methods in Molecular Biology* **2011,** *751*, 239-266.

14. Luckerath, T.; Koynov, K.; Loescher, S.; Whitfield, C. J.; Nuhn, L.; Walther, A.; Barner-Kowollik, C.; Ng, D. Y. W.; Weil, T., DNA-Polymer Nanostructures by RAFT Polymerization and Polymerization-Induced Self-Assembly. *Angew Chem Int Ed Engl* **2020**.

15. Messina, M. S.; Messina, K. M. M.; Bhattacharya, A.; Montgomery, H. R.; Maynard, H. D., Preparation of biomolecule-polymer conjugates by grafting-from using ATRP, RAFT, or ROMP. *Progress in Polymer Science* **2020,** *100*.

16. Yang, L.; Liang, M.; Cui, C.; Li, X.; Li, L.; Pan, X.; Yazd, H. S.; Hong, M.; Lu, J.; Cao, Y. C.; Tan, W., Enhancing the Nucleolytic Resistance and Bioactivity of

Functional Nucleic Acids by Diverse Nanostructures through in Situ Polymerization-Induced Self-assembly. *Chembiochem* **2021,** *22* (4), 754-759.

17. D'Agosto, F.; Rieger, J.; Lansalot, M., RAFT-Mediated Polymerization-Induced Self-Assembly. *Angew Chem Int Ed Engl* **2020,** *59* (22), 8368-8392.

18. Mcnally, R. G., Optimising Conditions for Low-Volume RAFT-mediated PISA. *University of Birmingham* **2019**.

19. Boyer, C.; Bulmus, V.; Davis, T. P.; Ladmiral, V.; Liu, J.; Perrier, S., Bioapplications of RAFT Polymerization. *Chemical Reviews* **2009,** *109* (11), 5402-5436.

20. McMinn, R. A. H. B. A. P. H., Determination of Free-Radical Propagation Rate Coefficients for Alkyl Methacrylates by Pulsed-Laser Polymerization. *Macromolecules* **1997,** *30*, 3490-3493.

21. Chapman, R.; Gormley, A. J.; Stenzel, M. H.; Stevens, M. M., Combinatorial Low-Volume Synthesis of Well-Defined Polymers by Enzyme Degassing. *Angew Chem Int Ed Engl* **2016,** *55* (14), 4500-2503.

22. Tan, J.; Liu, D.; Bai, Y.; Huang, C.; Li, X.; He, J.; Xu, Q.; Zhang, L., Enzyme-Assisted Photoinitiated Polymerization-Induced Self-Assembly: An Oxygen-Tolerant Method for Preparing Block Copolymer Nano-Objects in Open Vessels and Multiwell Plates. *Macromolecules* **2017,** *50* (15), 5798-5806.

23. Ng, G.; Prescott, S. W.; Postma, A.; Moad, G.; Hawker, C. J.; Boyer, C., Strategies for Achieving Oxygen Tolerance in Reversible Addition–Fragmentation Chain Transfer Polymerization. *Macromolecular Chemistry and Physics* **2023**.

24. Sugihara, S.; Blanazs, A.; Armes, S. P.; Ryan, A. J.; Lewis, A. L., Aqueous dispersion polymerization: a new paradigm for in situ block copolymer self-assembly in concentrated solution. *J Am Chem Soc* **2011,** *133* (39), 15707-13.

25. Charleux, B.; Delaittre, G.; Rieger, J.; D'Agosto, F., Polymerization-Induced Self-Assembly: From Soluble Macromolecules to Block Copolymer Nano-Objects in One Step. *Macromolecules* **2012,** *45* (17), 6753-6765.

26. Ratcliffe, L. P. D.; Ryan, A. J.; Armes, S. P., From a Water-Immiscible Monomer to Block Copolymer Nano-Objects via a One-Pot RAFT Aqueous Dispersion Polymerization Formulation. *Macromolecules* **2013,** *46* (3), 769-777.

27. Rosselgong, J.; Armes, S. P.; Barton, W.; Price, D., Synthesis of Highly Branched Methacrylic Copolymers: Observation of Near-Ideal Behavior using RAFT Polymerization. *Macromolecules* **2009,** *42* (16), 5919-5924.

28. Rosselgong, J.; Armes, S. P.; Barton, W. R. S.; Price, D., Synthesis of Branched Methacrylic Copolymers: Comparison between RAFT and ATRP and Effect of Varying the Monomer Concentration. *Macromolecules* **2010,** *43* (5), 2145-2156.

29. Rosselgong, J.; Armes, S. P., Quantification of Intramolecular Cyclization in Branched Copolymers by 1H NMR Spectroscopy. *Macromolecules* **2012,** *45* (6), 2731-2737.

30. Genix, A. C.; Oberdisse, J., Nanoparticle self-assembly: from interactions in suspension to polymer nanocomposites. *Soft Matter* **2018,** *14* (25), 5161-5179.

31. Camassa, R.; Harris, D. M.; Hunt, R.; Kilic, Z.; McLaughlin, R. M., A first-principle mechanism for particulate aggregation and self-assembly in stratified fluids. *Nat Commun* **2019,** *10* (1), 5804.

32. Boles, M. A.; Engel, M.; Talapin, D. V., Self-Assembly of Colloidal Nanocrystals: From Intricate Structures to Functional Materials. *Chem Rev* **2016,** *116* (18), 11220-89.

33. Arndt, C.; Koristka, S.; Bartsch, H.; Bachmann, M., Native Polyacrylamide Gels. Humana Press: 2012; pp 49-53.

34. Tuma, R. S.; Beaudet, M. P.; Jin, X.; Jones, L. J.; Cheung, C.-Y.; Yue, S.; Singer, V. L., Characterization of SYBR Gold Nucleic Acid Gel Stain: A Dye Optimized for Use with 300-nm Ultraviolet Transilluminators. *Analytical Biochemistry* **1999,** *268* (2), 278-288.

35. Williams, L. R., Staining nucleic acids and proteins in electrophoresis gels. *Biotechnic & Histochemistry* **2009,** *76* (3), 127-132.

36. Leal, C.; Moniri, E.; Pegado, L.; Wennerström, H., Electrostatic Attraction between DNA and a Cationic Surfactant Aggregate. The Screening Effect of Salt. *The Journal of Physical Chemistry B* **2007,** *111* (21), 5999-6005.

37. Gebe, J. A.; Delrow, J. J.; Heath, P. J.; Fujimoto, B. S.; Stewart, D. W.; Schurr, J. M., Effects of Na+and Mg2+on the Structures of Supercoiled DNAs: Comparison of Simulations with Experiments. *Journal of Molecular Biology* **1996,** *262* (2), 105-128.

38. Tan, Z. J.; Chen, S. J., Nucleic acid helix stability: effects of salt concentration, cation valence and size, and chain length. *Biophys J* **2006,** *90* (4), 1175-90.

39. Hu, Y.; Chen, Z.; Hou, Z.; Li, M.; Ma, B.; Luo, X.; Xue, X., Influence of Magnesium Ions on the Preparation and Storage of DNA Tetrahedrons in Micromolar Ranges. *Molecules* **2019,** *24* (11).

40. Mirzabekov, A. D., DNA sequencing by hybridization — a megasequencing method and a diagnostic tool? *Trends in Biotechnology* **1994,** *12* (1), 27-32.

41. Ami, T.; Fujimoto, K., Fluorescence labeling of DNA based on photochemical ligation. *Science and Technology of Advanced Materials* **2006,** *7* (3), 249-254.

42. Nuovo, G. J., PCR In Situ Hybridization. Humana Press: pp 223-242.

43. Mehta, A.; Maggioncalda, J.; Bagasra, O.; Thikkavarapu, S.; Saikumari, P.; Valyi-Nagy, T.; Fraser, N. W.; Block, T. M., In situ DNA PCR and RNA hybridization

detection of herpes simplex virus sequences in trigeminal gangliaof latently infected mice. *Virology* **1995,** *206* (1), 633-640.

44. Fiegler, H.; Carr, P.; Douglas, E. J.; Burford, D. C.; Hunt, S.; Smith, J.; Vetrie, D.; Gorman, P.; Tomlinson, I. P. M.; Carter, N. P., DNA microarrays for comparative genomic hybridization based on DOP-PCR amplification of BAC and PAC clones. *Genes, Chromosomes and Cancer* **2003,** *36* (4), 361-374.

45. Bloomfield, V. A.; Crothers, D. M.; Tinoco, I., *Nucleic acids : structures, properties, and functions*. University Science Books: 2000.

46. Pörschke, D.; Eigen, M., Co-operative non-enzymatic base recognition III. Kinetics of the helix—coil transition of the oligoribouridylic · oligoriboadenylic acid system and of oligoriboadenylic acid alone at acidic pH. *Journal of Molecular Biology* **1971,** *62* (2), 361-381.

47. Pörschke, D.; Uhlenbeck, O. C.; Martin, F. H., Thermodynamics and kinetics of the helix-coil transition of oligomers containing GC base pairs. *Biopolymers* **1973,** *12* (6), 1313-1335.

48. Grunwell, J. R.; Glass, J. L.; Lacoste, T. D.; Deniz, A. A.; Chemla, D. S.; Schultz, P. G., Monitoring the Conformational Fluctuations of DNA Hairpins Using Single-Pair Fluorescence Resonance Energy Transfer. *Journal of the American Chemical Society* **2001,** *123* (18), 4295-4303.

49. Jung, J.; Van Orden, A., A Three-State Mechanism for DNA Hairpin Folding Characterized by Multiparameter Fluorescence Fluctuation Spectroscopy. *Journal of the American Chemical Society* **2006,** *128* (4), 1240-1249.

50. Inoué, S., Foundations of Confocal Scanned Imaging in Light Microscopy. In *Handbook Of Biological Confocal Microscopy*, Pawley, J. B., Ed. Springer US: Boston, MA, 2006; pp 1-19.

51. Tsien, R. Y.; Ernst, L.; Waggoner, A., Fluorophores for Confocal Microscopy: Photophysics and Photochemistry. In *Handbook Of Biological Confocal Microscopy*, Pawley, J. B., Ed. Springer US: Boston, MA, 2006; pp 338-352.

52. Hell, S. W.; Dyba, M.; Jakobs, S., Concepts for nanoscale resolution in fluorescence microscopy. *Current Opinion in Neurobiology* **2004,** *14* (5), 599-609.

53. Klocker, N.; Weissenboeck, F. P.; Rentmeister, A., Covalent labeling of nucleic acids. *Chem Soc Rev* **2020,** *49* (23), 8749-8773.

54. Liyanage, V. R.; Jarmasz, J. S.; Murugeshan, N.; Del Bigio, M. R.; Rastegar, M.; Davie, J. R., DNA modifications: function and applications in normal and disease States. *Biology (Basel)* **2014,** *3* (4), 670-723.

55. Dong, Y.; Yao, C.; Zhu, Y.; Yang, L.; Luo, D.; Yang, D., DNA Functional Materials Assembled from Branched DNA: Design, Synthesis, and Applications. *Chemical Reviews* **2020,** *120* (17), 9420-9481.

56. Hashimoto, H.; Vertino, P. M.; Cheng, X., Molecular coupling of DNA methylation and histone methylation. *Epigenomics* **2010,** *2* (5), 657-669.

57. Fantoni, N. Z.; El-Sagheer, A. H.; Brown, T., A Hitchhiker's Guide to Click-Chemistry with Nucleic Acids. *Chem Rev* **2021,** *121* (12), 7122-7154.

58. Gramlich, P. M.; Wirges, C. T.; Manetto, A.; Carell, T., Postsynthetic DNA modification through the copper-catalyzed azide-alkyne cycloaddition reaction. *Angew Chem Int Ed Engl* **2008,** *47* (44), 8350-8.

59. Forget, D.; Domecq, C.; Coulombe, B., Use of site-specific protein-DNA photocrosslinking of purified complexes to analyze the topology of the RNA polymerase II transcription initiation complex. *Methods Mol Biol* **2009,** *543*, 439-51.

60. Pukhrambam, C.; Vvedenskaya, I. O.; Nickels, B. E., XACT-seq: A photocrosslinking-based technique for detection of the RNA polymerase active-center position relative to DNA in Escherichia coli. *STAR Protocols* **2021,** *2* (4), 100858.

61. Sakamoto, T.; Shigeno, A.; Ohtaki, Y.; Fujimoto, K., Photo-regulation of constitutive gene expression in living cells by using ultrafast photo-cross-linking oligonucleotides. *Biomater Sci* **2014,** *2* (9), 1154-1157.

62. Fujimoto, K.; Yamada, A.; Yoshimura, Y.; Tsukaguchi, T.; Sakamoto, T., Details of the ultrafast DNA photo-cross-linking reaction of 3-cyanovinylcarbazole nucleoside: cis-trans isomeric effect and the application for SNP-based genotyping. *J Am Chem Soc* **2013,** *135* (43), 16161-7.

63. Ferraz, R. A. C.; Lopes, A. L. G.; da Silva, J. A. F.; Moreira, D. F. V.; Ferreira, M. J. N.; de Almeida Coimbra, S. V., DNA-protein interaction studies: a historical and comparative analysis. *Plant Methods* **2021,** *17* (1), 82.

64. Rajendran, A.; Endo, M.; Katsuda, Y.; Hidaka, K.; Sugiyama, H., Photo-cross-linking-assisted thermal stability of DNA origami structures and its application for higher-temperature self-assembly. *J Am Chem Soc* **2011,** *133* (37), 14488-91.

65. Halpin, D. R.; Lee, J. A.; Wrenn, S. J.; Harbury, P. B., DNA display III. Solid-phase organic synthesis on unprotected DNA. *PLoS Biol* **2004,** *2* (7), E175.

66. Chaimueangchuen, S.; Frommer, J.; Ferguson, C. T. J.; O'Reilly, R. K., Surface Hybridization Chain Reaction of Binary Mixture DNA-PEG Corona Nanostructures Produced by Low-Volume RAFT-Mediated Photopolymerization-Induced Self-Assembly. *Bioconjug Chem* **2023**.

67. Paciaroni, N. G.; Ndungu, J. M.; Kodadek, T., Solid-phase synthesis of DNA-encoded libraries via an "aldehyde explosion" strategy. *Chem Commun (Camb)* **2020,** *56* (34), 4656-4659.

68. Katayama, S.; Hirai, K., Liquid-Phase Synthesis of Oligonucleotides. In *Synthesis of Therapeutic Oligonucleotides*, Obika, S.; Sekine, M., Eds. Springer Singapore: Singapore, 2018; pp 83-95.

69. Creusen, G.; Akintayo, C. O.; Schumann, K.; Walther, A., Scalable One-Pot-Liquid-Phase Oligonucleotide Synthesis for Model Network Hydrogels. *Journal of the American Chemical Society* **2020,** *142* (39), 16610-16621.

70. Brzezinska, J.; Trzciński, S.; Strzelec, J.; Chmielewski, M. K., From CPG to hybrid support: Review on the approaches in nucleic acids synthesis in various media. *Bioorganic Chemistry* **2023,** *140*, 106806.

71. Baddam, V.; Välinen, L.; Tenhu, H., Thermoresponsive Polycation-Stabilized Nanoparticles through PISA. Control of Particle Morphology with a Salt. *Macromolecules* **2021,** *54* (9), 4288-4299.

72. Ning, Y.; Fielding, L. A.; Ratcliffe, L. P.; Wang, Y. W.; Meldrum, F. C.; Armes, S. P., Occlusion of Sulfate-Based Diblock Copolymer Nanoparticles within Calcite: Effect of Varying the Surface Density of Anionic Stabilizer Chains. *J Am Chem Soc* **2016,** *138* (36), 11734-42.

73. North, S. M.; Armes, S. P., Aqueous solution behavior of stimulus-responsive poly(methacrylic acid)-poly(2-hydroxypropyl methacrylate) diblock copolymer nanoparticles. *Polymer Chemistry* **2020,** *11* (12), 2147-2156.

74. Baddam, V.; Välinen, L.; Kuckling, L.; Tenhu, H., Morphological transitions of cationic PISA particles by salt, triflate ions and temperature; comparison of three polycations. *Polymer Chemistry* **2022,** *13* (25), 3790-3799.

4 : Surface hybridization chain reaction of binary mixture DNA-PEG corona nanostructures produced by low-volume RAFT-mediated photoinitiated polymerization-induced self-assembly.

4.1. Introduction

As outlined in the introduction, DNA-polymer hybrids are adaptable functional materials with numerous applications ranging from nanotechnology to biomedicine.[1] So far, most synthetic routes have resulted in low yields, mainly due to the general difficulty of coupling macromolecules and the challenge of finding conditions compatible with both the DNA and polymer segments. The direct extension of DNA strands with polymers has recently been reported using reversible addition-fragmentation chain-transfer mediated polymerization-induced self-assembly (RAFT mediated PISA) to overcome these limitations.[2] PISA allows the direct construction of polymeric nanoparticles of various morphologies, normally spheres, vesicles, or worms.[1-4] Yang *et al.* showed that DNA-poly(2-hydroxypropyl methacrylate) (DNA-PHPMA) worms and vesicles had enhanced nuclease resistance and increased cellular uptake.[4] Previous Chapter, the direct extension of DNA strands with polymers has been reported using RAFT-mediated PISA allowing the direct construction of polymeric nanoparticles of two morphologies, which are spherical micelles and worms. The study observed that the pure corona DNA on DNA-polymer particles exhibited instability in the presence of salts and buffer solutions, resulting in a hindered ability to study the hybridization of the DNA-polymer particles.

Most natural DNA forms a double helix structure with its complementary DNA (cDNA) through hybridization, which is used *in vivo* for storing and transmitting genetic information. Due to the high sequence-specificity of DNA hybridization, it is possible to construct even large and complicated DNA structures, making precise DNA sequence design the key to unlocking structure- and/or sequence-driven DNA-based materials in nanoscience. The advantage of an increased cellular uptake and nuclease resistance make DNA-polymer hybrids the perfect candidate for the development of a new class of a

responsive bio-compatible material. However, not much is known about the ability to build DNA structures *in situ* after DNA-polymer assembly and how DNA hybridization impacts the size and/or morphology of the DNA-polymer particles.

Over the past decade, signal amplification using nucleic acids has become an attractive tool in biotechnology. Among DNA signal amplification techniques, hybridization chain reaction (HCR) is a simple yet powerful molecular tool with various applications in biosensing, bioimaging, bioanalysis and biomedical research.[5] The concept behind HCR is a multi-hybridization event between two species of DNA hairpins which are initiated by an initiator ssDNA, yielding into a nicked DNA duplex with repeating units x. In the past, HCR products were obtained with variety of functional moieties such as fluorophores,[6] gold nanoparticles (NPs),[7] and electrochemical reagents[8] to achieve biosensing, signal transduction, or transforming input molecules. As we know, corona modification of nanoparticles influences the surface characteristics and properties of the nano-objects. To the best of our knowledge, HCR on DNA-polymer nano-objects has not been investigated before and represents an important step towards responsive DNA-polymer hybrids. Hence, here we aim to apply HCR to DNA-particles to prove the possibility to build larger DNA constructs on top of a short starting sequence covalently bound to the particle as a response to the availability of the initiator DNA to produce a fluorescence read-out and signal amplification. We believe this represents not only key knowledge to achieve interactive DNA particles to act as biosensor, but moreover we show that DNA-polymers can be used as foundation for larger DNA constructs without disturbing particle morphology.

Interestingly, the DNA-*b*-PHPMA particles obtained in chapter 3 formed only spherical micelles, which were proved to be unstable in salts/buffer solutions leading to unstable to

hybridize with cDNA due to the repulsive force of the negative charge from DNA on particle surface. Even when attempting to add salt during performing PISA, the resulting pure DNA block copolymer was also found to be unstable. To address this limitation, we propose the idea of reducing the repulsive charge on the particle surface through the addition of a non-ionic block copolymer. Trithiocarbonate-based poly(ethylene glycol) (PEG_{113}) macroCTA was chosen as a non-ionic macroCTA due to its biocompatible properties being extensively studied *in vivo* to protect DNA from degradation, and its similar molecular weight to $ssDNA_{14}$-macroCTA.[9]

In this chapter, the combination of trithiocarbonate-based $ssDNA_{14}$-macroCTA and PEG-macroCTA was firstly reported for the novel fabrication of binary mixtures of DNA_{14}-*b*-$PHPMA_{400}$ and PEG_{113}-*b*-$PHPMA_{400}$ corona nanomaterials without addition of external photoinitiator or photocatalyst *via* low-volume RAFT-mediated photo-PISA under enzyme-assisted degassing approach. Systematic variation of the relative proportions of $ssDNA_{14}$ and PEG_{113}-macroCTAs resulted in the formation of diblock copolymer spheres, lumpy rod, or vesicles, where decreasing the ratio of DNA led to the formation of higher order morphologies and more stable particles in salt/buffer solutions. Moreover, the resulting particles were further hybridized with TAMRA-cDNA. In addition, HCR was firstly applied to hybrid nanoparticles to enhance DNAs amount on particle surface without disturbing particles morphology obtaining a fluorescence signal.

Bioconjugate Chemistry

pubs.acs.org/bc

Article

Surface Hybridization Chain Reaction of Binary Mixture DNA-PEG Corona Nanostructures Produced by Low-Volume RAFT-Mediated Photopolymerization-Induced Self-Assembly

Siriporn Chaimueangchuen, Jennifer Frommer, Calum T. J. Ferguson, and Rachel K. O'Reilly*

Cite This: *Bioconjugate Chem.* 2023, 34, 2007−2013

Read Online

ACCESS | Metrics & More | Article Recommendations | Supporting Information

ABSTRACT: DNA-polymer hybrids have been attracting interest as adaptable functional materials by combining the stability of polymers with DNA nanotechnology. Both research fields have in common the capacity to be precise, versatile, and tunable, a prerequisite for creating powerful tools which can be easily tailored and adapted for bio-related applications. However, the conjugation of hydrophilic DNA with hydrophobic polymers remains challenging. In recent years, polymerization-induced self-assembly (PISA) has attracted significant attention for constructing nano-objects of various morphologies owing to the one-step nature of the process, creating a beneficial method for the creation of amphiphilic DNA-polymer nanostructures. This process not only allows pure DNA-polymer-based systems to be produced but also enables the mixture of other polymeric species with DNA conjugates. Here, we present the first report of a DNA-PEG corona nano-object's synthesis without the addition of an external photoinitiator or photocatalyst via photo-PISA. Furthermore, this work shows the use of DNA-macroCTA, which was first synthesized using a solid-support method resulting in high yields, easy upscaling, and no need for HPLC purification. In addition, to the formation of DNA-polymer structures, increasing the nucleic acid loading of assemblies is of great importance. One of the most intriguing phenomena of DNA is the hybridization of single-stranded DNA with a second strand, increasing the nucleic acid content. However, hybridization of DNA in a particle corona may destabilize the nanomaterial due to the electrostatic repulsive force on the DNA corona. Here, we have investigated how changing the DNA volume fraction in hybrid DNA-polymer self-assembled material affects the morphology. Moreover, the effect of the corona composition on the stability of the system during the hybridization was studied. Additionally, the hybridization chain reaction was successfully applied as a new method to increase the amount of DNA on a DNA-based nano-object without disturbing the morphology achieving a fluorescence signal amplification.

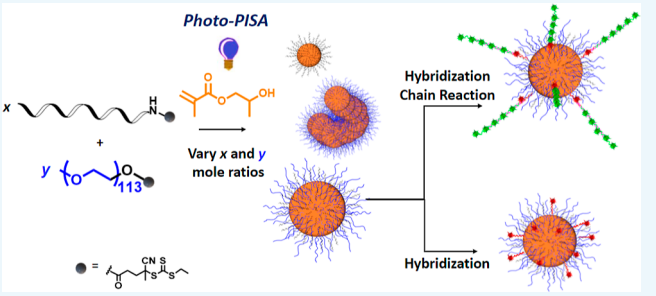

INTRODUCTION

DNA-polymer hybrids are adaptable functional materials with numerous applications ranging from nanotechnology to biomedicine.[1] Both solution phase and solid support synthesis approaches have been used to create DNA-polymer hybrids.[2−5] Unfortunately, so far, most synthetic routes have resulted in low yields, arising from the general difficulty of coupling macromolecules. Additionally, it is often challenging to find conditions compatible with both the DNA and polymer segments. Recently, to overcome these limitations the direct extension of DNA strands with polymers has been reported using reversible addition-fragmentation chain transfer-mediated polymerization-induced self-assembly (RAFT-mediated PISA) has been developed.[6] PISA allows the direct construction of polymeric nanoparticles (NP) of various morphologies, normally spheres, vesicles, or worms.[7] Control over particle composition, morphology, and functionality can be achieved by varying the monomer, macromolecular chain transfer agent (macroCTA), and concentration.[1] In 2020, Luckerath et al. suggested that DNA−polymer conjugates can self-assemble to nano-objects by thermal RAFT PISA through the grafting from approach.[6] This reaction was performed in a low volume system, relying on enzyme degassing using glucose, glucose oxidase, and sodium pyruvate to get rid of oxygen in the system which would hinder the polymerization. This resulted in high monomer conversions in a system where the monomer to initiator ratio could be precisely controlled, allowing the manipulation of architectures formed. Yang et al. modified a photochain transfer agent (photo-CTA) to perform the first aqueous RAFT photo-PISA of functional DNA-polymer nanostructures under an enzyme-assisted approach.[8]

Received: July 4, 2023
Revised: September 25, 2023
Published: October 16, 2023

https://doi.org/10.1021/acs.bioconjchem.3c00293
Bioconjugate Chem. 2023, 34, 2007−2013

Scheme 1. Concept for photoPISA from $ssDNA_{14}$ or PEG_{113}[a]

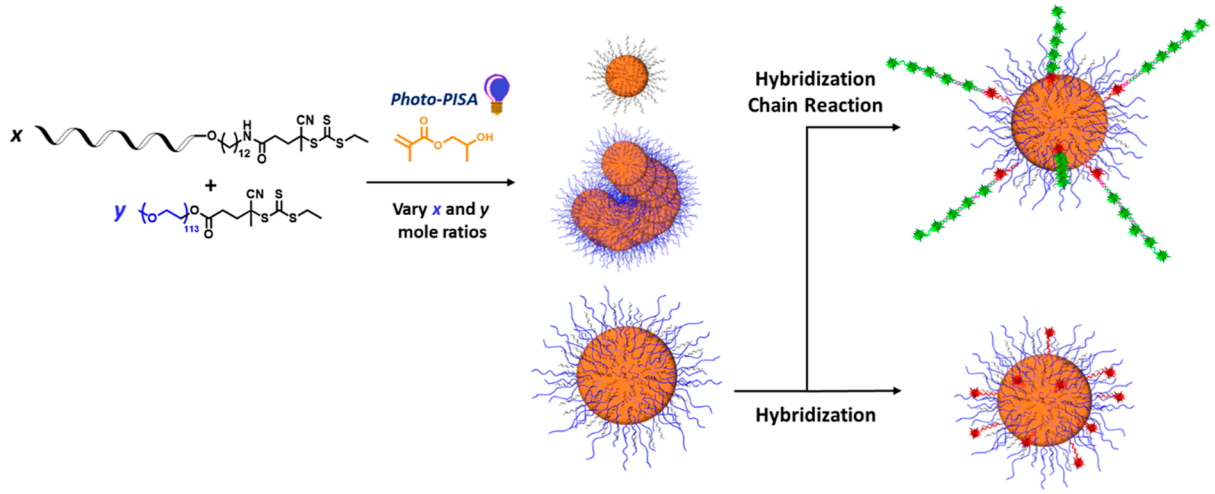

[a]CEPA-functionalized $ssDNA_{14}$ and CEPA-PEG_{113} served as the macroCTAs in RAFT-PISA polymerization for the generation of functional DNA-copolymer conjugates. DNA−polymer nanostructures of various shapes were obtained by altering mole ratio of DNA_{14}-macroCTA and PEG_{113}-macroCTA, establishing a new platform technology toward functional DNA−polymer nanostructures. Moreover, hybrid vesicles were used in hybridization and HCR.

2-hydroxypropyl methacrylate (HPMA) was used as a monomer to manipulate the DNA-polymer nanostructure. This work showed that DNA-poly(2-hydroxypropyl methacrylate) (DNA-PHPMA) particles had enhanced nuclease resistance and increased cellular uptake.

Most natural DNA forms a double helix structure through hybridization, which is used in vivo for storing and transmitting genetic information. Hybridization is promoted by the formation of hydrogen bonds between the nucleobases of single-stranded DNA (ssDNA) with its complementary DNA (cDNA). Due to the high sequence-specificity of DNA hybridization, it is possible to construct even large and complicated DNA structures. Thus, precise DNA sequence design is the key to unlocking structure and/or sequence driven DNA-based materials in nanoscience. The advantage of an increased cellular uptake and nuclease resistance make DNA-polymer hybrids the perfect candidate for the development of a new class of a responsive biocompatible material. However, not much is known about the ability to build DNA structures in situ after DNA-polymer assembly and how DNA hybridization impacts the size and/or morphology of the DNA-polymer particles. Over the past decade, signal amplification using nucleic acids has become an attractive tool in biotechnology. Among DNA signal amplification techniques, hybridization chain reaction (HCR) is a simple yet powerful molecular tool with various applications in biosensing, bioimaging, bioanalysis, and biomedical research.[9] The concept behind HCR is a multihybridization event between two species of DNA hairpins which are initiated by an initiator ssDNA, yielding a nicked DNA duplex with repeating units *x*. In the past, HCR products were obtained with a variety of functional moieties such as fluorophores,[10] gold NPs,[11] and electrochemical reagents[12] to achieve biosensing, signal transduction, or transforming input molecules. As we know, corona modification of NPs influences the surface characteristics and properties of the nano-objects. To the best of our knowledge, HCR on DNA-polymer nano-objects has not been investigated before and represents an important step toward responsive DNA-polymer hybrids. Hence, here we aim to apply HCR to DNA-particles to prove the possibility of building larger DNA constructs on top of a short starting sequence covalently bound to the particle. The presence of the initiator DNA to gives a fluorescence read-out and signal amplification. We believe this represents not only key knowledge to achieve interactive DNA particles to act as biosensor, but moreover we show that DNA-polymers can be used as foundation for larger DNA constructs without disturbing particle morphology.

In this work, we report the first synthesis of trithiocarbonate-based $ssDNA_{14}$-macroCTA by solid support synthesis, resulting in high yields, scalability, and high purity without the need for further high-performance liquid chromatography (HPLC) purification. This macroCTA has been combined with trithiocarbonate-based poly(ethylene glycol) (PEG) macroCTA for the novel fabrication of binary mixtures of PEG_{113}-$PHPMA_{400}$ and DNA_{14}-$PHPMA_{400}$ nanomaterials. No additionl external photoinitiator or photocatalyst was required and the synthesis was undertaken via low-volume RAFT-mediated photo-PISA using enzyme-assisted degassing. Systematic variation of the relative proportions of PEG_{113} and $ssDNA_{14}$ macroCTAs resulted in the formation of diblock copolymer spheres, lumpy rods, or vesicles, where increasing the ratio of PEG_{113} led to the formation of higher order morphologies and more stable particles in salt/buffer solutions. Moreover, the resulting particles were further hybridized with TAMRA-cDNA. In addition, HCR was first applied to hybrid NPs to enhance the amount of DNA on the particle surface without disturbing particle morphology obtaining a fluorescence signal (Scheme 1).

RESULTS AND DISCUSSION

In order to synthesize the DNA-loaded particles, a high yielding, easily scalable, and simple method for synthesizing DNA-macroCTA was needed. The $ssDNA_{14}$ macromolecular chain transfer agent ($ssDNA_{14}$-macroCTA) was formed by the conjugation of $ssDNA_{14}$-NH_2 (5′-5AmMC12-TGTAGCGTTGTTGC-3′) with a 4-cyano-4-(dodecylsulfanylthiocarbonyl) sulfanyl pentanoic acid group (CEPA) at its

https://doi.org/10.1021/acs.bioconjchem.3c00293
Bioconjugate Chem. 2023, 34, 2007−2013

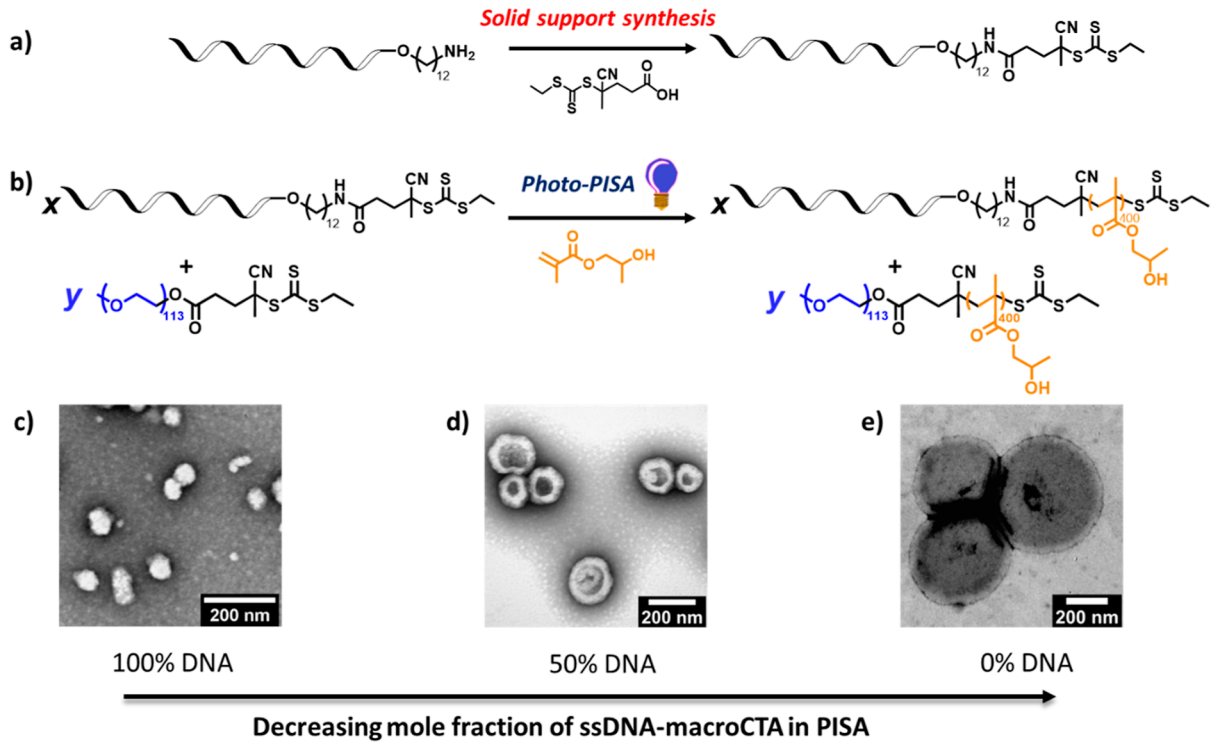

Figure 1. (a) Reaction scheme for the synthesis of ssDNA-macroCTAs via solid support synthesis, (b) reaction scheme for the low-volume photo-PISA for the synthesis of *x* DNA_{14}−$PHPMA_{400}$ and *y* PEG_{113}−$PHPMA_{400}$ diblock copolymer mixtures, and (c) schematic TEM images of mixed DNA and PEG based particles with different percentages of DNA in the corona.

5′ terminus via solution or solid support approaches (Figure 1a). By using a solid support, DNA is selectively bound to an inert solid support, i.e., diethylaminoethanol (DEAE) sepharose, followed by chemical reaction in pure *N*,*N*-dimethylformamide (DMF) and is finally eluted from the solid support without the need for further purification. The solid support-mediated synthesis is separated into four stages. During stage 1, $ssDNA_{14}$-NH_2 was bound to the solid support. In stage 2, the small molecule was added as activated ester to the adsorbed DNA in DMF. In stage 3, the excess small molecules including degraded side products were removed by washing with DMF, while the modified DNA remained adsorbed to the solid support. During the final stage the modified DNA was eluted using a water-based elution buffer.[13]

The purity of the $ssDNA_{14}$-macroCTA was confirmed by using HPLC equipped with a UV−vis detector monitoring the eluted DNA solution at 260 and 309 nm as the maximum absorbance of the DNA and trithiocarbonate group, respectively. High conversion and purity (95%) of the targeted $ssDNA_{14}$-macroCTA strand was achieved with the solid support approach, represented by the occurrence of one DNA-species signal at both detector wavelengths 260 and 309 nm (Figure S1). LC/MS furthermore confirmed the successful formation of the desired product. Meanwhile, the solution approach shows a second signal at 309 nm, indicating an impurity from the trithiocarbonate-group-containing starting material. Additional HPLC purification and extensive purification steps including spin filtration and ethanol precipitation were required to obtain a comparable purity. Such time-consuming purification steps are not feasible especially if high amounts of $ssDNA_{14}$-macroCTA are required (Figure S1). Our results show that the solid support-mediated synthesis of the desired macroCTA-modified DNA is not only superior in terms of yield and purity but is moreover easy to apply to large-scale DNA reactions (up to 100 nmol) without the need of further purification, while the solution method is limited to 2 nmol DNA in each reaction batch. Thus, we accomplished the synthesis of the $ssDNA_{14}$-macroCTA in a few hours with the large quantities, high yields, and purity, needed for further utilization in a DNA nano-object PISA reaction.

A series of PEG_{113}-$PHPMA_{400}$ and DNA_{14}-$PHPMA_{400}$ diblock copolymer NPs were synthesized by systematically varying the PEG_{113} and $ssDNA_{14}$ macroCTAs mole fractions via low-volume RAFT-mediated photo-PISA. These CTAs are photoiniferters, which can be cleaved by light at 405 nm to generate a thiocarbonylthio radical.[14−16] This radical subsequently serves the dual roles of initiating the polymerization of a monomer and acting as a RAFT agent, eliminating the requirement for additional initiators or catalysts. Thus, this is the first report of DNA-polymer nanostructures produced via low-volume PISA (50 μL) without adding an external photoinitiator or photocatalyst. PEG_{113}-macroCTA was chosen due to its biocompatible properties being extensively studied *in vivo* to protect DNA from degradation, and its similar molecular weight to $ssDNA_{14}$-macroCTA.[17] HPMA was chosen due to the literature precedent for forming a hydrophobic polymer block with hydrophilic polymer chain such as PEG.[18] Low-volume aqueous RAFT-mediated photo-PISA of HPMA was undertaken under 405 nm visible light irradiation at 37 °C using an enzyme degassing approach, i.e., glucose oxidase.[19,20] Mineral oil was added on top of the 50 μL solution to prevent diffusion of residual oxygen into the solution, which inhibits the polymerization.

Table S1 summarizes the targeted diblock copolymer compositions, HPMA monomer conversions, molecular weight

https://doi.org/10.1021/acs.bioconjchem.3c00293
Bioconjugate Chem. 2023, 34, 2007−2013

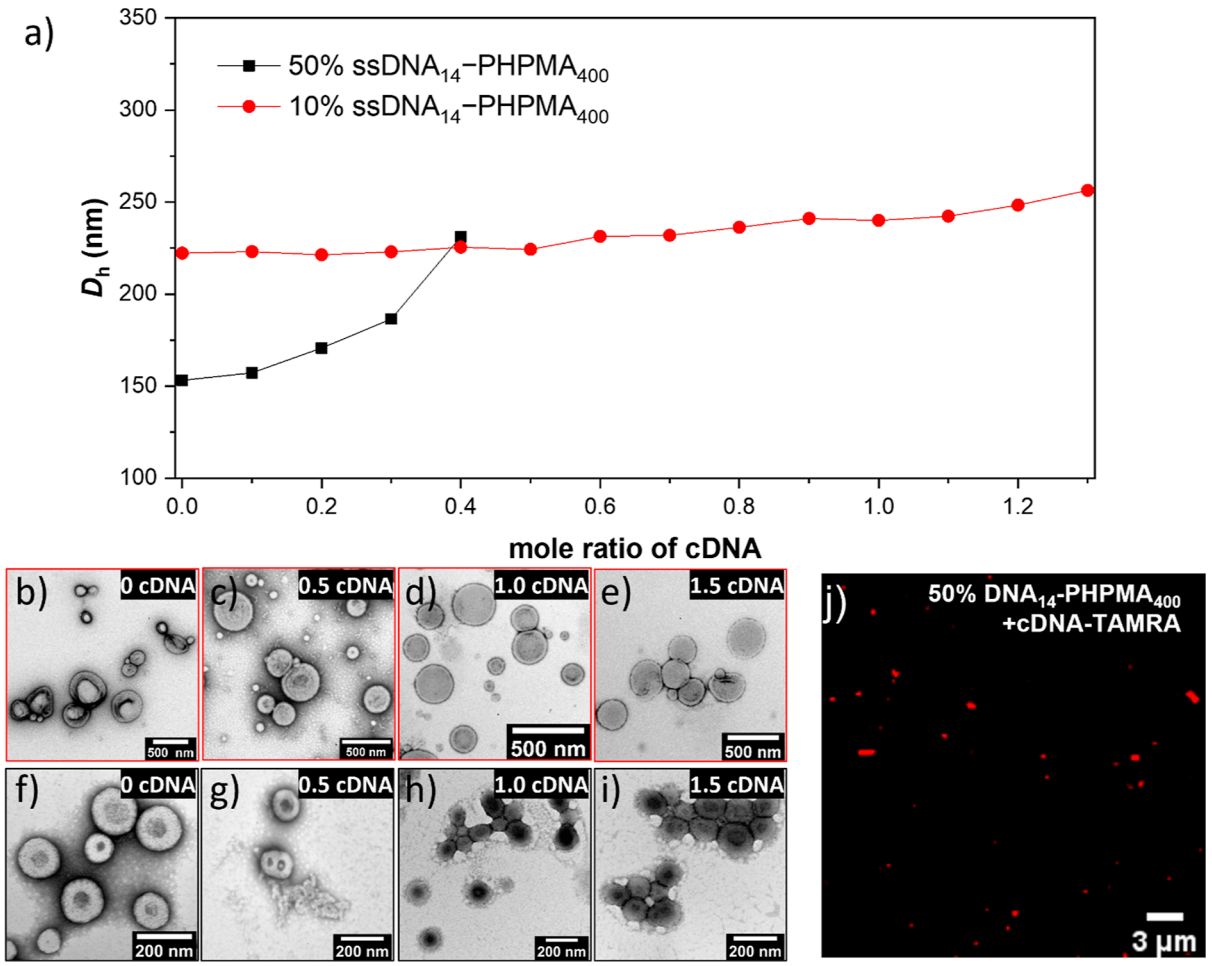

Figure 2. Hybridization study of DNA containing NPs. (a) Hydrodynamic radius of 50% (black) and 10% (red) DNA containing particles measured by DLS with the increase in quantity of additional DNA added. (b−e) TEM images of 10% DNA containing structures with the increase in additional DNA content. (f−i) TEM images of 50% DNA containing structures with the increase in additional DNA content. (j) Confocal images in the fluorescent field. Scale bar: 3 μm. Images are shown for 50% DNA corona NPs mixed with cDNA-functionalized TAMRA.

data, dynamic light scattering (DLS) data, and morphological assignments. High monomer conversions (>70%) were achieved after 2 h of reaction, as determined by ^{1}H NMR spectroscopy. It is important to note that the targeted degree of polymerization for PHPMA is 400. However, incomplete polymerization conversion might have an effect on the resulting morphology of the self-assembled nanostructure. PHPMA was successfully polymerized with a significant increase in molecular weight confirmed by size exclusion chromatography analysis (in DMF) (Figure S2). Zeta potentials have been applied to measure the surface electrical charge of particles. The zeta potential of 100% DNA-PHPMA$_{400}$ was found to be around −32.4 ± 9.7 mV revealing the presence of negative charge from DNA on the outer surface of particles, whereas pure PEG$_{113}$-PHPMA$_{400}$ exhibited a nearly neutral surface charge (−0.6 ± 3.1 mV). The 50% DNA-PHPMA$_{400}$ displayed a negative charge of approximately −28.6 ± 7.0 mV, which falls between the values of the 100% DNA and PEG$_{113}$-PHPMA$_{400}$ systems. This rationally indicated that the negative charge from DNA on the particle surface decreases when the fraction of DNA is reduced.

The morphology of the self-assembled nanostructures was determined by transmission electron microscopy (TEM) and cryogenic TEM (Cryo-TEM) images of each diblock composition was used to assign the copolymer morphology, as shown in Figures 1c−e and S3, respectively. When 100% ssDNA$_{14}$−PHPMA$_{400}$ diblock copolymer chains self-assembled only spherical particles formed (Figure 1c). This morphology is most likely due to the strong repulsive electrostatic forces of the DNA block on the corona, as also previously reported with anionic corona of block copolymers.[21] When 90% of the DNA based diblock copolymer was used, a mixture of spheres, lumpy rods, and vesicles was observed (Figure S4a). Interestingly, for all systems with 50% DNA copolymer or less DNA content, only vesicles were observed. This morphology transition was observed because increasing the mole fraction of the PEG$_{113}$-macroCTA reduces the electrostatic repulsion from DNA chains in the corona. Thus, as the proportion of the PEG$_{113}$-macroCTA is increased, the volume fraction of electrostatic chains in the coronal layer is gradually reduced, which means that the volume fraction of the hydrophobic PHPMA block required to access the lumpy rods or vesicles is correspondingly lower. DLS was used to measure the hydrodynamic diameter (D_h), where the 100% ssDNA$_{14}$−PHPMA$_{400}$ copolymer displayed a unimodal particle size distribution with D_h approximately 90 nm (Figure S5a), the 90% DNA system had a multimodal particles size distribution (Figure S5b). In the 50, 10, and 0% DNA systems, unimodal particle size distributions were observed with the D_h increasing from 150 to 460 nm as the DNA content decreased (Table S1 and

https://doi.org/10.1021/acs.bioconjchem.3c00293
Bioconjugate Chem. 2023, 34, 2007−2013

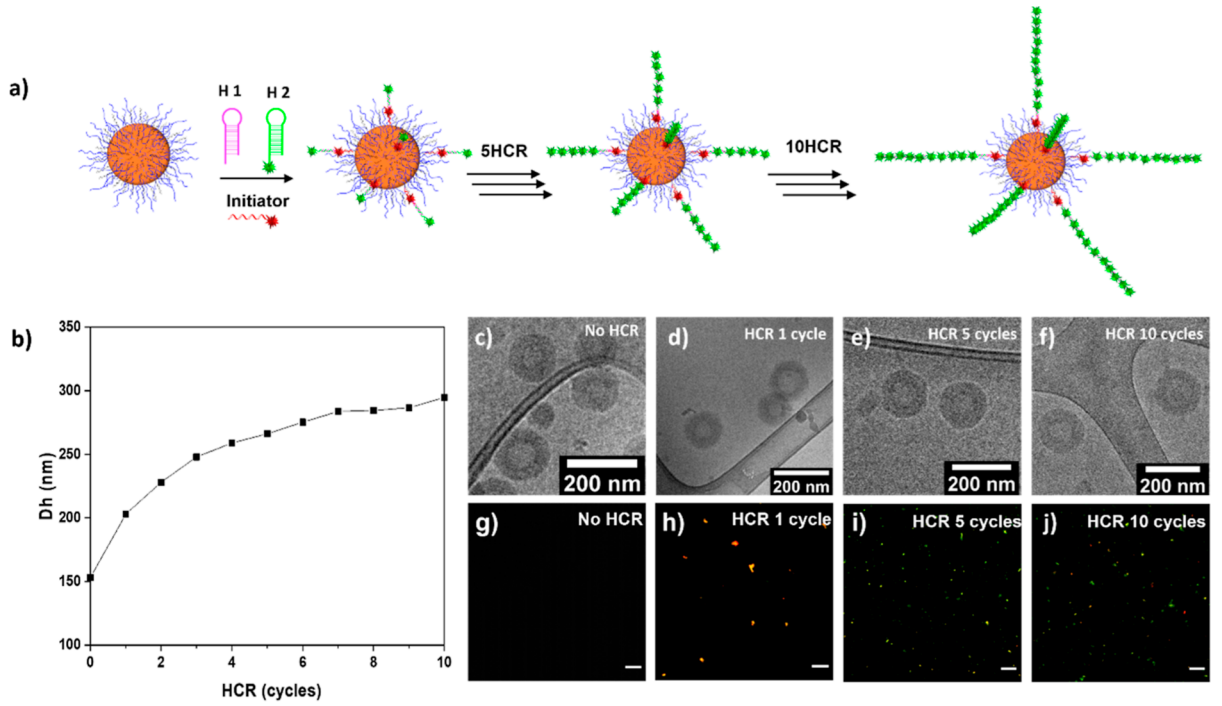

Figure 3. HCR study of 50% DNA corona NPs particles. (a) Schematic cartoon of HCR on particle. (b) Hydrodynamic radius of particles measured by DLS. (c–f) Cryo-TEM images. Scale bar: 200 nm. (g–j) Overlay of confocal images acquired using the 488 and 561 nm excitation channels. Scale bars: 5 μm. Images are shown for (c,g) 50% DNA corona NPs, (d,h) particles at the HCR 1 cycle, (e,i) particles at the HCR 5 cycle, and (f,j) particles at the HCR 10 cycle.

Figure S5c–e). This increase in hydrodynamic diameter is consistent with the formation of higher order polymeric morphologies, as the bilayer structure of the vesicles increases the size of the nanomaterial.

DNA hybridization technology allows for the postmodification of DNA due to its intrinsic functional property. In this work, DLS was used to primarily investigate the hybridization of ssDNA on different NPs. A salt/buffer solution is required to study hybridization in order to screen the effect of DNA. When 100 and 90% DNA corona composition systems were investigated, the DLS could not detect particles in salt/buffered solution due to aggregation as confirmed by TEM images. This may be due to the influence of magnesium ions (Mg^{2+}) from the salt solution on the self-assembly process (Figure S6).[22] As expected, when the mole fraction of DNA on particles decreased, the screening effect had less of an effect, and particles are more stable. Subsequently, the DNA functionality for hybridization of NPs with varying DNA content (50 and 10%) was probed by DLS using a complementary DNA strand (cDNA) (5′-GCA ACA ACG CTA CA-3). For NPs with 50% DNA, the size of particles gradually increased until a cDNA ratio = 0.4 at which point the quality of the DLS data deteriorated, indicating aggregation as also confirmed by TEM (Figure 2f–i). At the decreased volume fraction of DNA corona of 10%, the NPs were more stable when adding cDNA, until a 1.2 mol-ratio where aggregation was observed (Figure 2a). PEG chains are uncharged, and thus, positively charged salts in solution cannot interact with the PEG chains, lowering the cross-system interaction between the negatively charged DNA strands and positively charged salts which are very likely responsible for aggregation. Additionally, when the mole fraction of DNA in the corona is decreased, the DNA density on the particle surface is also decreased, while the PEG density is higher, leading to more flexible space on the particle's surface. Thus, the relative amount of cDNA that can hybridize with the DNA in the particle corona increases when a decreasing DNA mole fraction is used. This results in relatively more stable particles due to less charge repulsion and salt interactions.

To confirm that hybridization of cDNA was occurring on the surface of the NPs, confocal fluorescence microscopy was used; this method directly images the fluorescent cDNA-particles hybridized on the DNA-corona which means the turbidity or the effect from photobleaching of fluorophores is negated. The 50% DNA system was selected to study hybridization with fluorescent TAMRA-cDNA by confocal fluorescence microscopy, as it has a high DNA mole fraction but is still stable. A mixture of TAMRA-cDNA and DNA containing NPs were clearly observed as stable dots in the fluorescence images (Figure 2j). Conversely, a mixture of cDNA and ssDNA, as a control, resulted in fluorescent specks being observed, which can happen when dyed molecules aggregate (Figure S7a). For DNA containing NPs alone, particles had no observable fluorescence (Figure S7b). To confirm that cDNA was not entangled but hybridized on the surface of DNA-polymer particles, we mixed PEG_{113}-*b*-$PHPMA_{400}$ with TAMRA-cDNA. PEG_{113}-*b*-$PHPMA_{400}$ particle were not observed in the fluorescent field; therefore confirming that there is no interaction between PEG and cDNA (Figure S7c). Thus, confocal imaging confirmed the presence of DNA at the particle surface and its ability to hybridize with a complementary strand. This means DNA-polymer particles can simply be functionalized after the assembly process by adding fluorophore-labeled cDNA with a maximum 0.4:1 mol ratio of cDNA to the 50% DNA corona containing NPs. However, if greater loadings of nucleic acid are required for larger DNA constructs the system becomes destabilized and alternative strategies are required.

https://doi.org/10.1021/acs.bioconjchem.3c00293
Bioconjugate Chem. 2023, 34, 2007–2013

To quantify the amount of DNA that could be functionalized on each particle, static light scattering (SLS) was used to obtain aggregation numbers (N_{agg}) for the 50% DNA corona NPs. Here, for this mixed DNA and PEG based system, each particle consists of approximately 2700 chains (see Figure S8). Therefore, DNA constitutes about 1350 chains per particle. From the hybridization study, approximately 500 cDNA chains were able to hybridize with DNA on the surface of particle without negatively impacting the colloidal stability of the system. This means that less than half of the DNA chains on the surface of the particle can be hybridized before the system destabilizes.

To increase the amount of nucleic acid loading on the particle corona, we investigated using HCR to increase DNA content while also producing a fluorescence read-out signal, which is desired for the adaptation of DNA-polymers as biosensors. HCR is an interesting approach because of its enzyme-free nature, use of isothermal conditions, uncomplicated protocols, and exceptional amplification efficiency.[9] Furthermore, the initiator strand can be seen as a target sequence for future biosensor applications. Again we investigated using a 50% DNA corona NP as it is stable in salt/buffer conditions and shows vesicle nanostructure which could be investigated by confocal microscopy using fluorescently labeled DNA hybridization technology. HCR was carried out using the $ssDNA_{14}$ chain on the particle surface by hybridization with the 50mer initiator sequence (**I**) in step 1, followed by the addition of hairpin 1 (**H1**) and hairpin 2 (**H2**) representing 1 cycle of HCR (Figure 3a), whereas the DNA sequences are shown in Table S2. Initiator **I** was added with a ratio of 0.2 relative to the ssDNA covalently bound on the particle surface to ensure that all of **I** hybridized with the particle surface, and the particles do not form aggregates. It should be noted that the two hairpin species (**H1** and **H2**) can only hybridize in the presence of the initiator DNA (**I**) on the particle surface (Figure S8) noting that only the one addition of **I** is necessary. To increase the number of performed HCR cycles, **H1** and **H2** were added stepwise up to 10 cycles, forming linear duplex DNA chains on the particle surface. Successful hybridization on the toehold of the added hairpin triggers the unfolding or opening of the hairpin structure revealing the next available single stranded DNA for hybridization in a staggered pattern. HCR study was investigated by DLS, Cryo-TEM, and confocal fluorescence microscopy. DLS data show D_h increase significantly from approximately 150 to 300 nm (Figure 3b). Interestingly, Cryo-TEM images show that the particle size does not significantly change. The distinction between these outcomes arises from the fundamental disparity in how the two techniques quantify particle dimensions. Since the diameter of double-helix DNA is approximately 2 nm, Cryo-TEM primarily images the size of the phase-separated core material, while it is unable to visualize the solvated corona due to limitations in machine resolution. Consequently, the size of the particles remained constant when the HCR process was employed to extend the corona. In contrast, DLS determines the D_h of particles, measuring not only the particle core size but also any surface structure or solvated corona. Thus, D_h undergoes a significant change when the corona length is extended through the HCR process. Moreover, this evidence suggested that the stability of 50% $DNA\text{-}PHPMA_{400}$ NPs was maintained even when a substantial amount of DNA was added to their surface. To confirm successful multicycle HCR on the particle surface, TAMRA-labeled initiator (TAMRA-**I**) and FAM-labeled hairpin 2 (FAM-**H2**) were used and investigated by confocal fluorescent spectroscopy in merged fluorescent channel. As expected, the starting material particles did not show any fluorescence (Figure 3g). After the addition of TAMRA-**I** the particles show a red fluorescence from the TAMRA dye due to hybridization between TAMRA-**I** with the particles (Figure S9). Particle fluorescence changed to yellow when **H1** and FAM-**H2** were hybridized to particle-**I** after 1 HCR cycle caused by a combination of the fluorescence emission from TAMRA-**I** (λ_{em}: 580 nm) with the fluorescence emission from FAM-**H2** (λ_{em}: 517 nm) at an equal ratio (Figure 3h). When the number of HCR cycles increased, the particles exhibit higher fractions of green fluorescence due to increased ratios of FAM-**H2** (Figure 3i,j). The relative fluorescence intensity in the 488 nm excitation channel versus HCR cycles is reported in Figure S10; fluorescence values were calculated for each particle from the CLSM images in Figure 3g–j. The data showed an increase in fluorescence intensity as the HCR cycles increased, providing quantitative confirmation of the extension of DNA chains on the DNA-polymer NPs and a successful fluorescence signal amplification. Hence, this confirms that DNA-polymer particles were successfully functionalized on its surface by HCR for up to 10 cycles without aggregation and disturbing particle morphology. To predict the quantitative DNA chains on particle that are able to form HCR, SLS data were applied to investigate if ∼270 DNA strands per particle were able to form HCR.

CONCLUSIONS

In conclusion, we have introduced the first synthesis of trithiocarbonate-based $ssDNA_{14}$-macroCTA by solid support synthesis, resulting in high yields, easy upscaling, and purity without the need for further purification. With the use of low-volume RAFT-mediated photo-PISA under enzyme-assisted degassing conditions, this $ssDNA_{14}$-macroCTA has been combined with trithiocarbonate-based PEG_{113}-macroCTA to fabricate the first mixture of PEG and a DNA hybrid. Crucially, the particles were further applied with hybridization and HCR techniques with the simple addition of complementary DNA strands. This provides a convenient route for the synthesis of ssDNA-macroCTA, performing simple PISA in the construction of complex DNA–PEG polymer architectures, and straightforward applications with hybridization for bioimaging. HCR was first applied with DNA–PEG polymer architectures as a tool obtaining a large DNA construct on the particle surface without disturbing the particle's morphology while producing a fluorescence read-out. These methods could address the challenges of applying DNA nanotechnology to engineer on polymer surfaces for constructing responsive nanomaterials.

ASSOCIATED CONTENT

Supporting Information

The Supporting Information is available free of charge at https://pubs.acs.org/doi/10.1021/acs.bioconjchem.3c00293.

Experimental section, additional characterization of the DNA based nanoobjects, and details on the hybridization of the DNA-based structures (PDF)

https://doi.org/10.1021/acs.bioconjchem.3c00293
Bioconjugate Chem. 2023, 34, 2007−2013

AUTHOR INFORMATION

Corresponding Author

Rachel K. O'Reilly − *School of Chemistry, University of Birmingham, Birmingham B15 2TT, U.K.*; orcid.org/0000-0002-1043-7172; Email: r.oreilly@bham.ac.uk

Authors

Siriporn Chaimueangchuen − *School of Chemistry, University of Birmingham, Birmingham B15 2TT, U.K.*

Jennifer Frommer − *School of Chemistry, University of Birmingham, Birmingham B15 2TT, U.K.*

Calum T. J. Ferguson − *School of Chemistry, University of Birmingham, Birmingham B15 2TT, U.K.*

Complete contact information is available at: https://pubs.acs.org/10.1021/acs.bioconjchem.3c00293

Author Contributions

The manuscript was written through contributions of all authors. All authors have given approval to the final version of the manuscript.

Notes

The authors declare no competing financial interest.

ACKNOWLEDGMENTS

S.C. thanks Development and Promotion of Science and Technology Talents Project (DPST), Royal Government of Thailand scholarship. We also gratefully acknowledge Dr. Tom Wilks for the DNA design and Dr. Spyridon Varlas for the construction of the photoreactor. Alisha Miller, Dr. Stephen Fielden, and Dr. Marjolaine Thomas are thanked for Cryo-TEM images. Dr. Maria Chiara Arno and Dr. Yujie Xie are thanked for confocal images.

ABBREVIATIONS

cDNA, complementary DNA; CEPA, 4-cyano-4-(dodecylsulfanylthiocarbonyl) sulfanyl pentanoic acid; DNA, deoxyribonucleic acid; HCR, hybridization chain reaction; HPLC, high-performance liquid chromatography; HPMA, 2-hydroxypropyl methacrylate; macroCTA, macromolecular chain transfer agent; PEG, poly(ethylene glycol); PHPMA, poly(2-hydroxypropyl methacrylate); RAFT-mediated PISA, reversible addition fragmentation chain transfer mediated polymerization-induced self-assembly; ssDNA, single-stranded DNA

REFERENCES

(1) Mai, Y.; Eisenberg, A. Self-assembly of block copolymers. *Chem. Soc. Rev.* **2012**, *41* (18), 5969−5985.

(2) Lee, K.; Povlich, L. K.; Kim, J. Label-Free and Self-Signal Amplifying Molecular DNA Sensors Based on Bioconjugated Polyelectrolytes. *Adv. Funct. Mater.* **2007**, *17* (14), 2580−2587.

(3) Oishi, M.; Hayama, T.; Akiyama, Y.; Takae, S.; Harada, A.; Yamasaki, Y.; Nagatsugi, F.; Sasaki, S.; Nagasaki, Y.; Kataoka, K. Supramolecular Assemblies for the Cytoplasmic Delivery of Antisense Oligodeoxynucleotide: Polyion Complex (PIC) Micelles Based on Poly(ethyleneglycol)-SS-Oligodeoxynucleotide Conjugate. *Biomacromolecules* **2005**, *6*, 2449−2454.

(4) Oishi, M.; Nagatsugi, F.; Sasaki, S.; Nagasaki, Y.; Kataoka, K. Smart polyion complex micelles for targeted intracellular delivery of PEGylated antisense oligonucleotides containing acid-labile linkages. *Chembiochem* **2005**, *6* (4), 718−725.

(5) Li, Z.; Zhang, Y.; Fullhart, P.; Mirkin, C. A. Reversible and Chemically Programmable Micelle Assembly with DNA Block-Copolymer Amphiphiles. *Nano Lett.* **2004**, *4* (6), 1055−1058.

(6) Luckerath, T.; Koynov, K.; Loescher, S.; Whitfield, C. J.; Nuhn, L.; Walther, A.; Barner-Kowollik, C.; Ng, D. Y. W.; Weil, T. DNA-Polymer Nanostructures by RAFT Polymerization and Polymerization-Induced Self-Assembly. *Angew. Chem., Int. Ed. Engl.* **2020**, *59*, 15474−15479.

(7) Warren, N. J.; Armes, S. P. Polymerization-Induced Self-Assembly of Block Copolymer Nano-objects via RAFT Aqueous Dispersion Polymerization. *J. Am. Chem. Soc.* **2014**, *136* (29), 10174−10185.

(8) Yang, L.; Liang, M.; Cui, C.; Li, X.; Li, L.; Pan, X.; Yazd, H. S.; Hong, M.; Lu, J.; Cao, Y. C.; Tan, W. Enhancing the Nucleolytic Resistance and Bioactivity of Functional Nucleic Acids by Diverse Nanostructures through in Situ Polymerization-Induced Self-assembly. *Chembiochem* **2021**, *22* (4), 754−759.

(9) Bi, S.; Yue, S.; Zhang, S. Hybridization chain reaction: a versatile molecular tool for biosensing, bioimaging, and biomedicine. *Chem. Soc. Rev.* **2017**, *46* (14), 4281−4298.

(10) Huang, J.; Wu, Y.; Chen, Y.; Zhu, Z.; Yang, X.; Yang, C. J.; Wang, K.; Tan, W. Pyrene-excimer probes based on the hybridization chain reaction for the detection of nucleic acids in complex biological fluids. *Angew. Chem., Int. Ed. Engl.* **2011**, *50* (2), 401−404.

(11) Liu, P.; Yang, X.; Sun, S.; Wang, Q.; Wang, K.; Huang, J.; Liu, J.; He, L. Enzyme-free colorimetric detection of DNA by using gold nanoparticles and hybridization chain reaction amplification. *Anal. Chem.* **2013**, *85* (16), 7689−7695.

(12) Hou, T.; Li, W.; Liu, X.; Li, F. Label-Free and Enzyme-Free Homogeneous Electrochemical Biosensing Strategy Based on Hybridization Chain Reaction: A Facile, Sensitive, and Highly Specific MicroRNA Assay. *Anal. Chem.* **2015**, *87* (22), 11368−11374.

(13) Halpin, D. R.; Lee, J. A.; Wrenn, S. J.; Harbury, P. B. DNA display III. Solid-phase organic synthesis on unprotected DNA. *PLoS Biol.* **2004**, *2* (7), No. E175.

(14) Blackman, L. D.; Doncom, K. E. B.; Gibson, M. I.; O'Reilly, R. K. Comparison of photo- and thermally initiated polymerization-induced self-assembly: a lack of end group fidelity drives the formation of higher order morphologies. *Polym. Chem.* **2017**, *8* (18), 2860−2871.

(15) Easterling, C. P.; Xia, Y.; Zhao, J.; Fanucci, G. E.; Sumerlin, B. S. Block Copolymer Sequence Inversion through Photoiniferter Polymerization. *ACS Macro Lett.* **2019**, *8* (11), 1461−1466.

(16) Hartlieb, M. Photo-Iniferter RAFT Polymerization. *Macromol. Rapid Commun.* **2022**, *43* (1), No. e2100514.

(17) Jeong, J. H.; Kim, S. W.; Park, T. G. Novel Intracellular Delivery System of Antisense Oligonucleotide by Self-Assembled Hybrid Micelles Composed of DNA/PEG Conjugate and Cationic Fusogenic Peptide. *Bioconjugate Chem.* **2003**, *14* (2), 473−479.

(18) Boyer, C.; Bulmus, V.; Davis, T. P.; Ladmiral, V.; Liu, J.; Perrier, S. Bioapplications of RAFT Polymerization. *Chem. Rev.* **2009**, *109* (11), 5402−5436.

(19) Chapman, R.; Gormley, A. J.; Stenzel, M. H.; Stevens, M. M. Combinatorial Low-Volume Synthesis of Well-Defined Polymers by Enzyme Degassing. *Angew. Chem., Int. Ed. Engl.* **2016**, *55* (14), 4500−4503.

(20) Tan, J.; Liu, D.; Bai, Y.; Huang, C.; Li, X.; He, J.; Xu, Q.; Zhang, L. Enzyme-Assisted Photoinitiated Polymerization-Induced Self-Assembly: An Oxygen-Tolerant Method for Preparing Block Copolymer Nano-Objects in Open Vessels and Multiwell Plates. *Macromolecules* **2017**, *50* (15), 5798−5806.

(21) Semsarilar, M.; Ladmiral, V.; Blanazs, A.; Armes, S. P. Anionic polyelectrolyte-stabilized nanoparticles via RAFT aqueous dispersion polymerization. *Langmuir* **2012**, *28* (1), 914−922.

(22) Hu, Y.; Chen, Z.; Hou, Z.; Li, M.; Ma, B.; Luo, X.; Xue, X. Influence of Magnesium Ions on the Preparation and Storage of DNA Tetrahedrons in Micromolar Ranges. *Molecules* **2019**, *24* (11), 2091.

4.3. Experimental section

4.3.1 Materials

Poly(ethylene glycol) methyl ether (average Mn=5,000 g mol-1, PEG-OH), carbon disulfide (anhydrous, ≥99%), glucose oxidase from Aspergillus niger (100 000–250 000 U/g), sodium ethanethiolate, N,N′-dicyclohexylcarbodiimide (99%, DCC), 4-(dimethylamino)pyridine (≥98%, DMAP), were purchased from Sigma Aldrich and used without further purification. Iodine, D-Glucose, Diethyl ether, dichloromethane (DCM), and Magnesium chloride ($MgCl_2$) were purchased from Fisher Scientific. Ethyl acetate was purchased from VWR Chemicals. 2-Hydroxypropyl methacrylate (mixture of isomers, 98%, HPMA) was purchased from Alfa Aesar and was passed through a column of basic alumina to remove inhibitor prior to use and stored at 4 °C. Dry solvents used in the experiments were obtained by passing over a column of activated alumina using an Innovative Technologies solvent purification system. Formvar-coated copper grids were purchased from EM Resolutions. SYBR™ Gold Nucleic acid gel stain (10,000X concentrate in DMSO) was purchased from ThermoFisher. Tris-acetate-EDTA (TAE) buffer was purchased from Sigma-Aldrich and contains 0.4 M Trisacetate and 0.01 M EDTA. Oligonucleotides were purchased from Integrated DNA technologies, Inc. and resuspended in 18 MΩ H_2O to a concentration of 100 µM or 1 mM before use. Concentrations were calculated from the absorbance values at 260 nm using the reported extinction coefficients.

4.3.2 Instrumentations and analysis

^{1}H-NMR spectra were recorded at 400 MHz on a Bruker DPX-400 spectrometer using chloroform-*d* (CDCl3) and methanol-*d4* (CD_3OD) as the solvent. Chemical shifts of

protons are reported as δ in parts per million (ppm) and are relative to tetramethylsilane (TMS) at δ = 0 ppm when using solvent residual peak (CH_3OH, δ = 3.31 ppm).

Reversed Phase High Performance Liquid Chromatography (RP-HPLC) analysis of oligonucleotides was performed on a modular Shimadzu instrument with the following modules: CBM-20A system controller, LC-20AD solvent deliver module, SIL-20AC HT autosampler, CTO-20AC column oven, SPD-M20A photodiode array UV-Vis detector, RF-20A spectrofluorometric detector and a FRC-10 fraction collector. Chromatography was performed on a Waters XBridge™ OST C18 2.5 µM column heated to 60 °C. Flow rate was set at 0.8 mL min^{-1} using buffers A and B: buffer A, 0.1 M triethylammonium acetate (TEAA, pH 7.0), in a 95:5 mixture of H_2O and acetonitrile; buffer B, 0.1 M TEAA (pH 7), 30:70 mixture of H_2O and acetonitrile. The buffer gradient for analysis and purification was 1% buffer B for 5 minutes, 1% to 30% B over 15 minutes, 30% to 95% B over 5 min, 95% to 1% B over 1 min and finally 1% B for 3 min.

Liquid Chromatography-Mass Spectrometry (LC-MS) analysis of oligonucleotides was performed on an Agilent 1200 HPLC system coupled to a Bruker AmazonX high resolution ion trap, in negative ion mode. The desalted oligonucleotide samples were eluted through a XBridge oligonucleotide BEH C18 column (130 Å, 2.5 µm, 4.6 x 50 mm) using a 5 vol% MeOH, 10 mM ammonium acetate (buffer A) and a 70 vol% MeOH, 10 mM ammonium acetate (buffer B) solvent system at 0.8 mL/min flow. The data was processed using Compass Data Analysis (Bruker) v.4.1 software, and the MaxEnt integrated deconvolution algorithm. Alternatively, LCMS analysis was performed on a Waters ACQUITY UPLC system coupled to a Xevo G2-XS QToF mass spectrometer in negative ion mode. The oligonucleotides were eluted through an AQUITY UPLC oligonucleotide BEH C18 column (130Å, 1.7 µm, 2.1 x 50 mm) using a 75 mM triethylammonium acetate (TEAA, pH 7.0) solution in H_2O (buffer A) and a 75 mM

TEAA solution in MeCN (buffer B) at 60 °C and a 0.2 mL/min flow. Leucine enkephalin was used as the reference for the LockSpray correction. The raw continuum data was deconvoluted to produce zero charge mass spectra using ProMass HR for MassLynx (Novatia) software.

Gel Electrophoresis - Native polyacrylamide gel (10%) was prepared by mixing 2.5 mL 30% 29:1 acrylamide:bisacrylamide, 4.25 mL H_2O, 0.75 mL 10×TAE, 75 µL 10% (w/v) ammonium persulfate (APS), and 7.5 µL tetramethylethylenediamine (TEMED). Different percentage gels were prepared by varying the proportions of acrylamide and water. After removing well combs, wells were rinsed with running buffer (1×TAE) using a pipette before loading 2 µL samples typically diluted to 200 nM in loading buffer (1×TAE, 50% glycerol). Native polyacrylamide gels were run at room temperature in 1×TAE buffer at 180 V using a vertical nucleic acid electrophoresis cell connected to a PowerPack basic power supply (BioRad). Samples were combined with 20% loading buffer (0.05% bromophenol blue, 25% glycerol, 1xTAE) prior to running. Non-fluorescent DNA was stained using a 1:1000 aqueous SYBR® Gold nucleic acid gel stain (ThermoFisher) and visualized using a BioRad ChemiDoc™ MP Imaging system. The images were processed using ImageLab software v 6.0.1.

1×TAE buffer consisted of 40 mM Tris-acetate and 1 mM EDTA. 1×TAE buffer consisted of 10 mM Tris-HCl and 1 mM EDTA. The native loading buffer consisted of 25 % glycerol and 0.05 % bromophenol blue in 1×TAE buffer, and was diluted five-fold before use.

Size Exclusion Chromatography (SEC) analysis was performed on a system composed of a Varian 390-LC-Multi detector suite equipped with a Varian Polymer Laboratories guard column (PLGel 5 µM, 50 × 7.5 mm), two Mixed-C Varian Polymer Laboratories columns

(PLGel 5 μM, 300 × 7.5 mm) and a PLAST RT auto-sampler. Detection was conducted using a differential refractive index (RI) and an ultraviolet (UV) detector set to λ = 309 nm. The mobile phase used was DMF (HPLC grade) containing 5 mM NH4BF4 at 50 ˚C at a flow rate of 1.0 mL min-1. Poly(methyl methacrylate) (PMMA) standards were used for calibration. Molecular weights and dispersities were determined using Cirrus v3.3 SEC software.

Zeta potential was measured by the technique of microelectrophoresis, using a Malvern Zetasizer Nano ZS instrument, at room temperature at 633 nm. All reported zeta potential values were the average of at least three runs with at least 40 measurements recorded for 3 runs. Zeta potential was calculated from the corresponding electrophoretic mobilities (μE) by using the Henry's correction of the Smoluchowski equation ($\mu E = 4\pi\ \varepsilon 0\ \varepsilon r\ \zeta\ (1+\kappa r)/6\pi\ \mu$).

Hydrodynamic diameters (D_h) of particles were determined by dynamic light scattering (DLS) using a Malvern Zetasizer Nano ZS with a 4 mW He-Ne 633 nm laser module operating at 25 °C. Measurements were carried out at an angle of 173° (back scattering), and results were analyzed using Malvern DTS 7.03 software. All determinations were repeated 4 times with at least 10 measurements recorded for each run. D_h values were calculated using the Stokes-Einstein equation where particles are assumed to be spherical, while for cylindrical particles DLS was used to detect multiple populations and obtain dispersity information.

Static Light Scattering (SLS). For the particles in deionized water, light scattering data was collected over the whole angular range, $30 < \theta < 50°$ with the sample maintained at 25°C. Autocorrelation functions calculated by the ALV LSE-5004 correlator unit were recorded at each (θ, c) and the REPES algorithm was used to determine relaxation times,

$\tau(\theta, c)$. The data set $\tau(\theta, c)$ was then analyzed to estimate the mean translational diffusion coefficient according to the Stokes-Einstein equation. An empirical measurement was made of the refractive index increment for the polymer in deionized water using a differential refractometer, model DnDc1260 supplied by PSS GmbH. The light scattering experiments were conducted at 0.01, 0.02, 0.05, 0.10 and 0.20 $mg \cdot mL^{-1}$ to account for concentration effects. Following Andersson *et al.*[19], a Zimm plot was constructed using the Debye method (**Equation 1** and **Equation 2**) to determine the R_g of the nanoparticles. To do this, the R_θ/Kc versus q^2 data were plotted and a third order polynomial model was used to extrapolate $q \rightarrow 0$. The fit's intercept provided the molecular mass according to light scattering (M_{LS}) while the slope at $q^2 = 0$ can be utilized to retrieve R_g at the different concentrations. A first order model was utilized for the $c \rightarrow 0$ extrapolation yielding R_g and M_{LS}.

$$\frac{R_\theta}{Kc} = -\frac{MR_g{}^2}{3}q^2 + M \qquad \textbf{(1)}$$

$$\frac{\partial\, R_\theta/Kc}{\partial q^2} = -\frac{MR_g{}^2}{3} \qquad \textbf{(2)}$$

The mean translational diffusion coefficient (D_{app}) was calculated from the relaxation times at each angle, $\tau(\theta, c)$ determined from the autocorrelation functions at each angle (θ, c) by the REPES algorithm. The Stokes-Einstein equation was used to determine the hydrodynamic radius (R_h) of the particles. The R_g/R_h ratio gives information about the inside of the spherical particle. A value of 1 indicates a hollow sphere with all the mass in the outer shell (*i.e.* vesicle). The 50%DNA-PHPMA$_{400}$ nanoparticles have a R_g/R_h ratio of 1.02. The aggregation number ($M_{w,theo}/M_{LS}$) was calculated to be 2.73×10^3 which is in line with a vesicle morphology.[20]

Transmission Electron Microscopy (TEM) analysis was performed on a JEOL 2100 electron microscope at an acceleration voltage of 200 kV. All samples were diluted with deionized water and then deposited onto formvar-coated copper grids. After roughly 1 min, excess sample was blotted from the grid and the grid stained with an aqueous 1 wt% uranyl acetate (UA) solution for 1 min prior to blotting, drying and microscopic analysis.

Cryogenic Transmission Electron Microscopy (Cryo-TEM) imaging was performed on a JEOL JEM-2100 plus microscope operating at an acceleration voltage of 200 kV. Samples for cryo-TEM were prepared on lacey carbon grids (EM Resolutions). After 200-fold dilution with deionized water, 8 µL of sample were deposited onto the grid followed by blotting for approximately 5 s and plunging into a pool of liquid ethane, cooled using liquid nitrogen in order to vitrify the samples. Then, transfer into a pre-cooled cryo-TEM holder using liquid nitrogen, was performed prior to the microscopic analysis.

Confocal Laser Scanning Microscopy (CLSM) was performed on FV3000 (Olympus) confocal microscope and the 60x oil lens was used for imaging. Images were acquired using the 488 nm (green channel) and the 561 nm (red channel) excitation wavelengths. Freshly prepared and purified solutions of FAM-**H2** (green-emitting dye), TAMRA-cDNA (red-emitting dye) and mixed 50% DNA-PHPMA$_{400}$ copolymer nano-objects at 100-fold dilution were deposited on a glass slide before imaged by CLSM. Images were processed using cellSens (Olympus) and ImageJ image processing software.

The LAD-1 LED array driver was purchased from Bio Research Centre Co., Ltd. The array was composed of 405 nm LEDs which each output a light power of 20 mW at 13.5 V when measured with an LMP-100 light power sensor (sensor area: 5.5 mm x 4.8 mm), placed directly above an array LED. For the Thermomixer setup, the LED-array was suspended over the sample holder *via* a clamp stand. For the Incubator setup the LED-

array was placed upon a shaker plate, face up with a 96-microwell plate placed directly upon it, into which 150 µL eppendorfs containing sample were placed.

4.3.3 Synthetic Method

Synthesis of 4-cyano-4-[(ethylsulfanylthiocarbonyl)sulfanyl] pentanoic acid (CEPA)

CEPA was synthesized using procedures similar to the previous literature.[10] Description of the protocol can be found in the experimental section of Chapter 2.

Synthesis of poly(ethylene glycol)$_{113}$-CEPA macro-CTA (PEG$_{113}$-macroCTA)

PEG$_{113}$-macroCTA was synthesized using procedures similar to the previous literature.[10] Description of the protocol can be found in the experimental section of Chapter 2.

Synthesis of ssDNA$_{14}$-macroCTA by *solid support* approach

Description of the protocol can be found in the experimental section of Chapter 3.

Synthesis of PEG$_{113}$-*b*-PHPMA$_{400}$ and ssDNA$_{14}$-*b*-PHPMA$_{400}$ diblock copolymer by photoinitiated polymerization-induced self-assembly

ssDNA$_{14}$-macroCTA (varied amount, 20 mg/mL, varied eq) and PEG$_{113}$-macroCTA (varied amount, 40 mg/mL, varied eq) was added in a centrifuge tube containing HPMA (5 mg, 400 eq). Then, glucose solution (6 µL, 0.84 M), nanopure water (varied amount) and GOx solution (4 µL, 25 µM) were added into the mixing vial, respectively, resulting in a total volume of 50 µL. The mixture was shaken *via* vortexer to produce a clear colourless solution which was then transferred to pointed base PCR plate. Mineral oil was added around 200 µL on top of the mixture and the plate was covered by plate seal, and placed in LED array setup, which was contain in an incubator to maintain a temperature of 37 °C. The solution was then exposed to 405 nm light for 2 h, resulting in the solution turning opaque and milky white.

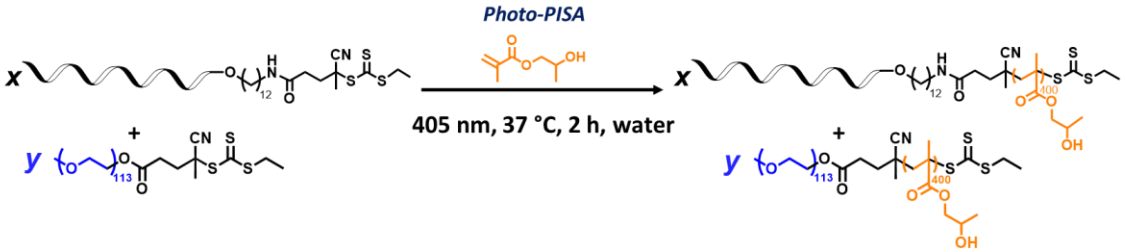

Scheme 4.1. Synthesis of DNA−polymer conjugates by photo-PISA.

In order to study the DNA hybridization of the particle surface, a 10 mM $MgCl_2$ in 1×TAE solution was used as a buffer to provide optimal DNA hybridization conditions. The surface hybridisation of nano-objects formed using different ratios of ssDNA and PHPMA containing diblock copolymers was investigated. Nanopure water (177 or 159 µL) was added into $MgCl_2$ (2 µL, 1M), nano-object solution (1 µL, 100 mg/ml), TAE (20 µL, 10×) to prepare the particle solution under buffered condition (10 mM) in 1.5 mL tube. The tube was shaken at room temperature at least 30 min and then transferred to a DLS microcuvette. DLS was used to investigate particle size and size dispersity. Subsequently, varying systematic amounts of cDNA (100 µM) was added to the centrifuge tubes, containing the nano-objects with varying ratios of ssDNA. The centrifuge tube was shaken at room temperature for at least 30 min before investigation by DLS, TEM and confocal microscopy.

Hybridization chain reaction (HCR) study

The HCR reaction was performed under the same conditions for the free ssDNA and for the ssDNA containing nano-object systems. Before performing HCR, hairpin1 (H1) (50 µM, 5 µL) and hairpin2 (H2) (50 µM, 5 µL) were incubated at 95 °C for 2 min then quenched at -20 °C for 1 min. The initiator (I) (0.2 eq), H1 (varied eq.), and H2 (varied eq.) were added to the ssDNA or ssDNA containing nano-object systems (10 µM, 1 eq) under 10 mM $MgCl_2$ in 1×TAE condition in a 1.5 mL tube at room temperature for 30

min. The ssDNA samples were analyzed by native PAGE. ssDNA containing nano-object systems were also analysed by DLS, TEM, Cryo-TEM and confocal microscopy.

Table 4.1. List of ssDNA-copolymer nanoparticles obtained from RAFT aqueous dispersion photo-PISA and summary of characterization data

Sample	**Targeted DP**	**Actual DP[a]**	**Convers.[a] (%)**	M_n [b] **(kg·mol^{-1})**	$Đ_M$[b]	D_h[c] **(nm)**	**PD[c]**	**Morpho-logy[d]**
DNA – $PHPMA_{400}$	400	320	~80	123	1.5	90	0.12	S
90% DNA–$PHPMA_{400}$	400	288	~72	108	1.9	219	0.42	S+LR+V
50%DNA– $PHPMA_{400}$	400	385	~96	137	1.5	154	0.04	V
10%DNA]-$PHPMA_{400}$	400	356	~89	54	1.5	186	0.09	V
PEG_{113}– $PHPMA_{400}$	400	352	~88	68	1.4	459	0.03	V

[a] Calculated from ^{1}H NMR spectroscopy (400 MHz) in deuterated MeOD.

[b] Determined by DMF SEC with poly(methyl methacrylate) (PMMA) standards.

[c] Determined by DLS using z-average data.

[d] Determined by TEM. S = Spheres, LR = Lumpy Rod, and V = Vesicle.

Table 4.2. DNA sequences

Name	**DNA sequence (5'- 3')**	**Extinction coefficient (L (mole·cm)$^{-1}$)**
$ssDNA_{14}$	TGTAGCGTTGTTGC	128,400
$ssDNA_{14}$-NH_2	/5AmMC12/ TGTAGCGTTGTTGC	128,400
cDNA	GCAACAACGCTACA	139,600
TAMRA- cDNA	/56-TAMN/GCAACAACGCTACA	168,700
ncDNA	TGTAGCGTTGTTGC	128,400
I	GAGGAGGGCAGCAAACGGGAAGAGTCTTC CTTTACGGCAACAACGCTACA	496,900
TAMRA-**I**	/56-TAMN/ GAGGAGGGCAGCAAACGGGAAGAGTCTTC CTTTACGGCAACAACGCTACA	526,000
H1	CGTAAAGGAAGACTCTTCCCGTTTGCTGCC CTCCTCGCATTCTTTCTTGAGGAGGGCAGC AAACGGGAAGAG	677,600
H2	GAGGAGGGCAGCAAACGGGAAGAGTCTTC CTTTACGCTCTTCCCGTTTGCTGCCCTCCTC AAGAAAGAATGC	678,200
FAM-**H2**	/FAM/GAGGAGGGCAGCAAACGGGAAGAGT CTTCCTTTACGCTCTTCCCGTTTGCTGCCCT CCTCAAGAAAGAATGC	688,200

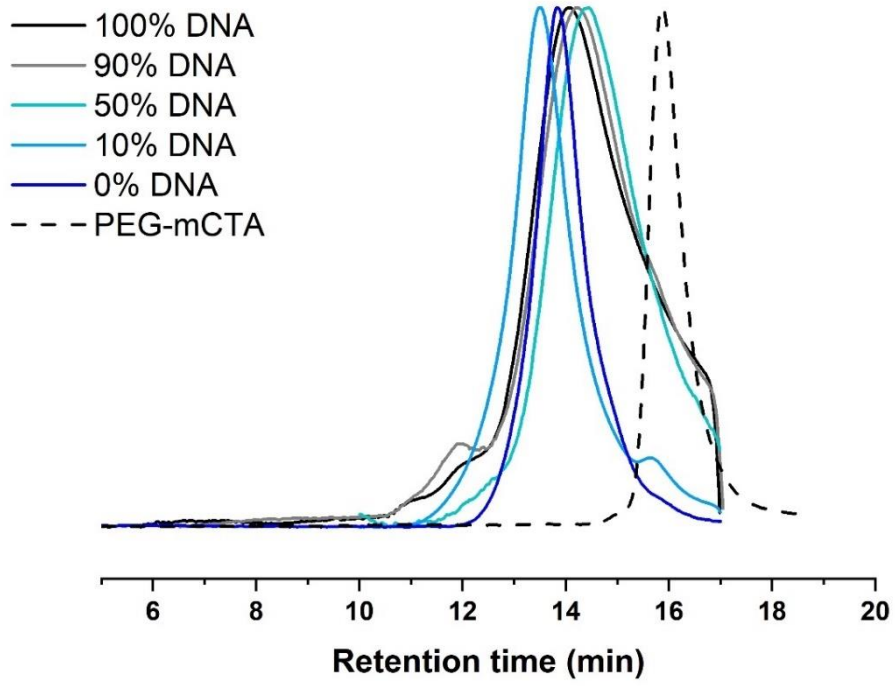

Figure 4.1. SEC RI traces of PEG-macroCTA (dot line) and the DNA/PEG polymer conjugates (solid lines) as measured by DMF GPC using polymethylmethacrylate (PMMA) calibration standards.

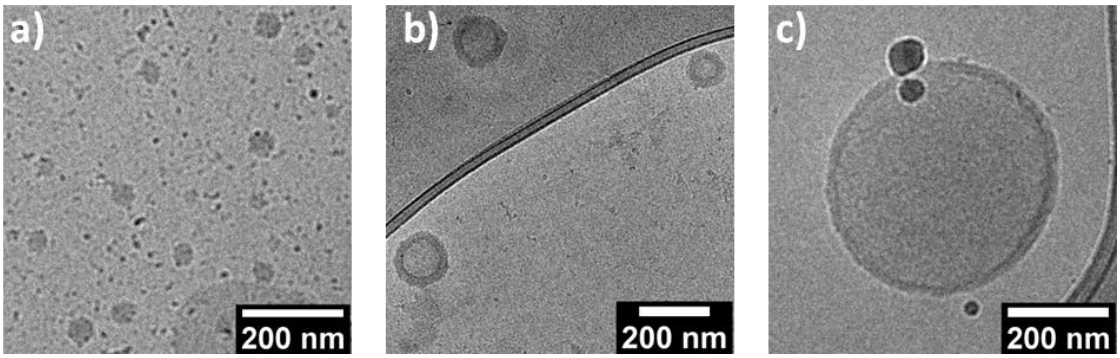

Figure 4.2. Cryogenic transmission electron microscopy (Cryo-TEM) images of a) DNA – $PHPMA_{400}$, b) 50%$ssDNA_{14}$ – $PHPMA_{400}$, and c) PEG_{113}– $PHPMA_{400}$ assign the copolymer morphology.

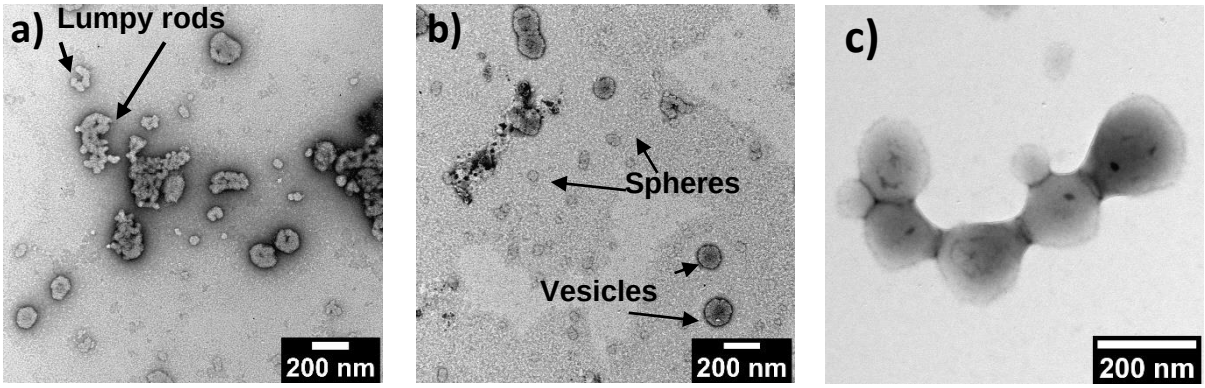

Figure 4.3. Transmission electron microscopy (TEM) images of a) and b) 90%DNA-PHPMA$_{400}$ and c) 10% DNA-PHPMA$_{400}$ diblock copolymer.

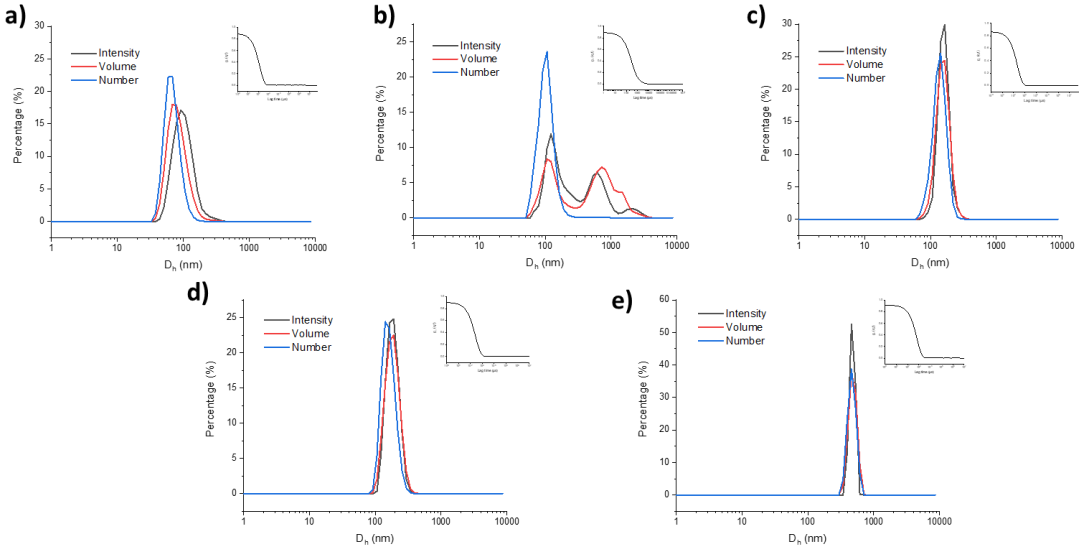

Figure 4.4. Dynamic light scattering (DLS) of mixed DNA and PEG based objects with different percentages of DNA in the corona a) 100% DNA, b) 90% DNA, c) 50% DNA, d) 10% DNA, and e) 0% DNA.

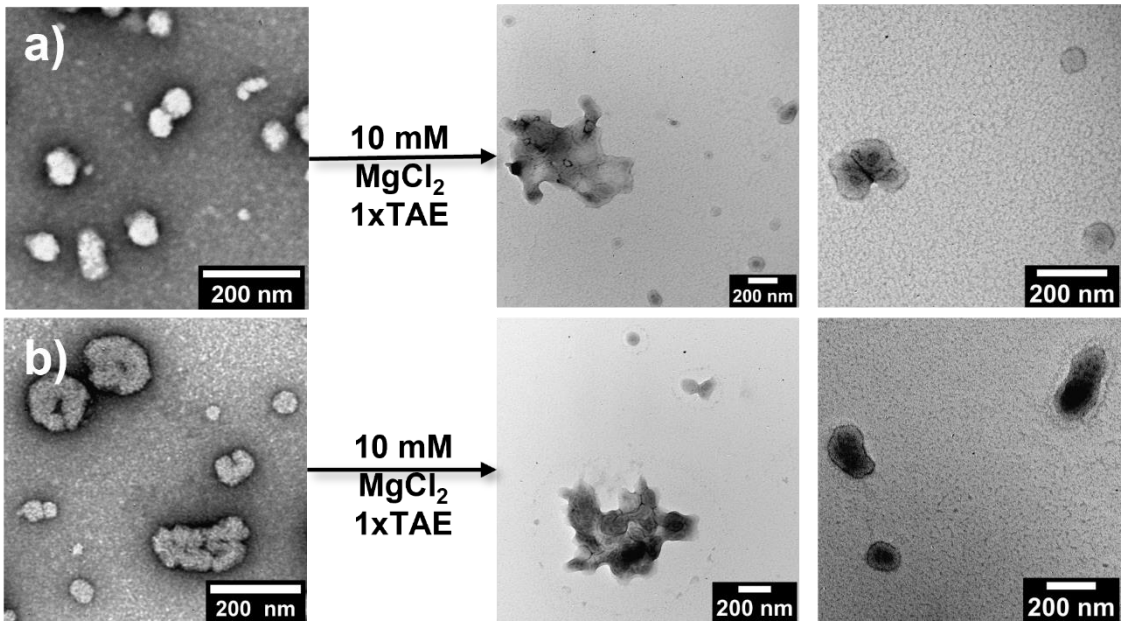

Figure 4.5. TEM images of a) DNA-PHPMA$_{400}$ particles and b) 50%DNA-PHPMA$_{400}$ particles aggregated when salt/TAE buffer was added.

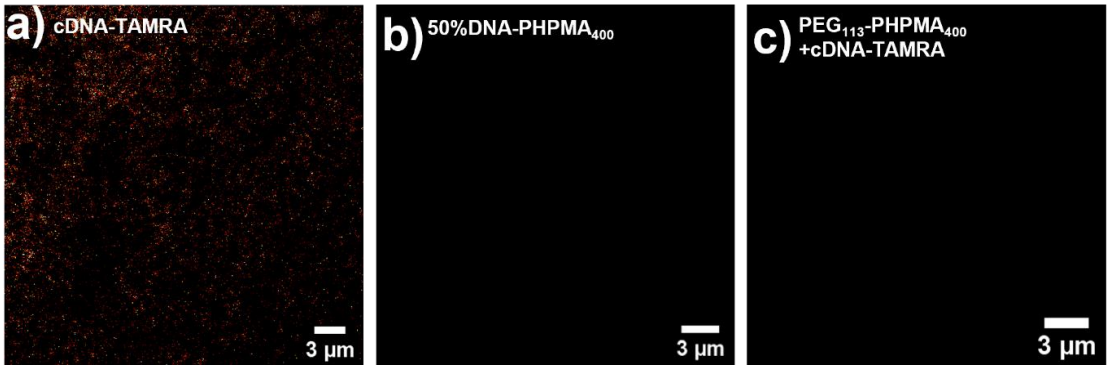

Figure 4.6. Confocal images of hybridization studying which a) TAMRA-cDNA, b) 50%DNA-PHPMA$_{400}$, and c) PEG$_{113}$-*b*-PHPMA$_{400}$+ TAMRA-cDNA.

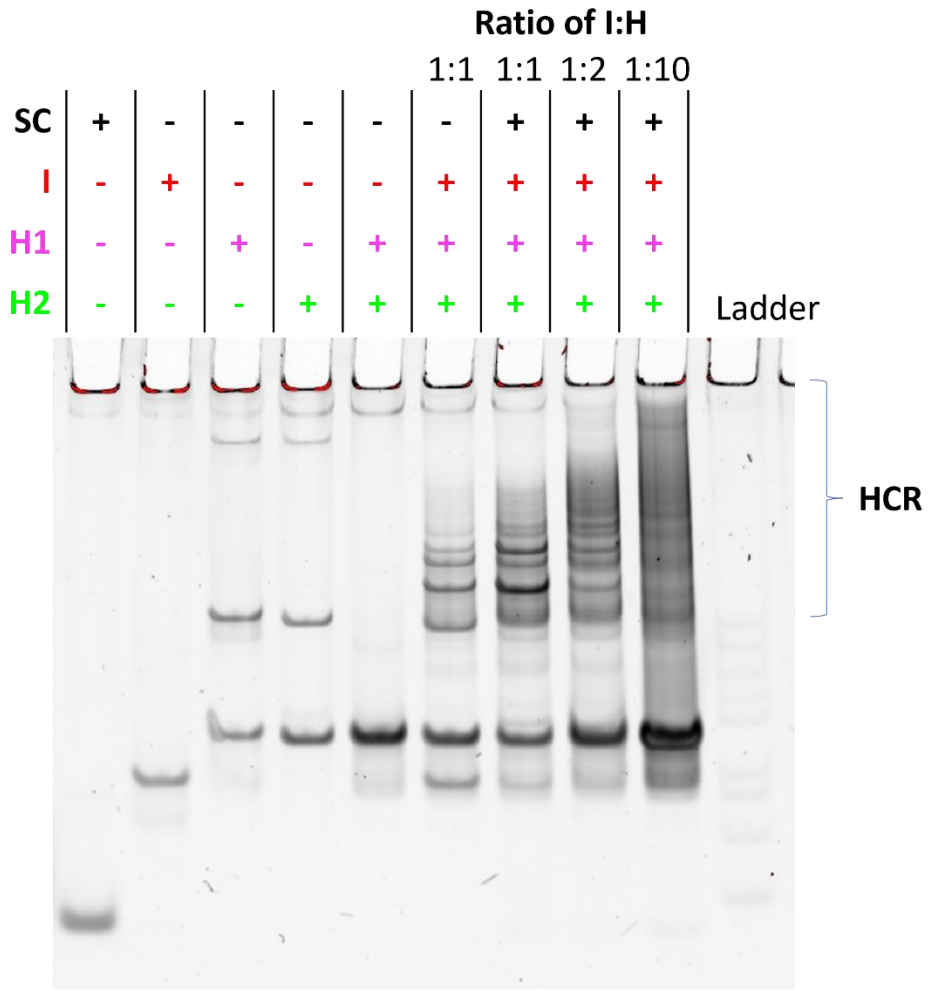

Figure 4.7. Native poly(acrylamide) gel electrophoresis (10%) of hybridization chain reaction (HCR) study utilizing the ssDNA (SC). The ratios of initiator's concentration to hairpin DNA's concentration (**I**:**H**) were 1:1, 1:2, and 1:10 with a constant final concentration of 5 µM hairpin DNAs. **H1** and **H2** do not hybridize before triggered by I, so no reaction is observed (lane 5). HCR products are only formed when **I** is present (lane 6). Effect of I:H ratio on HCR amplification (Lanes 7–9): three different ratios of **I**:**H** (1:1, 1:2, and 1:10) in a 5 µM mixture of ssDNA(SC), **I**, **H1** and **H2** were tested. Before mixing, **H1** (50 µM, 10 µL) and **H2** (50 µM, 10 µL) were incubated at 95 °C for 2 min then quenched at -20 °C for 1 min.

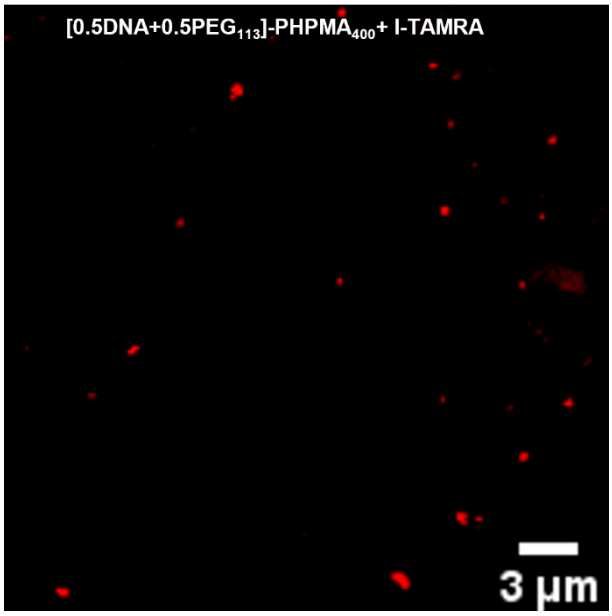

Figure 4.8. Confocal images of hybridization chain reaction studying of 50%DNA - $PHPMA_{400}$ + TAMRA-**I**.

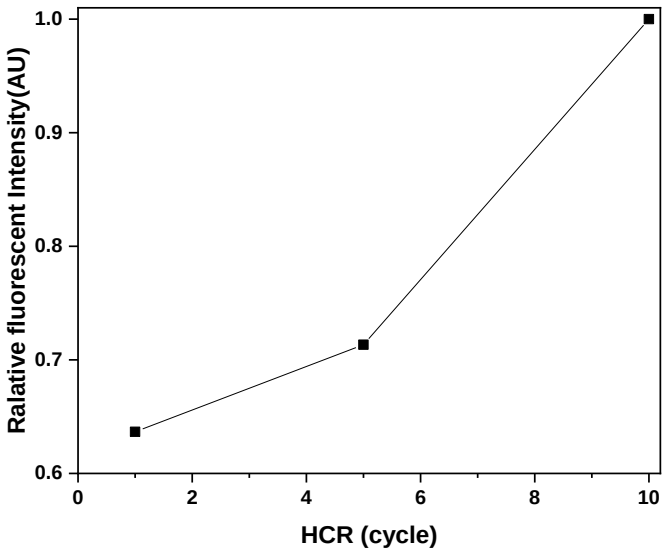

Figure 4.9. Fluorescence intensity analysis at different HCR Cycles. The presented values were calculated for each particle using the CLSM images from Figure 3g-j, obtained through ImageJ analysis of the CLSM images in the green channel.

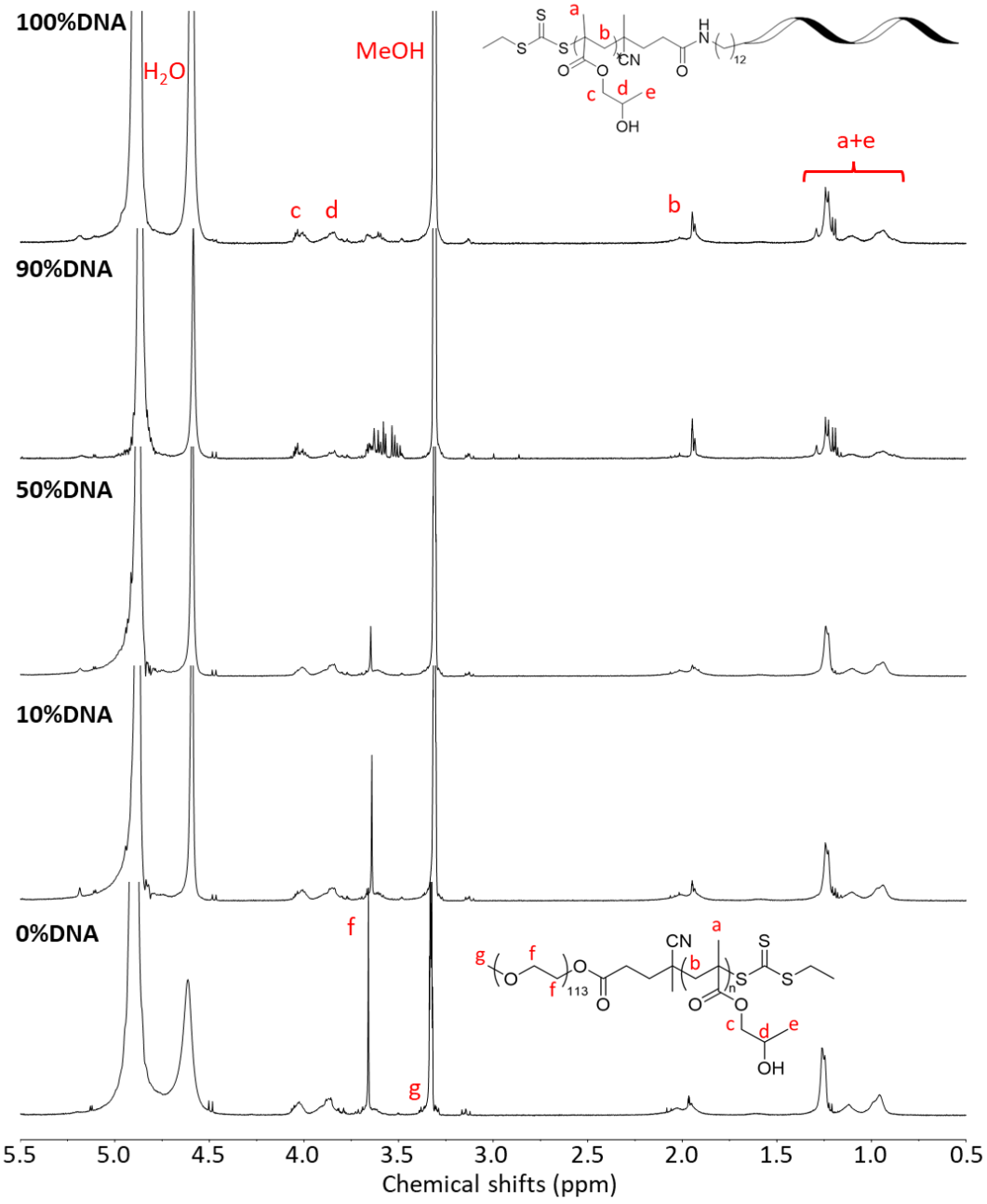

Figure 4.10. ^{1}H-NMR spectra of different mole fractions of DNA/PEG polymer conjugates in MeOD

4.5. References

1. Mai, Y.; Eisenberg, A., Self-assembly of block copolymers. *Chemical Society Reviews* **2012,** *41* (18), 5969-5985.

2. Luckerath, T.; Koynov, K.; Loescher, S.; Whitfield, C. J.; Nuhn, L.; Walther, A.; Barner-Kowollik, C.; Ng, D. Y. W.; Weil, T., DNA-Polymer Nanostructures by RAFT Polymerization and Polymerization-Induced Self-Assembly. *Angew Chem Int Ed Engl* **2020**.

3. Warren, N. J.; Armes, S. P., Polymerization-Induced Self-Assembly of Block Copolymer Nano-objects via RAFT Aqueous Dispersion Polymerization. *Journal of the American Chemical Society* **2014,** *136* (29), 10174-10185.

4. Yang, L.; Liang, M.; Cui, C.; Li, X.; Li, L.; Pan, X.; Yazd, H. S.; Hong, M.; Lu, J.; Cao, Y. C.; Tan, W., Enhancing the Nucleolytic Resistance and Bioactivity of Functional Nucleic Acids by Diverse Nanostructures through in Situ Polymerization-Induced Self-assembly. *Chembiochem* **2021,** *22* (4), 754-759.

5. Bi, S.; Yue, S.; Zhang, S., Hybridization chain reaction: a versatile molecular tool for biosensing, bioimaging, and biomedicine. *Chemical Society Reviews* **2017,** *46* (14), 4281-4298.

6. Huang, J.; Wu, Y.; Chen, Y.; Zhu, Z.; Yang, X.; Yang, C. J.; Wang, K.; Tan, W., Pyrene-excimer probes based on the hybridization chain reaction for the detection of nucleic acids in complex biological fluids. *Angew Chem Int Ed Engl* **2011,** *50* (2), 401-4.

7. Liu, P.; Yang, X.; Sun, S.; Wang, Q.; Wang, K.; Huang, J.; Liu, J.; He, L., Enzyme-free colorimetric detection of DNA by using gold nanoparticles and hybridization chain reaction amplification. *Anal Chem* **2013,** *85* (16), 7689-95.

8. Hou, T.; Li, W.; Liu, X.; Li, F., Label-Free and Enzyme-Free Homogeneous Electrochemical Biosensing Strategy Based on Hybridization Chain Reaction: A Facile, Sensitive, and Highly Specific MicroRNA Assay. *Anal Chem* **2015,** *87* (22), 11368-74.

9. Jeong, J. H.; Kim, S. W.; Park, T. G., Novel Intracellular Delivery System of Antisense Oligonucleotide by Self-Assembled Hybrid Micelles Composed of DNA/PEG Conjugate and Cationic Fusogenic Peptide. *Bioconjugate Chemistry* **2003,** *14* (2), 473-479.

Supporting Information

Surface hybridization chain reaction of binary mixture DNA-PEG corona nanostructures produced by low-volume RAFT-mediated photopolymerization-induced self-assembly.

Siriporn Chaimueangchuen,[†] Jennifer Frommer,[†] Calum T. J. Ferguson,[†] and Rachel K. O'Reilly[*,†]

[†] School of Chemistry, University of Birmingham, Edgbaston, Birmingham, B15 2TT, UK

*Corresponding Authors: r.oreilly@bham.ac.uk (R.K.O.R.)

Experimental Procedure

Chemicals

Poly(ethylene glycol) methyl ether (average Mn=5,000 g mol-1, PEG-OH), carbon disulfide (anhydrous, ≥99%), glucose oxidase from Aspergillus niger (100 000–250 000 U/g), sodium ethanethiolate, N,N′-dicyclohexylcarbodiimide (99%, DCC), 4-(dimethylamino)pyridine (≥98%, DMAP), were purchased from Sigma Aldrich and used without further purification. Iodine, D-Glucose, Diethyl ether, dichloromethane (DCM), and Magnesium chloride ($MgCl_2$) were purchased from Fisher Scientific. Ethyl acetate was purchased from VWR Chemicals. 2-Hydroxypropyl methacrylate (mixture of isomers, 98%, HPMA) was purchased from Alfa Aesar and was passed through a column of basic alumina to remove inhibitor prior to use and stored at 4 °C. Dry solvents used in the experiments were obtained by passing over a column of activated alumina using an Innovative Technologies solvent purification system. Formvar-coated copper grids were purchased from EM Resolutions. SYBR™ Gold Nucleic acid gel stain (10,000X concentrate in DMSO) was purchased from ThermoFisher. Tris-acetate-EDTA (TAE) buffer was purchased from Sigma-Aldrich and contains 0.4 M Trisacetate and 0.01 M EDTA. Oligonucleotides were purchased from Integrated DNA technologies, Inc. and resuspended in 18 MΩ H_2O to a concentration of 100 μM or 1 mM before use. Concentrations were calculated from the absorbance values at 260 nm using the reported extinction coefficients.

Methods

^{1}H-NMR spectra were recorded at 400 MHz on a Bruker DPX-400 spectrometer using methanol-*d4* (CD_3OD) as the solvent. Chemical shifts of protons are reported as δ in parts per million (ppm) and are relative to tetramethylsilane (TMS) at δ = 0 ppm when using solvent residual peak (CH_3OH, δ = 3.31 ppm).

Reversed Phase High Performance Liquid Chromatography (RP-HPLC) analysis of oligonucleotides was performed on a modular Shimadzu instrument with the following modules: CBM-20A system controller, LC-20AD solvent deliver module, SIL-20AC HT autosampler, CTO-20AC column oven, SPD-M20A photodiode array UV-Vis detector, RF-20A spectrofluorometric detector and a FRC-10 fraction collector. Chromatography was performed on a Waters XBridge™ OST C18 2.5 μM column heated to 60 °C. Flow rate was set at 0.8 mL min^{-1} using buffers A and B: buffer A, 0.1 M triethylammonium acetate (TEAA, pH 7.0), in a 95:5 mixture of H_2O and acetonitrile; buffer B, 0.1 M TEAA (pH 7),

30:70 mixture of H_2O and acetonitrile. The buffer gradient for analysis and purification was 1% buffer B for 5 minutes, 1% to 30% B over 15 minutes, 30% to 95% B over 5 min, 95% to 1% B over 1 min and finally 1% B for 3 min.

Liquid Chromatography-Mass Spectrometry (LC-MS) analysis of oligonucleotides was performed on an Agilent 1200 HPLC system coupled to a Bruker AmazonX high resolution ion trap, in negative ion mode. The desalted oligonucleotide samples were eluted through a XBridge oligonucleotide BEH C18 column (130 Å, 2.5 µm, 4.6 x 50 mm) using a 5 vol% MeOH, 10 mM ammonium acetate (buffer A) and a 70 vol% MeOH, 10 mM ammonium acetate (buffer B) solvent system at 0.8 mL/min flow. The data was processed using Compass Data Analysis (Bruker) v.4.1 software, and the MaxEnt integrated deconvolution algorithm. Alternatively, LCMS analysis was performed on a Waters ACQUITY UPLC system coupled to a Xevo G2-XS QToF mass spectrometer in negative ion mode. The oligonucleotides were eluted through an AQUITY UPLC oligonucleotide BEH C18 column (130Å, 1.7 µm, 2.1 x 50 mm) using a 75 mM triethylammonium acetate (TEAA, pH 7.0) solution in H_2O (buffer A) and a 75 mM TEAA solution in MeCN (buffer B) at 60 °C and a 0.2 mL/min flow. Leucine enkephalin was used as the reference for the LockSpray correction. The raw continuum data was deconvoluted to produce zero charge mass spectra using ProMass HR for MassLynx (Novatia) software.

Gel Electrophoresis - Native polyacrylamide gel (10%) was prepared by mixing 2.5 mL 30% 29:1 acrylamide:bisacrylamide, 4.25 mL H_2O, 0.75 mL 10×TAE, 75 µL 10% (w/v) ammonium persulfate (APS), and 7.5 µL tetramethylethylenediamine (TEMED). Different percentage gels were prepared by varying the proportions of acrylamide and water. After removing well combs, wells were rinsed with running buffer (1×TAE) using a pipette before loading 2 µL samples typically diluted to 200 nM in loading buffer (1×TAE, 50% glycerol). Native polyacrylamide gels were run at room temperature in 1×TAE buffer at 180 V using a vertical nucleic acid electrophoresis cell connected to a PowerPack basic power supply (BioRad). Samples were combined with 20% loading buffer (0.05% bromophenol blue, 25% glycerol, 1x TAE) prior to running. Non-fluorescent DNA was stained using a 1:1000 aqueous SYBR® Gold nucleic acid gel stain (ThermoFisher) and visualized using a BioRad ChemiDoc™ MP Imaging system. The images were processed using ImageLab software v 6.0.1.

1 × TAE buffer consisted of 40 mM Tris-acetate and 1 mM EDTA. 1 × TAE buffer consisted of 10 mM Tris-HCl and 1 mM EDTA. The native loading buffer consisted of 25 % glycerol and 0.05 % bromophenol blue in 1 × TAE buffer, and was diluted five-fold before use.

Size exclusion chromatography (SEC) analysis was performed on a system composed of a Varian 390-LC-Multi detector suite equipped with a Varian Polymer Laboratories guard column (PLGel 5 μM, 50 × 7.5 mm), two Mixed-C Varian Polymer Laboratories columns (PLGel 5 μM, 300 × 7.5 mm) and a PLAST RT auto-sampler. Detection was conducted using a differential refractive index (RI) and an ultraviolet (UV) detector set to λ = 309 nm. The mobile phase used was DMF (HPLC grade) containing 5 mM NH4BF4 at 50 ˚C at a flow rate of 1.0 mL min-1. Poly(methyl methacrylate) (PMMA) standards were used for calibration. Molecular weights and dispersities were determined using Cirrus v3.3 SEC software.

Zeta potential was measured by the technique of microelectrophoresis, using a Malvern Zetasizer Nano ZS instrument, at room temperature at 633 nm. All reported zeta potential values were the average of at least three runs with at least 40 measurements recorded for 3 runs. Zeta potential was calculated from the corresponding electrophoretic mobilities (μE) by using the Henry's correction of the Smoluchowski equation ($\mu E = 4\pi \varepsilon 0 \varepsilon r \zeta (1+\kappa r)/6\pi \mu$).

Hydrodynamic diameters (D_h) of particles were determined by dynamic light scattering (DLS) using a Malvern Zetasizer Nano ZS with a 4 mW He-Ne 633 nm laser module operating at 25 ^{o}C. Measurements were carried out at an angle of 173° (back scattering), and results were analyzed using Malvern DTS 7.03 software. All determinations were repeated 4 times with at least 10 measurements recorded for each run. D_h values were calculated using the Stokes-Einstein equation where particles are assumed to be spherical, while for cylindrical particles DLS was used to detect multiple populations and obtain dispersity information.

Static Light Scattering (SLS). For the particles in deionized water, light scattering data was collected over the whole angular range, $30 < \theta < 50°$ with the sample maintained at 25°C. Autocorrelation functions calculated by the ALV LSE-5004 correlator unit were recorded at each (θ, c) and the REPES algorithm was used to determine relaxation times, $\tau(\theta, c)$. The data set $\tau(\theta, c)$ was then analyzed to estimate the mean translational diffusion coefficient according to the Stokes-Einstein equation. An empirical measurement was made of the refractive index increment for the polymer in deionized water using a differential

refractometer, model DnDc1260 supplied by PSS GmbH. The light scattering experiments were conducted at 0.01, 0.02, 0.05, 0.10 and 0.20 mg·mL^{-1} to account for concentration effects. Following Andersson *et al.*[1], a Zimm plot was constructed using the Debye method (**Equation 1** and **Equation 2**) to determine the R_g of the nanoparticles. To do this, the R_θ/Kc versus q^2 data were plotted and a third order polynomial model was used to extrapolate $q \rightarrow 0$. The fit's intercept provided the molecular mass according to light scattering (M_{LS}) while the slope at $q^2 = 0$ can be utilized to retrieve R_g at the different concentrations. A first order model was utilized for the $c \rightarrow 0$ extrapolation yielding R_g and M_{LS} (Table S5).

$$\frac{R\theta}{Kc} = -\frac{MRg^2}{3}q^2 + M \quad (1)$$

$$\frac{\partial\, R\theta/Kc}{\partial q^2} = -\frac{MRg^2}{3} \quad (2)$$

The mean translational diffusion coefficient (D_{app}) was calculated from the relaxation times at each angle, $\tau(\theta, c)$ determined from the autocorrelation functions at each angle (θ, c) by the REPES algorithm. The Stokes-Einstein equation was used to determine the hydrodynamic radius (R_h) of the particles. The R_g/R_h ratio gives information about the inside of the spherical particle. A value of 1 indicates a hollow sphere with all the mass in the outer shell (i.e. vesicle). The 50%DNA-PHPMA$_{400}$ nanoparticles have a R_g/R_h ratio of 1.02. The aggregation number ($M_{w,theo}/M_{LS}$) was calculated to be 2.73×10^3 which is in line with a vesicle morphology.[2]

Transmission Electron Microscopy (TEM) analysis was performed on a JEOL 2100 electron microscope at an acceleration voltage of 200 kV. All samples were diluted with deionized water and then deposited onto formvar-coated copper grids. After roughly 1 min, excess sample was blotted from the grid and the grid stained with an aqueous 1 wt% uranyl acetate (UA) solution for 1 min prior to blotting, drying and microscopic analysis.

Cryogenic Transmission Electron Microscopy (Cryo-TEM) imaging was performed on a JEOL JEM-2100 plus microscope operating at an acceleration voltage of 200 kV. Samples for cryo-TEM were prepared on lacey carbon grids (EM Resolutions). After 200-fold dilution with deionized water, 8 µL of sample were deposited onto the grid followed by blotting for approximately 5 s and plunging into a pool of liquid ethane, cooled using liquid nitrogen in order to vitrify the samples. Then, transfer into a pre-cooled cryo-TEM holder using liquid nitrogen, was performed prior to the microscopic analysis.

Confocal Laser Scanning Microscopy (CLSM) was performed on FV3000 (Olympus) confocal microscope and the 60x oil lens was used for imaging. Images were acquired using the 488 nm (green channel) and the 561 nm (red channel) excitation wavelengths. Freshly prepared and purified solutions of FAM-**H2** (green-emitting dye), TAMRA-**cDNA** (red-emitting dye) and mixed 50% DNA_{14}-$PHPMA_{400}$ copolymer nano-objects at 100-fold dilution were deposited on a glass slide before imaged by CLSM. Images were processed using cellSens (Olympus) and ImageJ image processing software. The LAD-1 LED array driver was purchased from Bio Research Centre Co., Ltd. The array was composed of 96 405 nm LEDs which each output a light power of 20 mW at 13.5 V when measured with an LMP-100 light power sensor (sensor area: 5.5 mm x 4.8 mm), placed directly above an array LED. For the Thermomixer setup, the LED-array was suspended over the sample holder *via* a clamp stand. For the Incubator setup the LED-array was placed upon a shaker plate, face up with a 96-microwell plate placed directly upon it, into which 150 µL eppendorfs containing sample were placed.

Experimental Procedures

Synthesis of 4-cyano-4-[(ethylsulfanylthiocarbonyl)sulfanyl] pentanoic acid (CEPA)

4-Cyano-4-[(ethylsulfanylthiocarbonyl)sulfanyl] pentanoic acid chain transfer agent (CEPA CTA) was synthesized according to a previously described process.[3] Sodium ethanethiolate (10.0 g, 0.119 mol, 1 eq) was suspended in 500 mL of dry diethyl ether at 0 °C. Carbon disulfide (7.74 mL, 0.131 mol, 1.1 eq) was subsequently added dropwise over 10 min, resulting to the formation of a thick yellow precipitate of sodium S-ethyl trithiocarbonate. After 2 h of stirring at room temperature, solid iodine (15.1 g, 0.059 mol, 0.5 eq) was added to the reaction medium. After 2 h, the solution was washed three times with aqueous sodium thiosulfate (1 M), water and finally saturated NaCl solution. The organic layer was thoroughly dried over $MgSO_4$ and the crude bis-(ethylsulfanylthiocarbonyl) disulfide was then isolated by rotary evaporation (16.0g, 0.058 mol, 98%).

A solution of bis-(ethylsulfanylthiocarbonyl) disulfide (16.0 g, 0.058 mol, 1 eq) and 4,4′-azobis(4-cyanopentanoic acid) (ACVA) (24.5 g, 0.087 mol, 1.5 eq) in 500 mL of ethyl acetate was heated at reflux for 18 h under N_2(g) atmosphere. Following rotary evaporation of the solvent, the crude CEPA was isolated by column chromatography using silica gel as the stationary phase and 75:25 DCM-petroleum ether as the eluent. The isolated product was

precipitated out of solution by using hexane leaving a yellow-light orange solid. The final product was collected and dried under reduced pressure to afford pure CEPA CTA (10.95 g, 0.042 mol, 36%). ^{1}H-NMR (400 MHz, $CDCl_3$): δ (ppm) 3.35 (q, 2H, S-CH_2-CH_3), 2.38-2.71 (m, 4H, CH_2-CH_2), 1.89 (s, 3H, C(CN)-CH_3), 1.36 (t, 3H, S-CH_2-CH_3). ^{13}C-NMR (100 MHz, $CDCl_3$): δ (ppm) 216.6 (Cc), 176.9 (Ci), 118.9 (Cf), 46.2 (Cd), 33.5 (Cg), 31.4 (Cb), 29.5 (Ch), 24.9 (Ce), 12.8 (Ca). FT-IR (neat): ν (cm^{-1}) 1709 (C=O), 1073 (C=S)), 810 (C-S). HR-MS: m/z $[C_9H_{13}NO_2S_3+Na]^+$ calc. 286.0001 g mol^{-1}, found 286.0001 g mol^{-1}.

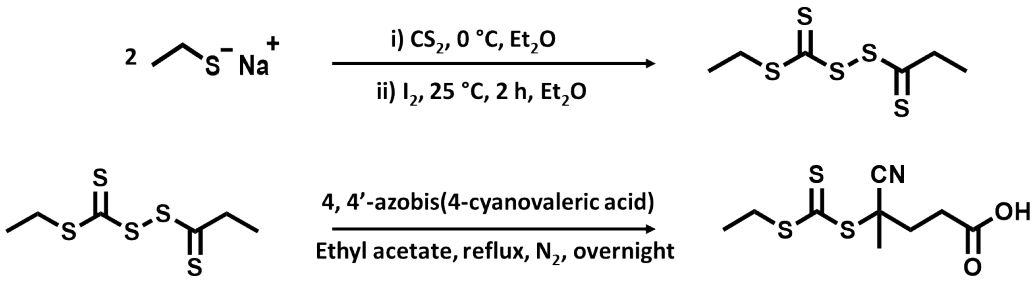

Scheme S1. Synthesis of CEPA-CTA.

Synthesis of poly(ethylene glycol)$_{113}$-CEPA macro-CTA (PEG_{113} macroCTA)

PEG_{113} macroCTA was synthesized according to a previously reported method with slight modification.[4] Poly(ethylene glycol) methyl ether (average M_n=5,000 g mol^{-1}, PEG_{113}-OH) (4.75 g, 0.98 mmol, 1 eq) was dissolved in 150 mL of dry DCM. The resulting solution was then purged with N_2(g) for 30 min. After complete dissolution, CEPA CTA (1 g, 3.8 mmol, 4 eq), DCC (392 mg, 1.9 mmol, 2 eq) and DMAP (23 mg, 0.19 mmol, 0.2 eq) were added to the reaction mixture. The esterification reaction proceeded with stirring at room temperature for 18 h under continuous N_2(g) flow. After this period, further DCC (392 mg, 1.9 mmol, 2 eq) and DMAP (23 mg, 0.19 mmol, 0.2 eq) were added to the reaction mixture and then stirred at room temperature for an additional period of 6 h under continuous N_2(g) flow. The solution was then filtered to remove unreacted DCC and DMAP. The product was collected by 5 times of precipitation using cold diethyl ether as non-solvent, redissolved in deionized water and dialyzed against nanopure water using a 1,000 kDa MWCO membrane for 1 day (yield = 58%). The received PEG_{113} macroCTA solution was lyophilized to give a light yellow powder as the final product (2.90 g, 0.55 mmol, 58%).^{1}H-NMR (400 MHz, $CDCl_3$): δ (ppm) 4.25 (m, 2H, CO_2-C$\boldsymbol{H_2}$), 3.44-3.82 (m, 2H, C$\boldsymbol{H_2}$O), 3.36 (s, 3H, O-C$\boldsymbol{H_3}$), 3.34 (q, 2H, CH_3-C$\boldsymbol{H_2}$), 2.64 (m, 2H, C$\boldsymbol{H_2}$-CO_2), 2.34-2.56 (m, 2H, C(CN)-C$\boldsymbol{H_2}$), 1.87 (s, 3H,

C***H***$_3$-C(CN)), 1.35 (t, 3H, C***H***$_3$-CH_2). SEC (5 mM NH_4BF_4 in DMF, λ = 309 nm) M_n = 4.97 kg mol^{-1}, $Đ_M$ = 1.17.

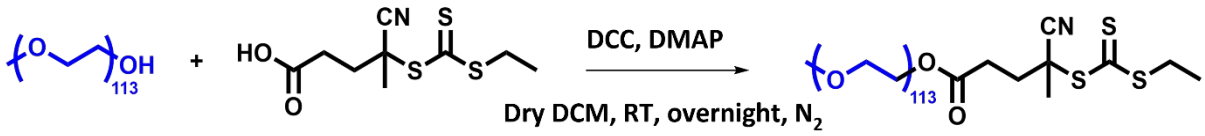

Scheme S2. Synthesis of PEG_{113} macroCTA.

Synthesis of ssDNA$_{14}$ macroCTA by solution approach

Amine-modified oligonucleotide (ssDNA$_{14}$-NH_2) (1 mM, 1 µl, 1 eq.) was mixed with borate buffer pH 7.5 (45 µl), then mixed with CEPA (0.5 M, 20 µL, 500 eq.), EDC·HCl (1 M, 10 µl, 500 eq), NHS (1 M, 10 µl, 500 eq), and DIPEA (1 M, 10 µl, 500 eq) in DMF at 21 °C 400 rpm overnight. Residual chemicals were removed *via* ethanol precipitation by adding 300 vol% ethanol to the reaction mixture and incubating the samples at -20 °C for 6 hours. After centrifugation at 15000 rpm for 30 min at 4 °C the supernatant was removed, and the DNA pellet washed with ice-cold 70% ethanol followed by a repeated centrifugations using the same settings as described above. The supernatant of the washing solution was removed and the DNA pellet was dried on air.

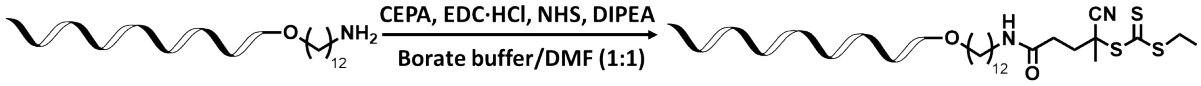

Scheme S3. Synthesis of ssDNA$_{14}$ macroCTA by solution approach.

Synthesis of ssDNA$_{14}$ macroCTA by solid support approach

250 µL of DEAE Sepharose suspension was used as solid support and pipetted into an empty Glen Research column housing and washed with 20 ml of H_2O followed by 12 ml of DEAE binding buffer (10 mM acetic acid and 0.005% Triton X-100) using a syringe. The DNA-NH_2 (10 µM, 1 ml, 1 eq) was loaded onto the column after dissolving in 1 ml of DEAE binding buffer. The column was then washed with 3 ml of DEAE binding buffer, followed by 1 mL of H_2O and 4 ml of DMF to switch the solvent system from water to DMF. At least 50

nmol of oligonucleotide can be loaded onto one 250-µL DEAE Sepharose column. The activated ester solution was composed of CEPA (0.5 M, 100 µL, 500 eq), EDC·HCl (1M, 50 µL. 500 eq), NHS (1 M, 50 µL. 500 eq), and DIPEA (1 M, 50 µL. 500 eq) in solvent (DMF) and was incubated at 21 °C for 30 min before use. The CEPA active ester solution was loaded onto the solid support column in 1 ml of DEAE bind buffer and incubated for 10 min. After the reaction was completed, the column was washed with 4 ml of the reaction solvent (DMF) followed by 3-5 ml of DEAE binding buffer. Finally, the DNA was eluted with 4 ml of DEAE elution buffer (1.5 M NaCl, 50 mM Tris-HCl [pH 8.0], and 0.005% Triton X-100) using a syringe. Product formation was verified via LC-MS: m/z [C159H211N50O91P14S3--H] calc. 4807.900 g mol-1, found 4807.314 g mol^{-1}.

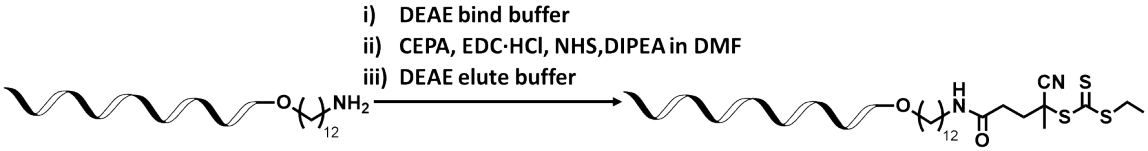

Scheme S4. Synthesis of $ssDNA_{14}$ macroCTA by solid support approach.

Synthesis of DNA−Polymer Conjugates by Photopolymerization-Induced Self Assembly

$ssDNA_{14}$-macroCTA (250.5 µL, 20 mg/mL, 1 eq) was added in a centrifuge tube containing HPMA (2.5 mg for 5%w/w, 5 mg for 10%w/w, 200,300,400 eq). Then, glucose solution (6 µL, 0.84 M), nanopure water (8.4 µL) and GOx solution (8 µL, 12.5 µM) were added into the mixing vial, respectively, resulting in a total volume of 50 μL. The mixture was shaken via vortexer to produce a clear colourless solution which was then transferred to pointed base PCR plate. Mineral oil was added around 200 µL on top of the mixture and the plate was covered by plate seal, and placed in LED array setup, which was contain in an incubator to maintain a temperature of 37 °C. The solution was then exposed to 405 nm light for 2 h, resulting in the solution turning opaque and milky white.

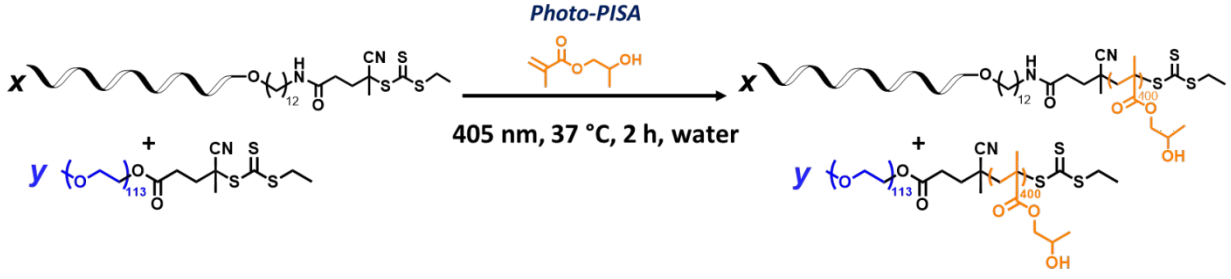

Scheme S5. Synthesis of DNA−Polymer Conjugates by Photopolymerization-Induced Self Assembly.

In order to study the DNA hybridization of the particle surface, a 10 mM $MgCl_2$ in 1×TAE solution was used as a buffer to provide optimal DNA hybridization conditions. The surface hybridisation of nanoobjects formed using different ratios of ssDNA and PHPMA containing diblock copolymers was investigated. Nanopure water (177 or 159 µL) was added into $MgCl_2$ (2 µL, 1M), nanoobject solution (1 µL, 100 mg/ml), TAE (20 µL, 10×) to prepare the particle solution under buffered condition (10 mM) in 1.5 mL tube. The tube was shaken at room temperature at least 30 min and then transferred to a DLS microcuvette. DLS was used to investigate particle size and size dispersity. Subsequently, varying systematic amounts of cDNA (100 µM) was added to the centrifuge tubes, containing the nanoobjects with varying ratios of ssDNA. The centrifuge tube was shaken at room temperature for at least 30 min before investigation by DLS, TEM and confocal microscopy.

Hybridization chain reaction (HCR) study

The HCR reaction was performed under the same conditions for the free ssDNA (SC) and for the ssDNA containing nanoobject systems. Before performing HCR, hairpin1 (**H1**) (50 µM, 5 µL) and hairpin2 (**H2**) (50 µM, 5 µL) were incubated at 95 °C for 2 min then quenched at -20 °C for 1 min. The initiator (**I**) (0.2 eq), **H1** (varied eq.), and **H2** (varied eq.) were added to the ssDNA (SC) or ssDNA containing nanoobject systems (10 µM, 1 eq) under 10 mM $MgCl_2$ in 1×TAE condition in a 1.5 mL tube at room temperature for 30 min. The ssDNA samples were analyzed by native PAGE. ssDNA containing nanoobject systems were also analysed by DLS, TEM, Cryo-TEM and confocal microscopy.

Table S1. List of ssDNA-copolymer nanoparticles obtained from RAFT aqueous dispersion Photopolymerization-Induced Self Assembly and Summary of Characterization Data

Sample	Targeted DP	Actual DP[a]	Conversion[a] (%)	M_n [b] (kg·mol^{-1})	$Đ_M$[b]	D_h[c] (nm)	PD[c]	Morpho-logy[d]
DNA – $PHPMA_{400}$	400	320	~80	123	1.5	90	0.12	S
90% DNA–$PHPMA_{400}$	400	288	~72	108	1.9	219	0.42	S+LR+V
50%DNA– $PHPMA_{400}$	400	385	~96	137	1.5	154	0.04	V
10%DNA]-$PHPMA_{400}$	400	356	~89	54	1.5	186	0.09	V
PEG_{113}– $PHPMA_{400}$	400	352	~88	68	1.4	459	0.03	V

[a] Calculated from ^{1}H NMR spectroscopy (400 MHz) in deuterated MeOD.

[b] Determined by DMF SEC with poly(methyl methacrylate) (PMMA) standards.

[c] Determined by DLS using z-average data.

[d] Determined by TEM. S = Spheres, LR = Lumpy Rod, and V = Vesicle.

Table S2. DNA sequences

Name	DNA sequence (5'- 3')	Extinction coefficient (L (mole·cm)$^{-1}$)
$ssDNA_{14}$ (SC)	TGTAGCGTTGTTGC	128,400
$ssDNA_{14}$-NH_2	/5AmMC12/ TGTAGCGTTGTTGC	128,400
cDNA	GCAACAACGCTACA	139,600
cDNA-TAMRA	/56-TAMN/GCAACAACGCTACA	168,700
ncDNA	TGTAGCGTTGTTGC	128,400
I	GAGGAGGGCAGCAAACGGGAAGAG TCTTCCTTTACGGCAACAACGCTACA	496,900
I-TAMRA	/56-TAMN/ GAGGAGGGCAGCAAACGGGAAGAGTCTTC CTTTACGGCAACAACGCTACA	526,000
H1	CGTAAAGGAAGACTCTTCCCGTTTG CTGCCCTCCTCGCATTCTTTCTTGAGGAGG GCAGCAAACGGGAAGAG	677,600
H2	GAGGAGGGCAGCAAACGGGAAGAGTCTTC CTTTACGCTCTTCCCGTTTGCTGCCCTCCTC AAGAAAGAATGC	678,200
H2-FAM	/FAM/GAGGAGGGCAGCAAACGGGAAGAGT CTTCCTTTACGCTCTTCCCGTTTGCTGCCCT CCTCAAGAAAGAATGC	688,200

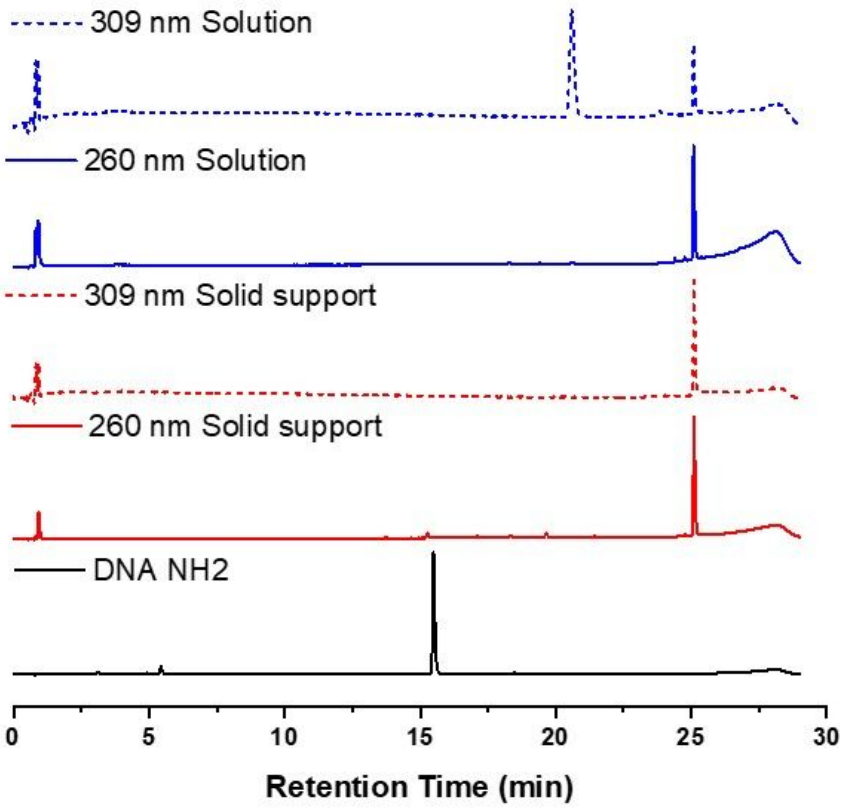

Figure S1. RP-HPLC chromatograms of DNA macroCTA synthesized by solution method (blue line), solid support method (red line) using NH_2-ssDNA as a starting material (black solid line). The chromatograms were investigated at detector wavelength 309 nm (dash line) and detector wavelength 260 nm (solid line). Products eluted with a gradient of buffer A, 0.1 M triethylammonium acetate (TEAA), in a 95:5 mixture of H_2O and acetonitrile and buffer B, 0.1 M TEAA, in a 30:70 mixture of H_2O and acetonitrile.

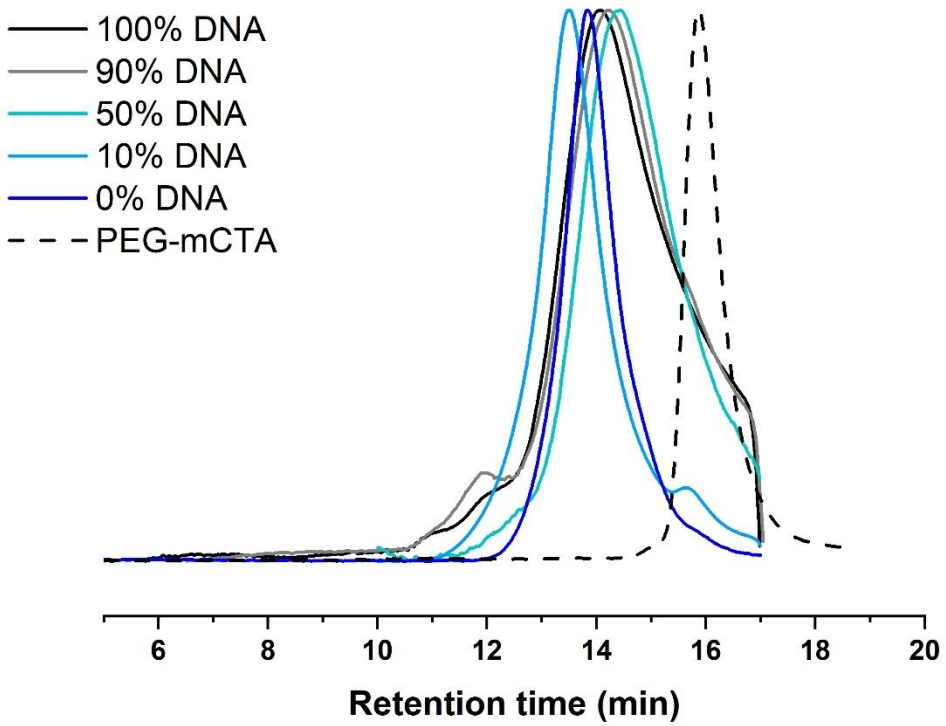

Figure S2. GPC traces of PEG-macroCTA (dot line) and the DNA/PEG polymer conjugates (solid lines) as measured by DMF GPC using polymethylmethacrylate (PMMA) calibration standards.

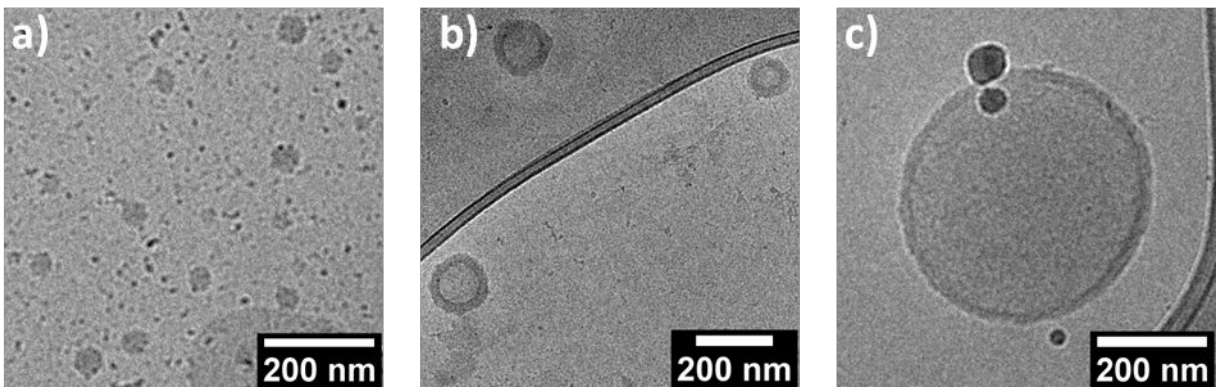

Figure S3. Cryogenic transmission electron microscopy (Cryo-TEM) images of a) DNA – $PHPMA_{400}$, b) 50%ssDNA_{14} – $PHPMA_{400}$, and c) PEG_{113}– $PHPMA_{400}$ assign the copolymer morphology.

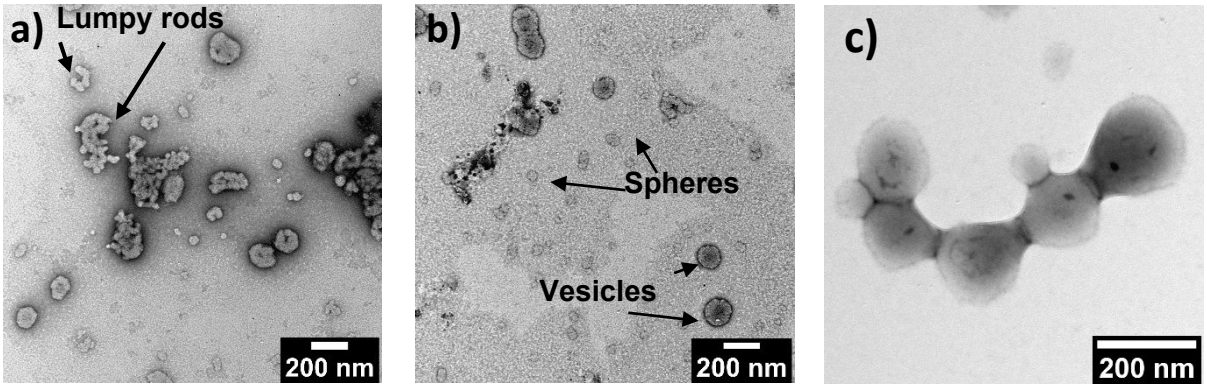

Figure S4. Transmission electron microscopy (Cryo-TEM) images of a) and b) 90%DNA – $PHPMA_{400}$ and b) 10% DNA – $PHPMA_{400}$ diblock copolymer.

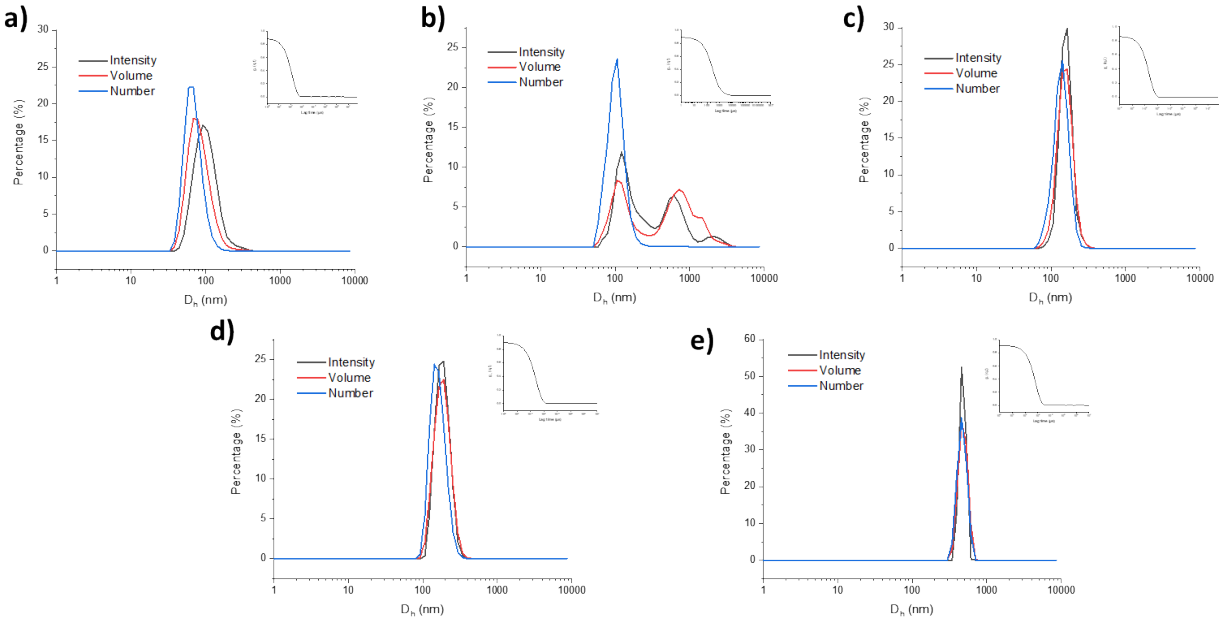

Figure S5. Dynamic light scattering (DLS) of mixed DNA and PEG based objects with different percentages of DNA in the corona a) 100% DNA, b) 90% DNA, c) 50% DNA, d) 10% DNA, and e) 0% DNA.

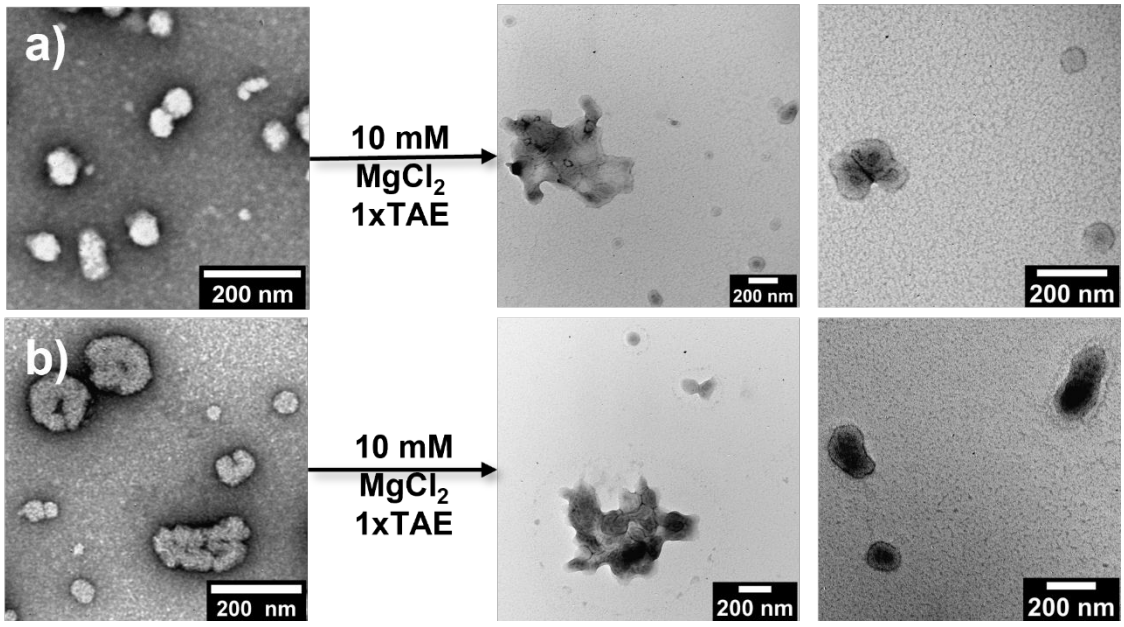

Figure S6. TEM images of a) DNA-PHPMA$_{400}$ particles and b) 50%DNA-PHPMA$_{400}$ particles aggregated when salt/TAE buffer was added.

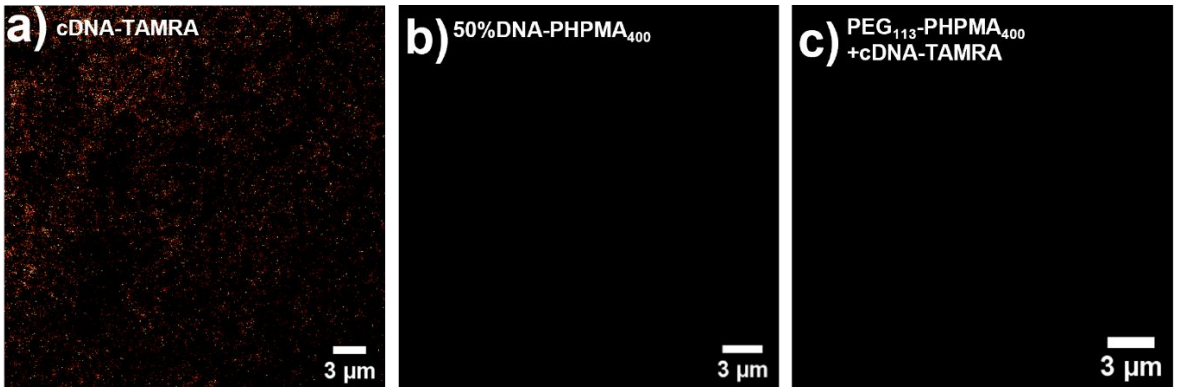

Figure S7. Confocal images of hybridization studying which a) TAMRA-cDNA, b) 50%DNA-PHPMA$_{400}$, and c) PEG$_{113}$-PHPMA$_{400}$+ TAMRA-cDNA.

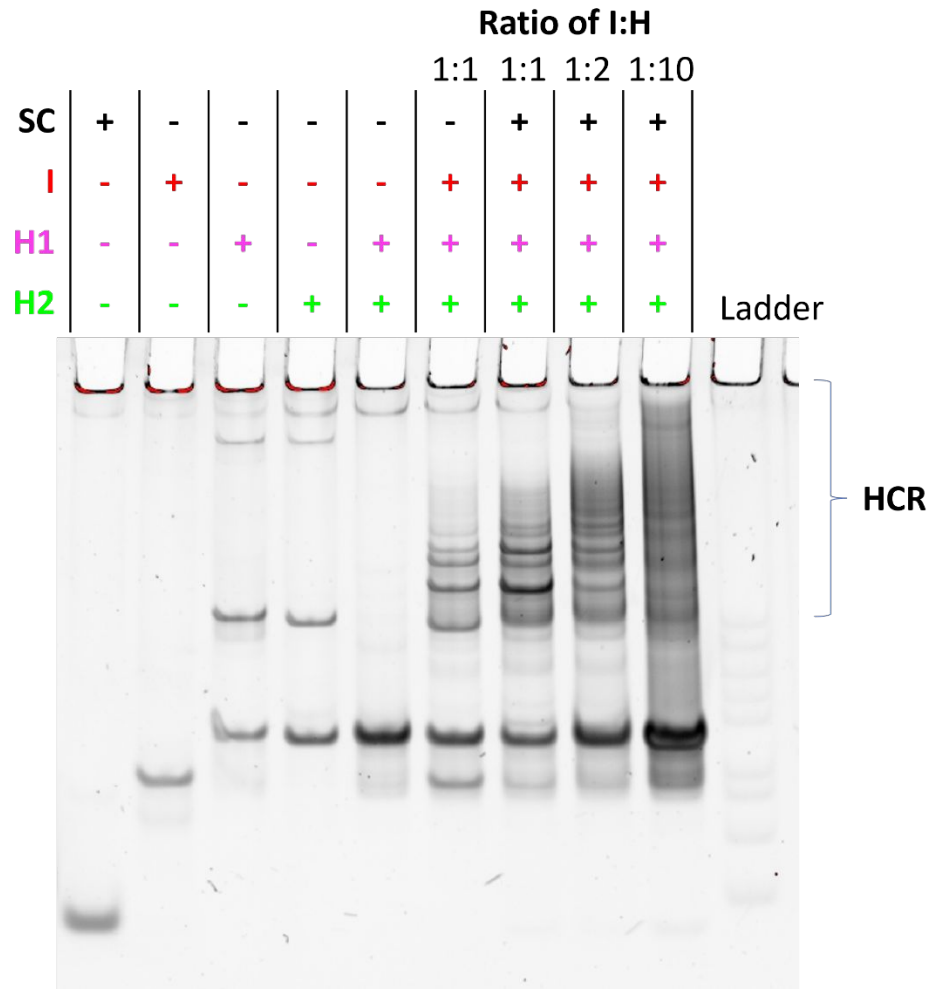

Figure S8. Native poly(acrylamide) gel electrophoresis (10%) of hybridization chain reaction (HCR) study utilizing the ssDNA (SC). The ratios of initiator's concentration to hairpin DNAs' concentration (**I**:**H**) were 1:1, 1:2, and 1:10 with a constant final concentration of 5 μM hairpin DNAs. **H1** and **H2** do not hybridize before triggered by **I**, so no reaction is observed (lane 5). HCR products are only formed when **I** is present (lane 6). Effect of **I**:**H** ratio on HCR amplification (Lanes 7–9): three different ratios of **I**:**H** (1:1, 1:2, and 1:10) in a 5 μM mixture of **ssDNA(SC)**, **I**, **H1** and **H2** were tested. Before mixing, **H1** (50 μM, 10 μL) and **H2** (50 μM, 10 μL) were incubated at 95 °C for 2 min then quenched at -20 °C for 1 min.

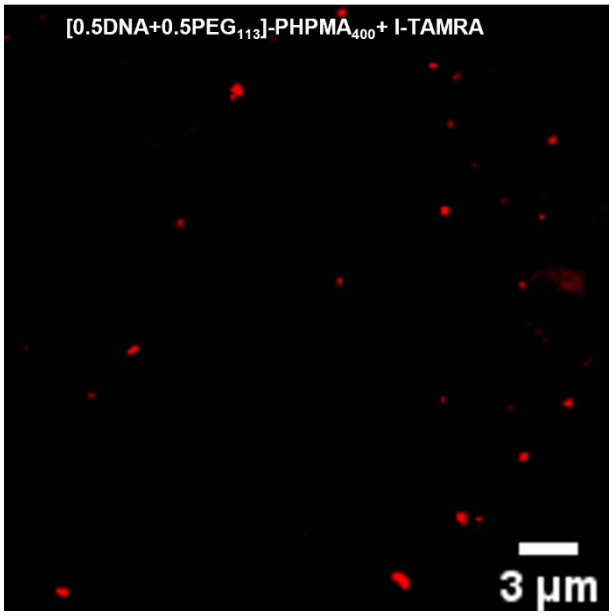

Figure S9. Confocal images of hybridization chain reaction studying of 50%DNA - $PHPMA_{400}$ + I-TAMRA.

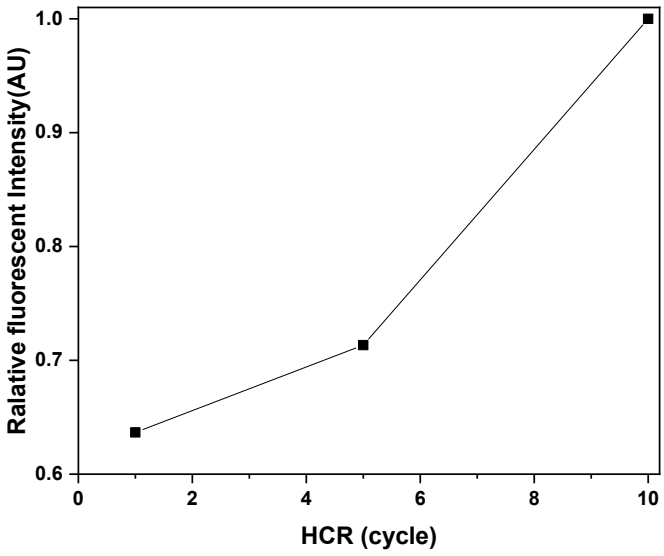

Figure S10. Fluorescence intensity analysis at different HCR Cycles. The presented values were calculated for each particle using the CLSM images from Figure 3g-j, obtained through ImageJ analysis of the CLSM images in the green channel.

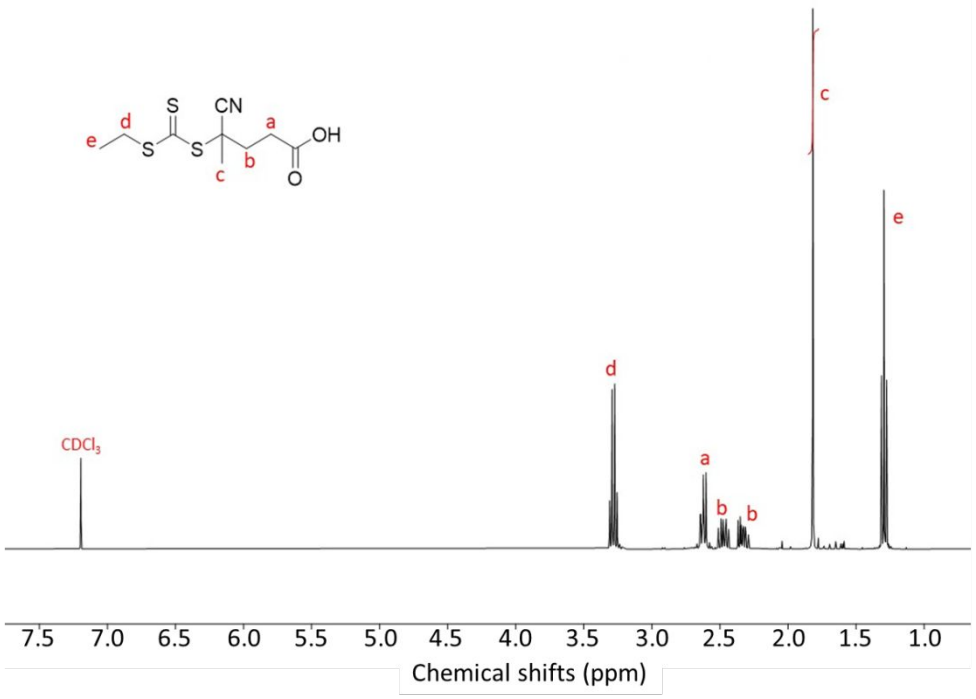

Figure S11. ^{1}H-NMR spectrum of CEPA-CTA in $CDCl_3$.

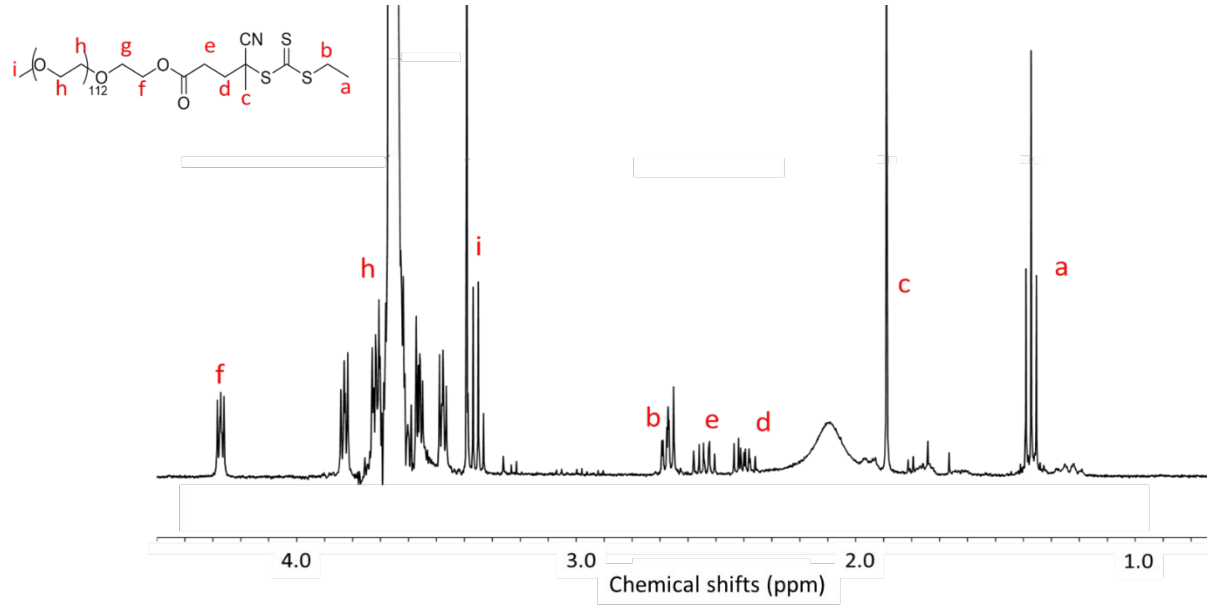

Figure S12. ^{1}H-NMR spectrum of PEG_{113}-macroCTA in $CDCl_3$.

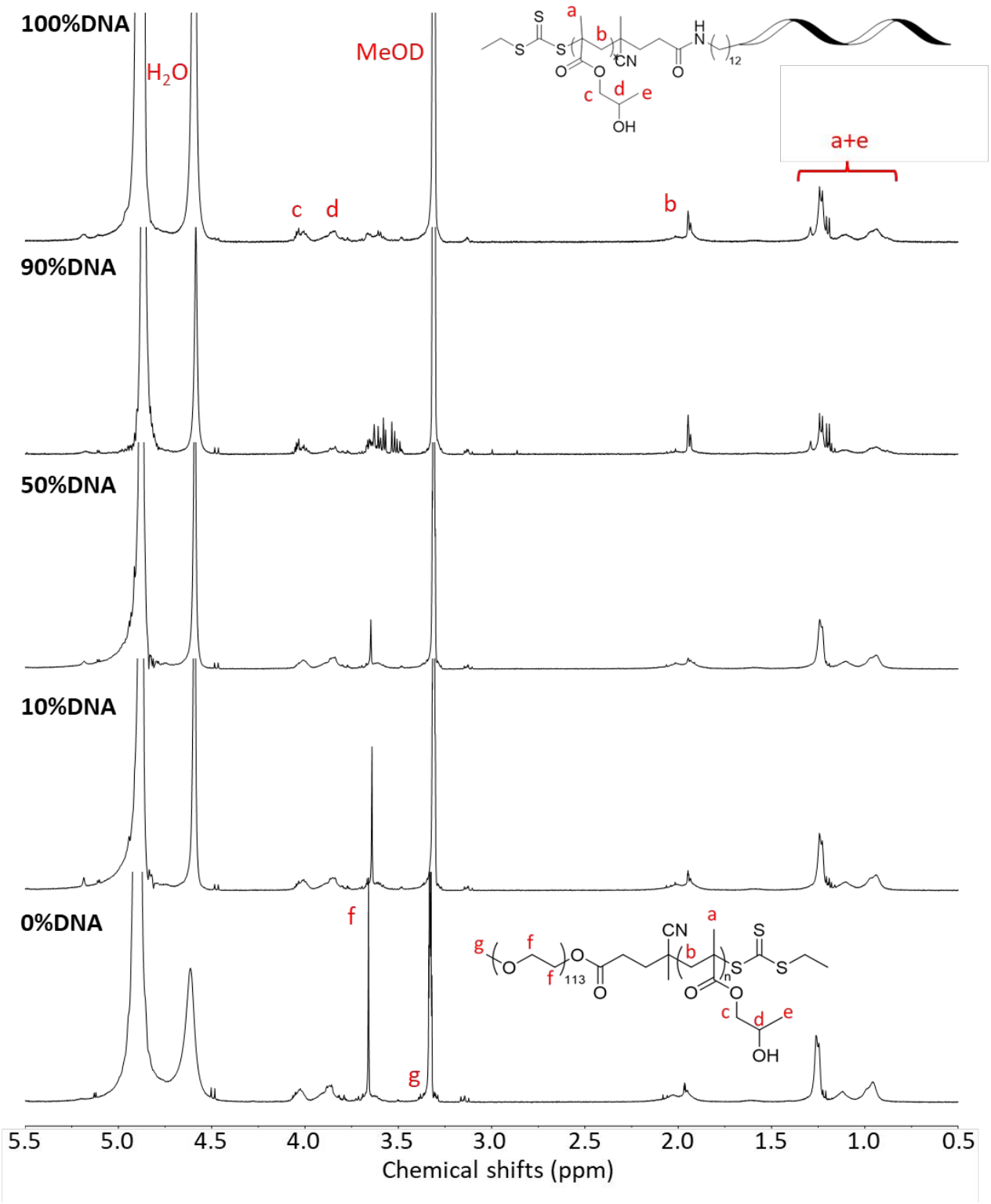

Figure S13. [1]H-NMR spectra of different mole fractions of DNA/PEG polymer conjugates in MeOD

References

1. Andersson, M.; Wittgren, B.; Wahlund, K.-G., Accuracy in Multiangle Light Scattering Measurements for Molar Mass and Radius Estimations. Model Calculations and Experiments. *Analytical Chemistry* **2003,** *75* (16), 4279-4291.
2. Patterson, J. P.; Robin, M. P.; Chassenieux, C.; Colombani, O.; O'Reilly, R. K., The analysis of solution self-assembled polymeric nanomaterials. *Chem Soc Rev* **2014,** *43* (8), 2412-25.
3. Johnson, R. N.; Burke, R. S.; Convertine, A. J.; Hoffman, A. S.; Stayton, P. S.; Pun, S. H., Synthesis of statistical copolymers containing multiple functional peptides for nucleic Acid delivery. *Biomacromolecules* **2010,** *11* (11), 3007-3013.
4. Tan, J.; Sun, H.; Yu, M.; Sumerlin, B. S.; Zhang, L., Photo-PISA: Shedding Light on Polymerization-Induced Self-Assembly. *ACS Macro Letters* **2015,** *4* (11), 1249-1253.

5 : Conclusions and future work

The overall aim of this thesis was to develop low-volume reversible addition-fragmentation chain transfer (RAFT)-mediated photoinitiated polymerization-induced self-assembly (photo-PISA) for the synthesis of DNA-corona polymeric nanostructures. The DNA-polymer nanoparticles were achieved by using a poly(ethylene glycol) macromolecular chain transfer agent (PEG_{113}-macroCTA), a deoxyribonucleic acid macromolecular chain transfer agent (DNA-macroCTA), and 2-hydroxypropyl methacrylate (HPMA) monomer.

Chapter 1 introduced polymer and DNA self-assembly, discussed various polymerization methodologies, including reversible addition-fragmentation chain transfer (RAFT) polymerization and polymerization-induced self-assembly (PISA), and delved into the topics of photo-PISA and low-volume PISA. A brief overview of the DNA nanotechnology, DNA assembly, and DNA-polymer hybrids was presented including a discussion on the important method of achieving morphology and size control nanostructures.

Chapter 2 explored the optimal conditions for low-volume RAFT-mediated photo-PISA, employing a PEG_{113}-macroCTA and HPMA as the core-forming monomer. Two methods (nitrogen glove bag and enzyme-mediated method) were investigated. Here, the reaction was conducted in a 50 µL volume using pointed base PCR plates with final concentrations of 2 µM glucose oxidase (GOx), and 0.1 M glucose was identified as the optimal condition with reasonable reaction time, conversion, particle size, and dispersity of polymerization. In contrast, the nitrogen glove bag method yielded low conversion and showed irreproducibility. We therefore undertook further investigations such as the study of the phase diagram of PEG_{113}-*b*-$PHPMA_X$ which revealed higher-order morphologies with increased DP or solid contents.

In Chapter 3, DNA-macroCTA was utilized as a macroCTA in the optimal low-volume RAFT-mediated photo-PISA under enzyme-assisted degassing from Chapter 1. This chapter was divided into two parts, each focusing on the source of synthesizing DNA-macroCTA *i.e.*, from the Sleiman group and from our group. Part I, DNA-macroCTA from the Sleiman group, synthesized a series of DNA–polymer conjugates derived from HPMA monomers, resulting in high conversion, narrow molecular weight distributions, and narrow particle size distributions. Moreover, the resulting DNA particles were further studied by screening effect from salt, hybridization capability, and functionalization with a fluorescent complementary DNA (cDNA) and imaged by confocal fluorescence microscopy to clearly confirm both hybridization and the presence of DNA on the particle surface. Part II of this chapter focuses on the synthesis of high-purity DNA-macroCTA, as impurities in the DNA-macroCTA can have a large impact on the actual DP of secondary polymer blocks. Part II demonstrates that the synthesis of DNA-macroCTA using *solid support* methods resulted in high purity, a high yield, and scalability without the requirement for HPLC purification, rendering it a more suitable method when compared to the *in-solution* method. Nonetheless, the DNA-polymer nanoparticles obtained from high-purity DNA-macroCTA were not stable in salt solutions *i.e.*, $MgCl_2$, which prevented the study of hybridization under the same conditions as in Part I. The aggregation and deformation of DNA-polymer particles caused by Mg^{2+} inspired the idea of conducting photo-PISA in a salt solution. Interestingly, the results demonstrated a transition in morphologies to higher-order structures, including spherical micelles, short wormlike micelles, long wormlike aggregates, and large rodlike aggregates with hollow cavities, as the salt concentrations increased.

In Chapter 4, the combination of PEG-macroCTA and DNA-macroCTA was investigated to facilitate morphological transitions in the mixed corona of DNA and PEG particles.

The lower DNA proportion on the corona results in reduced electrostatic repulsion on the particle surface, leading to the formation of higher-order morphologies, such as vesicles, and enhancing stability of nanoparticles in salts and buffer solutions. Furthermore, the utilization of hybridization and hybridization chain reaction (HCR) was explored with the mixed corona of PEG and DNA particles.

Compared to the 1 mL benchmark PISA reaction, the low-volume PISA reaction minimizes the usage of high-cost DNA-macroCTA. This low-volume method has the potential to produce reproducible diblock copolymer nanoparticles and DNA-decorated nanoparticles through a simple one-step photoPISA reaction.

Further research efforts may be directed towards exploring their potential applications in the fields of drug delivery and DNA nanotechnology. The selectivity and programmability of DNA, the variety of functional cDNAs or hairpin DNAs, and the stability of vesicular particles produced through PISA could serve as a potent and easily synthesized tool in drug delivery and various bio-related applications. Given the programmable surfaces of these assemblies on particles, they could also serve as a valuable tool for investigating biologically relevant interactions. An intriguing concept that arises is the utilization of a binary mixture of corona DNA-PEG nanoparticles to carry drugs to the targeting point where a drug has released precisely in the body. Utilizing the HCR concept, functional hairpins like aptamer cDNA designed for cancer cells could be incorporated into the particles. This would enable the particles to target specific cells capable of hybridizing or interacting with the aptamer. Potential directions of exploration could include their utilization in the investigation of self-assembled systems that respond to various stimuli, such as light or changes in pH. In the scenario where the responsive corona was modified with dyes exhibiting a solvochromatic shift or a hydration-dependent ON/OFF fluorescence response, these particles could potentially

be employed to detect changes in physiological conditions. The next stages of exploring the therapeutic potential of these particles would involve evaluating their *in vivo* biodistribution and assessing cell toxicity and the stability of particles within cells. Moreover, if therapeutic proteins are encapsulated within the particles, it would be intriguing to investigate the therapeutic proteins process.